University College London

Department of Chemical Engineering

An investigation of the influence of fines size distribution and high temperature on the fluidization behaviour of gas fluidized beds linked with rheological studies

Giovanna Bruni

September 2005

A thesis submitted for the degree of Doctor of Philosophy

in the University of London

ProQuest LLC
789 East Eisenhower Parkway
P.O. Box 1346
Ann Arbor, MI 48106-1346

to my mother and my father
who gave me roots
and wings to fly

Abstract

The influence of process conditions, such as temperature and presence of fines, on the fluidization behaviour of gas fluidized beds is of major importance in industrial fluid bed processes, which are often operated at temperatures well above ambient and where it is common practice to add fine particles to improve the reactor performance. Several works have demonstrated that process conditions can influence the role of the interparticle forces (IPFs) in the fluidization behaviour of powders. In particular, the beneficial effect on fluidization of adding fines to the bulk of the material is well known. However, the influence on fluidization of the different IPFs introduced when adding "big" fines (e.g. 26-45 μm) or "small" fines (e.g. 0-25 μm) has not been evaluated yet. Given the complexity of the phenomena involved, a direct quantification of the particle-particle interactions in fluidized beds and of their changes at process conditions is very difficult. Within this framework, powder rheology represents an appealing tool to evaluate indirectly the effects of the IPFs on fluidization.

The present work investigated the effects of adding different fines cuts on the fluidization and the rheological behaviour of an alumina powder. To this end, a two-fold approach was followed and a link between the two aspects of the work was sought.

On the one hand, the fluidization behaviour of the alumina was studied at process temperatures ranging from ambient to 400°C and by adding to the material previously deprived of fines two fine sub-cuts of nominal size 0-25 and 26-45 μm respectively. Experiments were carried out changing the total fines content from 22% to 30% by weight.

On the other hand, a new equipment (the msFBR) was designed, built and commissioned at ambient temperature to determine the rheological behaviour of the powders containing different fines sub cuts. Rheological experiments were carried out at different rates of aeration and impeller depths. In parallel, the failure properties of the materials were determined using a shear cell.

A model was developed, based on the failure properties of the materials, to determine the stress distribution corresponding to any given rate of aeration in the msFBR. This allowed a true comparison to be made between the rheological behaviour of different powders, aiding the assessment of the effect of fines size distribution on powder rheology. Moreover, the model allowed the prediction of the torque measured with the msFBR and the assessment of the effect of aeration on powder rheology.

The interpretation of the failure properties of the materials provided an indication of the capability of the powders to flow and underpinned the link between the fluidization and the rheological behaviour below the minimum fluidization conditions, interpreted as the capability of the powders to fail under a certain load and their capability to attain fluidization.

Acknowledgements

The most heartily thank you is for Dr Paola Lettieri. Paola has been a supervisor, a guide and a friend all rolled into one beautiful person. I cherish Paola for providing me with endless encouragement and affectionate criticism throughout the time of my PhD. I could have never asked for a better supervisor.

I owe a great debt to Dr David Newton for his technical insight and for his dedication in the final stage of the writing up of this thesis. In particular, I ought to thank David on behalf of the readers of this thesis, for having taught me that a sentence should not be longer than five lines. I also wish to thank Professor John Yates for his invaluable insight into fluidization, always conveyed with impeccable gentleman manners.

I am very thankful to Dr Tim Elson for having contributed to this work. I would also like to thank Alessandro Colafigli and Fred Balligand for their help with the rheological experiments.

I am grateful to Professor Massimo Poletto and Dr Diego Barletta from the University of Salerno for the inspirational collaboration. In particular, I would like to thank my dear friend Diego for all the invaluable discussions, always of great intellectual stimulation, for the likes of powder technology and the philosophy of life.

I would like to thank Professor Tim Druitt for introducing me to the fascinating world of volcanology and for being such a good example of what doing research passionately means.

Many thanks are due to the technical staff of the department of Chemical Engineering at UCL. In particular, to Martin Town and John Graham for their patience and sense of humour during the everything-goes-wrong times of the commissioning of the msFBR and to Julian Perfect for his unique philosophical insight into technical matters.

I acknowledge the financial support of the UK Engineering and Physical Science Research Council (EPSRC) and of BP Chemicals Ltd. I also acknowledge the Centre for Scientific Enterprise Ltd (CSEL) for a PhD extension scholarship to study the commercialisation of the technology developed in this PhD and for giving me access to London Business School MBA electives.

A tender thought goes to the memory of Jason Lum, the soul of the basement labs. Jason filled them with his calm and soothing presence and with his unfailing smile. This work contains a bit of him.

A special thanks goes to the "Italian gang" at UCL: Paolo "il Paglia", Damiano "l'amico Rossetti", Marcello "il Murru", Federica "I love you all", Andrea "Scuzz" and Luca "Pezz'asino" for making me feel at home even in the gloomiest British weather.

Thank you to all my PhD fellows Prim, Sarah, Carlos, Karolina, Marta, Wael and Max with whom I shared the darkness of the basement labs and the joyful brightness of a lager on a Friday night. Thank you also to Luca M., Olu, Liban and to my dear friend Rachele for their patient support in the stressful yet exhilarating time of the writing up of this thesis.

I am deeply grateful to my dear friends Maria Teresa and Nick, the artistic counterpart of my PhD years. Maria Teresa and Nick filled my PhD time with their unique, inventive and original perspective of the world, which enriched me and my working style immensely.

I would like to thank my "perfect" flatmate Sagit, for having shared with me much more than just a flat in these great four years of my life.

There are no words to thank Alessandra. Everybody embarking on a PhD should have a friend from childhood around. They are the only people who can understand, forgive and love a final year PhD student.

I would like to thank my grandmother, Nonna Gilda, born in 1906 and still one of the firmest believers in the progress of science and technology, for asking me what fluidization is and for having kindly listened to my answer.

Finally, my most heartfelt thought goes to Luigi, for his love, for understanding the importance of this experience and for having made distance nothing more than a geographical issue.

Contents

List of Figures

List of Tables

1 Introduction

Fluidization was first employed during World War II following a desperate need for aviation gasoline. Due to its great potential for gas-solid reaction engineering, fluidization was soon recognised to be an innovative and successful oil refining technology. Since then it has been applied to many other areas, becoming a firmly established technique in the processing industries.

1.1 The phenomenon of fluidization

"Fluidization is the operation by which solid particles are transformed into a fluid-like state through suspension in a gas or liquid" (Kunii and Levenspiel, 1991).

If a fluid is passed upward through a bed of particles at low velocity it merely percolates through the void spaces between the stationery particles. This is a fixed bed. The flow through a fixed bed is usually described by the Ergun equation (Ergun, 1952):

$$\Delta P = 150\frac{\mu H u}{(\phi d_p)^2}\frac{(1-\varepsilon)^2}{\varepsilon^3} + 1.75\frac{\rho_f u^2}{\phi d_p}\frac{(1-\varepsilon)}{\varepsilon^2} \qquad \text{Eq. 1}$$

where H and ε are the height and the voidage of the bed, μ and ρ_f are the viscosity and density of the fluid, u the fluid velocity and d_p and ϕ the particle diameter and sphericity respectively. According to the Ergun equation, the pressure drop across the bed due to the friction between the gas and the particles increases linearly with the gas superficial velocity in the laminar regime and with the square of the velocity when the inertial forces are dominant.

When increasing the fluid velocity, a point is reached where the drag force exerted by the fluid on the solids equals the buoyant weight of the bed. A further increase of the fluid velocity causes no further increase in the pressure drop across the bed. The pressure drop across the bed is equal to the weight of the bed per unit cross sectional area.

This phenomenon is known as fluidization and the bed is referred to as an incipient fluidized bed or a bed at minimum fluidization. The velocity of the fluid and the voidage of the bed at minimum fluidization condition are denoted as u_{mf} and ε_{mf} respectively.

In this condition the behaviour of the fluid-solid system is analogous to that of a liquid with an average density ρ_b:

$$\rho_b = (\rho_p - \rho_f)(1-\varepsilon) \qquad \text{Eq. 2}$$

where ρ_p and ρ_f are the solid and fluid densities, respectively. The surface of the bed maintains a horizontal level when the bed is tilted; when two beds are connected their levels equalize; objects with density lower than ρ_b will float on the bed surface while objects with density higher than ρ_b will sink to the bottom of the bed.

The behaviour of the fluid-solid suspension for further increases in fluid velocity depends on the physical and geometrical characteristics of the solid and on the physical properties of the fluid. At fluid velocities higher than u_{mf} the bed can either show a homogeneous expansion (particulate or homogeneous fluidization) or give rise to the formation of cavities with a solid concentration close to zero, similar to bubbles in a liquid, which rise to the bed surface (aggregative or bubbling fluidization). The velocity at which the first bubble forms is called the minimum bubbling velocity, u_{mb}.

Liquid-solid systems are often characterised by a homogeneous fluidization, while gas-solid systems do so only under special conditions, usually using fine light particles or fluidizing at high pressure.

The fluid-like properties of fluidized beds make them attractive for industrial processes where a solid (often the catalyst for a reaction) and a gas are to be put in contact. Moreover, the rapid mixing and circulation of solids in bubbling beds allows

Table 1 *Applications of Fluidized Beds*

Process	**Example / Products**	**Process Conditions**	**Fines Content (< 45 μm)**
Drying of solids	Inorganic materials	60-110°C; 1atm	variable
	Pharmaceuticals	60°C; 1atm	0-100%
Calcination	Limestone	770°C; 1atm	variable
	Alumina	550-600°C; 1atm	0-50%
Granulation	Soap powders	5°C; 1atm	< 5%
	Food; Pharmaceuticals	20-40°C; 2-3atm	0-100%
Coating	Food; Pharmaceuticals	20-80°C; 2-3atm	> 50%
Roasting	Food industry products	200°C;1atm	< 2-3%
	Sulphide ores (FeS_2)	650-1100°C; 1atm	< 2-3%
Synthesis Reactions	Phthalic anhydride	340-380°C; 2.7atm	< 10%
	Acrylonitrile	400-500°C; 1.5-3atm	> 20%; < 50%
	Ethylene dichloride	260-310°C;1-10atm	> 20%; < 30%
	Maleic anhydride	400-500°C; 4atm	> 20%; < 30%
	Polyethylene	75-120°C;15-30atm	0%
Thermal/ Catalytic Cracking	Ethylene; Propylene	750°C;1atm	10-30%
	FCC	650-750°C, 1-3atm	10-30%
Some Other Applications		**Process Conditions**	**Fines Content**
Combustion/Incineration of waste solid		800-900°C; 1-10atm	< 5%
Gasification of coal and coke/solid waste		800°C; 1-10atm	< 5%
Biofluidization, cultivation of micro-organism		30°C; 1atm	100%
Semiconductor Industries		300-100°C; 1atm	100%
Nuclear Industry		350°C	0%
Pyroclastic Flows		200-700°C	50%

for a uniform temperature in the system. Therefore, high temperature operations in fluidized beds can be controlled simply and reliably.
Some examples of industrial applications of fluidization are presented in Table 1. This reports the range of temperatures and pressures at which the processes are run and the amount of fines (particles with diameter below 45μm) generally employed in each case. Table 1 shows that a significant number of the industrial applications of fluidization are carried out at temperatures above ambient and with the addition of fine particles.

1.2 Objectives of the work

This work, sponsored by EPSRC and BP Chemicals Ltd, is aimed at investigating the flow properties of fluidized particles under realistic process conditions, such as temperature and addition of fines to the bulk of the material. In particular, the influence of fines size distribution, fines content and high temperature on the fluidization behaviour of an alumina powder was investigated. The rheological behaviour of the alumina powders was also studied at ambient temperature. The final goal of the project was to determine a link between the observed fluidization behaviour and the rheological measurements.

The industrial employment of many fluidized bed processes involves processes that are very dependent on the operating conditions, as shown in Table 1. However, a satisfactory understanding of the phenomena that are responsible for modifications in the behaviour of fluidized beds when changing the process conditions has not been achieved yet. Although a number of research works have been carried out on the influence of temperature on fluidization, findings are still controversial, as reported by Knowlton (1992) and Yates (1996) in their reviews on the subject. Much of the controversy still remains because the relative importance of the interparticle forces (IPFs) and the hydrodynamic forces (HDFs) on the flow behaviour of the particles at process conditions are undefined.
Most of the disagreement on the relative role of HDFs and IPFs on the fluidizability of powders lies in the uncertain nature on the IPFs involved and in the difficulty of measuring them directly. Seville and Clift (1984) approached this problem

introducing IPFs in a controlled manner and monitoring changes in the fluidization behaviour. Recent work (Lettieri, 1999) showed how the combined effect of temperature and presence of liquid can enhance the role of IPFs causing changes in the fluidization behaviour. However, the quantification of the IPFs involved in fluidization and of their effects on fluidization at process conditions remains unresolved.

The role of the IPFs on changes in the fluidization behaviour at process conditions can also be enhanced by the addition of fine particles (< 45μm). The beneficial effect on fluidization of adding fines is well known and widely reported (Rowe et al., 1978; Abrahamsen and Geldart, 1980; Newton, 1984). These works suggested that the IPFs can contribute to the stability of the bed, by increasing the voidage of the dense phase and increasing the capability of the bed to retain aeration gas. For this reason, it is typical for industrial applications which employ fines addition to add between 10-50% by weight of fine material in order to maximize reactor performance, as shown in Table 1.

However, the relative importance of the various fine sub-cuts (0-25, 26-45 μm) on the enhancement of the fluidization behaviour due to fines addition has not been fully evaluated as yet. In other words, the influence on fluidization of the IPFs introduced when adding "big" fines or "small" fines has not been fully explored and quantified yet. The present work addressed this issue by studying the effect on fluidization of adding big fines (25-45 μm) or small fines (0-25 μm) to the same fines-free material at ambient and with increasing temperature.

Given the complexity of the phenomena involved, a direct quantification of the particle-particle interactions in fluidized beds and of their changes at process conditions is very difficult. Studies on the rupture energy needed to separate two individual particles have been carried out at ambient and with increasing temperature (see Fairbrother, 1999; Pagliai, 2005). However, direct measurements of the particle-particle interactions in the bulk of the powder are far more difficult to set up.

Within this framework, powder rheology represents an appealing tool to evaluate indirectly the effects of the IPFs on fluidization. A great deal of research has been

carried out over the last fifty years in order to define and measure, by means of simple tests, parameters apt to characterize and predict the flow properties of solid materials. To this end various approaches have been undertaken. On one hand, stationary measurements (angle of repose, Hausner ratio etc.) have been proposed as simple tests to predict the flowability of bulk powders. On the other hand, dynamic tests (shear cell type tests and viscometer type tests) have been used as a mean for determining the flow characteristic of powders. However, the relationship between the rheological properties of powders and the corresponding fluidization behaviour is far from being unequivocally defined. Most of the works proposed only qualitative links between the rheological behaviour and the corresponding fluidization behaviour. In addition, findings are still very difficult to relate to each other, mostly due to the variety of the techniques employed which make standardisation of rheological tests very difficult.

Furthermore, little effort has been put into the study of the changes induced by process conditions (temperature, presence of fine, presence of liquid) on the rheological behaviour of powders.
Some works (Reiling, 1992; Newton et al., 1999; Kohe et al., 1991; Lettieri et al., 2001) attempted a parallel analysis of the effects of process conditions on the rheological and the fluidization behaviour. However, a more systematic assessment of the independent and the combined effects of process conditions on fluid bed rheology and fluidization still needs to be accomplished.

In this work a rheological approach was sought to determine the rheological properties of alumina powders at process conditions (addition of fines) and to find a link between their fluidization and rheological behaviour. In particular, the effect on fluidization and rheology of adding big fines (25-45 μm) or small fines (0-25 μm) to the same fines-free material was investigated.

1.3 The experimental approach

In order to tackle the problem of assessing the fluidization behaviour of powders at process conditions, a twofold approach was adopted in this study, as schematically presented in Figure 1. On the one hand the investigation of the fluidization behaviour

at process conditions by means of standard fluidization tests; on the other hand the characterization of the flow properties of the same powders by means of rheological tests. The challenge of the project was to link the rheological measurements to the corresponding fluidization behaviour of the powders in order to achieve a physical understanding of the effect of process conditions on fluidization.

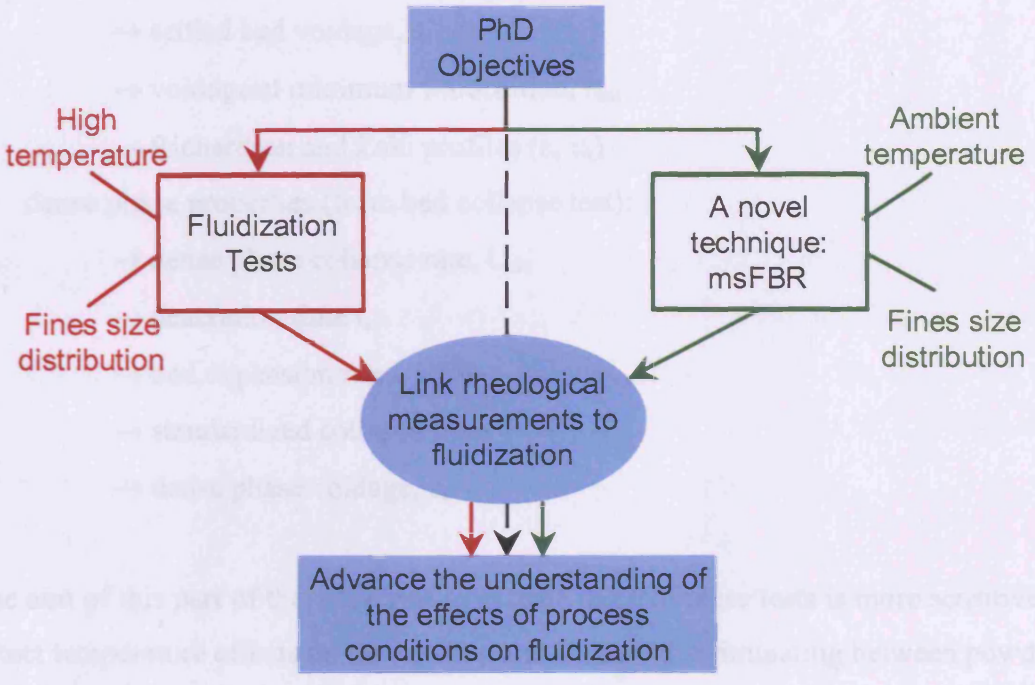

Figure 1 *Schematic representation of the aim and objectives of the work*

The main material chosen for this study was an alumina powder provided by BP Chemicals Ltd and obtained from Laporte Chemicals, where it is used as a base for catalysts. A modelling material such as soda glass ballotini was also used in the rheological part of this study (chapter 5) as a reference material. In order to study the effect on fluidization of changing the size distribution of the fines fractions, several samples of alumina were created by separating and blending different size fractions in different proportions. The effect of temperature on the fluidization behaviour of the alumina samples was studied by ranging the temperature from ambient to 400°C, a range chosen as it is representative of many industrial applications, as shown in Table 1.

The fundamental fluidization parameters were measured for each alumina sample with increasing temperature using a 140 mm diameter x 1000 mm tall heated gas fluidized bed. The parameters measured included:

- minimum fluidization velocity, u_{mf}
- bed expansion profiles:
  - → settled bed voidage, ε_s
  - → voidage at minimum fluidization, ε_{mf}
  - → Richardson and Zaki profiles (n, u_t)
- dense phase properties (from bed collapse test):
  - → dense phase collapse rate, U_{de}
  - → deaeration time t_s
  - → bed expansion ratio, BER
  - → standardized collapse time, SCT
  - → dense phase voidage, ε_d

The aim of this part of the work was to assess which of these tests is more sensitive to detect temperature effects on fluidization and is more discriminating between powders differing in the fines size distribution. Experimental values of u_{mf} and U_{de} were also compared with predictions, to evaluate the ability of some of the currently used correlations to predict the behaviour of powders at process conditions.

The rheological part of the work was carried out using a mechanically stirred Fluidized Bed Rheometer (msFBR), which has been specially designed, built and commissioned at University College London as a part of the present PhD work. The msFBR allows measurements of the torque exerted on an impeller rotating at low speeds in the bed. In particular, the experiments carried out in this study investigated the effect on the torque measurements, at ambient temperature and below the minimum fluidization condition, when changing:

- impeller depth , ID or z_i
- aeration rate, $\Delta P/\Delta P_c$

A Peschl Schear Cell was used to determine the failure properties of the alumina samples and the ballotini:

- static angle of internal friction and cohesion, φ and C
- dynamic angle of internal friction and cohesion, δ and C_δ
- angle of wall friction and adhesion, φ_w and A
- effective angle of internal friction φ_e

The failure properties measured with the Peschl Schear Cell were used to determine the stress distribution of the powders in the msFBR below minimum fluidization, by using a modified version of the Janssen's analysis for silo design (Janssen, 1895). The idea was to associate each torque measurement taken with the msFBR to the corresponding stress distribution and thus allow comparisons to be made between the rheological behaviour of different powders. In this way the effect of the fines size distribution on the rheological behaviour below u_{mf} could be assessed.

A model to predict the torque measured with the msFBR below the minimum fluidization conditions, based on the knowledge of the failure properties of the materials, was also derived. The model provided insight into the effect of aeration on the bed rheology of the powder analysed.

Finally, the ultimate goal of the experimental campaign was to find correspondences between the rheological and the fluidization behaviour of the various alumina samples analysed. In particular, a link was found between the differences detected by means of the fluidization tests and the differences in the rheological behaviour determined below the minimum fluidization conditions.

1.4 Commercialisation of the msFBR

The mechanically stirred Fluidized Bed Rheometer has gained the author of this thesis a scholarship from the Centre for Scientific Enterprise Ltd, a joint venture between University College London and London Business School aimed at creating and supporting interdisciplinary projects that join UCL scientific expertise with the

entrepreneurial know-how offered at LBS. The scholarship was intended to support the study of the commercial feasibility of an innovative technology and provided access to courses in entrepreneurial subjects within the London Business School MBA program.

In particular, the msFBR was the object of a study carried out as a group project within the course "New Technology Ventures". Appendix 2 of this thesis reports the document that was produced by the group at the end of the course.

The report was written for non technical people and it might contain some oversimplifications of the work carried out in this thesis. Nonetheless, it provides a different and interesting perspective on the approach to science and technology.

2 Literature Survey

In this chapter a literature survey on how process conditions affect fluidization and a brief review of works concerning powder flowability measurements tests are reported. The survey is introduced by the description of some classical fluidization concepts, such as powder classification (section 2.1). A brief review of the interparticle forces is given in section 2.2. Section 2.3 reports on the Richardson and Zaki equation.
Section 2.4 reports on works carried out to assess the effects on fluidization of process conditions, such as temperature (section 2.4.1) and presence of fines (section 2.4.2). Section 2.5 reports on the various methods employed to determine the "flowability" of powders. These are divided into methods where a stationery property is evaluated and related to the flow properties of the powder (section 2.5.1), shear cell type of measurements where the measurement is dynamic but the sample is confined and compressed (section 2.5.2) and tests where the rheological properties, namely the viscosity, are measured in the bulk of the powder (section 2.5.3). Finally, studies concerned with the search for a direct link between rheological properties of powders and fluidization behaviour are examined (section 2.6)

2.1 Geldart's classification of powders

Geldart (1973), in the attempt to classify the different fluidization behaviours, proposed an empirical classification based on the mean particle size and on the gas and particle densities. Boundaries between these groups were proposed in the form of a dimensional plot of $(\rho_p - \rho_f)$ versus d_p as shown in Figure 2.

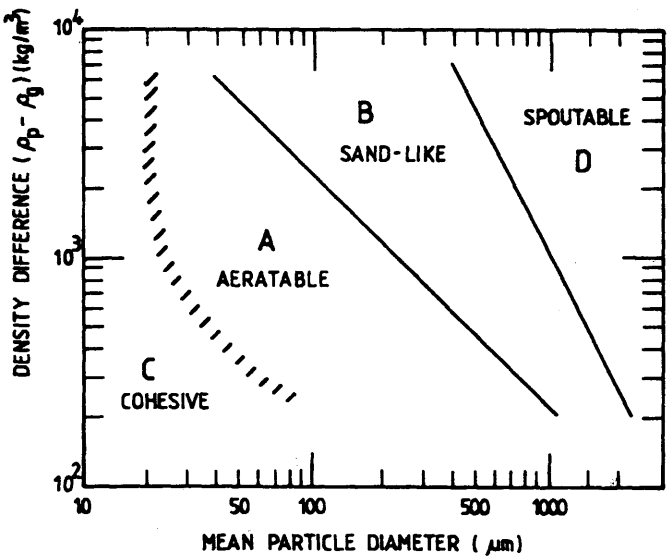

Figure 2 *Geldart classification for air at ambient conditions*

Geldart identified four typical fluidization regimes for materials fluidized with air at ambient conditions, which he indicated as A, B, C and D.

Group C materials are very difficult to fluidize due to their cohesive nature. The behaviour of this group of powders is strongly influenced by the interparticle forces, which are considered to be greater than those exerted by the fluidizing gas. The gas cannot readily separate particles and channelling occurs, causing in most cases poor mixing and heat transfer. Interparticle forces and their effect on the fluidization behaviour have been studied for many years. A brief survey on the subject is reported in section 2.2.

Group A powders are those which exhibit a stable region of non-bubbling expansion between u_{mf} and u_{mb}. Geldart (1973) defined these powders as those for which $u_{mb}/u_{mf}>1$. The phenomenon of uniform expansion, or delayed bubbling, has been the subject of much research and debate as to what the reasons are for this behaviour. The mechanism of bubble free expansion of gas fluidized beds has been assumed by some workers to be the same as the homogeneous expansion in a liquid fluidized bed, to which the Richardson and Zaki (1954) correlation applies. This is discussed in section 2.4.

At gas velocities above u_{mb} bubbles begin to appear. The flow of bubbles produces high solids and gas back mixing, which makes the powder circulate easily around fluidized units. Bed to surface heat transfer is good. A maximum stable bubble size, dependent on the particle diameter, has been defined for those materials, see Geldart (1986). When the fluidizing gas is suddenly cut off, the dense phase collapses at a constant rate, as shown in Figure 9b.

Group B powders are characterised by having $u_{mb}=u_{mf}$. Bed expansion is small and the bed collapses quickly when the gas supply is cut off, as shown in Figure 10. Bubbles rise faster than the interstitial gas velocity, coalescence is the dominant phenomenon and there is no evidence for a maximum bubble size, as defined by Geldart for group A materials. The interparticle forces are considered to be negligible for these powders.

Group D powders. The distinction between this and the previous groups concerns the rise velocity of the bubbles, which in general is less than the interstitial gas velocity. The gas velocity in the dense phase is high and solids mixing is relatively poor. Therefore, back mixing of the dense phase is small.

The boundary regions shown in Figure 2 are not fixed boundaries, especially when process conditions are taken into account. It has been reported in literature that materials can shift the C-A boundary in case of stronger surface forces, caused for instance by the relative humidity of the fluidizing gas, see Geldart et al. (1984). Seville and Clift (1984) added systematically small amounts of a light oil to a group B powder, thereby causing its behaviour to change to that of group A and, eventually, to group C. Lettieri (1999) showed how process conditions (high temperature, presence of liquid and the combination of the two) can cause some group A materials to behave like group C. Therefore, the suitability of using the Geldart classification to assess the flowability of powders is questionable when process conditions, such as temperature, addition of fines or presence of liquids are introduced.

2.2 Interparticle forces

Section 2.1 showed how the forces acting between adjacent particles can affect the fluidization behaviour of powders. It is well known that group C powders are difficult to fluidize. The commonly accepted reason for this behaviour is the dominance of surface forces over the hydrodynamic forces. The ratio of the surface forces to the body forces increase with diminishing particle size. It is also well established in the literature that interparticle forces also exist in group A powders, although their importance as compared to body forces is not yet unequivocally defined. This is mainly due to the difficulty in determining the nature of the interparticle forces involved and in quantifying their effect on the fluidization behaviour. In group B powders, body forces are believed to be dominant over interparticle forces.

Interparticle forces have been the subject of many studies over the years. However, the first systematic investigation of interparticle forces in fluidized beds did not appear until the study of Baerns in 1966 (Baerns, 1966). Since then, many authors have speculated as to the origins of these forces. They are probably caused by several different molecular mechanism. Sutton et al. (1976) listed at least five:

- Van der Waals forces, particularly significant for particles less than 10 μm
- Electrostatic forces, significant for substances which easily become charged
- Capillary (surface tension) forces, due to humidity
- Mechanical forces (asperities interactions and solids bridging)
- Magnetic forces

An extensive review on the subject is reported in Israelachvili (1991). Magnetic forces are only important for ferromagnetic or magnetisable materials and are therefore not relevant to this work. Mechanical forces, namely interlocking of particles due to surface asperities and solids bridging, should not be dominant in fluidized beds where particles are continually moving and taking part in collisions, unless presence of liquid causes particle aggregation. Electrostatic, capillary and van der Waals forces are said to be the most important to fluidized beds of fine powders. These forces depend on the particle size and the interparticle separation, usually becoming stronger with decreasing particle size and particle-particle separation. Other factors such as particle shape, surface roughness, gas humidity, moisture content and contamination

also play a role. These factors can be affected by process conditions, for example high temperature. Changes in these factors with increasing temperature can affect the interparticle forces and in turn the fluidization behaviour of powders. Lettieri (1999) reported extensively on the subject, showing how the combined effect of temperature and presence of liquid affects the relative role of IPFs and HDFs and in turn the fluidizability of the powders investigated.

Baerns (1966) maintained that powder cohesion is primarily due to van der Waals forces, especially in dry, neutrally charged powder systems.
Molecular or van der Waals forces arise from random motion of the electrons in the surface molecules. They are comprised of three types:

- Forces between polar molecules
- Forces between molecules polarised by fields of other molecules
- Forces of dispersion between non polar molecules, due to the local polarization produced in molecules by the random fluctuation of electrons.

Intermolecular and interparticle forces are very different. The intermolecular forces decay with increasing molecular separation, a, as a^{-7}, whereas the interparticle forces as a^{-2}. In order to scale up the van der Waals forces to bodies having sizes larger than the molecular dimension, the Hamaker theory (Hamaker, 1937) can be used. This assumes that the interaction energies between the isolated molecule and all the molecules in the large body are additive and non interacting. Thus, the net energy can be found by integrating the molecular interactions over the entire body. The attraction force, F_a, for two perfectly spherical and rigid particles having diameters d_1 and d_2 at a separation distance a is:

$$F_a = \frac{A_H R}{12a^2} \qquad \text{Eq. 3}$$

where $R=d_1d_2/(d_1+d_2)$, A_H is the Hamaker (materials-related) constant and a is the surface separation, which takes a minimum value of the order of the intermolecular

spacing (generally assumed to be 4 Å). Values for the constant A_H can be found in Israelachvili (1991). The range of values for the Hamaker constant are quite small. For most solids interacting across vacuum or air $A_H \sim 4 - 40 \times 10^{-20}$ J.

Rietema et al. (1993) calculated the minimum value for the parameter a taking into account a repulsive force as well as attractive and using a net force $F_{attractive}$-$F_{repulsive}$. In this way they evaluated a smaller value for the minimum surface separation of 2.23 Å. In the light of this calculation they estimated also the cohesion force due to van der Waals forces for two perfectly spherical and rigid particles having diameters and density of a typical Geldart's group A material. This was several orders of magnitude greater than the gravitational force. Rietema et al. (1993) also elaborated a fairly complicated model to account for particle deformation when evaluating the cohesive force between particles. Rietema and Piepers (1990) and Musters and Rietema (1977) interpreted the role of the van del Waals forces as the origin of the interparticle forces. They assumed that van der Waals forces are the controlling factor in the stable behaviour of group A powders.

Massimilla and Donsi'(1976) also used Equation 3 to calculate the van der Waals attractive forces between rigid particles. They used the following binomial formula to account for particle deformation:

$$F_a = \frac{A_H}{6a^2}\left(1 + \frac{A_H}{6\pi a^3 H_r}\right)R \qquad \text{Eq. 4}$$

where H_r is the hardness of the softer of the bodies in contact, which they quoted to be 10^7 N/m^2 for FCC catalysts. The cohesion force increased by several hundred times when using Equation 4. Massimilla and Donsi' (1976) stated that the second term in Equation 4 is negligible for materials having hardness greater than 10^7 N/m^2.

Johnson et al. (1971) developed a theory, called the JKR theory, for particle adhesion in the presence of surface forces. This is based on an earlier analysis performed by Hertz (1882) to determined the radius of the contact spot between two elastic spheres

brought into contact under an external load. Hertz's analysis assumes absence of surface forces and is therefore valid only for large spheres or when the surfaces are rough or dirty and the surface forces are not able to contribute. The JKR theory, on the other hand, considers situations in which the loads are small or the the surfaces are relatively smooth and therefore van der Waals forces become comparable with particle weight. In those cases the surface attractive forces pull the two surfaces together thus increasing the radius of the contact spot and this can happen also in absence of any applied load. The JKR theory allows also the calculation of the force necessary to separate the two sphere of diameter d:

$$W_p = \frac{3\pi\Gamma d}{8} \qquad \text{JKR "pull-off" force}$$

where Γ is the adhesion energy defined as the work required to separate two surfaces of unit area from contact to infinity (i.e. twice the surface free energy, γ)

2.3 Fluid bed expansion, Richardson and Zaki correlation

As illustrated in section 2.1, group A powders exhibit a uniform expansion for gas velocities between u_{mf} and u_{mb}. This homogeneous expansion can be described using the Richardson and Zaki (1954) equation, which was first used to describe the homogeneous expansions of liquid fluidized beds.

Richardson and Zaki (1954) developed a correlation to describe the sedimentation and fluidization of uniformly sized particles having diameter greater than 100μm and fluidized with liquids in tubes of various diameters:

$$\log u = n \log \varepsilon + \log u_t \qquad \text{Eq. 5}$$

where u is the liquid velocity of the suspension, n is the slope of the line and $\log u_t$ is the intercept on the logu axis corresponding to ε=1 (single particle, i.e. u_t = terminal fall velocity). From Equation 4 it follows that:

$$u = u_t \varepsilon^n \qquad \text{Eq. 6}$$

where the parameter n depends on the free fall particle Reynolds number Re_t and normally has values between 4.65 (viscous regime) and 2.4 (turbulent regime).

The applicability of the Richardson and Zaki equation to beds of particles fluidized by gas has been tested in a number of works.

Godard and Richardson (1968) carried out bed expansion experiments on a range of materials having very narrow particle size distribution and fluidized with air. They found that Equation 5 described well the relationship between the fluidizing velocity and the bed voidage. However, they found the values of the index n higher than those predicted for liquid fluidized beds of uniform spheres. Values for n were generally between 5 and 5.4, with higher values (n=8) for some phenolic resins. Also the values found for the terminal velocity extrapolated from the logarithmic voidage-velocity curves were generally higher than the terminal velocity of the particles u_t.
Geldart and Wong (1984) found that the Richardson and Zaki index n increased as the particle size decreased and the materials became more cohesive. They also observed that in a non cohesive system the terminal fall velocity u_t calculated using the Stokes equation is close to the velocity extrapolated from Equation 5, which they indicated as u_t'. They reported that materials having n/4.65>1 are also characterised by values of $u_t'/u_t>1$ and obtained the following relationship:

$$\frac{n}{4.65} = 1.26\left(\frac{u_t'}{u_t}\right)^{0.132} \qquad \text{Eq. 7}$$

Lettieri et al. (2002) used the Richardson and Zaki equation to describe the homogeneous expansions of FCC catalysts with increasing temperature. They compared the experimental n and u_t values with predictions given by the Richardson and Zaki $n=n(Re_t)$ correlations employed for liquids and by the drag equation for the settling of an individual particle, using the Stokes law:

$$Ga = 18 Re_t \qquad \text{for } Ga \leq 3.6 \qquad \text{Eq. 8 (a)}$$

$$Ga = 18 Re_t + 2.7 Re_t^{1.687} \qquad \text{for } 3.6 \leq Ga \leq 500 \qquad \text{Eq. 8 (b)}$$

and

$$n = 4.8 \qquad Re_t < 0.2 \qquad \text{Eq. 9 (a)}$$

$$n = 4.6 Re_t^{-0.03} \qquad 0.2 < Re_t < 1 \qquad \text{Eq. 9 (b)}$$

$$n = 4.6 Re_t^{-0.1} \qquad 1 < Re_t < 500 \qquad \text{Eq. 9 (c)}$$

The experimental n and u_t values were found to be much higher than the predicted ones, with the discrepancy being greater at lower temperature. The authors attributed this discrepancy to the formation of clusters and back calculated the cluster diameters from the experimental values of u_t. These findings underlined the importance of defining appropriate mean particle diameters to describe correctly the particle systems under study. Lettieri et al (2002), found lower values of the experimental u_t for those catalysts characterised by a higher content of fines.

Di Felice (1999) and Di Felice and Kehlenbeck (2000) reported values for the parameter n of the Richardson and Zaki equation obtained for dilute systems and noted that they were some 1.5 times greater than those obtained by Richardson and Zaki (1954) for concentrated systems. Therefore, the authors suggested a schematic velocity-voidage relationship covering the whole range of voidages shown in Figure 3. On the basis of this overall trend, they concluded that extrapolating the expansion profiles obtained for concentrated systems to zero voidage can lead to an underestimation of the terminal fall velocity u_t if the Richardson and Zaki equation (Equation 5) is used.

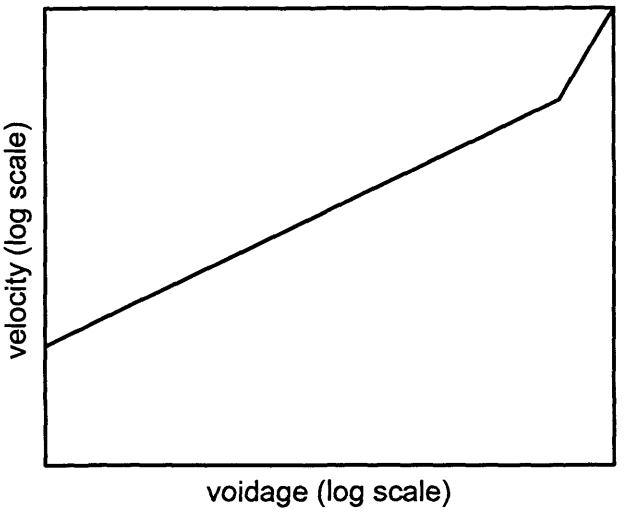

Figure 3 *Schematic velocity-voidage relationship from Di Felice (1999)*

Therefore, they proposed a modified form of the Richardson and Zaki equation to use for concentrated systems:

$$u = ku_t\varepsilon^n \qquad \text{Eq. 10}$$

with k<1. In support to their findings, the authors compared a range of literature values of k obtained for concentrated sedimenting suspensions of medium and large solids and showed that Richardson and Zaki (1954) were the only ones to report values of k close to or greater than 1. All the other authors reported values well below one, in the region of 0.8-0.9.

2.4 Effect of process conditions on fluidization

2.4.1 Temperature effect on the fluidization behaviour of solid materials

Most of the industrial applications of fluidization technology, such as catalytic conversions or coal combustion and gasification, are operations that involve temperatures well above ambient. The present understanding of the characteristics of fluidized beds at elevated temperature is far from being straightforward. For a long time the influence of the operative temperature on the fluidization parameters, such as

the minimum fluidization velocity, has been explained with the variation of gas properties with temperature, namely gas density and viscosity, without taking into account the possible modifications induced by temperature to the structure of the bed, i.e. the way the particles are arranged in a packing structure. In the past design criteria and performance predictions for fluid-bed units working at high temperature have been based on the extrapolation to elevated temperature of results and relationships available at ambient conditions. Such an approach is valid when only hydrodynamic forces control the fluidization behaviour and can produce misleading predictions in cases where the interparticle forces are not negligible or become dominant with respect to the HDFs, as demonstrated by Lettieri (1999).

2.4.1.1 The minimum fluidization conditions

The correlation most widely used to predict u_{mf} at ambient temperature is the Ergun equation, which is an expression for the pressure drop through a settled bed of solids. When combining the Ergun equation with the pressure drop expression for a fluidized bed, namely the overall force balance on the bed:

$$\Delta P = (\rho_p - \rho_f)(1 - \varepsilon_{mf})gH \qquad \text{Eq. 11}$$

a quadratic in u_{mf} is obtained:

$$(\rho_p - \rho_f)(1 - \varepsilon_{mf})gH = 150\frac{\mu H u_{mf}}{(\phi d_p)^2}\frac{(1-\varepsilon_{mf})^2}{\varepsilon_{mf}^3} + 1.75\frac{\rho_f u_{mf}^2}{\phi d_p}\frac{(1-\varepsilon_{mf})}{\varepsilon_{mf}^2} \qquad \text{Eq. 12}$$

In order to solve Equation 12 the value of the bed voidage at minimum fluidization, ε_{mf}, and the sphericity of the particles, ϕ, need to be known a priori.

Wen and Yu (1966) reported that in Equation 12 the groups containing the bed voidage and the particle sphericity were almost constant for a wide range of conditions. In particular they found that

$$\frac{1-\varepsilon_{mf}}{\phi^2\varepsilon_{mf}^2} \approx 11 \qquad \text{Eq. 13}$$

and

$$\frac{1}{\phi\varepsilon_{mf}^3} \approx 14 \qquad \text{Eq. 14}$$

Hence, according to their findings a correlation is available to predict u_{mf} just as a function of the physical properties of the fluidizing gas and of the particulate system:

$$Ga = 1650\,Re_{mf} + 24.5\,Re_{mf}^2 \qquad \text{Eq. 15}$$

where Ga is the Galileo number:

$$Ga = \frac{d_p^3\rho_f(\rho_s-\rho_f)g}{\mu^2} \qquad \text{Eq. 16}$$

and Re_{mf} is the Reynolds number at the minimum fluidization velocity

$$Re_{mf} = \frac{d_p u_{mf}\rho_f}{\mu} \qquad \text{Eq. 17}$$

Equation 15, known as the Wen and Yu equation, can be simplified in case of small and large particles, when the viscous and turbulent effects respectively are dominant. For small particles (below about 100μm) the viscous term of Equation 15 gives:

$$u_{mf} = \frac{d_p^2(\rho_p - \rho_f)g}{1650\mu} \qquad \text{Eq. 18}$$

whereas for larger particles the inertial term gives:

$$u_{mf}^2 = \frac{d_p(\rho_p - \rho_f)g}{24.5\rho_f} \qquad \text{Eq. 19}$$

Therefore, the Wen and Yu equation allows the qualitative effect of temperature on u_{mf} to be predicted considering only the changes with temperature of the gas density and viscosity. For small particles, Equation 18 shows that u_{mf} varies with $1/\mu$. Therefore, u_{mf} should decrease as temperature increases, when the viscous effects are dominant. Equation 19 shows that u_{mf} varies with $(1/\rho_f)^{0.5}$, thus u_{mf} should increase with temperature for large particles, when turbulent effects are dominant. Predictions obtained using Equation 18 and 19 do not take into account possible changes in the bed voidage that may occur with increasing temperature. The dependence of u_{mf} on changes in the bed voidage with increasing temperature was investigated by Formisani et al. (1998) and later by Lettieri (1999) and will be discussed in more details in the following pages.

Many authors reported on the effect of temperature on the minimum fluidization velocity. Generally, the experimental findings confirmed the trend predicted by the Wen and Yu equation. Nevertheless, predicted values were not always in agreement with experimental values. Knowlton (1992) reported that one of the reasons for this discrepancy lies in the evaluation of the correct mean particle size and shape factor. He suggested that the sphericity factor could be back-calculated from the Ergun equation using previously measured values of u_{mf}. By doing so, an effective value for the particle size and shape factor would be found.

Pattipati and Wen (1981) reported that the Ergun equation in the Wen and Yu form is capable of predicting changes in u_{mf} when temperature increases for sand materials. They did not observe significant changes with temperature in the voidage at minimum

fluidization and found good matching between experimental and predicted values of u_{mf}.

Botterill et al. (1982) investigated the fluidization behaviour of some Geldart's group B and D sand, ash and alumina powders, at temperatures up to 950°C. The hot fluidized bed was contained within a 188 mm diameter cylinder. They found that for the group B materials u_{mf} decreased with increasing temperature, and attributed it to the increase in gas viscosity. They compared their results with predictions from the Wen and Yu equation and noted that the decrease in u_{mf} with increasing temperature was less than that predicted, since a change in ε_{mf} had occurred. This is not in agreement with the results of Pattipati and Wen (1981). For the large group D powders, Botterill et al. observed an increase of the minimum fluidization velocity with temperature, and attributed it to the decrease of gas density. No change of the bed voidage at minimum fluidization with temperature was observed for those materials. Their experimental data matched predictions obtained from the Ergun equation, when using the values of ε_{mf} measured at the corresponding operating temperatures and using values of the shape factor back calculated from the Ergun equation.

Lucas et al. (1986) also found an increase of ε_{mf} with temperature but explained it on an hydrodynamic basis. They investigated the behaviour of beds of silica sand with sizes ranging from 170 to 750 μm at temperatures from ambient up to 950°C. The measurements were carried out in a 70 mm i.d. column. Changes of ε_{mf} with increasing temperature were analysed through the variation of the bed voidage as a function of the Reynolds number at minimum fluidization conditions. ε_{mf} was found to be approximately constant for $Re_{mf}<0.75$, decreasing for $0.75< Re_{mf} <2$ and again constant for $Re_{mf} >2$. The authors explained these results in terms of a variation in the fluid flow pattern inside the bed: at values of the Reynolds number between 0.75 and 2 separation of the boundary layer takes place and a wake appears at the rear of the particle, creating a low pressure zone. They suggested that the formation of such low-pressure zones contributes to attractive forces between the particles, causing a decrease of ε_{mf}. When Re_{mf} increases further the separation point moves towards the

rear of the particle and the wake shrinks, so that attractive forces decrease and ε_{mf} increases again.

Formisani et al. (1998) investigated the influence of temperature (ranging from ambient to 800°C) on the fluidization behaviour of cuts of silica sand, glass ballotini, salt and FCC with particle diameters ranging from 80 to 600 μm. The experimental apparatus was a 55 mm i.d. quartz column wrapped with heaters that allowed visual observation of the fluidized bed and therefore direct measurements of the bed height and voidage.
They observed a linear increase of ε_{mf} with increasing temperature for all the powders investigated. In contrast with Botterill et al (1982), Formisani et al. attributed this increase to changes in the packing properties caused by temperature, rather than to the action of the fluidising gas. In particular, they attributed the capability of the bed to form a looser structure to an increase of the Van der Waals forces with temperature.
They found support to this interpretation in the increase they observed in the voidage of the settled bed, ε_s, when increasing temperature. This increase was attributed to an increase of the interparticle forces, which are thought to stabilise the structure of the fixed bed, in the total absence of gas flow. The close similarity between the trends found for ε_s and ε_{mf} led the authors to conclude that the increase of ε_{mf} with temperature, and in turn the changes in u_{mf}, are not due solely to changes in the properties of the fluidizing gas but also to changes in the packing properties.
In agreement with the results of Botterill at al. (1982), Formisani et al. (1998) found that the Ergun equation was capable of predicting changes in the minimum fluidization velocity with temperature, when accounting for changes of ε_{mf} with temperature.

Lettieri (1999) also found that the Ergun equation was suitable to predict the minimum fluidization velocity for FCC catalysts at high temperature when changes of ε_{mf} with increasing temperature were accounted for.

In summary, many authors have reported on the variation of u_{mf} and ε_{mf} with temperature. There is general agreement that predictions of u_{mf} can be obtained using

the Ergun equation by accounting for the changes of ε_{mf} with increasing temperature. However, there is still disagreement about the phenomena that control such changes.

2.4.1.2 Bed expansion and minimum bubbling conditions

The voidage at minimum bubbling, ε_{mb}, represents the limiting condition for the stability of fluidized beds, i.e. the transition between the particulate and bubbling regimes. This subject has been at the centre of considerable controversy for the past two decades, due to the ill defined role of the HDFs and IPFs on the homogeneous expansion. Several theories and models have been proposed to predict the "condition" for the voidage at minimum bubbling based on two substantially different approaches. On the one hand, criteria have been developed based on the assumption that hydrodynamic forces are the controlling factor (Jackson, 1963; Verloop and Heertjes, 1970; Foscolo and Gibilaro, 1984; Jean and Fan, 1992). On the other hand, interparticle forces were considered to play the dominant role over the hydrodynamic forces (Musters and Rietema, 1977).

The hydrodynamic fluid-bed models of Foscolo and Gibilaro, later revisited by Jean and Fan, provide explicit formulation for the minimum bubbling conditions. Such predictions have been compared by various authors with experimental data at ambient and high temperature.

Rapagna' et al. (1994) investigated the effect of temperature on the minimum bubbling velocities of FCC powders of mean particle sizes of 65 and 103 μm in a 50 mm i.d. column, from ambient conditions up to 900°C. They used a fast responding pressure transducer connected to an oscilloscope to detect the passage of bubbles in the bed. They observed a decrease in the average bubble size and a delay of the onset of bubbling with increasing temperature for both FCC powders. This corresponded to an increase in the voidage at minimum bubbling with temperature. Also, a larger increase in ε_{mb} was observed for the finer material. Rapagna' et al. (1994) compared their experimental values of ε_{mb} with those predicted by the Foscolo and Gibilaro fluid-bed model and found good agreement for both powders at ambient and high temperatures. This confirmed their idea that the hydrodynamic forces control the stability of fluidized beds.

The onset of bubbling was also studied by Formisani et al. (1998). They measured changes in the minimum bubbling velocity of FCC catalysts and silica sand with increasing temperature from ambient up to 800°C in a 55 mm i.d. quartz column. They relied on visual observation to determine the commencement of bubbling. For all material tested they observed an increase of u_{mb} with increasing temperature with a trend very similar to the increase observed for u_{mf}. Unlike Rapagna' et al. (1994), they observed a very small bed expansion increase with increasing temperature.

Xie and Geldart (1995) reported values of u_{mb} and ε_{mb} for FCC powders having mean particle diameters 47 μm and 68 μm. The fluidization tests were run in a 152 mm i.d. stainless steel reactor at temperatures ranging from ambient to 500°C. Various high viscosity gases, such as argon, neon, carbon dioxide were used as fluidizing gas. The measured u_{mb} decreased with temperature for all gases and powders used, in disagreement with the findings of Formisani et al. (1998). On the basis of their experimental data obtained at high temperature, Xie and Geldart (1995) proposed an empirical correlation to predict u_{mb} as a function of particle diameter, fines content, gas density and viscosity. Such correlation was based on a previous correlation developed by Abrahamsen and Geldart (1980), which was obtained from measurements at ambient conditions using different gases. Xie and Geldart (1995) had compared their experimental data at high temperature with values given by the Abrahamsen and Geldart (1980) correlation and found that the latter over-predicted changes in u_{mb}. The authors attributed this scatter to the enhanced role of the IPFs when increasing temperature, which was not accounted for in the Abrahamsen and Geldart correlation.

Xie and Geldart (1995) investigated the role of the IPFs on the bubbling conditions with increasing temperature by measuring the voidage at minimum bubbling. They observed no significant change in ε_{mb} as temperature increased for any of the FCC catalysts investigated, in disagreement with the results of Rapagna' et al. (1994). They also reported that predictions of ε_{mb} given by the Foscolo and Gibilaro and the Jean and Fan equations matched experiments at ambient temperature for FCC powders larger that 60μm. However, both models overpredicted ε_{mb} values at ambient

temperature for the fines powders. The models also predicted significant changes in ε_{mb} with temperature, in contrast with the experimental results obtained by the authors. They interpreted the failure of the hydrodynamic models to predict correctly the transition between the particulate and bubbling regime as a result of not having included the interparticle forces in the models.

In summary, the importance of assessing the effect of temperature on the fluidization behaviour of solid materials has been clearly demonstrated. However, findings are still controversial, as the relative importance of the interparticle forces and the hydrodynamic forces on the flow behaviour of powders at high temperature has not been unequivocally defined.
Most of the disagreement on the relative role of the HDFs and the IPFs on the fluidizability of powders lies in the uncertain nature of the IPFs involved and in the difficulty of measuring them directly. Some kind of quantification of the effects of the IPFs on fluidization is needed to advance the understanding of fluidization at high temperature.

2.4.2 Influence of fine particles on fluidization

Fine particles are known to improve the fluidization quality of fluidized beds (Rowe et al., 1978; Abrahamsen and Geldart, 1980; Newton, 1984) and for this reason an established procedure currently employed in many industries is to add between 10-50%$_{wt}$ of fines in order to improve the fluid bed performance.
Many authors have investigated the effect of fines on the fluidization behaviour, in order to explain the reasons for such changes and determine the optimal amount of fine particles to be added.

Rowe et al. (1978) examined the dense phase voidage, ε_d, of freely bubbling fluidized beds containing different amounts of fines using the X-ray absorption technique. Voidage measurements were made by comparing the X-ray absorption of the dense phase of the freely bubbling bed with that of a calibration wedge containing the same material. The fluidized bed was contained in an aluminium vessel of rectangular cross section, 100 x 300 x 900 mm. The material examined was a commercial silica based

catalyst of surface mean particle diameter 52 μm originally containing about 28% of fines. To this powder, previously deprived of fines, 2.7, 20 and 27.6 % of fines were added and experiments carried out.

Rowe et al. found that both the dense phase voidage and the overall expansion of the bed increased with increasing fines content. In consequence, they inferred that the interstitial gas flow in a bubbling bed is much greater than the minimum fluidization flow and therefore they called into doubt the validity of applying the long-established "two-phase" theory of Toomey and Johnstone (1952) to beds of fines particles. This states that all gas in excess of that needed to bring a bed of particulate solids to minimum fluidization conditions passes through in the form of bubbles and that the voidage in the dense phase of a bubbling fluidized bed ε_d is equal to that at minimum fluidization ε_{mf}.

The authors concluded that, since the dense phase is much more effective in bringing about chemical reaction than the bubble phase, the overall performance of a catalytic fluidized bed reactor can be enhanced by fines addition.

Barreto et al. (1983) compared dense phase voidage values obtained from the X-ray absorption technique developed by Rowe et al. (1978) with those obtained with a bed collapse test technique. They used an aluminium container 0.064 m square and 0.60 m high with cracking catalyst type powders (Geldart group A) having mean particle diameter ranging from 40 to 70 μm. They found a good agreement between the dense phase properties obtained using the two techniques over the range of velocities studied.

Abrahamsen and Geldart (1980) also found the fraction of fines <45 μm to be an important parameter in predicting the fluidization behaviour of homogeneously fluidized beds of group A powders. They conducted an extensive study on the dependence of the dense phase voidage on the physical properties of the gas and the powder. Within this study, they reported on the dense phase voidage changes of different grades of ballotini varying in mean size from 42 to 70 μm and containing fines fractions ranging from 1.5 to 38%. The experiments were carried out in a 0.15 m diameter Perspex vessel. They used the bed collapse technique as a means to evaluate the dense phase properties in vigorously bubbling beds of fines particles and found

that the dense phase voidage increased as the fraction of fines <45 μm increased. However, as a comment to their results the authors stressed the need of studying the effects of fines fractions, mean diameter and size distribution independently. The authors pointed out that by changing the fines content of the powder the relative spread and the mean diameter are changed simultaneously. Therefore, it becomes difficult to distinguish between the effect of having just decreased the mean diameter and having increased the fines fraction. They carried out experiments on two powders having the same mean size and different fines content and showed that the independent effect of fines addition was to increase the dense phase voidage.

Newton (1984) and Yates et al. (1986) examined the influence of fines fractions on fluidization by monitoring the conversion in catalytic fluidized bed reactors containing different amounts of fines. The aim of the work was to test the conclusions from an earlier study of Rowe et al. (1978). This work highlighted that an increase in the conversion measured for a given throughput of reactant can be obtained by increasing the fines content and that this is due to changes caused by fines particles in the gas distribution between the dense phase and the bubble phase. Newton (1984) carried out experiments in a stainless steel reactor 0.84 m in height and 0.114 m in diameter at temperatures ranging from 250 to 330°C. The fluidized material employed was a commercial oxidation catalyst. Three batches were used for the experiments, containing 0, 16 and 27% of fines and having mean particle diameter of 81, 58 and 52 μm respectively.

Results at each temperature showed an increase in conversion with increasing fines content and for the same fine content an increase in conversion with temperature, therefore confirming the hypothesis that increasing fines content causes more gas to flow through the emulsion phase and less through the bubble phase. Moreover, the author performed a further series of experiments at 300°C in order to determine whether the effect of fine particles was chemical or hydrodynamic. To this end, they repeated the same experiments adding this time catalytically inactive fines (produced by heating the catalyst to 850°C in a furnace) and found that the conversion increased with increasing fines content even with inactive fines, as shown in Figure 4.

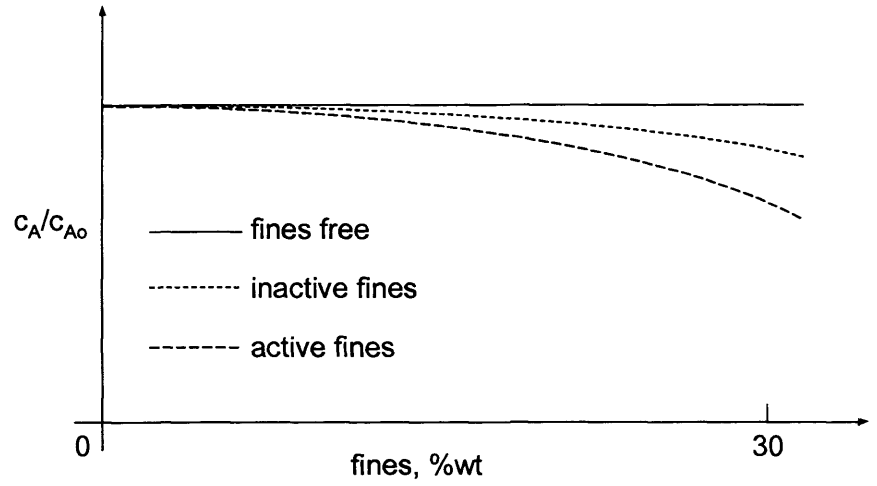

Figure 4 *Concentration profiles from Newton (1984)*

It is worth noting that an alternative interpretation for the improvement of conversion observed when adding fines particles can be found in the findings of Grace and Sun (1991). The authors showed that fine particles populate the bubbles, therefore improving the contact between gas and solid and enhancing reaction performance.

2.4.3 A geological application of fluidization "at process conditions": Pyroclastic Flows

The fluidization behaviour of fine particles at high temperature is of interest not only for industrial applications. In recent years fluidization has been recognised to be a subject extremely relevant in the geological field and in particular in the study of the volcanic phenomenon of pyroclastic flows.

Although the industrial and geological research communities look at totally different applications, in this area they share the study of the flow behaviour of fine materials at high temperature. Within this framework, this work has also contributed to the research developed as a part of a collaboration established between UCL and the Laboratoire Magmas et Volcanos of the University Blaise Pascal in Clermont-Ferrand, France. Results of this ongoing collaboration have been published in Geophysical Research Letters and the article is reported in Appendix 6.

The work highlighted the role of temperature on the fluidization behaviour of an ibrignite, a volcanic material having a mean diameter of 63 μm and a loose-packed bulk density at ambient temperature of 780 kg/m^3. Bed collapse tests at ambient

temperature showed group C behaviour, whereas at 200-565°C group A behaviour occurred. Mechanical agitation also increased the fluidizability of the ibrignite. Therefore, a combined effect of high temperature and shear was believed to promote group A behaviour for pyroclastic flows. Given the high flowability at high temperature of otherwise very frictional materials, the study also highlighted the need for an understanding of the rheological properties of volcanic materials at high temperature.

2.5 Powders flowability measurement tests

A great deal of research has been carried out over the last fifty years in order to define and measure, by means of simple tests, parameters apt to characterize and predict the flow properties of solid materials. To this end various approaches have been undertaken which span the whole range of aeration conditions, from frictional flow (no aeration) to fluidization. In the former case the flowing powders do not exhibit a "viscosity" and the overwhelming interaction between particles is friction. On the other hand, in the case of fluidized powders a concept of viscosity has been postulated by many authors as a kind of internal friction between the particles in the suspension forming the dense phase. For the intermediate cases (powders aerated below minimum fluidization) works available in literature seem to suggest a frictional behaviour where the frictional force is independent from shear rate (Barletta et al., 2004, Tardos, 2003, Bruni et al., 2005). This area of research, the flow of granular materials (aerated or not aerated), is commonly named powder rheology. However, a fundamental difference exists between powder rheology and rheology of fluids. Simple fluids cannot resist a shear stress and the shear rate will be proportional to the shear stress, whereas granular materials can resist a shear stress and the friction force caused by the shear varies very little with speed, so might be expected to be independent of shear rate. The case of fluidized beds is controversial as much debate has been taking place in the last decades on whether a concept of "fluid bed viscosity" can be defined and most importantly if such parameter can be measured.

This section describes the various approaches adopted by researchers on the subject of powder flow for both granular materials and aerated/fluidized powders.

On the one hand, stationary measurements (angle of repose, Hausner ratio etc.) have been proposed as simple tests to predict the flowability of bulk powders (Carr, 1965). On the other hand, dynamic tests have been used as a means for determining the flow characteristic of powders. These dynamic tests can be classified into two distinct groups: the shear cell type tests, first introduced by Jenike in 1953, and the viscometer type tests, whose study was initiated by Schugerl in the late sixties.

The former is a test performed on the powder in a compressed state where the shear measurements are used to obtain a yield locus that represents the limiting shear stresses under any normal stress when failure, i.e. flow, occurs. The shape of the yield locus is related to the cohesiveness of the material. The latter is based on the analogy between fluidized beds and liquids and in particular on the idea that in a fluidized bed a resistance against flow exists, just as in liquids, and this resistance is a kind of internal friction between the particles in the suspension forming the dense phase and resembles the concept of viscosity used in describing the rheology of liquids.

Another test widely used to determine the flow properties of powders is the bed collapsing technique, which provides a measurement of the capability of the dense phase to retain aeration gas.

These tests are reviewed in details in the following sections.

2.5.1 Measurements in the stationery status

Carr (1965) developed a classification system to predict the flow characteristics of a bulk of particulate solids. In Carr's method a numerical value is assigned to the results of several tests and it is summed to produce a relative flowability index for that particular bulk material. The method is further discussed in Carr (1970). Below are defined some of the main parameters used in Carr's method.

Angle of repose, Angle of fall, Angle of difference

The *angle of repose* is defined as the constant angle to the horizontal assumed by a cone like pile of the material. It is a direct indication of the potential flowability of a material: materials with good flowability are characterized by low angles of repose. The *angle of fall* is determined by dropping a small weight on the platform on which an angle of repose has been formed. The fall causes a decrease of the angle of repose

that is called angle of fall. The more free-flowing the material the lower the angle of fall. The *angle of difference* is the difference between the angle of repose and the angle of fall. The greater this angle, the better the flow.

Angle of internal friction, Angle of spatula

The *angle of internal friction* is defined (Carr, 1970) as the angle at which the dynamic equilibrium between the moving particles of a material and its bulk solid is achieved. This is of particular interest for flows in hoppers and bins.

The *angle of spatula* is a quick measurement of the angle of internal friction. It is the angle, measured from the horizontal, that a material assumes on a flat spatula that has been stuck into the dry material and then brought up and out of it. A free flowing material will have formed one angle of repose on the spatula's blade. A cohesive material will have formed several angles of repose on the blade, the average of these is taken. The higher the angle of spatula of a material the less it is flowable.

Cohesion

Cohesion is defined as the apparent cohesive forces existing on the surface of fine particles or powders. The cohesion test consists of passing the material through three vibrating sieves in series. The material left on each sieve is weighted and a cohesion index is determined from the relative amounts retained.

Hausner ratio and Powder Compressibility

The ratio between the loose and the packed bulk density is known as the Hausner Ratio (HR) and is used as an indication of the cohesiveness of the materials, see Geldart et al. (1984). The loose bulk density is measured by gently pouring a sample of powder into a container through a screen, whereas the packed or tapped bulk density is determined after settling and deaeration of the powder has occurred due to tapping of the sample. In addition to the HR, the powder compressibility is also used to define cohesiveness. This is expressed as $100(\rho_{BDP}-\rho_{BDL})/\rho_{BDP}$.

The main advantage of the tests listed above lies is their simplicity. This characteristic makes them an attractive tool to determine powders' flowability, which has been used to justify their wide use in industry and academia. However, these tests are scarcely

reproducible and most importantly the test procedures are very difficult to standardise, as amply discussed by Santomaso et al. (2003) with regard to the HR. Moreover, the link between the fluidization behaviour and static properties such as those described in this section is not at all straightforward, due to the uncertain relationship between the IPFs and the HDFs involved when gas is passed through a bed of particles. This is particularly true at process conditions, as discussed in section 2.1. The use of static methods to predict the fluidization behaviour of powders, despite being widely employed, is therefore questionable, especially when the fluidization behaviour needs to be assessed at process conditions.

2.5.2 Shear Cell

The Shear Cell was developed by Jenike in 1953. He analysed the flow of solids using the concept of plastic failure with the Mohr-Coulomb failure criteria and developed the flow, no-flow criterion for the design of hoppers and bins. Jenike assumed that a bulk solid can be approximated by a rigid-plastic Coulomb solid. From soil mechanics, such a solid is characterized by a yield locus that defines the limiting shear strength under any normal stress. A Coulomb solid has a linear yield locus. Plotting shear stress τ against the normal stress σ_n, the yield locus for a Coulomb material intersects the τ axis at a value of τ which is defined as cohesion, C. The slope of the locus, the angle φ, is defined as the angle of internal friction of that material. Figure 5 shows typical yield loci for a free flowing and a cohesive material.

In the Jenike cell the test powder is consolidated in a shallow cylindrical chamber that is split horizontally. The lower half of the cell is fixed and a shear force is applied to the upper movable part at a constant low rate. Shearing is carried out for each of a series of normal loads on pre-consolidated samples, so that at the end of the test the relationship between the shear stress and normal stress at various bulk densities are obtained. From a yield locus, corresponding to a specific consolidation, an angle of internal friction can be derived. From a family of yield loci, each corresponding to a different consolidation, a flow function can be derived.

Jenike carried out many experimental measurements on free-flowing and cohesive materials. He found that the yield locus of a dry material would be a straight line passing through the origin. The term "cohesionless" was therefore used to describe

materials that have negligible shear strength under zero normal load. On the other hand, Jenike found that the yield loci of cohesive materials differ significantly from a straight line and have non-zero intercept. Moreover, the position of the locus for a cohesive powder depends strongly on the compaction of the material.

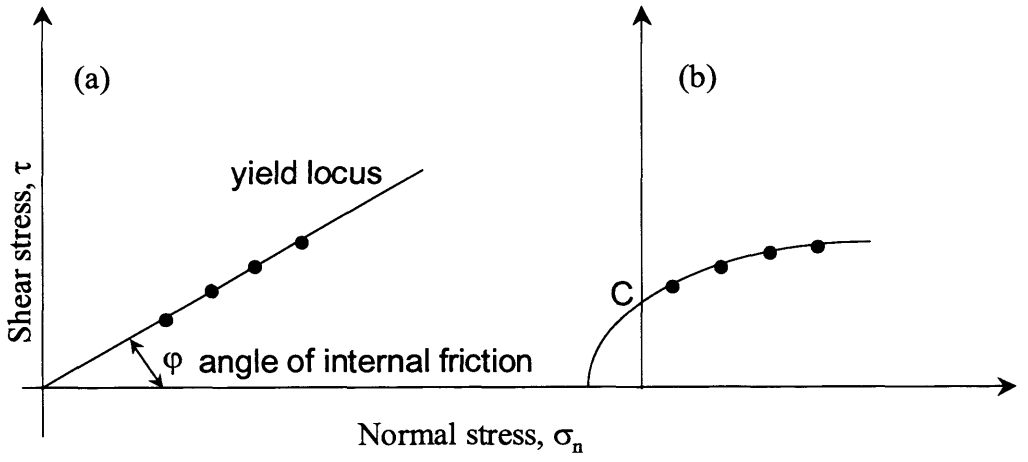

Figure 5 *Yield loci of (a) free-flowing materials; (b) cohesive materials*

Barletta et al. (2004) developed an aerated shear cell, modifying a commercial Peschl Shear cell by replacing the bottom of the cell with a porous plate. With some modifications due to the presence of aeration gas, they ran standard shear measurements on an FCC powder having a mean diameter of 70 μm. They reported results on the flow functions under non-aerated conditions and when the ΔP across the sample was 36% of the pressure drop corresponding to full support, ΔP_c. The two functions were the same, showing that aeration did not change rheological properties of the FCC powder. Similar results were obtained also by Klein et al. (2003) and Johanson and Barletta (2004) with a modified ring shear cell. In this work the effect of aeration on powder rheology is also investigated. Results are reported in section 5.2.5.3.

Shear Cell measurements are widely used to assess the flowability of powders for applications that involve powder discharge. These tests were originally used to design bunkers, but have become increasingly useful for general characterisation of particulate materials. However, as for the static tests described in section 2.5.1 , a direct link between the failure properties of the material measured with a Shear Cell

and the corresponding fluidization behaviour is not straightforward. Moreover, existing Shear Cells are not designed to operate at high temperature, because applications involving powder discharge are run at ambient temperature. Therefore, Shear Cells are not capable of detecting possible changes in the settled bed packing with increasing temperature.

Furthermore, shear testers are known to be very useful to predict the solid flow from a tall silo, in which the relatively high loading pressure of the solids is prevailing. However, due to the very small or zero loads on the bulk of a fluidized powder, standard shear testers are unlikely to provide an accurate characterization of fluid bed behaviour, as values of the failure properties need to be extrapolated from data at higher loads. Barletta et al. (2004) overcame this problem in their modified Peshl Shear Cell by introducing a cinematic chain to counterbalance the weight of the lid of the cell and therefore allow measurements under low normal stresses (see section 3.7.1).

The measurements of the rheological properties of powders using shear cells represent a very established field in powder technology. Therefore, even if the relationship between the conditions under which a shearing test is carried out and fluidization is not straightforward, shear cells are widely used to assess the flow properties of fluidized powders. In this regard, Kohe et al. (1991) proposed a multidisciplinary approach to powder flow characterization where shear measurements were related to bed collapse test results. A detailed description of their work is reported in section 2.6. The present PhD work proposes a new approach to the use of shear cells for the assessment of the flow properties of fluidized powders. Sections 5.2.4-5.2.6 are dedicated to this aspect.

2.5.3 Fluid bed rheology

In this section works in which a "viscosity" has been attributed to beds of fluidized particles are reported. The bottom line of these works is that particles fluidized by a gas can be treated as a continuum at length scales much larger than the particle diameter. The rheology of such a continuum results from a cumulative effect of microscopic (at length scale of the particles) forces due to the interaction between

particles, such as Van der Waals, capillary or electrostatic forces and hydrodynamic drag forces.

The following section reports some fundamental definitions concerning fluid rheology and highlights the difference between the rheology of fluidized beds and of non fluidized granular materials. Section 2.5.3.2 reports research works in which definitions and methods developed for characterising fluid rheology were applied to fluidized powders.

2.5.3.1 Rheological characteristics and models

Viscosity is a measure of the resistance of a fluid to deformation under shear stress. It is commonly perceived as "thickness" or resistance to pouring. Viscosity describes a fluid's internal resistance to flow and may be thought as a measure of fluid friction.

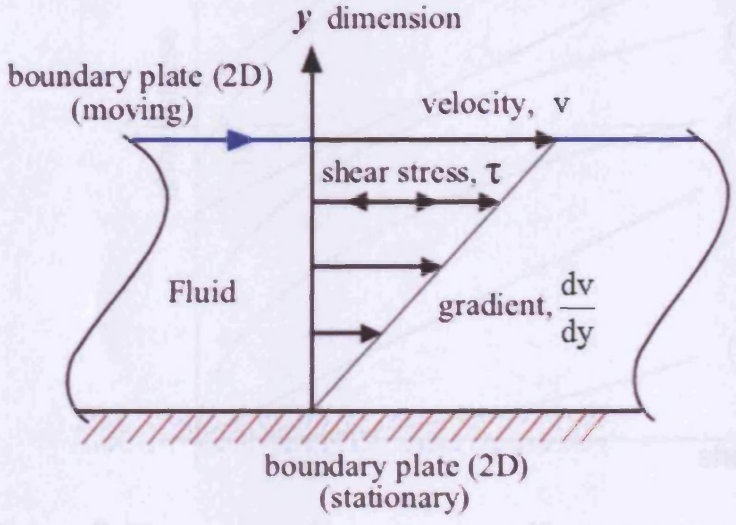

Figure 6 *Laminar shear of fluid between two plates. Friction between the fluid and the moving boundaries causes the fluid to shear. The force required for this action is a measure of the fluid's viscosity.*

Isaac Newton postulated that for a straight, parallel and uniform flow (see Figure 6) the shear stress τ between layers is proportional to the velocity gradient dv/dy in the direction perpendicular to the layers:

$$\tau = \mu \frac{dv}{dy}$$

where the constant of proportionality, μ, is the viscosity of the fluid. Fluids characterised by such behaviour are called Newtonian fluids. The viscosity of Newtonian fluids is constant and independent of the magnitude of the shear stress or shear rate. Consequently, the flow curve for such fluids is a straight line passing through the origin (line 5 in Figure 7); the slope of the line gives the viscosity of the fluid.

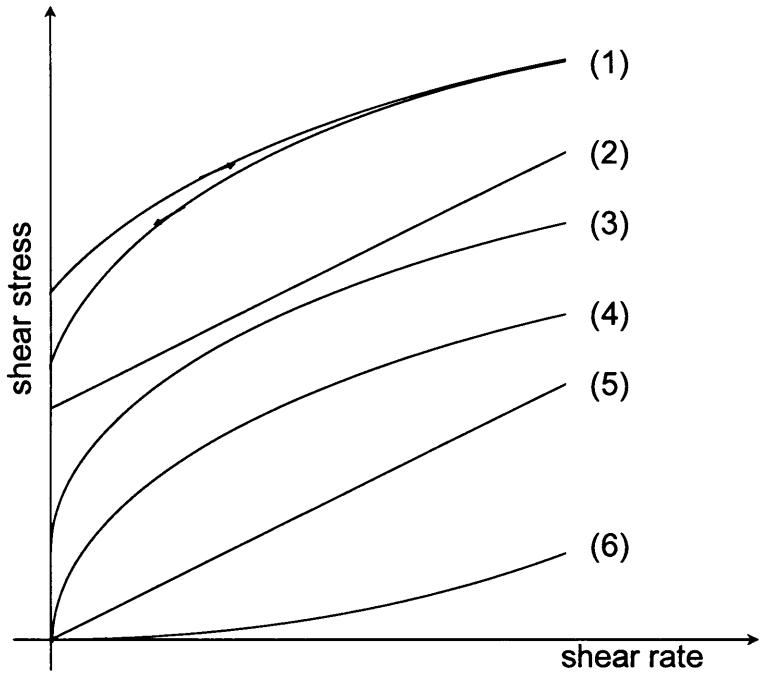

Figure 7 *Flow curves for various non-Newtonian materials. (1) Thixotropic; (2) Bingham plastic; (3) general non-Newtonian; (4) Pseudoplastic; (5) Newtonian; (6) Dilatant.*

Fluids diverging from this behaviour are called non-Newtonian fluids. The most common types of non-Newtonian behaviours are:

1) Time independent

These may be subdivided as follows:

a) Shear thinning or pseudoplastic (line 4 in Figure 7)
   "Apparent viscosity", i.e. the ratio of the instantaneous shear stress to shear rate, falls as the shear rate increases.
b) Shear thickening or dilatant (line 6 in Figure 7)
   "Apparent viscosity" increases as the shear rate increases.
c) Bingham plastic (line 2 in Figure 7)
   These fluids are characterised by a yield stress which must be exceeded before flow commences. Typical examples include toothpaste or fresh cement/concrete.

2) Time dependent

These may be sub-divided into:

a) Thixotropic (line 1 in Figure 7)
   At any given shear rate the "apparent viscosity" decreases with time. It is rather like a pseudoplastic material but with a time effect.
b) Rheoplastic or antithixotropic
   At any given shear rate the "apparent viscosity" increases with time. It is rather like a dilatant material but with a time effect.

3) Viscoelastic

These are materials whose properties show some resemblance to those of solids. These fluids exhibit elastic recovery from deformations which occur during flow. In spite of such effects, however, during steady state flow a viscoelastic fluid is often similar to a pseudoplastic material.

In practice, combinations of different types of behaviour are also possible.

Rheological models

Many equations have been used to describe rheological data mathematically. Ideally, a model for non-Newtonian flow should give an accurate fit of the experimental data and should have a minimum number of independent constants. For dilatant and pseudoplastic fluids with no yield stress, the logarithmic plot of shear stress against shear rate is often found to be a straight line over a limited range of shear rate. As a

result, an empirical functional relationship known as power law is used to characterise these materials. The relation may be written as:

$$\tau = k'\dot{\gamma}^{n'}$$

where $0 < n' < 1$ for pseudoplastic materials and for dilatant materials.
The higher k' the more viscous the fluid. n' is a measure of the degree of non-Newtonian behaviour with $n' = 1$ giving non-Newtonian fluids. The greater the departure from unity, the more non-Newtonian the character of the material.
Other commonly used rheological equations are:

$\tau = \tau_y + \mu_p\dot{\gamma}$	$\tau > \tau_y$	Bingham plastic
$\tau = \sqrt{\tau_y} + A\sqrt{\dot{\gamma}}$	$\tau > \tau_y$	Casson fluid
$\tau = \tau_y + k'\dot{\gamma}^{n'}$		general Bingham plastic/Herschel-Bulkley

Granular materials react to shear differently to fluids. While simple fluids cannot resist a shear stress granular materials can and the friction force between shearing layers varies very little with speed, so might be expected to be independent of shear rate. This aspect was investigated in this work as reported in details in Appendix A4 and in Bruni et al. (2005). This work showed that an aerated bed of particles – at gas velocities smaller than the minimum fluidization velocity - will exhibit a constant shear stress/torque when sheared by an impeller at different speeds.
However, a different picture arises when the bed of particle is fluidized. In this case the work (Bruni et al., 2005) demonstrated that an increase in the shear rate caused an increase in the shear stress when the bed was fluidized, therefore showing a "viscosity" effect at the minimum fluidization velocity.

Fluid bed viscosity represents an extremely attractive parameter to characterise fluid bed behaviour. Rheological properties of fluidized beds, in the form of flow constitutive equations, would allow the estimation of an essential component of the averaged continuum equations for flow of fluidized particles. For this reason a number of authors have tried to measure the viscosity of fluidized beds. The following

section reports a selection of the works available in literature on the subject of fluid bed viscosity.

2.5.3.2 Fluid bed viscosity

Newton et al. (1999) reviewed the results of the studies available in literature and reported that different orders of magnitude for the bed viscosity were obtained using different methods.
It should be noted that the viscosity is influenced by the shape of the particles, the voidage of the bed, the fluidizing velocity and the fluidizing gas viscosity. Moreover, according to Rietema (1991) making measurements in a freely bubbling bed is pointless because when a bubble collides with the measuring device the shear stress will locally approach zero. Therefore, only the measurement of the viscosity of the dense phase seems to be meaningful.

Various measuring devices have been employed to determine the viscosity of powders. Conventional type viscometers are those where the material is sheared by a rotating element (Stormer, Brookfield and Couette) and the resistance to the rotation is measured. Other methods are the floating and falling ball and the torsion pendulum. In the method developed by Grace (1970) the measurement of the shape of rising bubbles is used to indirectly calculate the bed viscosity. All these methods are in some ways "intrusive", as an external object is immersed in the bed in all cases. An indirect method is the quasi-solid emulsion viscosity method developed by Kono et al. (2002), where the viscosity is measured indirectly through the measurement of fluidization parameters. Experimental works carried out using these methods are reviewed in this section.

Shugerl (1971) reported that the only viscosity data measurements that can be considered quantitative are those obtained with a Couette viscometer (two concentric rotating cylinders) at low angular velocities of the inner cylinder or measured with a torsion pendolum at low amplitude, i.e. made at very low shear rates. The torsion pendulum provides measurement of the rate of decay of the amplitude of an oscillating cylinder immersed in the bed oscillating around its vertical axis, see

Hagyard et al. (1966) for a more detailed description of the technique. Shugerl also pointed out that reliable viscosity measurements can only be obtained provided that a Newtonian behaviour has been established.

Whether a fluidized bed has to be considered a Newtonian or a non-Newtonian fluid is still a controversial question, though most the recent works have demonstrated a non-Newtonian behaviour.
In the early studies of gas fluidized beds rheology, the viscosity was obtained from the measured resistance to the rotation of an impeller (paddle or dumbbell) (Matheson, 1949; Kramers, 1951; Diekman, 1953; Furukawa, 1958; Shuster, 1960) or from the terminal velocity of falling spheres (Daniels, 1965; Peters, 1953). An assumption implicit in these studies was that the fluidized beds behave as a Newtonian fluid. These early works have been criticized because the immersed body rotated too quickly (Hagyard et al., 1966), so that the immersed body peripheries moved at linear superficial velocity greater or only slightly less than the linear fluidization velocity of the fluidising gas. Therefore, the bed conditions near the immersed body differed markedly from those in the bulk of the bed. Moreover, it has to be noted that the measured viscosity in these works was the overall value due to the dense phase and the bubble phase, and therefore meaningless according to Rietema (1991).

Anjaneyulu et al. (1995) determined the apparent bed viscosity of a fluidized bed of glass beads using an annular geometry in a small range of gas flow rates close to the minimum fluidization velocity. The materials investigated were fairly coarse (ranging from 500 to 900 μm mean diameter). They reported a Bingham fluid behaviour, therefore non-Newtonian visco-plastic, for the materials. Visual observations using silvered glass beads as tracer particles showed that particle motion occurred only in an annular layer near the rotating cylinder, while outside the layer the particles were nearly stationary. The rheological parameters were obtained by fitting the flow equation (momentum balance) for the specific geometry to the experimental data. The predictions obtained using the Bingham plastic equation as a constitutive equation for the fluid matched the experimental data reasonably well.

Yaomin et al. (2000) also described fluidized beds using a Bingham fluid model. They adopted the falling sphere technique, using an expression for the drag force modified for an object in a Bingham fluid. This was done by adding to the classical Stokes formula a term that represents the influence of yield stress on the drag force. They performed experiments in 4.6 cm fluidized bed 24 cm high. The materials studied were silica sands with average size of 88 μm. The authors applied their model also to the experimental data published by Daniels (1965) on glass beads of 87, 117, 147 and 175 μm. Daniels (1965) had used the ball dropping technique but modelled the fluidized bed as a Newtonian fluid, obtaining a great scatter between experimental data and predictions.

The method consisted in measuring the terminal velocity of the sphere and solving the motion equation of the sphere to evaluate the drag coefficient. Then, the effective viscosity was calculated from the aforementioned drag coefficient equation. The relationship between the experimental viscosity and the relative velocity between sphere and fluidizing gas was found to be the same as the one predicted assuming Bingham fluid behaviour, thus confirming the hypothesis of Bingham fluid behaviour for the fluidized bed. Moreover, when the fluidized bed was modelled as a Bingham fluid, also the entire experimental data set of Daniels (1965) fitted this theoretical approach.

Kai et al. (1991) also used the falling sphere method, but assumed Newtonian behaviour for the fluidized bed when calculating the apparent viscosity from the measured terminal fall velocity of the sphere. They found that the viscosity measurements increased with increasing diameter of the sphere and explained it with the frictional force caused by the compaction of the dense phase near the sphere. Therefore, they obtained the apparent viscosity as the extrapolation to zero sphere diameter. By measuring the apparent viscosities of a wide range of powders differing in mean diameter (35 – 83 μm) and particle density (920 – 2360 kg/m^3), they found a correlation between the apparent bed viscosity and the voidage of the bed, the mean particle diameter and the particle density:

$$\mu_A = \frac{5.58*10^{-5} d_p^{0.634} \rho_p^{1.39} (1-\varepsilon)}{(\varepsilon - 0.98\varepsilon_{mf})^{0.494}} \qquad \text{Eq. 20}$$

The average deviation of the predictions obtained using Equation 20 from the experimental data was 7.7%. The measured viscosities ranged from 10^{-3} to 10^{-2} Pa s. Kai et al. also expressed the apparent kinetic viscosity ν_A , $\nu_A=\mu_A/\rho_p(1-\varepsilon)$, as a function of the gas density and viscosity by using a correlation previously developed by the authors themselves (Kai et al., 1987) between the bed voidage and the particle and gas properties:

$$\nu_A = \frac{\mu_A}{\rho_p(1-\varepsilon)} = \frac{5.58*10^{-5} d_p^{0.634} \rho_p^{0.39}}{(4.03/N^* + 0.02\varepsilon_{mf})^{0.494}} \qquad \text{Eq. 21}$$

where N* is given by

$$N^* = \sqrt{d_p^3 g(\rho_p - \rho)}(\rho_{air}/\rho)^{0.12}/\mu \qquad \text{Eq. 22}$$

The authors suggested that Equations 21 and 22 can be used taking into account changes of gas properties with increasing temperature, to predict the variation of the apparent bed viscosity with increasing temperature.

Is is worth noting that objects moving in fluidised beds can attract a defluidised region in front of them and a void behind them, therefore questioning the nature of the property of the bed which is being measured when using a falling sphere technique.

Grace (1970) used an indirect method to determine the viscosity of the dense phase, where the interference with the fluidized bed is claimed to be eliminated or substantially reduced. This consists of estimating the effective viscosity of the dense phase from the shape of bubbles in the fluidized bed. The assumption in this work was that the dense phase behaves as a Newtonian fluid. The idea is that the wake angle for

a spherical-cap bubble, ϑ, in a Newtonian liquid depends on the bubble Reynolds number Re_b, from which the liquid viscosity is obtained. Grace proposed the following relationship:

$$Re_b = 23\exp(-0.04\vartheta) \qquad \text{Eq. 23}$$

where:

$$Re_b = \frac{d_b u_b \rho_p (1-\varepsilon_{mf})}{\mu_A} \qquad \text{Eq. 24}$$

d_b and u_b are the diameter and the bubble rise velocity respectively. The viscosity was calculated by X-Ray observations of gas bubbles in a three-dimensional fluidized bed. Fluidizing bed viscosities ranging from 0.4 to 1.3 Ns/m^2 were obtained.

Table 2 *Viscosity data from Reiling (1992)*

	μ_A (Nsm^{-2}) Ammoxidation Catalyst			μ_A (Nsm^{-2}) FCC Catalyst		
Ultrafine level	0%	1%	10%	0%	1%	10%
$u = 0$	3.2	3.69	3.32	3.24	3.31	3.55
$u = u_{mf}$	0.48	0.384	0.277	0.256	0.222	0.180
$u = u_{mb}$	0.05	0.042	0.02	0.067	0.038	0.0155

Reiling (1992) carried out an extensive experimental programme measuring the apparent viscosities of fine catalyst powders (FCC and ammoxidation catalysts) using an 8-speed Brookfield 4-bladed paddle viscometer. The technique was calibrated against various fluids of known viscosities (pure silicone oils) and apparent viscosities were determined at 60 rpm paddle speeds. Measurements were conducted in a 6-inch diameter Plexiglass fluid-bed at ambient temperature. The influence of fluidizing gas velocity on the apparent viscosities was investigated for both powders. Relatively high viscosity values (3.2 to 3.7 Nsm^{-2}) were obtained when there was no gas flow.

Over the non-bubbling regime the apparent viscosity decreased rapidly with increasing bed voidage (from 0.256 at u_{mf} to 0.067 at u_{mb} for the FCC catalyst). In the same work, the author also studied the influence on viscosity of adding quantities (up to 10% by weight) of very small Geldart group C powders (d_p=0.014 μm). Results of this analysis are reported in Table 2. For both powders the level of fines did not affect the apparent viscosity significantly when the bed was not aerated (u = 0). A small decrease was recorded for the bed viscosity with increasing ultrafines content in the whole range of gas velocities investigated.

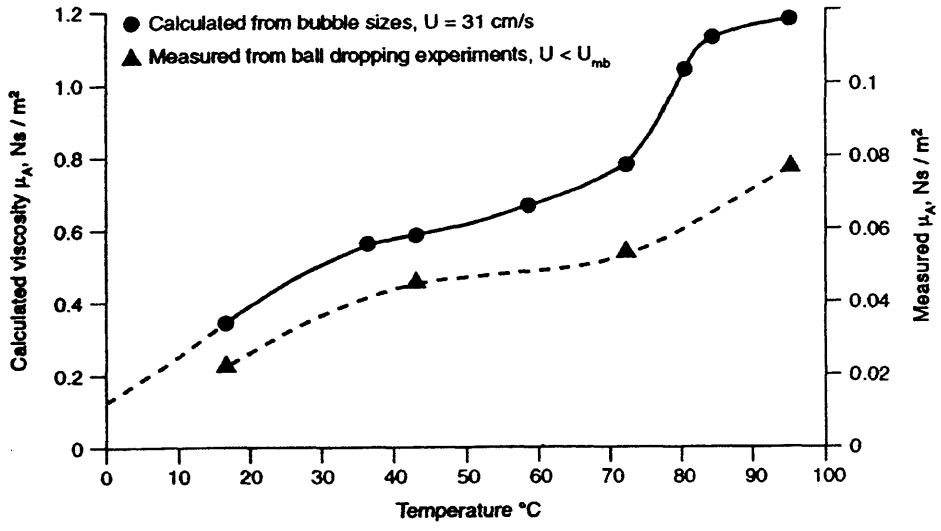

Figure 8 *Apparent viscosity versus temperature (Newton et al., 1999)*

Newton et al. (1999) studied the effect of temperature on the dense phase viscosity for fresh and E-Cat FCC samples (Geldart group A) and a group B material (LLDPE = Linear Low Density Polyethylene), using the ball dropping technique over the non-bubbling regime. They performed experiments at ambient and high temperatures up to 500°C. The ball fall was monitored using the X-ray imaging technique. The technique was calibrated with known viscosity fluids, i.e. mixtures of water and glycerol. The fluidized bed used was a 100 mm diameter x 1000 mm quartz reactor. For all the powders analysed Newton et al. did not find discernable differences in dense phase viscosities over the non-bubbling region. Increasing the temperature resulted in a small increase in viscosity for the E-cat powder over the non-bubbling region, and in a decrease in bed voidage. The authors' interpretation of these results was that the E-cat

powder had retained some carbon deposit and higher molecular weight hydrocarbon species that probably increased the interparticle forces between the particles as the temperature was increased. A set of experiments was also run on the LLDPE polymer using the bubble terminal rise velocity technique. Both techniques produced an increasing trend for the viscosity with increasing temperature (see Figure 8). However, the viscosities measured with the two techniques differed by an order of magnitude, therefore showing the objective difficulty of tailoring a universal test for powder flow characterization.

H.O. Kono and his collaborators have reported on their extensive studies on the rheological parameters of the homogeneously aerated, expanded dense phase of fine powders. Kono's approach, in line with the stability model by Rietema and the work of Massimilla et al. (1972), is based on the assumption that the interparticle forces between cohering particles give rise to a powder structure with a certain mechanical strength even in the expanded state of the homogeneous fluidization.

Kono reported that tensile strength methods, such as a shear stress tester, are not suitable for fluidized beds, as most of the industrial fine powders (e.g. FCC, 30-70 μm) have very low powder structure tensile strengths in the powder packing structures typical of fluid bed processes. Therefore, the tensile strength measured may be too small to be detected with satisfactory accuracy if using a shear strength tester.

In order to evaluate the tensile strength of powders, Kono et al. (1994) introduced the definition of three rheological parameters, the *fracture strength at minimum bubbling* $\sigma_{f,mb}$, the *plastic deformation* coefficient Y, and the *quasi-solid emulsion phase viscosity* μ_e.

The fracture strength at the minimum bubbling point $\sigma_{f,mb}$, was defined as the tensile strength of the aerated powder (between u_{mf} and u_{mb}) at which the first fracture in the homogeneous packing structure occurs and a first bubble appears. $\sigma_{f,mb}$ was correlated to the fluidization parameters (u_{mf} , u_{mb} , ε_{mf} and ε_{mb}) by equating the energy needed for the dense phase deformation, i.e. expansion, to the energy that the excess gas (u_{mb}-u_{mf}) would have spent if the pressure drop across the bed continued to increase linearly above u_{mf}. The resulting expression for $\sigma_{f,mb}$ is:

$$\sigma_{f,mb} = \frac{\Delta P^{**}}{1+(\varepsilon_{mb}/\varepsilon_{mf})(1-\varepsilon_{mf})/(1-\varepsilon_{mb})} \qquad \text{Eq. 25}$$

where

$$\Delta P^{**} = 150 d_p \frac{(1-\varepsilon_{mf})^2}{\varepsilon_{mf}^3} \frac{\mu}{(\phi d_p)^2} (u_{mb} - u_{mf}) \qquad \text{Eq. 26}$$

A more extensive treatment of this theory can be found in Kono et al. (1994). It is worth noting that Equations 25 and 26 allow the evaluation of $\sigma_{f,mb}$ by means of only experimentally measured fluidization parameters.

The second rheological parameter, the plastic deformation Y, was defined in analogy with the Young's modulus for a solid structure, i.e. the ratio between stress and strain, which for an aerated powder structure would be:

$$Y = \frac{\Delta P^{**}}{(H_{mb} - H_{mf})/H_{mf}} \qquad \text{Eq. 27}$$

Again, this rheological parameter can be evaluated by using only experimental fluidization data.

Finally, Kono et al. (2002) defined the quasi-solid dense phase viscosity μ_e assuming a visco-elastic behaviour for the emulsion phase between u_{mb} and u_{mf}. In particular, μ_e was determined by performing a strain retardation test, which consisted of setting the gas velocity at u_{mb} and instantaneously reducing it to u_{mf}, while recording the change of bed height. A strain retardation curve S(t) was obtained from the profile of bed height with time. The solution of a known rheological model (the Voigt-Kelvin model) was fitted to the curve:

$$S = S_0 e^{-\frac{t}{\tau}} \qquad \text{Eq. 28}$$

where $\tau = \frac{\mu_e}{Y}$ is the relaxation time for the homogeneously aerated expanded phase , i.e. the time required for the stress to reduce to 1/e of his initial value.

If the strain retardation curve S(t) and Y are obtained experimentally, τ can be calculated and therefore the quasi-solid viscosity of the dense phase μ_e can be evaluated.

The treatment developed by Kono et al. has the virtue of being very simple and straightforward and of producing simple equations to determine the rheological parameters of the dense phase from the knowledge of experimental fluidization data. It also allows the evaluation of the rheological parameters without introducing any external object into the fluidized bed, therefore producing an indirect method for rheological analysis. The capability of the model developed by Kono of predicting the fluidization behaviour will be analysed in section 2.6.

2.5.4 Dense phase characterization using the bed collapsing technique

A Bed Collapse Test consists of suddenly turning off the gas supply to a vigorously bubbling fluidized bed and recording the deflation of the bed with time.

The Bed Collapse Test (BCT) technique was first introduced in the late sixties (see Rietema, 1967, Sutton and Richmond, 1973) within a study concerning the storage of fine powders in hoppers by using aeration. Since then several workers have used the bed collapse test with different aims, in particular to evaluate properties of the dense phase in bubbling beds, such as dense phase voidage and the gas velocity in the dense phase. The collapse experiment tests the capability of powders to retain aeration gas. Given that in industrial FCC units the ability to circulate the catalysts continuously around the system is fundamental for stable operation, a slow collapse rate is desirable. Therefore, for these applications the BCT represents a way to assess the capability of the powder to withstand sudden changes in flow in the unit. The more aeratable the powder, i.e. capable of retaining aeration gas, the better the "quality" of the fluidization.

In this work BCTs were run with increasing temperatures. Visualization and recording of the bed height with time was obtained by means of the X-ray technique described in section 3.4.

2.5.4.1 Stages in the collapse process

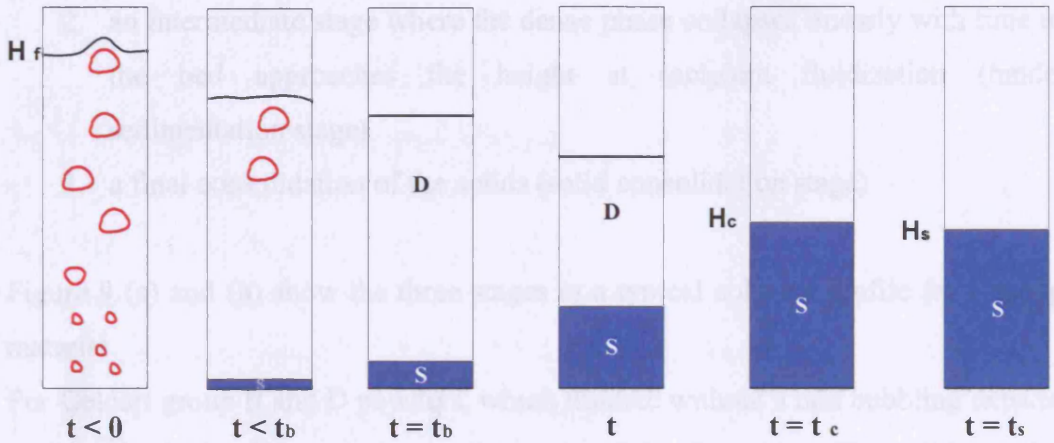

(a)

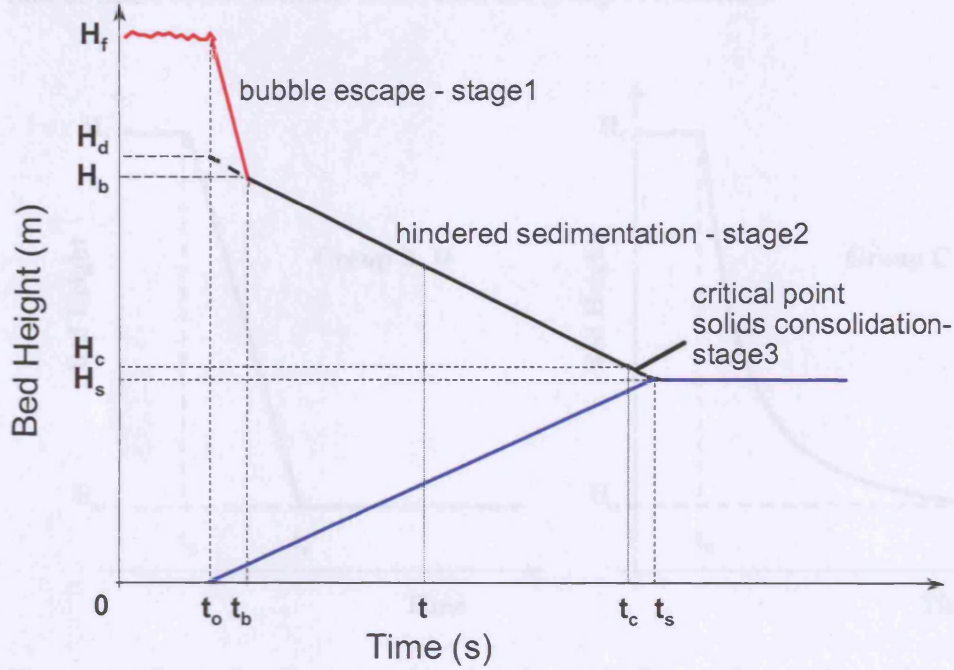

(b)

Figure 9 (a) and (b) *Stages of a Bed Collapse Test for Geldart Group A powders*

When the fluidising gas is suddenly shut off, the bed material will exhibit different collapse profiles depending on the properties of the powders. For a gas-solid system, a typical Geldart Group A material will show a three stage profile:

1. a rapid initial collapse when bubbles leave the bed (bubble escape stage)
2. an intermediate stage where the dense phase collapses linearly with time until the bed approaches the height at incipient fluidization (hindered sedimentation stage)
3. a final consolidation of the solids (solid consolidation stage)

Figure 9 (a) and (b) show the three stages in a typical collapse profile for a group A material.

For Geldart group B and D powders, which fluidize without a non bubbling expansion regime, the bed collapse curve consists only of the first stage. The solids reach the final static bed height as soon as the bubbles are expelled and therefore the collapse rate of these solids is much faster than for group A materials.

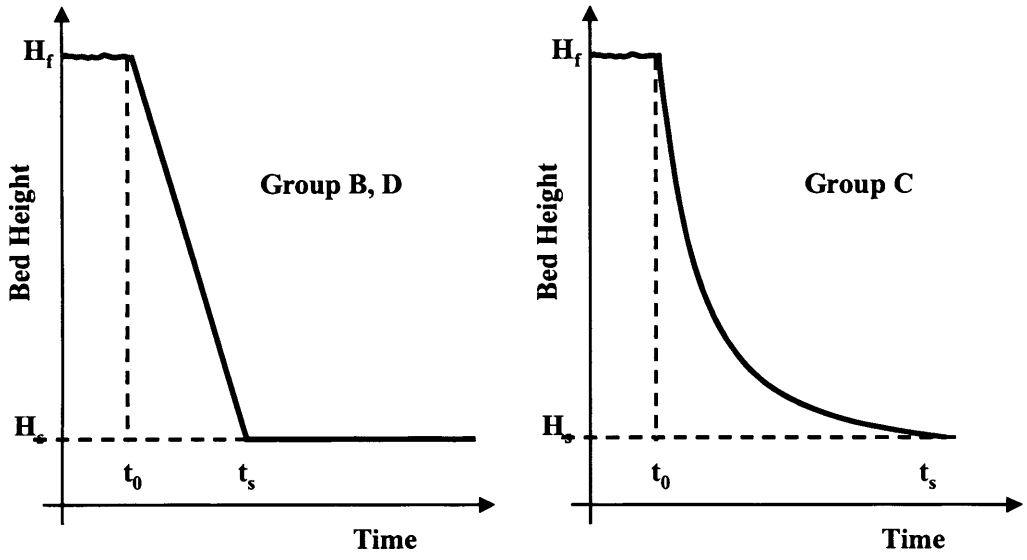

Figure 10 *Typical collapse profiles for Group B, D and Group C powders*

For group C powders, which do not bubble even at high gas velocities, there is no hindered sedimentation stage, but only consolidation. Bed expansion in group C powders is caused by the presence of cavities and cracks. Geldart et al. (1984) and Geldart and Wong (1985) reported that when the gas is switched off, the largest cracks close up rapidly and further collapse proceeds more slowly. Hence, the rate of collapse is controlled by the rate at which gas can escape from vertical channels.

Geldart and Wong (1985) reported that the decrease of bed height for group C powders is exponential with time.

Typical collapses for group B and D and group C powders are shown in Figure 10.
The bed collapse profiles obtained from the BCT provide interesting information on the fluidization of powders and allow the definition and evaluation of several fluidization parameters.
As shown in Figure 9 (b), by extrapolating to t = 0 the hindered sedimentation curve, the height of the dense phase, H_d, can be found and therefore the average voidage of the dense phase, ε_d, can be calculated (see Equation 33 in section 3.2.2).
The following parameters obtained from the BCT, have also been identified as meaningful indicators of the fluid bed performance and will be investigated during this work:

Table 3 *Bed Collapse Test parameters*

Dense Phase Collapse Rate, U_{de}	$U_{de} = \frac{H_d - H_s}{t_s - t_0}$
Bed Expansion Ratio, BER	$BER = \frac{H_d - H_s}{H_s} x100$
Standardized Collapse Time, SCT	$SCT = \frac{t_c - t_0}{H_s} x100$

It is clear that the three parameters calculated from the bed collapse test are not independent, as the SCT can be calculated as the ratio between BER and U_{de}.

Barreto et al (1983) found good agreement between the results for the dense phase voidage in bubbling beds obtained using the BCT technique and those obtained via direct observation of the internal structure of the bed using the X-rays absorption technique.

Abrahamsen and Geldart (1980) investigated the effects of powder characteristics and experimental settings on the dense phase properties evaluated using the BCT. In

particular, they found that in beds of group A powders the voidage of the dense phase ε_d increases as:

- the particle density decreases
- the mean particle size decreases
- the fraction of fines <45 mm increases
- the gas viscosity (temperature) increases
- the gas density (pressure) increases

Abrahamsen and Geldart (1980) also developed a correlation at ambient temperature to predict the dense phase collapse rate U_{de}:

$$U_{de} = \frac{0.314\rho_f^{0.023}(\rho_p - \rho_f)^{0.271} d_p^{1.282} \exp(0.50F_{45})}{\rho_f^{0.5} H_s^{0.244}} \qquad \text{Eq. 29}$$

where F_{45} is the fines content. Equation 29 predicts that U_{de} should decrease with increasing temperature, i.e. the dense phase should collapse at a slower rate as temperature rises. Lettieri (1999) found a good agreement between Equation 29 and the experimental values for U_{de} measured for FCC catalysts at temperatures ranging from ambient to 650°C. Within this range of temperature, Lettieri reported a decrease of 25-50% for the FCC catalysts.

Lettieri (1999) used the BCT to study the influence of temperature on the fluidization behaviour of some FCC catalysts and an E-Cat catalyst containing process residuals. Lettieri found that the SCT was the most discriminating parameter to distinguish between systems of powders dominated by the interparticle forces (IPFs) or the hydrodynamic forces (HDFs). The SCT increased with increasing temperature for those powders dominated by the HDFs (the fresh FCC catalysts). It decreased with increasing temperature for those materials for which the increasing influence of the IPFs caused formation of aggregates within the bed (E-Cat catalyst).

Khoe et al. (1991) reported on the effect of mean particle diameter and particle size distribution (PSD) on the BCT parameters. They analysed the collapsing parameters of an FCC powder and a glass powder. For each powder they created three samples having a narrow size distribution and differing in mean particle diameter (83, 53 and 34 μm for the FCC and 113, 72 and 37 μm for the glass), which they used to investigate the effect of changing the mean particle diameter independently from the PSD. Then for each powder they also created two more samples having the same mean particle diameter as the intermediate narrow sample (~53 μm for the FCC and ~72 μm for the glass), but having PSD wide and bimodal respectively. These samples were used to investigate the effect of changing the PSD independently from the mean d_p.

They found that the effect of increasing the mean particle diameter for both powders was to:

- decrease the voidage of the dense phase, in agreement with Abrahamsen and Geldart (1980)
- increase the dense phase collapse rate
- decrease the standardised collapse time

When comparing the FCC samples having same d_p and different PSD they found that:

- $\varepsilon_{d,\,narrow} > \varepsilon_{d,\,wide} = \varepsilon_{d,\,bimodal}$
- $U_{de,narrow} < U_{de,wide} = U_{de,bimodal}$
- $STC_{wide} > STC_{narrow} = STC_{bimodal}$

The ballotini gave slightly different results:

- $\varepsilon_{d,\,narrow} > \varepsilon_{d,\,wide} > \varepsilon_{d,\,bimodal}$
- $U_{de,narrow} < U_{de,wide} = U_{de,bimodal}$
- $STC_{bimodal} > STC_{wide} = STC_{narrow}$

The most aeratable FCC sample, i.e. the one giving the greatest collapse time, was the one having a wide distribution. The most aeratable glass sample was the one having a bimodal distribution. In order to understand the latter finding the authors analysed the number based size distribution, in which the various size fractions are weighed according to the number of particles within the size fraction and not to the weight. They found that the number surface mean particle diameter d_{ns} for the bimodal sample was much smaller (31.7 μm) than for the other two samples (66.8 μm and 46.1 μm for the narrow and wide respectively). Therefore, they concluded that the overwhelming number of fines was responsible for the good aeratability of the bimodal glass. The authors pointed out that the particle diameter that would give the best powder characterization depends on the specific application.

2.6 Link between rheological measurements and fluidization

Although a great deal of research work has been carried out towards the understanding of the rheological behaviour of fluidized beds, as shown in section 2.5, the relationship between the rheological properties of powders and the corresponding fluidization behaviour is far from being unequivocally defined. Furthermore, little effort has been put into the study of the changes induced by process conditions on the rheological behaviour of powders. This section reviews some significant works where the link between rheology and fluidization have been investigated.

Reiling (1992) looked into the link between the apparent viscosities of fine catalyst powders measured with a Brookfield paddle viscometer and the bubble size. In particular, he studied the effects on viscosity of adding ultrafine silica cuts to the bed of catalyst (see Table 2). Reiling questioned the validity of the instability/wave perturbation theory (Rice and Wilhelm, 1958; Romero and Johanson, 1962), according to which low viscosity and low density fluid beds should favour the suppression or destruction of large bubbles and contain smaller bubbles than fluid beds of high viscosity or high density. The experimental data reported by Reiling did not support this conclusion. The addition of ultrafine silica had a large effect on the dense phase voidage but only a small effect on the viscosity of the fluidized bed.

Therefore, Reiling concluded that the link between bubble size and apparent viscosity is not supported by a viscous mechanism.

Newton et al. (1999) also tried to relate the bubble size and bubble number to the viscosities measured with increasing temperature (17-96°C) for a group B polymer powder (LLDPE). As reported already in section 2.5, they used a ball dropping technique to determine the viscosities of the bed at different temperatures. The authors reported that the effect of increasing temperature on the polymer cohesiveness and stickiness was demonstrated through significant changes to the mean bubble size and bubbles number. However, the viscosities measured through the ball dropping technique did not show dramatic changes with increasing temperature. Newton et al. (1999), in line with the findings of Reiling (1992), concluded that viscosity effects do not explain bubble sizes in the case of the LLDPE powder and that they could not assign a viscosity to the dense phase.

Kai et al. (1991) related the apparent kinetic viscosity ν_A evaluated using Equation 21 to the bubble diameter and to pressure fluctuation measurements. In particular, they used the maximum deviation of the pressure fluctuation, measured when changing the gas velocity, and used it as an index for fluidization quality: the smaller the maximum deviation the better the fluidization. They also measured bubble diameters using an optical probe and choosing a set velocity (0.1 m/s) for all the measurements.
They plotted the maximum deviation of the pressure fluctuation against the kinetic viscosity and found that experimental data obtained with several powders differing in mean diameter (35 – 83 μm) and particle density (920 – 2360 kg/m^3) fell on the same curve. The authors claimed that this relationship, although dependent on the type of apparatus, could provide a means for predicting fluidization quality within the same system. Moreover, in disagreement with Reiling (1992) and Newton et al. (1999), they found that the bubble diameter increased with increasing kinetic viscosity. The authors also carried out experiments with increasing temperature. They did not state clearly what trend they found for the apparent viscosity with increasing temperature. However, they showed that the experimental data for the bubble diameter and the kinetic viscosity at high temperatures followed the same relationship found at ambient temperature. They obtained similar results when plotting experimental data obtained

at high pressure by Weimer and Quarderer (1985). The authors concluded that changes of the apparent bed viscosity with temperature can be predicted by Equation 21 when changes of the gas density and viscosity are accounted for.

Khoe et al. (1991) analysed the fluidization and the rheological behaviour of sets of powders differing in PSD and fines content. Using the method described by Molerus (1975, 1978), they used shear tests measurements, the experimental values of ε_{mf} and of the surface to volume diameter d_{sv} to derive the adhesive force per contact, F. The method assumes each powder as a semi-continuum and derives the average tensile strength, from which the average F-value at the contact points between monosized particles of diameter d_{sv} is calculated. Khoe et al. (1991) found that the adhesive force per contact, F, correlated very well with the ratio $(\varepsilon_{mb}-\varepsilon_{mf})/\varepsilon_{mf}$ obtained experimentally. In particular F increased when the maximum dense phase expansion increased, which the authors found plausible. Khoe et al. used the F values obtained from the shear cell measurements also to question the commonly accepted assumption that at minimum bubbling the average adhesive forces counterbalance the overall hydrodynamic forces. They developed a model to calculate a theoretical ΔF which would be needed to reach the minimum bubbling without expanding the bed, and compared it with the measured values of F. They found that $\Delta F << F$, showing that the energy needed to reach minimum bubbling without expanding the bed is much smaller than the average interparticle bond strength. They also reported visual observations of small volcano-like shapes erupting at the bed surface. Khoe et al. concluded that vertically elongated microcavities are responsible for premature weakening of the bed structure, allowing bubbling to start at a much lower value of the hydrodynamic force than F. This result was in agreement with findings by Donsi' and Massimilla (1973), who also observed cavities and microchannels in the homogeneous expansion of group A powders.

Kono et al. (1994) performed a series of fluidization tests on several powders, different in size, shape, density, chemical properties and surface characteristics but all fluidizable and free from any agglomeration or segregation phenomena. They used spent FCC, glass beads, carbon black and various starch powders with sizes ranging from 15 to 70 μm. The fluidization tests were carried out in a column of 100 mm

diameter equipped with electric heaters. For each powder the fracture strength σ_f and the plastic deformation Y (see Equation 25 and 27) were evaluated at ambient temperature and for the FCC experiments were carried out at temperatures up to 500°C as well as ambient. The authors found a correlation between Y and σ_f:

$$\sigma_f = 0.11 Y^{0.90} \qquad \text{Eq. 30}$$

which held true for all the experimental data, regardless of the type of powder, properties or operating temperature. Kono et al. (1994) interpreted this line as a flow characteristic line, where all powders characterised by smooth fluidization should fall. This idea was supported by the fact that, when powders forming agglomerates were fluidized or wall effects were significant, the rheological parameters could not be related using Equation 30. Furthermore, a qualitative correspondence was found between the measured rheological parameters and the observed fluidization behaviour. The smaller the values of Y and/or $\sigma_{f,mb}$, the larger the expansion of the dense phase at u_{mb}, and the smaller the values of bubble size in freely fluidized beds observed in a 2-D fluidised bed. Therefore, moving along the linear relationship given by Equation 30, different degrees of flowability among fluidizable powders could be predicted. In particular, points obtained with increasing temperature systematically shifted along the line towards the small values of the rheological parameters, which was in agreement with the widely reported positive effect of temperature on the fluidization behaviour of free flowing materials (see Lettieri, 1999).

Recently, Freeman Technology (Freeman, 2000) presented a rheometer to determine the flow properties of powders (FT3). This device measures the energy required to displace a powder sample contained in a vessel with a specifically designed blade. These energies are derived from the measurements of the axial force and torque acting on the blade in an up and down cycle. From the energy measured, a series of indexes are derived which are related to the flow properties of powders. Freeman's rheometer can be operated also in a fluidized mode, where the bottom of the vessel is replaced with a porous plate through which gas is passed. However, no experimental findings

have been found in literature in which the powder rheometer was used in the fluidization mode.

Lettieri et al. (2001) tested the capability of the powder rheometer developed by Freeman Technology (Freeman, 2000) to predict the effect of the IPFs on the fluid bed behaviour of fresh and equilibrium (E-cat) FCC catalysts (group A) and a fine silica material (group C) at ambient temperature. The relative role of the IPFs and HDFs on the fluidization behaviour of these powders had been previously investigated by means of pressure drop profiles and bed collapse measurements. The energy consumed during a downward test traverse of the impeller was plotted as a function of the different blade tip speeds. The silica powder was found to have the best flowability, as it required the lowest amount of energy to be stirred (between 180-220 mJ). This result was related to the capability of the material to retain aeration gas, as the silica exhibited a great capability to retain aeration gas with SCTs ranging from 80-130 s/m. The equilibrium catalysts, on the other hand, needed higher energies to be stirred (between 300-800 mJ) and was also found to be by far the most sensitive to changes in the blade tip speed, with the material becoming much less free flowing (higher energies) at lower speeds. This property was quantified by means of a Flow Rate Flowability index, defined as the ratio between the energy required for the test traverse at 10 mm/s blade tip speed and that required for the test at 100 mm/s. The equilibrium catalyst showed to be the most sensitive to changes in the flow rate with an index of 2.61, whereas values of 1.10 and 1.62 were measured for the fresh catalyst and the silica respectively. A qualitative comparison between the fluidization results of these materials and the results obtained using the FT3 showed that the E-cat FCC was the most difficult material to fluidize due to the dominant role of the IPFs. In agreement with this, it required the highest amount of energy to be stirred and was characterised by the highest value of the flowability index. Both the silica powder and the fresh FCC were easy to fluidize with the silica being characterised by a greater aeratability. In agreement with this, these materials required the lower amount of energy to be stirred. However, the flowability index was found to be lower for the FCC than for the silica material.

Thus, Lettieri et al. (2001) concluded that a full correspondence between the fluidization behaviour of the materials investigated and the flowability index proposed could not be established.

The works described in this section all sought to find, in different ways, a link between the rheological and the fluidization behaviour of powders. Some interesting findings were obtained on the relationship between the rheological properties and the mechanism underlying the homogeneous expansion of group A powders (Kono et al., 1994; Kohe et al., 1991). However, most of the works proposed only qualitative links between the rheological behaviour and the corresponding fluidization behaviour. In addition, findings are still very difficult to relate to each other, mostly due to the variety of techniques employed which make standardization of rheological tests very difficult.

Furthermore, the effect of process conditions on the bed rheology and in turn on the fluidization behaviour, still remains undefined. Section 2.4 showed the great influence that high temperature, presence of fines or presence of liquid can have on the fluidization behaviour in industrial processes as well as in the flow of granular material materials during volcanic eruptions. Many works (Reiling, 1992; Newton et al., 1999; Kohe et al., 1991; Lettieri et al., 2001) attempted a parallel analysis of the effects of process conditions on the rheological and the fluidization behaviour. However, a more systematic assessment of the independent and the combined effects of process conditions on fluid bed rheology and fluidization still needs to be accomplished.

3 Materials and experimental methods

This chapter reports on the materials used in this work and on the experimental methods employed: fluidization tests, rheological measurements using the mechanically stirred Fluidized Bed Rheometer (msFBR) and shear cell measurements. The main material used for this study was an alumina powder provided by BP Chemicals Ltd and obtained from Laporte Chemicals, Runcorn, UK. Soda glass ballotini were also used in the rheological part of this study (Chapter 5) as a reference material. The properties of the alumina and the ballotini are reported in section 3.1.

Sections 3.2 and 3.3 are dedicated to the description of the fluidization tests used in this work and of the fluidization rig utilised. Section 3.4 describes briefly the X-ray imaging technique used in most of the fluidization tests.

The msFBR, specifically designed and developed for this experimental work, is illustrated in section 3.5. Section 3.6 is dedicated to the different experimental procedure chosen for the experiments carried out with the msFBR below the minimum fluidization. Preliminary experiments carried out to assess the best procedure are also reported.

Section 3.7 reports on the apparatus and the methodology used to measure the failure properties of the materials. The Peschl Shear Cell used in this part of the work is described in section 3.7.1 and the experimental procedure followed to measure the failure properties of the powders are reported in sections 3.7.2-3.7.4.

The links between the two types or rheological experiments (msFBR and shear cell) are discussed further in chapter 5.

3.1 Particle physical properties

3.1.1 Particle size

There are many different definitions of particle size. In fluidization it is generally accepted that the surface-volume diameter d_{sv}, i.e. the diameter of a particle having the same external surface to volume ratio as a sphere, is the most appropriate.

Several authors (Lettieri, 2002; Kohe, 1991) have underlined the importance of using also different diameters (namely the surface average, the volume average or the number-surface or number-volume diameters) in order to better understand the physical reasons underlying the fluidization behaviour of powders.

Nevertheless, most if not all the correlations used in fluidization characterise powders according to their surface-volume diameter. Hence, in this study we used the surface-volume diameters, pointing out when a different definition of particle size is appropriate.

The surface-volume diameter is calculated as:

$$d_p = d_{SV} = \frac{1}{\sum_i \frac{x_i}{d_i}} \qquad \text{Eq. 31}$$

where x_i is the mass fraction of particles in each size range given by the sieve aperture d_i.

3.1.2 Particle size distribution (PSD)

The aim of the study presented in this thesis was to investigate the fluidization and rheological behaviour of powders differing in the particle size distribution of the fines fractions. To this end, several samples of alumina had to be created by separating and blending again different sub fractions in different proportions. This section describes the procedure followed for the preparation of the samples used in this study and reports the resulting particle size distributions and mean particle diameters.

The starting material for this study was an alumina powder containing around 50%wt of fines below 45μm. An air classifier was used to separate the fines below 45 μm from the rest and successively divide the collected fines into sub-cuts (cuts of particles below 45 μm, e.g. 0-25 μm or 26-45 μm).

The characteristics of the powders obtained after separation are reported in Table 4, which shows that a complete separation was not achieved. However, in each batch the fraction within the required size cut was at least 53%wt.

Table 4 *Powders obtained after separation with the air classifier*

	Nominal Size (μm)	% within range	d_p (μm)
A0	>45	96.8	75.1
A1	25-45	53	31.8
A2	0-25	62	15.6

The next step was to create two new powders, A3 and A4, by mixing the nominal >45 μm sample (A0) with each of the two fine sub-cuts, A1 and A2. Special attention was paid to blending the powders so to obtain two powders with the same total fines content, with similar overall particle size distribution (PSD) and differing in the PSD of the fines sub-cut fractions. The mean particle diameters of the two powders A3 and A4 resulting from the blending were kept as close as possible. However, it was difficult to obtain exactly the same mean particle diameter and at the same time keep the total fines content the same. Therefore, the author decided to keep the same total fines content and similar PSD for the two powders and to allow a consequent small difference between the mean particle diameter, as reported in Table 5.

Figure 11 shows the particle size distributions for A0 and for the samples A3 and A4 resulting from the blending, where A3=A0+A1 and A4=A0+A2. Figure 11 illustrates that A3 and A4 have a similar particle size distribution, which differs only for the size distribution of the fines fraction below 45 μm. A0 contains a relatively small amount of fines whereas A3 and A4 have the same total fine content (~22%wt) but shifted towards bigger (26-45 μm) or smaller (0-25 μm) size cuts respectively.

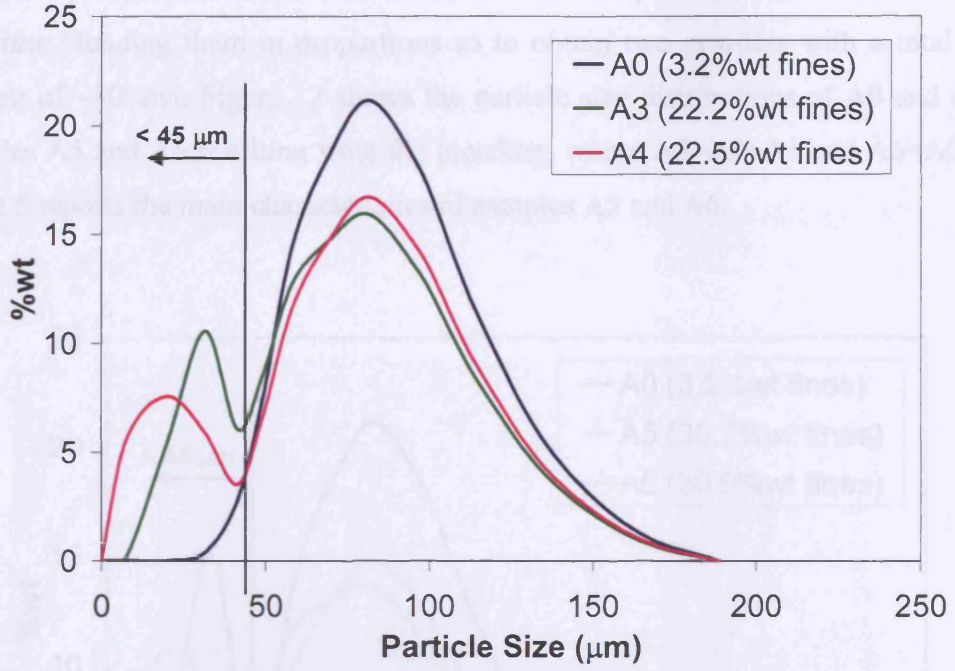

Figure 11 *Particle Size Distributions of A0, A3 and A4 (A3, A4 = 22%wt fines) obtained with laser diffraction (Malvern Instrument)*

Table 5 *Properties of samples A0, A3, A4, A5 and A6*

	d_p (μm)	F_{45} (%)	%wt 0-25 μm	%wt 25-45 μm
A0	75.1	3.2	0	3.2
A3	54.9	22.2	5.6	**16.6**
A4	41.7	22.5	**13.1**	9.4
A5	49.1	30.7	8.1	**22.6**
A6	36.0	30.9	**18.8**	12.1

The particle size distribution of the three powders was measured again at the end of each set of the experiments and the loss of any elutriated fines was monitored. No significant changes in the PSD were noticed and a negligible amount of fines (less than 1% of initial fines content) was lost during the experiments.

Table 5 reports the main characteristics of the three powders. F_{45} indicates the weight percentage of fines in the powder.

The same procedure was followed to create two more powders from A0, A1 and A2, this time blending them in proportions so to obtain two powders with a total fines content of ~30%wt. Figure 12 shows the particle size distributions of A0 and of the samples A5 and A6 resulting from the blending, where A5=A0+A1 and A6=A0+A2. Table 5 reports the main characteristics of samples A5 and A6.

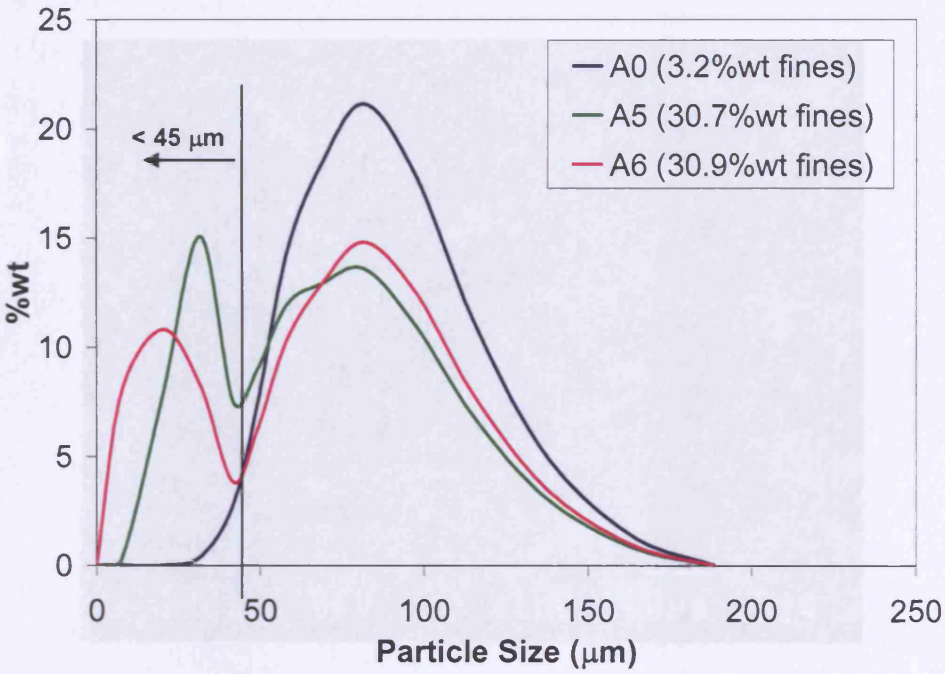

Figure 12 *Particle Size Distributions of A0, A5 and A6 (A5, A6 = 33%wt fines) obtained with laser diffraction (Malvern Instrument)*

The ballotini used in this study had a narrow size distribution and a mean particle diameter d_p = 350 μm.

3.1.3 Particle Density

The particle density of the alumina and the ballotini were determined by mercury intrusion analysis and were performed by BP Chemicals. The particle density was calculated from the mid-pressure plateau region of the intrusion curve. The measured particle densities were 1730 kg/m^3 for the alumina and 2500 kg/m^3 for the ballotini.

3.1.4 Particle shape

In this study a direct measurement of the particle shape was not attempted, but shape characteristics of the material under investigation were observed and photographed using a Scanning Electron Microscope (SEM). Figure 10 is an SEM taken on the original alumina (containing 50%wt of fines), which shows that the particles are not perfectly spherical.

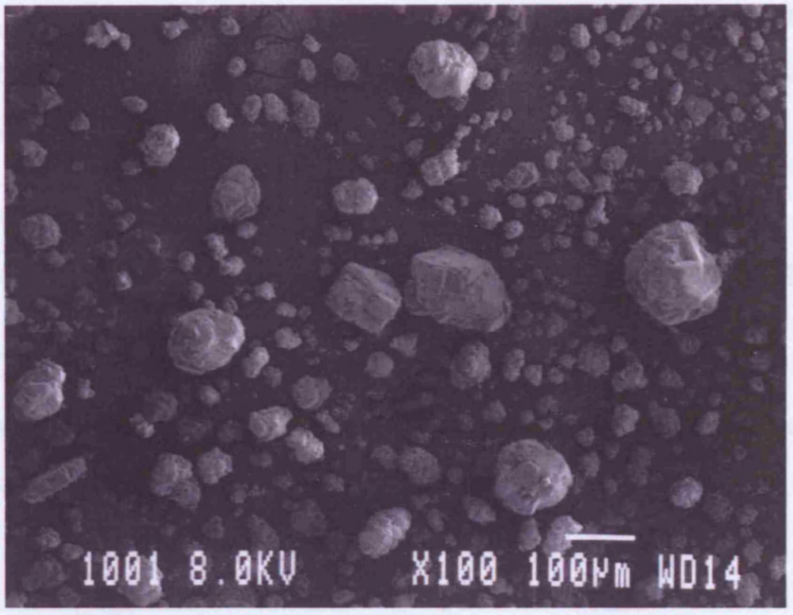

Figure 13 *Original alumina, SEM analysis at magnification X=100*

The shape of the ballotini was assumed to be perfectly spherical.

3.2 Fluidization tests - Methodology

3.2.1 Minimum fluidization velocity

The minimum fluidization velocity, u_{mf}, was obtained in this study from the plots of the pressure drop profile across the bed as a function of the fluidizing gas velocity. The fluidizing gas flow rate was increased in small steps from calibrated rotameters and the bed pressure drop recorded at each step. When the bed was well fluidized the same step wise procedure was followed until the bed was settled. Figure 14 shows a

typical pressure drop profile for a Geldart group A powder. The experimental minimum fluidization velocity is determined from the intersection of the horizontal fluidized bed line and the sloping packed bed line, obtained when decreasing the gas flow rate, as shown in Figure 14. Measurements were repeated three times to check the reproducibility of the results and averaged values are taken.

The experimental pressure drop profile represents a powerful tool to discriminate between powders in terms of cohesiveness and flowability. For systems that are easy to fluidize, and which are free from any dominant effect of interparticle forces, the experimental pressure drop at minimum fluidization conditions should be equal to the predicted one, ΔP_c:

$$\Delta P_c = \frac{Mg}{A} \qquad \text{Eq. 32}$$

where M is the weight of the bed material, A is the cross section area occupied by the bed material and g is the acceleration due to gravity.

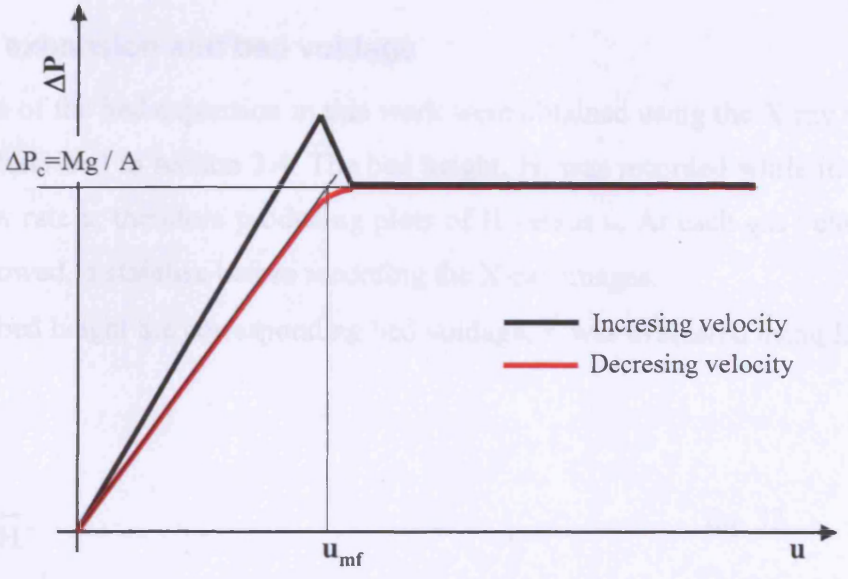

Figure 14 *Typical pressure drop profile for a Geldart Group A powders*

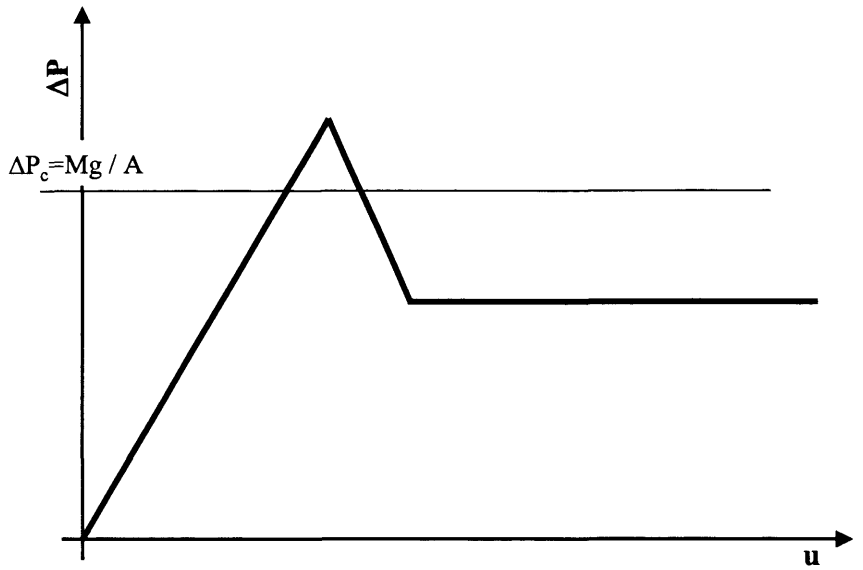

Figure 15 *Typical pressure drop profile for Geldart Group C powders*

When the IPFs dominate over the HDFs, as in the case of cohesive powders, a type C behaviour is observed, as shown in Figure 15, where the pressure drop corresponding to full bed support ΔP_c is never attained.

3.2.2 Bed expansion and bed voidage

The profiles of the bed expansion in this work were obtained using the X-ray imaging technique described in section 3.4. The bed height, H, was recorded while increasing the gas flow rate u, therefore producing plots of H versus u. At each gas velocity the bed was allowed to stabilise before recording the X-ray images.

From each bed height the corresponding bed voidage, ε, was evaluated using Equation 33:

$$\varepsilon = 1 - \frac{M}{A\rho_p H} \qquad \text{Eq. 33}$$

3.2.3 Minimum bubbling velocity

The minimum bubbling velocity, u_{mb}, in this work was determined as the velocity at which the maximum bed height of the homogeneous expansion was attained. The first

bubble appearance was also visualised by means of the X-ray technique, but this method was not considered very reliable given the poor contrast generated by the alumina powders in the X-ray images. For this reason experimental values of u_{mb} are not presented in this work.

3.2.4 Bed Collapse Test procedure

The bed collapse tests were carried out setting the flow rate of the fluidizing gas at a predetermined value above u_{mb} and suddenly shutting off the gas supply to the bed, while recording bed height using the X-rays technique described in section 3.4.

Abrahamsen and Geldart (1980) reported that the bed collapse test parameters depend on the starting fluidizing velocity when the superficial gas velocity at the beginning of the collapse is below a certain value, which for the powders they examined was found to be 6 cm/s. In this study, however, due to the crucial role of fine particles, the initial velocity was set to 1.5 cm/s in order to minimise elutriation from the bed. This velocity was the highest velocity which would keep the visually observed elutriated fines to a minimum. The small amount of fines collected in the top section of the bed at the end of each collapse (less than 1% of the initial fines content) confirmed the appropriateness of this choice. Moreover, the author is well aware of potential segregation problems due to the bimodal nature of the PSD of powders A3, A4, A5 and A6. Therefore, the bed was kept bubbling for a minimum amount of time to ensure good mixing before starting the collapse experiments.

Lettieri (1999) showed that despite the sensitivity of the fluidization parameters to the initial gas velocity, the trends with increasing temperature of these parameters do not change with changing initial gas velocity. This finding suggests that as long as the experiments are carried out in a consistent fashion, i.e. at the same initial fluidizing velocity, a meaningful assessment of the influence of process conditions can be achieved. Therefore, in this work, given the low value of the initial gas velocity chosen, the results from the bed collapses are not to be taken as absolute values but can be used to compare the fluidization behaviour under different process conditions.

The BCTs in this work are operated using the dual-drainage method, as described in section 3.3, where the fluidizing gas trapped in the windbox is vented out as the gas supply to the bed is cut off. Park et al. (1991) showed that in the single-drainage

method, the measured voidage and gas velocity in the dense phase increase with increasing windbox volume, gas flow resistance of distributor and gas velocity, whereas in the dual-drainage method, the dense phase properties are independent of distributor resistance and windbox volume.

3.3 Fluidization Rig

The experimental rig used for the fluidization tests was built and commissioned at BP Chemicals Ltd, Sunbury for a previous PhD study at high temperature (Lettieri, 1999). The fluidized bed, the associated pipe work and the electrical control box were mounted together on a wheeled trolley, as shown in Figure 16.

A 140 mm diameter x 1000 mm tall Inconel vessel, see (2) in Figure 16, with a wall thickness of 3 mm was used to test powders at ambient pressure. The vessel is fitted with a very fine (20 μm) stainless steel sinter mesh type distributor plate to ensure a high pressure drop and therefore a good and even fluidization in the bed.

The windbox, or plenum chamber, was a 150 mm high Inconel cylinder placed below the distributor plate and packed with 10 mm ceramic balls to improve heat transfer.

The vessel was closed at the top by a stainless steel disengaging section 500 mm high with a cross section increasing from 140 to 250 cm in diameter, in order to reduce the gas velocity (-69% from bottom to top) and contain the loss of fines, see (3) in Figure 16.

A 38.1 mm diameter stainless steel pipe line was connected to the disengaging section to vent the fluidizing gas out of the bed, see (4) in Figure 16. To reduce loss of any elutriated fine material, a removable stainless steel filter was installed on the vent line inside the disengaging section. The filter consists of a cylinder having 5 mm diameter holes on the surface, around which a 45 μm stainless steel mesh is wrapped twice. The fine material escaped from the system was recovered in a filter bag fitted at the end of the vent line, see (5) in Figure 17.

Connected to the side of the disengaging section was another stainless steel pipe line that acts as a pressure relief valve, see (6) in Figure 16. Any pressure built up in the bed was released through this pipe line into a stainless steel cylindrical tank (1700 mm tall x 130 mm diameter) containing water, see (7) in Figure 17. The height of the

column of water was worked out so to give a pressure drop of 150 cmH_2O, which means that any pressure higher than this would lead the gas to bubble through the water.

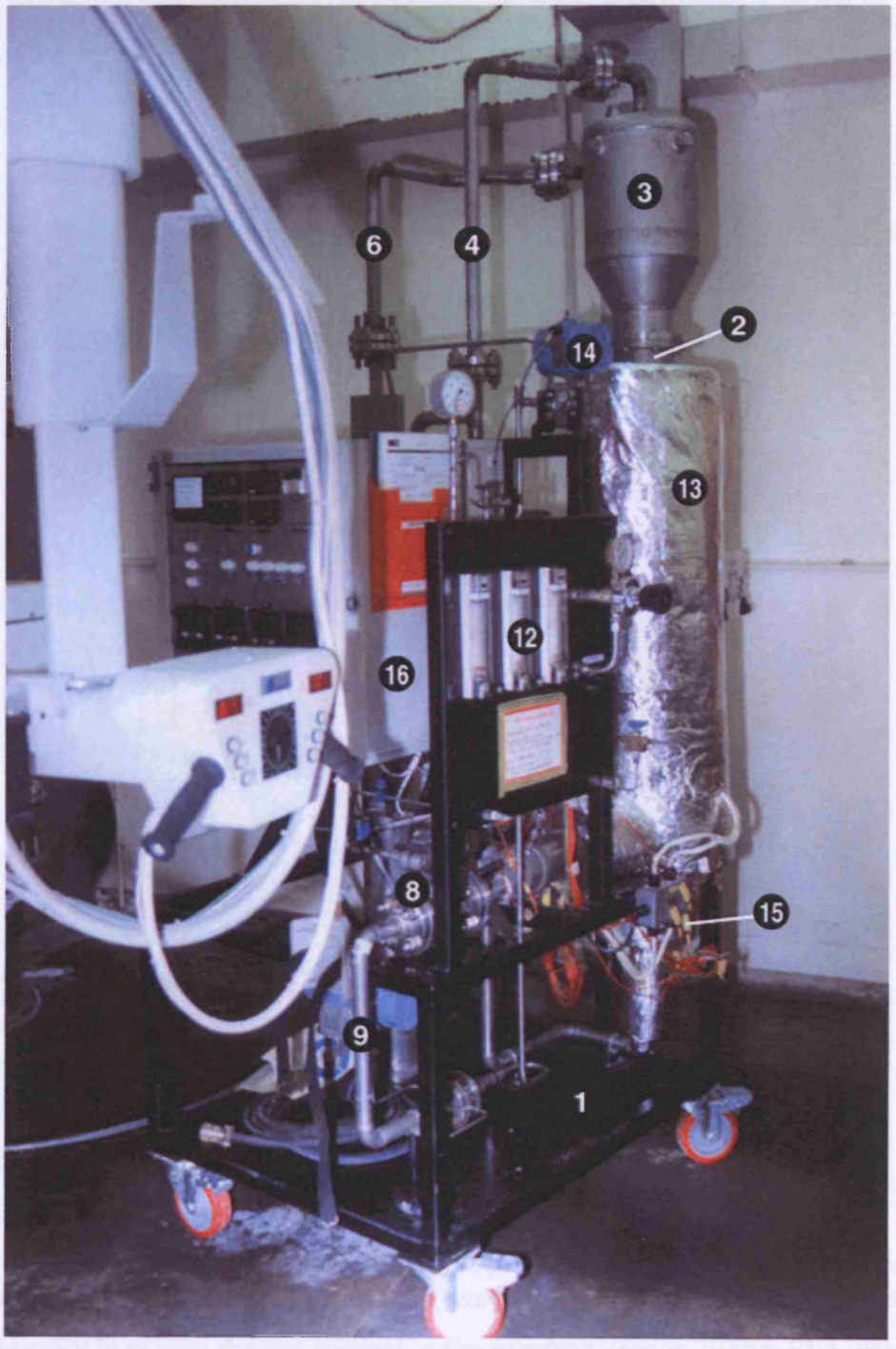

Figure 16 *Fluidization Rig (Front view)*

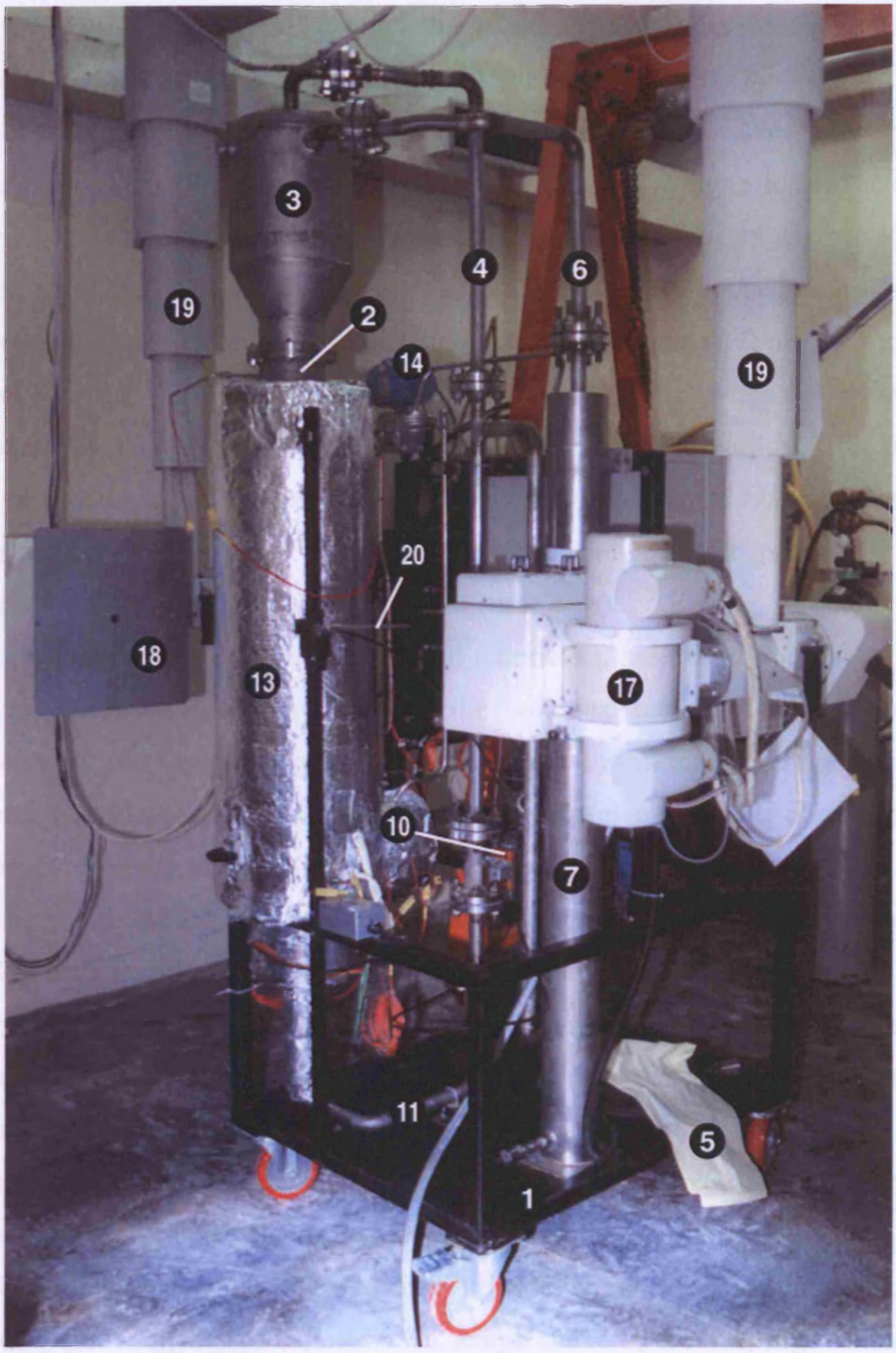

Figure 17 *Fluidization Rig (Rear view), X-Ray Equipment*

Two solenoid valves are fitted on the rig, one (SV1) to cut the gas supply to the bed, the other (SV2) to vent the gas trapped in the windbox section. Valve SV1, see (8) in Figure 16, was installed on a 38.1 mm pipe line leading from the rotameter panel to the side of the windbox, see (9) in Figure 16.

Valve SV2, see (10) in Figure 17, was installed on a 38.1 mm pipe leading to the vent line from the bottom of the windbox, see (11) in Figure 17. This system of solenoid valves was used during the bed collapse experiments. The two valves were operated remotely from outside the X-ray cell where the fluidization rig is located and were synchronized to switch position simultaneously: when the fluidising gas was shut off by closing valve SV1, valve SV2 was opened allowing the gas trapped in the windbox to be vented. Moreover, a horizontal pointer, see (20) in Figure 17, made of material opaque to X-rays was connected to the solenoid valves so that when the valves were switched over the pointer changed position from horizontal to vertical. This pointer, externally mounted next to the vessel, can be moved along its height so as to be always in the field of view of the X-ray image and therefore provide a visible indication of the start of the bed collapse test (time zero).

Fluidizing gas was metered from calibrated rotameters, see (12) in Figure 16, before being preheated while passing through the windbox section. The windbox was wrapped with 800 watt heating tapes. High temperatures in the vessel were achieved by means of ceramic heaters wrapped around the vessel and capable of providing an operating temperature up to 1250°C. The two ceramic heaters cover 900 mm of the vessel height. Since this material was not transparent to X-rays, the heaters were fitted so to leave a vertical window, 70 mm wide, on both sides of the vessel to let X-rays through. All hot surfaces were insulated using two layers of 1.5 cm thick Super-wool, covered by a 7 cm thick layer of Rockwool wrapped with silver tape, see (13) in Figure 16.

A Rosemount Model 1151 differential pressure transducer, see (14) in Figure 16, was used to measure the pressure drop across the fluidised bed.

A system of thermocouples allowed monitoring of the temperature in the fluidized bed, see (15) in Figure 16. Indicators for temperatures in the bed, high temperature alarms and bed pressure drop were displayed on a panel external the electrical control box, see (16) in Figure 16. Switches to activate heaters and the solenoid valves system were also installed on this panel.

3.4 X-Ray Technique

X-rays represent a non-intrusive tool to provide quantitative real time information on the internal structure of a rapidly changing 3D system. The pulsed high energy X-ray beam is passed through the test vessel where attenuation occurs depending on the amount and distribution of fluids and solids within the vessel (see Figure 18).

The X-ray facility used in this study is located in the Department of Chemical Engineering at University College where it is housed in a radiation proof room.

3.4.1 X-Ray Unit

The X-ray unit consists of generator, tube and image intensifier. The tube and image intensifier, see (17) and (18) in Figure 17 respectively, are mounted on a twin column ceiling mounted suspension unit, see (19) in Figure 17, which allows the columns to be moved along the length of the room. The lateral movement of each column allows the distance between the tube and the image intensifier to be changed. Each column can also be moved in a vertical plane either independently or synchronised as a pair. This motion is motorized and could be remotely controlled from outside the room.

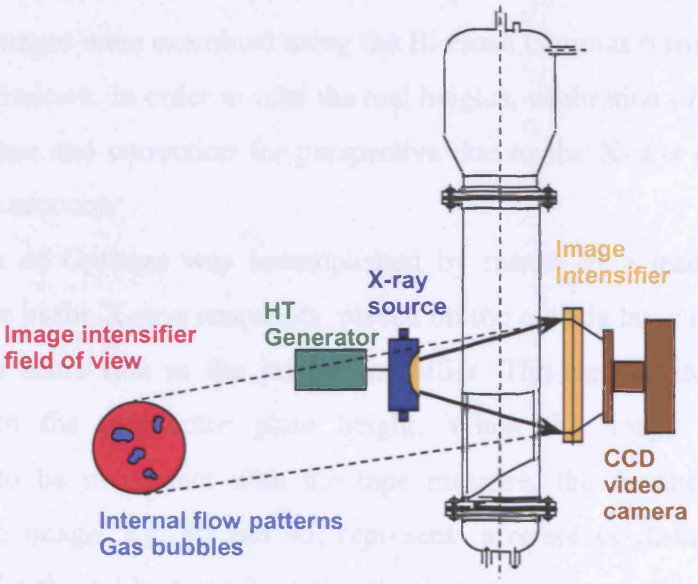

Figure 18 *X-Ray Imaging technique*

The X-ray tube (Machlett Dynamax Super 50-60(B) model) was designed to operate at up to 150 kVp (kilovolts peak). The image intensifier is a Thompson TH9432 HP H671 VR23 circular model with a diameter of 30 cm.
All X-ray operations were carried out from the main control console located outside the radiation proof room.

3.4.2 Image Recording

The images were displayed on a 12 inch monitor located outside the X-ray room and recorded using a JVC BR-S600E video cassette recorder using VHS cassettes. Frame numbers and insert text can be displayed on the monitor so to be recorded on the image and stored permanently with it, in order facilitate the identification and analysis of the experiments.
The recorded tape was then played on a JVC BR-S611E videocassette recorder, which allowed the images to be searched at a variable speed and to be analysed frame by frame.

3.4.3 Image Analysis

The recorded images were examined using the BioScan Optimas 6 software operating in Microsoft Windows. In order to read the real heights, calibration of Optimas with a reference distance and correction for perspective due to the X-rays distortion effect were taken into account.
The calibration of Optimas was accomplished by means of a lead tape measure, therefore visible in the X-rays snapshots, placed on the outside layer of the insulating material on the same side as the image intensifier. The zero of the tape measure corresponded to the distributor plate height. When the image intensifier was positioned so to be in contact with the tape measure, the distance between two numbers on the image, e.g. 40 and 45, represents a reference distance, e.g. 5 cm, which is used for the calibration; from this the distance between the midline and the distributor can be determined.
The X-ray distortion effect can be visualized in Figure 19. This is caused by the diverging X-ray beam (usually 13°). Therefore, the projected heights are equal to the

real ones only for objects positioned on the midline, i.e. at the height of the X-rays emission point. If the bed surface is above or below the midline, a correction is needed according to its distance to the midline.

When the bed surface is above the midline, its projection on the image intensifier is that of the point closer to the X-Rays source (point E), thus the distance between bed surface and midline measured with Optimas is DC.

The real bed height is:

$$H_{bed} = H_{midline} + HC \qquad \text{Eq. 34}$$

Due to the similarity of triangles ACD and EHD,

$$DH = \frac{EH}{AC} DC \qquad \text{Eq. 35}$$

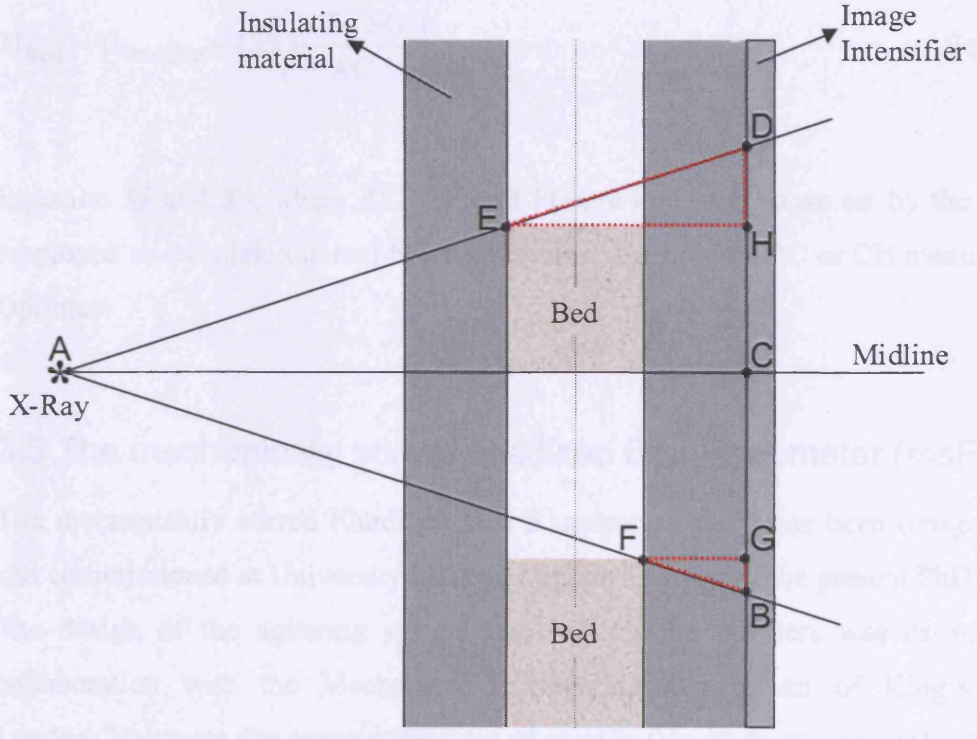

Figure 19 *X-Rays distortion effect*

Hence,

$$HC = DC - DH = DC\left(\frac{AC - EH}{AC}\right) \qquad \text{Eq. 36}$$

Substituting Equation 36 in Equation 34 gives:

$$H_{bed} = H_{midline} + DC\left(\frac{AC - EH}{AC}\right) \qquad \text{Eq. 37}$$

When the bed surface is below the midline, its projection on the image intensifier is that of the point closer to the Image intensifier (point F), thus the distance between the bed surface and the midline measured with Optimas is CB.
Similarly to the previous case,

$$H_{bed} = H_{midline} - CB\left(\frac{AC - FG}{AC}\right) \qquad \text{Eq. 38}$$

Equation 37 and 38, where AC, EH and FG are known because set by the user, are employed to calculate the real bed heights from the heights DC or CB measured with Optimas.

3.5 The mechanically stirred Fluidized Bed Rheometer (msFBR)

The mechanically stirred Fluidized Bed Rheometer (FBR) has been designed, built and commissioned at University College London as a part of the present PhD work.
The design of the agitating system used to stir the powders was carried out in collaboration with the Mechanical Engineering Department of King's College London. However, the experimental set up used in this study was a simplified version of the complete equipment, and features an existing agitating system kindly provided by Dr Tim Elson, from University College London and adapted to the msFBR.

A detailed description of the agitating system developed in collaboration with King's College London, which is suitable for future work at high temperature, is reported in Appendix A3.

The msFBR was mounted on a free standing, wheeled stainless steel frame, see (1) in Figure 20. It consists of a fluidization unit (2), an agitating system (3), a data acquisition unit (4) and a control box (5). The control box and the data acquisition unit stand on a bench next to the equipment (see Figure 20).

Figure 20 *The msFBR unit*

3.5.1 Fluidization Unit

A 14 cm diameter x 30 cm tall Pyrex vessel with a wall thickness of 0.3 cm, see Figure 21, was used for testing the powders. The diameter of the fluidized bed was chosen as to match that of the Fluidization Rig described in section 3.3. The vessel

was made of pyrex in order to withstand high temperatures and also to allow direct observation of the powders' behaviour at ambient temperature. The vessel was fitted with a very fine stainless steel distributor plate to ensure a high pressure drop and therefore attain an even distribution of the fluidizing gas entering the bed.
The windbox below the distributor plate was 7 cm high and was packed with 10 mm ceramic balls to improve heat transfer, for when the equipment is operated at high temperature, and to enhance a uniform gas distribution on the distributor plate.

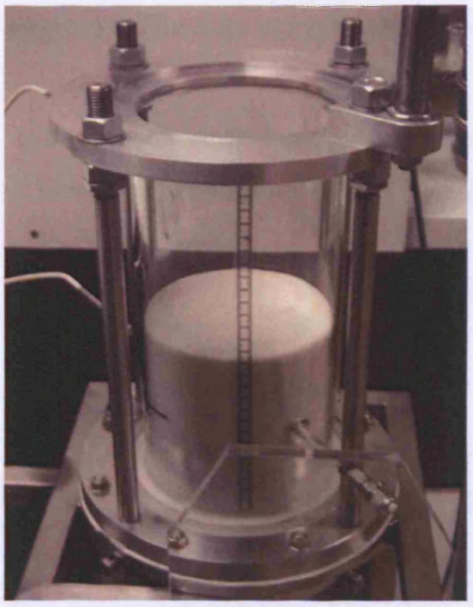

Figure 21 *msFBR – Fluidization vessel*

The vessel is closed at the top by means of a two-half-moon lid, specifically designed to allow loading and emptying of the bed without removing the shaft. The lid contains four holes for venting gas and are covered with fine wire meshes in order to retain entrained fines. An alternative version of the lid is available for the high temperature operating mode, where the lid is solid and the hot gas exhausts through an insulated pipe connected to the lid and vented in water.
Fluidizing nitrogen gas comes from a cylinder placed next to the rig and is metered via rotameters before entering the windbox.
In the high temperature configuration, the gas is preheated in the windbox, which in this case is wrapped with a 300W heating tape (HT95506, Electrothermal Engineering). High temperatures in the vessel are achieved by means of a 1200W

heating tape (HT95524, Electrothermal Engineering) wrapped around the vessel and capable of providing an operating temperature up to 450°C.
A system of thermocouples allows monitoring of the temperature in the bed and on the skin of vessel and windbox. The temperature in the bed is measured my means of a sliding thermocouple placed 5 cm above the distributor plate and in the middle of the bed. After the temperature reading, the thermocouple can be pulled out so to allow the impeller to stir the bed. Indicators for temperatures and the switches to activate the heaters are installed in the control box, see (5) in Figure 20, and are manually operated. The high temperature mode was not utilised in this work.

The pressure drop across the bed is measured by means of an ultra low pressure differential sensor (RS model 395-229), capable of measuring pressure drops in the range 0-72 cmH_2O.

3.5.2 Agitating system

The agitator consists of a 165 mm stainless steel shaft, fitted with two-flat-bladed paddles (36 mm diameter × 7 mm height and 0.7 mm thickness). A bigger two-flat-bladed paddle (63 mm diameter × 12 mm height and 1 mm thickness) was also used for some experiments. The shaft is driven by a rotational rheometer (Contraves Rheomat 30), which is clamped to the vessel and operates as follows: the impeller is motor-driven (30 speed steps subdivided in geometrical progression within a range of 350 to 0.048 rpm), the braking torque exerted on the bob is measured and the signal is sent to the data acquisition card (DAQ). Both the motor and its gear box are bolted to the casing of the fluidized bed.

3.5.3 Data Acquisition Unit

The data acquisition unit consists of a PC (HP Vectra VL420 Desktop) acquiring data through its serial ports as well as a data acquisition card connected to it (National Instruments Multifunction DAQ PCI-6036E). The PC deals with the data by means of LabVIEW 6.1 Full Development System for Windows (National Instruments P/N: 776670-03). LabVIEW, which stands for Laboratory Virtual Instruments

Experimental Workbench, is a software for graphical programming used to acquire and analyse measurement data as well as driving instruments.
In the work presented here LabVIEW was used to collect measurements of the Pressure Drop across the bed and of the Torque exerted on the shaft. Data are acquired through the DAQ and sent to LabVIEW where the variation with time of the measured variables can be recorded, plotted in real time and stored in Excel files.
When operating the agitating system described in Appendix 3, LabVIEW can also be used to simultaneously drive the motors for the rotational and axial movement of the shaft through the PC serial ports.

3.6 Determination of the experimental procedure for the msFBR

Given the novelty of the in-house built equipment and the lack of an established experimental procedure for it, a number of preliminary tests was carried out in order to determine the key parameters affecting the torque measurements and the optimal experimental procedure to be adopted.
To this end, the first step was to identify a suitable procedure to precondition the bed prior to each torque measurement. This is reported in section 3.6.1. Then the dependence of the torque measurements upon impeller speed and stirring time were investigated both below u_{mf} and at the minimum fluidization velocity. Results of this preliminary investigation are discussed in sections 3.6.2 and 3.6.3, where conclusions are drawn regarding the most appropriate experimental procedure in each case.

The study on the effect of the torque measurements with changing the rate of aeration and the impeller depth forms the main body of the experimental results of this rheological work and is discussed in chapter 5.

3.6.1 Preconditioning

Prior to each torque measurement the bed was preconditioned by fully fluidizing it and then decreasing the flow rate to the desired value. In this way, the initial packing of the bed in each experiment was the loosely packed state obtained by the random

readjustment of the particles after fluidization and any previous "history" of the structure of the material was erased.

3.6.2 Experiments at u < u_{mf}

3.6.2.1 Effect of impeller speed

Preliminary tests were carried out in order to investigate the effect of the impeller speed on the torque measurements below the minimum fluidization velocity.

At a set rate of aeration and impeller depth, torque measurements were taken for each increasing impeller speed from 0 rpm up to 8.79 rpm and then decreasing down to 0 rpm. It ought to be stressed that the preconditioning was performed only at the beginning of the experiment and not between measurements at increasing/decreasing impeller speed N and that a delay of approximately 5 minutes was used between increasing/decreasing impeller speeds.

During the experiments, the pressure drop across the bed and the bed height were also monitored and recorded.

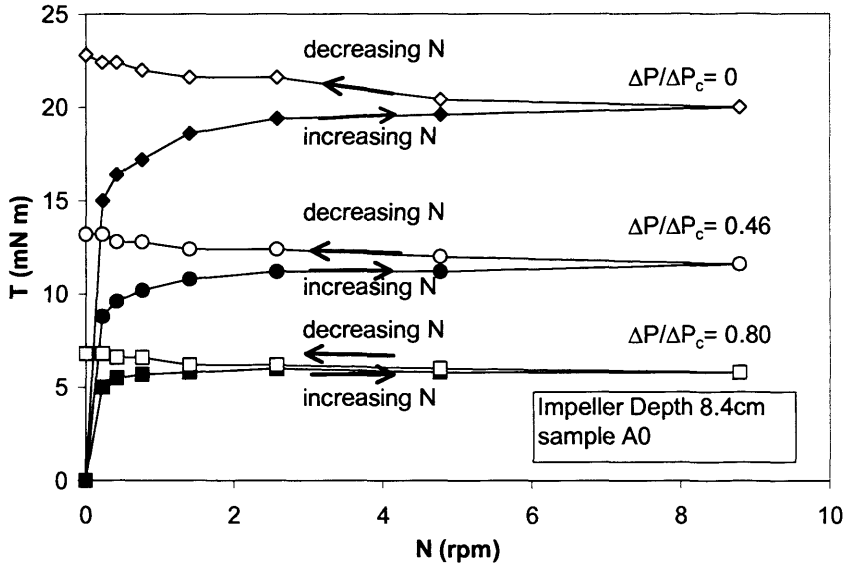

Figure 22 *Torque profiles with increasing aeration at 8.4 cm impeller depth – Alumina A0*

Figure 22 reports the torque profiles for the alumina sample A0 at different rates of aeration, defined as $\Delta P/\Delta P_c$, equal to 0, 0.46 and 0.80, at an impeller depth equal to 8.4 cm (about half of the total bed height). For each rate of aeration, when increasing the impeller speed a significant increase in the torque was recorded up to about 3 rpm. Then the torque continued to increase at a lower rate. When decreasing the impeller speed, the torque kept increasing and when the impeller came to a complete stop the torque never dropped to zero, showing a residual strength.

In order to assist the interpretation of the observed trends with increasing impeller speed, the variation of pressure drop across the bed and bed height with increasing impeller speed were also analysed and are shown in Figure 23 and Figure 24 for the $\Delta P/\Delta P_c = 0.46$ experiment.

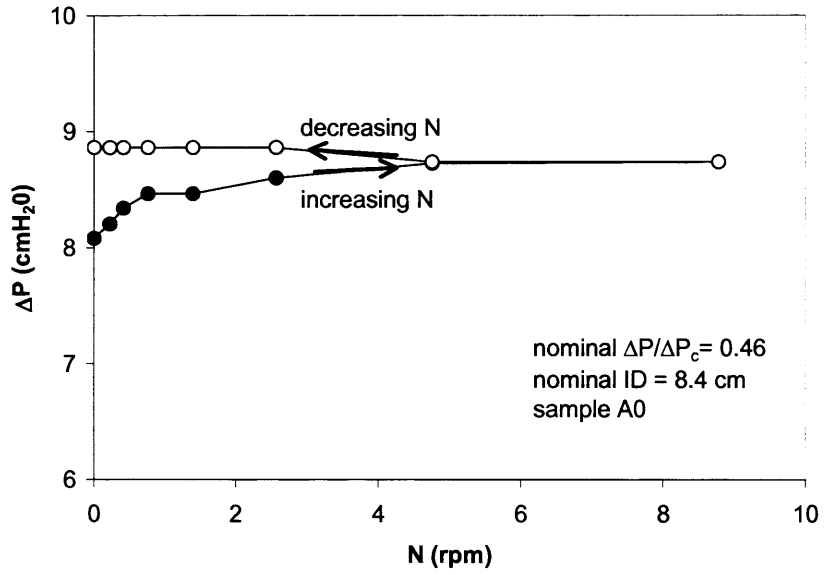

Figure 23 *Pressure Drop profile at 0.46 $\Delta P/\Delta P_c$ and 8.4 cm impeller depth – Alumina A0*

When increasing the impeller speed N, the pressure drop across the bed systematically increased (Figure 23) and this was accompanied by a little decrease of the bed height, as shown in Figure 24. When decreasing the impeller speed, both the pressure drop and the bed height did not show significant changes with N. This type of profile was observed at each aeration rate below u_{mf}. A similar behaviour was reported also by Hobbel and Scarlett (1985) in a couette geometry.

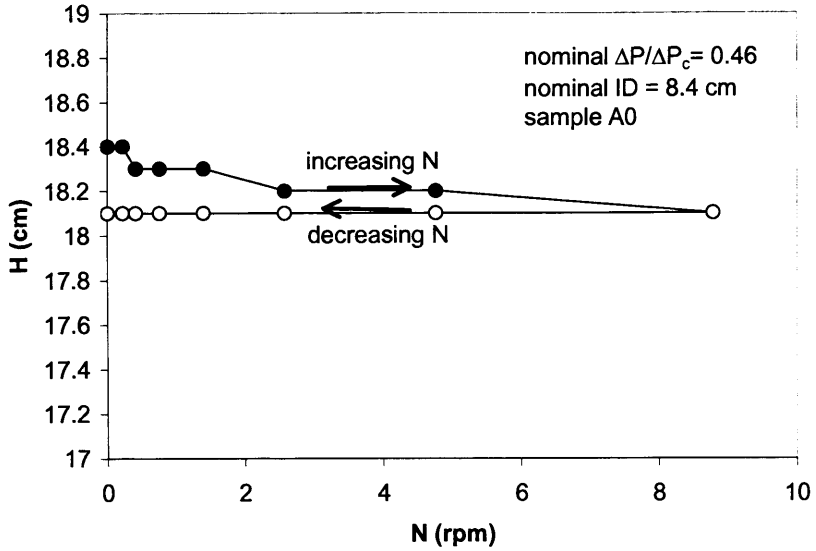

Figure 24 *Bed height profile at 0.46 $\Delta P/\Delta P_c$ and 8.4 cm impeller depth – Alumina A0*

The observed behaviour may be due to the initial packing conditions of the bed at the beginning of the experiment. The bed is loosely packed as it is settling from the fluidized state and therefore the "disturbance" caused by the rotation of the impeller acts to agitate the bed and causes the particles to settle into a more packed structure. The decrease in the bed voidage is in turn causing the increase in the pressure drop across the bed, according to the Ergun equation (Eq. 1). Therefore, the increase in the torque measurements observed when increasing the impeller speed could be related to the simultaneous decrease in bed voidage, as a higher torque is needed to stir a more packed bed.

When the impeller speed was decreased, unexpectedly the torque continued to increase even if the bed height seemed to have stabilised at a fixed value. This may be explained considering that the torque is very sensitive to changes in the local voidage around the impeller. The bed height, on the other hand is sensitive to changes in the overall voidage, and might not show changes in the local voidage. Barnes *et al* (1987) also showed that liquid suspension viscosity is very sensitive to small changes in voidage. It ought to be pointed out also that the bed height measurements were taken by visual observation with an experimental uncertainty of ± 0.1 cm, which may be too big to detect changes due to very small changes in the voidage of the bed.

A similar behaviour was observed for the ballotini sample, for which an increase in the torque measured with increasing and decreasing impeller speed was also observed at each aeration rate. The pressure drop profile and the bed height profile for the ballotini sample were also similar to those shown in Figure 23 and Figure 24 for the alumina.

3.6.2.2 Effect of stirring time

The compaction effect described in section 3.6.2.1 highlighted the need to investigate the dependence of the torque measured on the duration of the stirring. If a time effect exists, then the torque increase observed with increasing impeller speed shown in Figure 22 could in fact just depend on the time step used to increase the impeller speed rather than on a real effect of changing impeller speed.

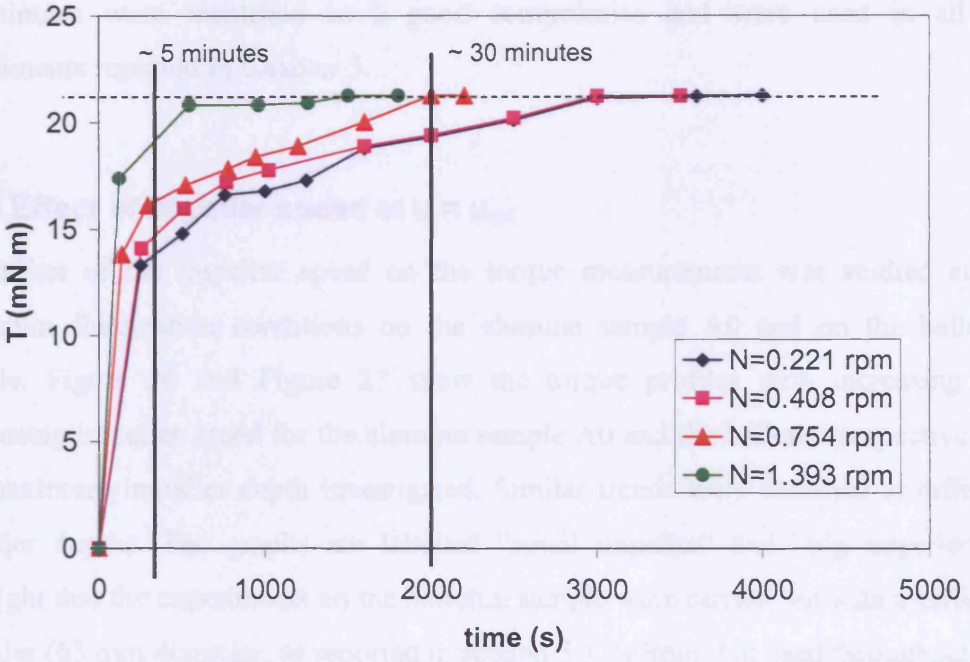

Figure 25 *Effect of impeller speed on torque variation with time – Alumina A0*

In order to look into this problem, an additional set of experiments was carried out in which a given impeller speed was set and the torque variation with time was monitored. The experiment was then repeated at different impeller speeds.

Figure 25 shows clearly that the torque reaches the same maximum value, regardless of the impeller speed adopted. Therefore, the impeller speed is not a key parameter in this investigation, provided that a sufficient time is allowed before readings are taken. This result also shows that running experiments with increasing impeller speed and using a short time step can be misleading. In particular, Figure 25 shows that a stable value of the torque is reached faster at higher impeller speeds.

The same results were obtained with each powder analysed in this work and therefore the experimental procedure adopted when measuring the torque below the minimum fluidization conditions was to set the impeller rate at a chosen value and wait for a constant value of the torque to be achieved. In particular, in order to create as low a disturbance as possible to the bed of particles, the impeller speed was chosen as to be the slowest impeller speed which still allowed a reasonably short time to reach a steady state value of the torque. A value of N = 0.754 rpm and a reading time of about 30 minutes were identified as a good compromise and were used in all the experiments reported in Chapter 5.

3.6.3 Effect of impeller speed at $u = u_{mf}$

The effect of the impeller speed on the torque measurements was studied at the minimum fluidization conditions on the alumina sample A0 and on the ballotini sample. Figure 26 and Figure 27 show the torque profiles with increasing and decreasing impeller speed for the alumina sample A0 and the ballotini respectively at the maximum impeller depth investigated. Similar trends were obtained at different impeller depths. The graphs are labelled "small impeller" and "big impeller" to highlight that the experiments on the ballotini sample were carried out with a different impeller (63 mm diameter, as reported in section 5.1.2) from that used throughout this study. The reason for this change was to be able to detect the small values of the torque recorded for the ballotini at the minimum fluidization, as the measured torque increases with increasing impeller diameter.

The torque profiles found at $u = u_{mf}$ were different from those below u_{mf}. As in the experiments below u_{mf}, the torque measurements exhibited an increasing trend with increasing impeller speed, as shown in Figure 26 and Figure 27. However, at

minimum fluidization the bed height and pressure drop across the bed did not change during the experiments. Therefore, the observed increase in the torque measurements with increasing impeller speed was attributed to a "viscous" effect rather than to a consolidation effect. This is confirmed by the fact that the torque this time decreased when decreasing the impeller speed, as one would expect when stirring a liquid. This result can be interpreted as a change from a solid-like behaviour (torque independent upon impeller speed) to a liquid-like behaviour (viscous effects) when fluidization is attained.

Given the absence of consolidation at $u=u_{mf}$, and therefore of any time effect on the torque measurements, and given the observed dependence of the torque measurements upon the impeller speed, the experimental procedure envisaged for the experiments at minimum fluidization is to analyse the torque variation with increasing and decreasing impeller speed rather than with time.

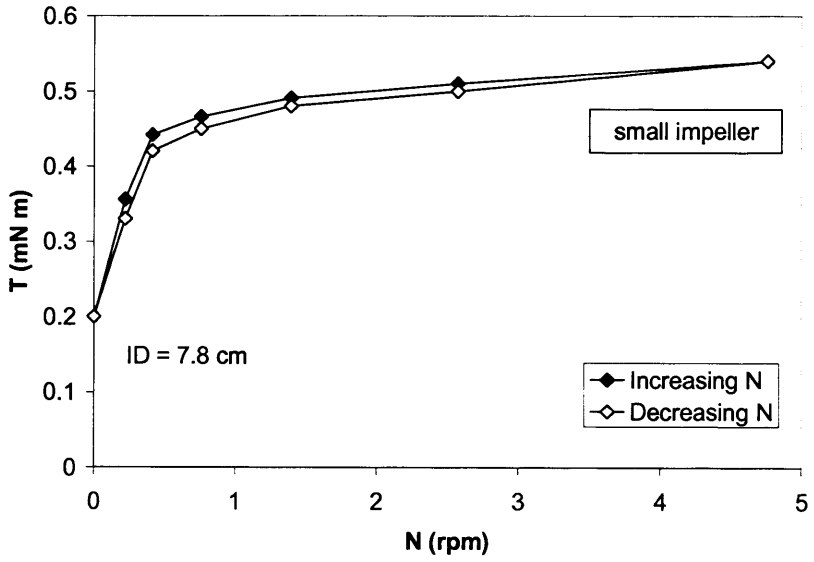

Figure 26 *Torque as a function of impeller speed - Alumina A0; $\Delta P/\Delta P_c$ = 1; ID = 7.8 cm*

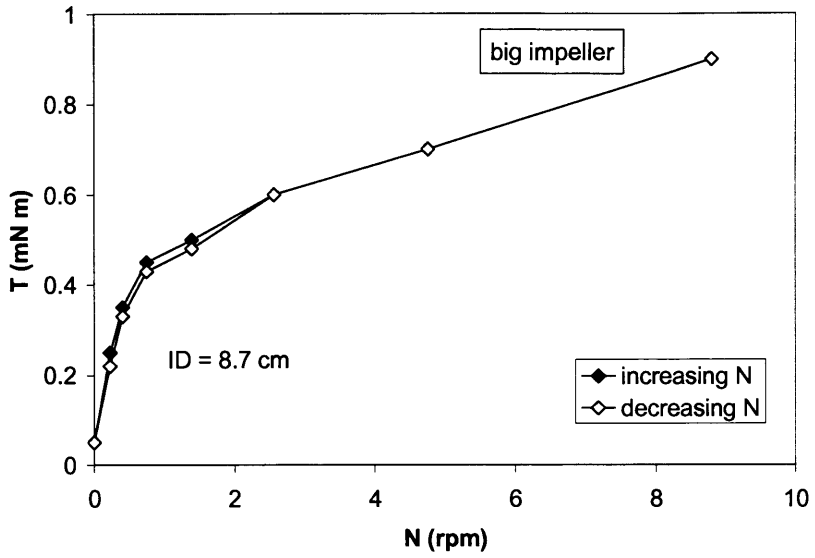

Figure 27 *Torque as a function of impeller speed - Ballotini; $\Delta P/\Delta P_c$ = 1; ID = 8.7 cm*

3.7 Shear Cell measurements

Shear cells are generally used to determine the powder properties which influence powder flow and handling. Some of these properties are concerned with quantitative, design purposes (for example for hopper design) and are called failure properties. These include the effective angle of internal friction, the angle of wall friction, the failure (or flow) function, the cohesion and ultimate tensile strength. The requirement for getting powders to flow is that their strength is less than the load put on them, i.e. they must fail, hence the name failure properties. Other properties are concerned with qualitative comparisons of powder behaviour, flowability, cohesiveness or any other such definition of powder characteristic. These properties are used for fingerprinting or for quality control.

In this work, some of the properties measured using a shear cell have been used to determine the stress distribution in an aerated bed of particles (see section 5.2.4). This section describes the experimental procedure followed to determine the properties needed for the purpose of this study. For a complete review see Schwedes (2003).

The experiments reported in this section and the model described in section 5.2.4 were developed within an ongoing collaboration with the Powder Technology Group of the University of Salerno, Italy.

3.7.1 Modified Peschl Shear Cell

The shear cell used in this study was a Peschl shear tester (rotational split level shear tester RO-200; see Peschl, 1976), located in the University of Salerno, Italy, and shown in Figure 28. The cell has a 61 mm diameter and is 15 mm high. The commercial Peschl shear cell was modified by the Powder Technology Group of the University of Salerno, by adding a cinematic chain to the apparatus in order to counterbalance the weight of the top of the cell, therefore allowing measurements at low values of the consolidation stress (Barletta et al., 2004). This modification was ideal for the present work, as it is expected to have low normal stresses in a 18 cm deep bed of particles subjected to gravity only.

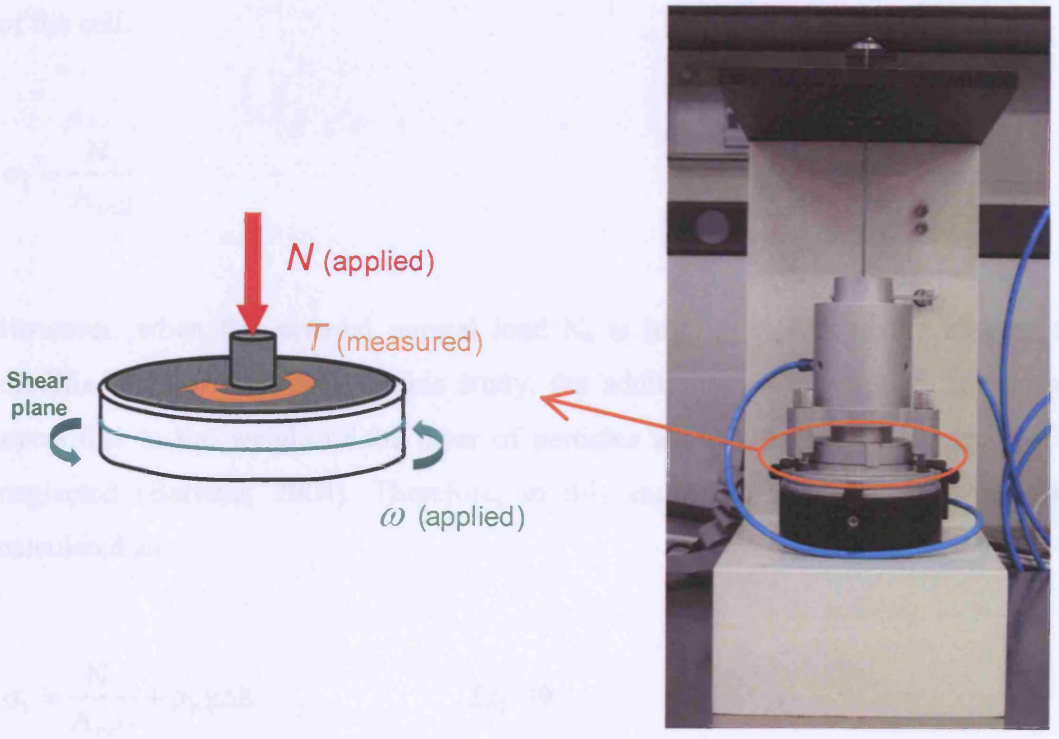

Figure 28 *The Peschl Shear Cell (courtesy of the University of Salerno, Italy)*

The cell was also modified to allow aeration of the powder sample during the shear experiments. However, in the present work the cell was only used in the non aerated mode.

3.7.2 Construction of the static internal yield locus

Once the shear cell was loaded with the powder specimen, the maximum load chosen, N_c, was applied on the cell lid and the preshearing phase started. When a steady state value was attained for the measured shear stress, the shearing was stopped. Then the shearing phase started under a normal load N_1 lower than N_c and a peak value of the shear stress was reached corresponding to the material failure. The sequence of preshearing and shearing phases was then repeated, keeping the same value of the normal load for each preshearing phase, N_c, and using decreasing normal loads for each shearing phase, i.e. $N_1>N_2>N_3>\ldots>N_N$.

Following the theory of Jenike (Jenike, 1961), the solid normal stress acting in the shear plane in general can be calculated by simply dividing the external normal load by the shear surface area, which is assumed to correspond to the cross sectional area of the cell.

$$\sigma_i = \frac{N_i}{A_{cell}}$$

However, when the external normal load N_c is low, as it was in the case of the modified Peschl Cell used in this study, the additional contribution to the normal stress due to the weight of the layer of particles above the shear plane can not be neglected (Barletta, 2004). Therefore, in this study the solid normal stress was calculated as:

$$\sigma_i = \frac{N_i}{A_{cell}} + \rho_b g \Delta h \qquad \text{Eq. 39}$$

where ρ_b is the powder bulk density , g is the acceleration due to gravity and Δh is the thickness of the powder layer above the shear plane.

Figure 29 reports a typical shear stress chart and the derived yield locus corresponding to the applied consolidation stress. The yield locus is the interpolation of the experimental points (σ,τ) corresponding to failure. It is worth pointing out that different yield loci are obtained when applying different consolidation stresses σ_c. The choice of the normal stresses used in the shearing phases and the number of phases used in each experiment, on the other hand, are arbitrary as all the (σ, τ) points obtained in the shearing phases will belong to the same yield locus provided that the same consolidation stress is applied in the preshearing phases. In this study four or five points were measured for the construction of each yield locus and each measurement point was repeated twice.

The values of the static angle of internal friction φ and the cohesion C were worked out as the slope and the intercept with the τ axis of the yield locus, respectively, as shown in Figure 29.

Then, the Mohr-Coulomb failure analysis (see Nedderman, 1992, chapter 3.3) was used to determine the principal stresses corresponding to the consolidation applied. In particular, the average of the steady state shear stress values obtained under the consolidation stress σ_c is reported on the σ, τ plane. The Mohr circle passing through the latter point and tangent to the yield locus is drawn.

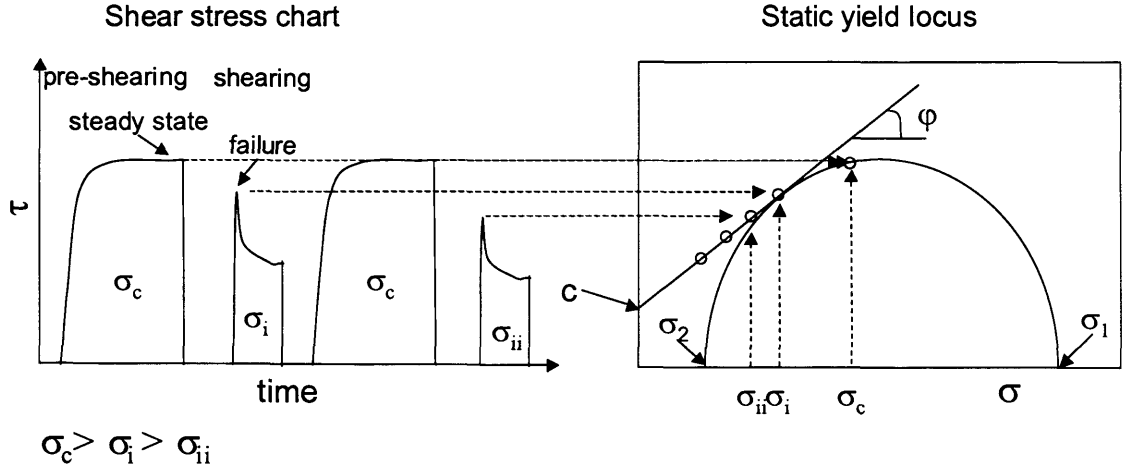

Figure 29 *Construction of the static yield locus*

The two intercepts of this Mohr circle and the σ axis are the major principal stresses σ_1 and σ_2 corresponding to the consolidation applied. By repeating the whole experiment with different consolidation loads N_c, a family of incipient yield loci was obtained. As a result, different angles of internal friction and values of the cohesion were obtained as a function of the major principal stress σ_1. Results on the yield loci for the powders under analysis in this study are reported in section 5.1.1

3.7.3 Construction of the wall yield locus

The Peschl cell was also used to obtain the angle of wall friction φ_w and the wall adhesion A for each material.

The angle of wall friction is the simplest of the failure properties. It is equivalent to the angle of friction between two solid surfaces except that one of the two surfaces is now a powder. It describes the friction between the powder and the material used to confine the powder. The wall friction causes some of the powder weight to be supported by the walls of the container.

The criterion for the existence of incipient slip along a wall can be expressed in the form $\tau_w = f(\sigma_w)$, where σ_w and τ_w are the normal and shear stresses on the wall.

In particular we can assume a linear relationship:

$$\tau_w = \sigma_w \tan\varphi_w + A \qquad \text{Eq. 40}$$

where φ_w and A are the wall friction angle and the wall adhesion of the powder on a given surface material.

The experimental procedure to determine φ_w and A consisted of replacing the base of the shear cell with a Pyrex sample (the wall material the msFBR is made of) and measuring the shear stresses under progressively increasing values of the normal stress and repeating the shearing three times for each load so ensure a steady state to be reached each time. This time, however, no pre-shearing was performed. Therefore, the wall yield locus so obtained represents a general property of the specific matching wall material/powder analysed, i.e. it is not dependent on the consolidation stress as it

was in the case of the internal yield locus described in section 3.7.2. Hence, for each powder a single value for the angle of wall friction and for the wall adhesion on pyrex were obtained and are reported in section 5.1.2.

3.7.4 Construction of the dynamic internal yield locus

The dynamic yield locus represents the steady state deformation, as opposed to the static yield locus which represents the incipient failure. The dynamic yield locus is constructed by plotting on a σ, τ plane the principal Mohr circles obtained for various consolidation stresses. The dynamic yield locus will be the curve or straight line tangent to all circles, as shown in Figure 30.

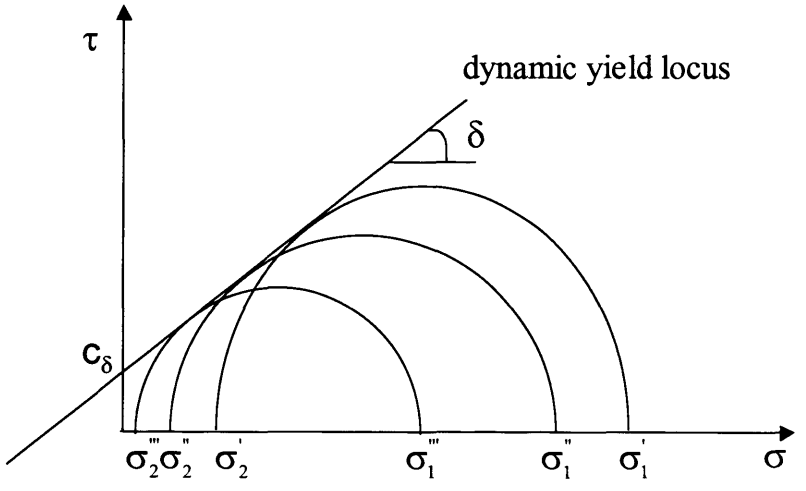

Figure 30 *Dynamic yield locus*

The dynamic angle of internal friction δ and cohesion C_δ are properties of the material which are independent of the consolidation stress. δ and C_δ were obtained as the slope and the intercept at $\sigma = 0$ of the dynamic yield locus of the powder.

An approximation of the dynamic yield locus is given by the effective yield locus, provided that $C_\delta = 0$. The effective yield locus is the straight line drawn through the

origin and tangentially to the Mohr's circle represented in Figure 29 (see Figure 31). Since it passes through the origin, this straight line represents a cohesionless material with an angle of internal friction φ_e. This angle is denoted the effective angle of internal friction of the material. The difference between the effective and the internal angle of friction can be an indication of the degree of cohesiveness of the powder (Molerus, 1975).

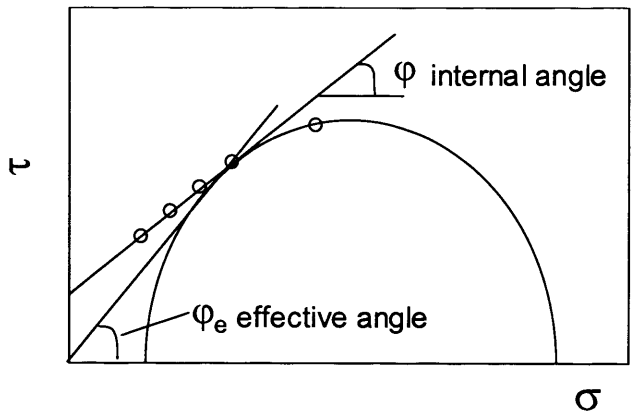

Figure 31 *Effective angle of internal friction*

4 Fluidization results and discussion

In this chapter the results of the fluidization tests performed on the alumina samples A0, A3, A4, A5 and A6 are reported. The five powders analysed can be divided in three groups: powder A0, virtually fines free, is used as a base line to investigate the effect of fines addition on fluidization; powders A3 and A4, containing the same amount of fines, 22%wt, and differing in the fines size distribution; powders A5 and A6, containing the same amount of fines, 30%wt, and differing in the fines size distribution. The properties of these powders were reported in Table 5 in section 3.1.2. This is reported again below for convenience.

The results obtained on the two sets of powders with different fines content, A3 - A4 and A5 - A6, are presented together throughout sections 4.1-4.5. The main focus in these sections is the investigation of the influence on fluidization of adding the same amount of smaller (0-25 μm) or bigger (26-45 μm) fines to the same virtually fines free material, i.e. A3 versus A4 and A5 versus A6, and the investigation of the effect of temperature on the fluidization behaviour of each powder. In addition, comparisons between A3 and A5, and between A4 and A6, are also reported to highlight the effect of increasing the total fines content from 22% to 30%wt.

Table 5 *Properties of samples A0, A3, A4, A5 and A6*

	d_p (μm)	F_{45} (%)	%wt 0-25 μm	%wt 25-45 μm
A0	75.1	3.2	0	3.2
A3	54.9	22.2	5.6	**16.6**
A4	41.7	22.5	**13.1**	9.4
A5	49.1	30.7	8.1	**22.6**
A6	36.0	30.9	**18.8**	12.1

In sections 4.1 the pressure drop profiles are analysed for each powder and the minimum fluidization velocity u_{mf} is obtained. Comparisons between experimental values of u_{mf} and values calculated using equations reported in the literature are also discussed.

The experimental expansion profiles are shown in section 4.2 and are used in section 4.2.2 to determine the parameters of the Richardson and Zaki equation for both sets of powders containing 22%wt (A3 and A4) and 30%wt (A5 and A6) of fines.

The results of the bed collapse tests are discussed in section 4.4, where the main differences in the collapsing behaviour of powders having the same total fines content but differing in the fines size distribution and the effect of temperature are highlighted and discussed.

Finally, the suitability of the Richardson and Zaki equation to describe the collapse mechanism, and in particular the dense phase collapse rate, is assessed for both sets of powders A3, A4 and A5, A6 in sections 4.5.

4.1 Pressure drop profiles and u_{mf}

The performance of a fluidized bed reactor can be significantly improved by the addition of fines, as discussed in section 2.4.2. However, excessive fines can cause the powder to become too cohesive for proper fluidization. Therefore, the first step in this study was the assessment of fluidization through the pressure drop profiles, to verify in each case that the addition of fines had not caused the powder to become too cohesive.

The pressure drop profiles were analysed as a first indication of the quality of fluidization. These were obtained, as described in section 3.2.1, by increasing the gas flow rate in small steps and recording the pressure drop across the bed at each step ("Fluidizing" curves in Figure 33 and Figure 35). Once the bed was well fluidized the gas flow rate was then decreased until the bed settled and the pressure drop recorded with the same step by step procedure ("Defluidizing" curves in Figure 32 - Figure 35). The pressure drops in Figure 32 - Figure 35 are plotted as ratios $\Delta P / \Delta P_c$, where ΔP is the measured pressure drop and ΔP_c is the calculated pressure drop when full bed support is achieved, as defined by Equation 32 in section 3.2.1.

Therefore, a ratio $\Delta P / \Delta P_c$ close to 1 is an indication of good fluidization behaviour, i.e. the gas supports the whole bed, whereas a ratio below 1 indicates poorer fluidization, indicating that parts of the bed are not fluidized possibly due to channelling.

Figure 32 and Figure 33 report the pressure drop profiles for samples A3 and A4, both containing 22%wt of fine particles but richer in bigger and smaller fines respectively. Figure 32 shows the defluidizing pressure drop profiles at temperatures from ambient to 400°C for powder A3 and shows that the powder reaches full bed support at each temperature. A similar behaviour was also observed when defluidizing powder A4. Figure 33 reports the fluidizing and defluidizing curves for powder A4 at the minimum and maximum temperatures employed (ambient and 400°C). A small overshooting in the "Fluidizing" curve is noticeable at both temperatures and was also observed at each intermediate temperature analysed, showing a slight degree of cohesiveness, as is typical for group A powders, and the effect of friction at the wall. Similar results where obtained when fluidizing samples A3.

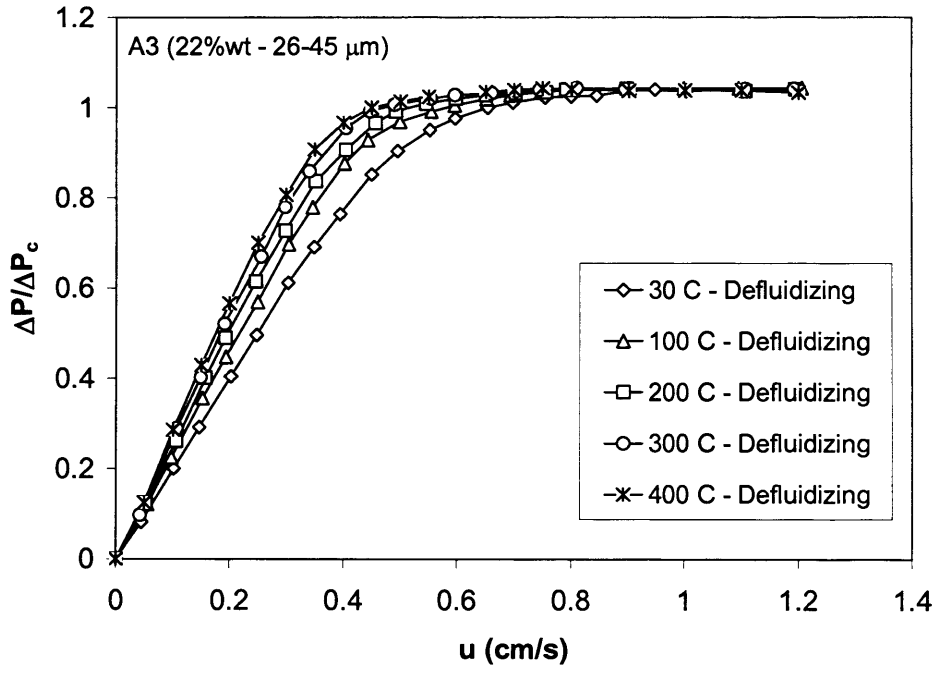

Figure 32 *Pressure Drop profiles. Defluidizing curves. Sample A3 (F_{45}=22%wt)*

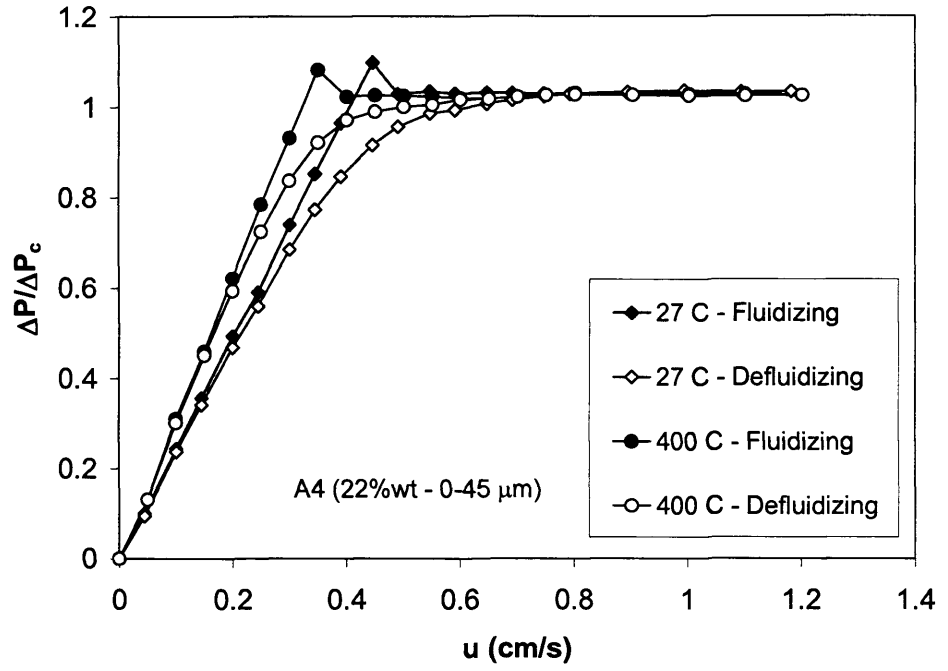

Figure 33 *Pressure Drop profiles at ambient temperature and 400°C. Sample A4 (F_{45}=22%wt)*

A similar behaviour to that exhibited by samples A3 and A4 was observed for samples A5 and A6, both containing 30%wt of fines, but richer in bigger and smaller fines respectively. Figure 34 shows that the full bed support was achieved at each temperature for powder A5. A similar behaviour was also observed for powder A6. Figure 35 highlights the presence of an overshooting in the fluidizing curve for powder A6 and this was also observed for powder A5.

Moreover, when comparing Figure 33 and Figure 35, the overshooting seems to be more pronounced for samples A6 (and A5) than for samples A4 (and A3), showing an increase in cohesiveness and in friction at the wall when increasing the fines content from 22%wt to 30%wt. However, full bed support was reached at each temperature for powders A5 and A6, indicating that the HDFs still dominate the fluidization behaviour of these powders at ambient and with increasing temperature.

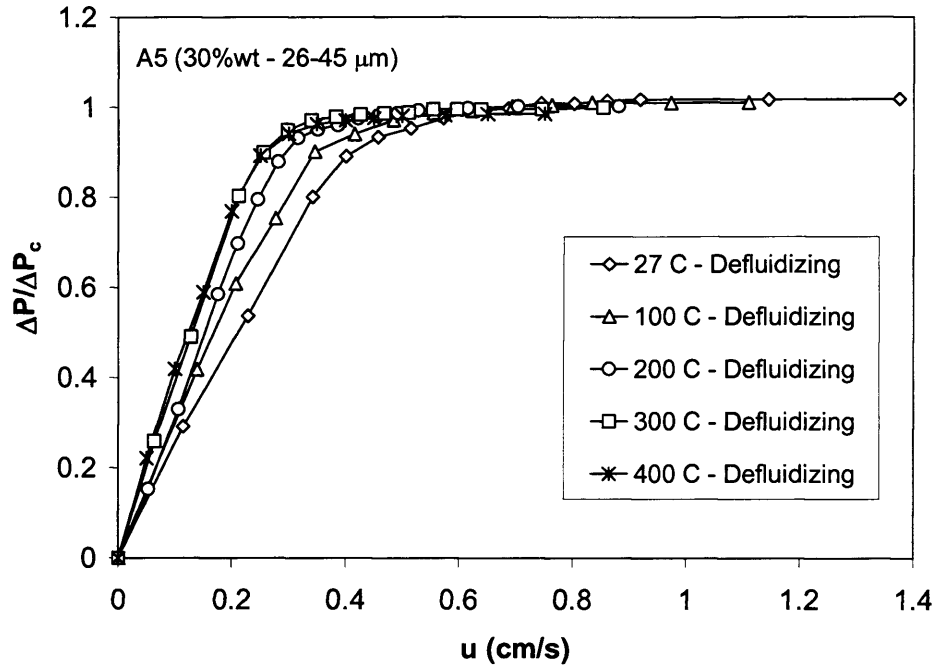

Figure 34 *Pressure Drop profiles. Defluidizing curves. Sample A5 (F_{45}=30%wt)*

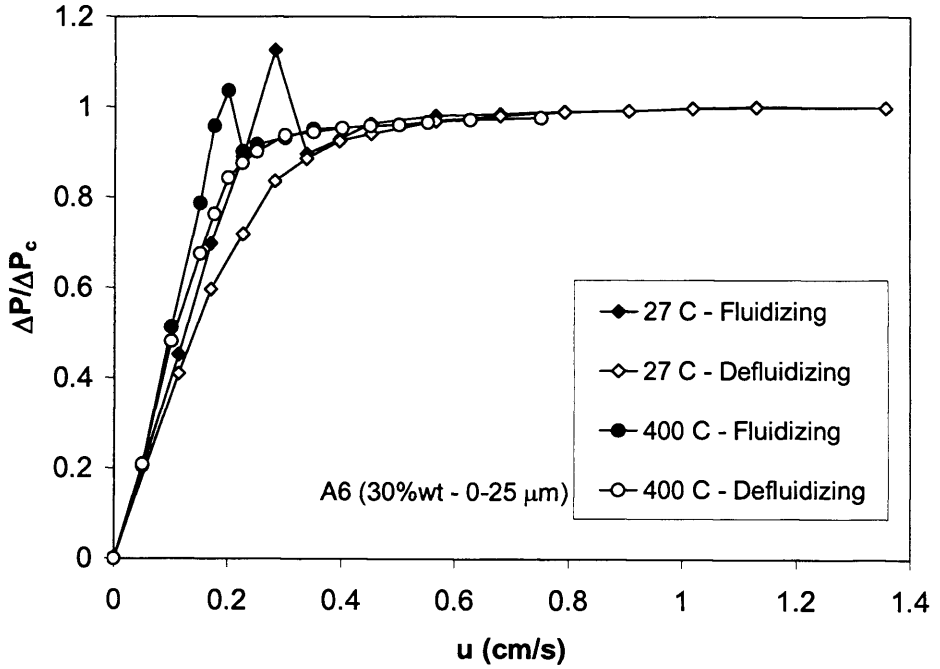

Figure 35 *Pressure Drop profiles at ambient temperature and 400°C. Sample A6 (F_{45}=30%wt)*

The minimum fluidization velocity was determined from the defluidizing pressure drop profiles at each temperature and for each powder as described in section 3.2.1. Results are reported in Appendix 1, Table A1.1.

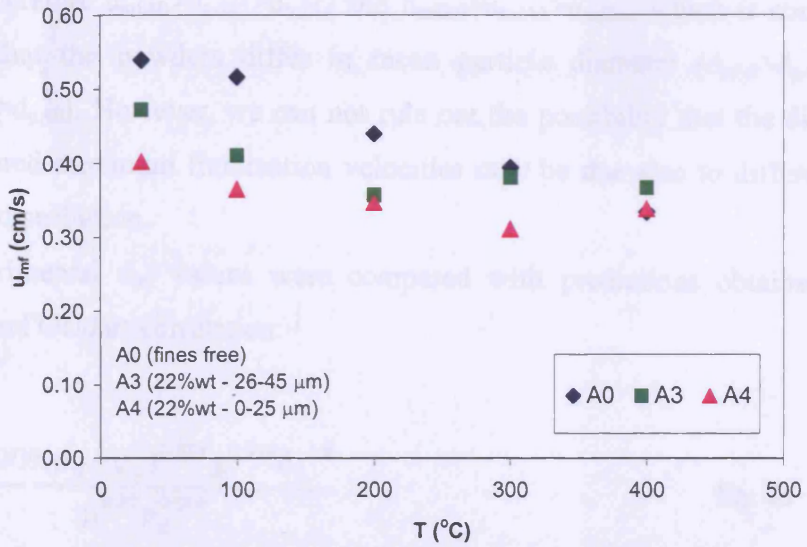

Figure 36 *Minimum fluidization velocity with increasing temperature for powders A0, A3 and A4*

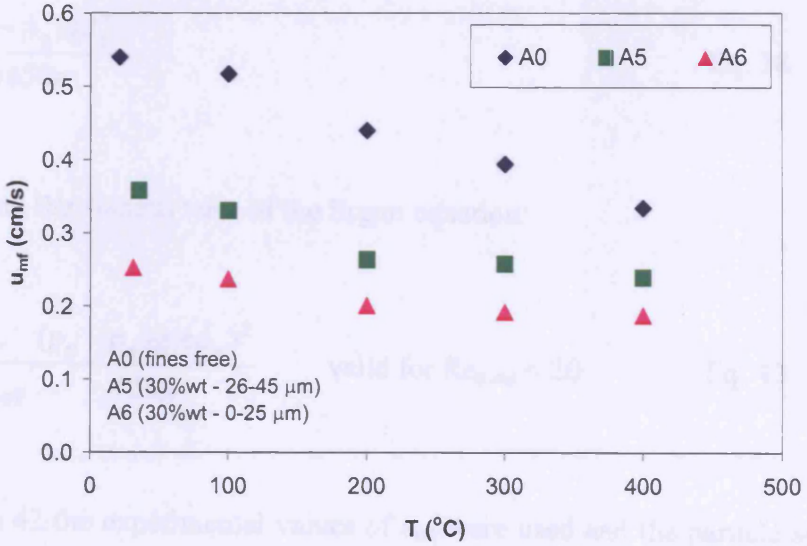

Figure 37 *Minimum fluidization velocity with increasing temperature for powders A0, A5 and A6*

Figure 36 and Figure 37 show that all powders exhibited a decreasing trend with temperature for the minimum fluidization velocity, in agreement with Yates (1996), that levels off at temperatures above 200°C. Figure 36 and Figure 37 show also that at each temperature $u_{mfA0}>u_{mfA3}>u_{mfA4}$ and $u_{mfA0}>u_{mfA5}>u_{mfA6}$, which is consistent with the fact that the powders differ in mean particle diameter ($d_{pA0}>d_{pA3}>d_{pA4}$ and $d_{pA0}>d_{pA5}>d_{pA6}$). However, we can not rule out the possibility that the differences in the measured minimum fluidization velocities may be due also to differences in the fines size distribution.

The experimental u_{mf} values were compared with predictions obtained from the Baeyens and Geldart correlation:

$$u_{mf} = \frac{0.0009(\rho_p - \rho_g)^{0.934} g^{0.934} d_p^{1.8}}{\mu^{0.87} \rho_g^{0.066}} \qquad \text{Eq. 41}$$

and with the gas viscosity dominated term of the Wen and Yu correlation, which was presented as Equation 18 in section 2.4.1.1:

$$u_{mf} = \frac{(\rho_p - \rho_g) g d_p^2}{1650\mu} \qquad \text{Eq. 18}$$

and also with the viscous term of the Ergun equation:

$$u_{mf} = \frac{\varepsilon_{mf}^3}{1-\varepsilon_{mf}} \frac{(\rho_p - \rho_g) g (\phi d_p)^2}{150\mu} \qquad \text{valid for } Re_{p,mf} < 20 \qquad \text{Eq. 42}$$

In Equation 42 the experimental values of ε_{mf} were used and the particle sphericity ϕ of each powder was back-calculated from Equation 42 using the experimental values of u_{mf} and ε_{mf} at ambient conditions, as suggested by Knowlton (1992) and successfully applied by Lettieri (1999) to FCC powders fluidized at high temperatures. The value of ϕ so obtained was then kept constant for higher

temperatures. Table 6 shows that the values obtained for ϕ are below 1 for sample A0, virtually fines free, very close to 1 for samples A3 and A5, containing bigger fines (26-45 μm) and above 1 for samples A4 and A6, containing smaller fines (0-25 μm). Values of the sphericity greater than 1 do not bear any physical meaning. Therefore, in these cases ϕ is just acting as a "fudge" factor, to adjust the mean particle diameter in order for the Ergun equation to match the experimental data.

Table 6 *Sphericity factor back-calculated from the Ergun equation*

	A0	**A3**	**A4**	**A5**	**A6**
ϕ	0.78	0.97	1.25	1.08	1.46

Khoe et al. (1991) reported on the effects of the PSD on the minimum fluidization velocity. They found that the minimum fludization velocity of a bimodal glass powder (dp = 73 μm) was considerably smaller (0.35 cm/s) than the minimum fluidization velocity of two powders of the same kind having the same mean diameter but characterised by a narrow and wide size distribution respectively (0.50 and 0.59 cm/s). They attributed this discrepancy to the error implicit when estimating u_{mf} for a bimodal powder using the conventional method described in section 3.2.1, i.e. extrapolating the low u and high u linear portions of the ΔP vs u plot. They pointed out that the fluidization of a bimodal powder occurs over a broad velocity range because of the two distinct and widely spaced sizes. Therefore, for a bimodal powder predictions for the minimum fluidization velocity based on a mean diameter can be incorrect.

Measured and predicted values for the three alumina powders A0, A3 and A4 are plotted in Figure 38 - Figure 40 and for the two alumina samples A5 and A6 in Figure 43 - Figure 44. A decrease of u_{mf} with increasing temperature is predicted by all the equations, because of the controlling effect of viscosity. Predicted values from the Baeyens and Geldart correlation and from the Wen and Yu equation are however lower than those obtained experimentally. The Ergun equation, which takes into account the voidage changes with temperature and the appropriate "sphericity" factor, described well the trends obtained experimentally, as shown in Figure 38 - Figure 40 and Figure 43 - Figure 44. This is in agreement with results reported by Botterill et al.

(1982) and later by Formisani et al. (1998), who also pointed out that changes of u_{mf} with temperature can be predicted by the Ergun equation when accounting for changes in ε_{mf} (see section 2.4.1.1).

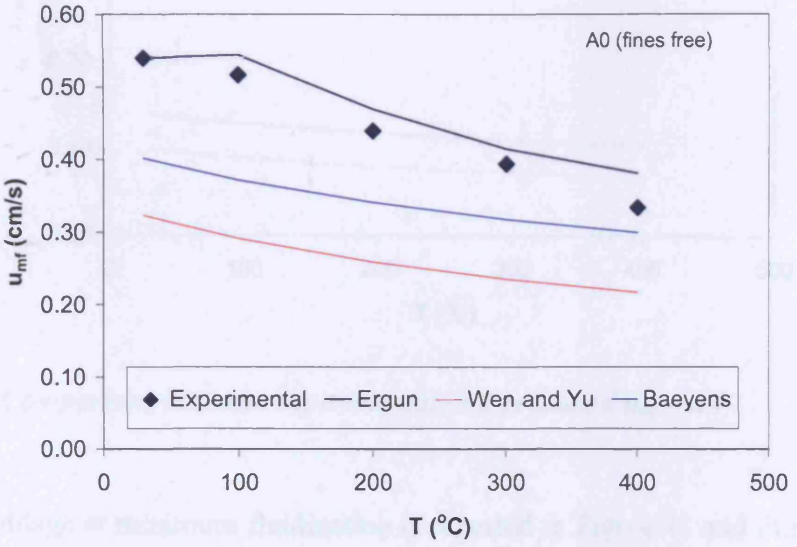

Figure 38 *Comparison between experimental and predicted u_{mf} – A0*

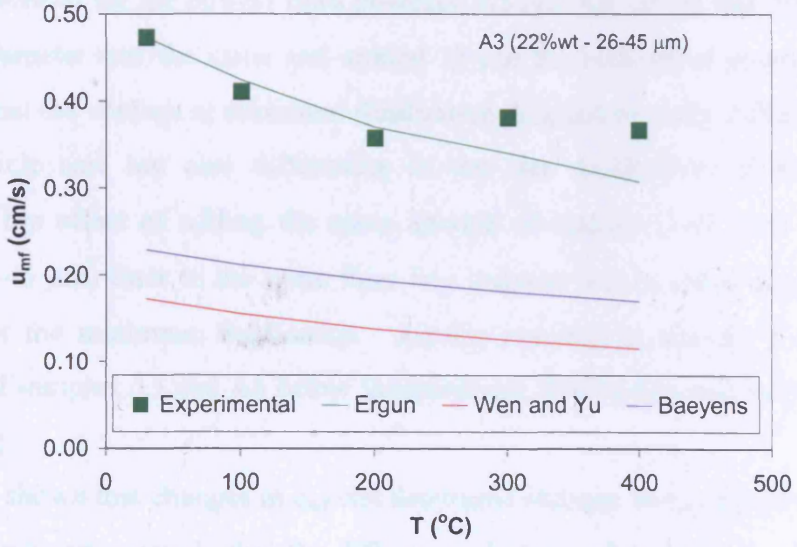

Figure 39 *Comparison between experimental and predicted u_{mf} – A3*

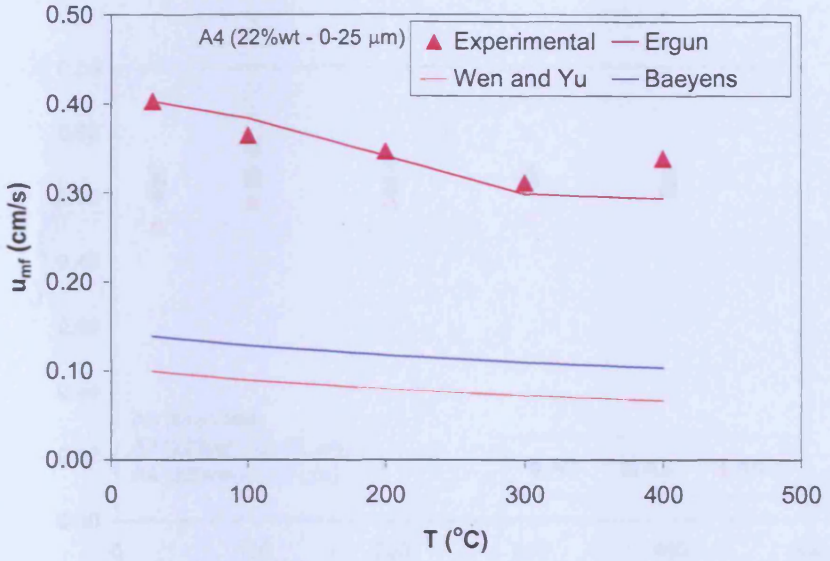

Figure 40 *Comparison between experimental and predicted u_{mf} – A4*

The bed voidage at minimum fluidization is reported in Figure 41 and Figure 42. It is clear that the effect of increasing fines content was to decrease the bed voidage. Moreover, although being very similar, the voidage of sample A3 was at each temperature slightly bigger than the voidage of sample A4. This difference was much more pronounced for the 30%wt fines powders, A5 and A6. Given that the difference in mean diameter was the same and around 13 μm for both set of powders, we can conclude that the voidage at minimum fluidization detected not only differences in the mean particle size but also differences in the size distribution of the fines. In particular, the effect of adding the same amount of smaller (1-25 μm) rather than bigger (25-45 μm) fines to the same fines free material was to create a more packed structure at the minimum fluidization. Results reported in chapter 5 on the bed rheology of samples A5 and A6 below the minimum fluidization will help explaining this finding.

It has been shown that changes in ε_{mf} can determine changes in u_{mf} (Formisani, 1998). Therefore, we can conclude that the differences between the experimental values of the minimum fluidization velocity of powders A3 and A4 or of powders A5 and A6, shown in Figure 36 and Figure 37 respectively, are partially due also to differences in the fines size distribution and not only to differences in the mean particle diameter.

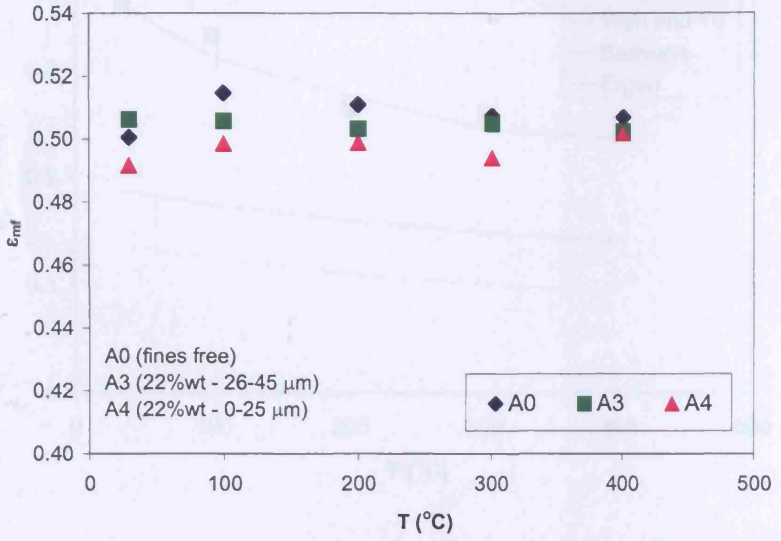

Figure 41 *Bed voidage at minimum fluidization with increasing temperature for powders A0, A3 and A4*

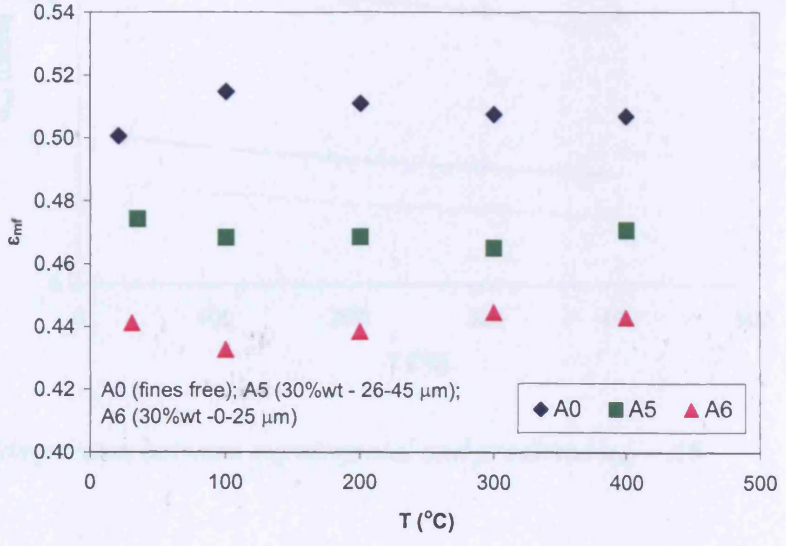

Figure 42 *Bed voidage at minimum fluidization with increasing temperature for powders A0, A5 and A6*

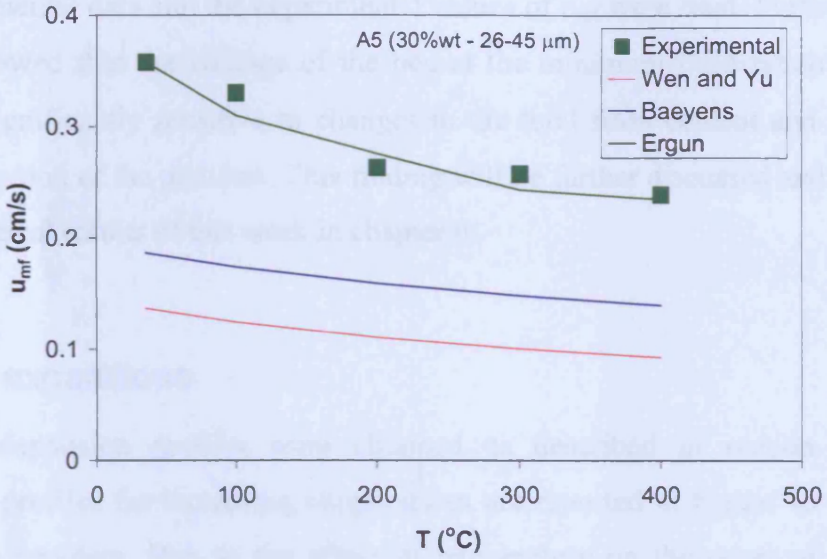

Figure 43 *Comparison between experimental and predicted u_{mf} – A5*

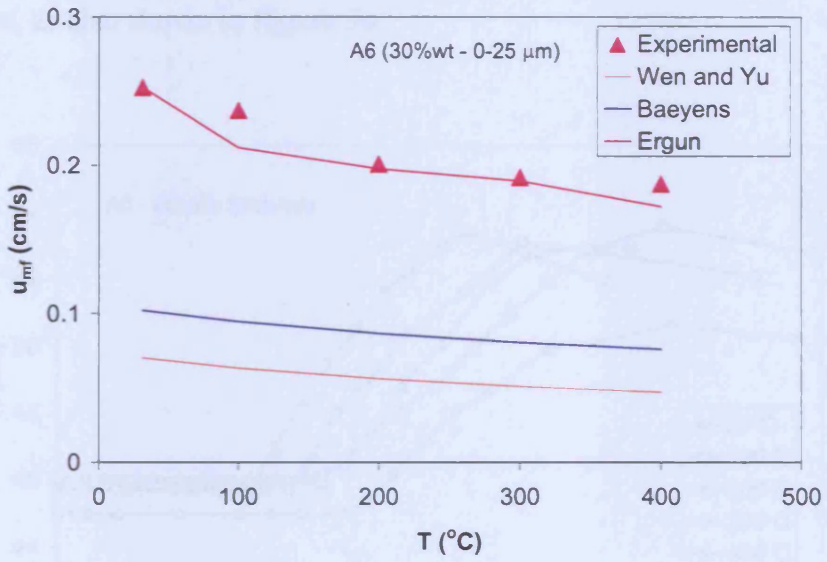

Figure 44 *Comparison between experimental and predicted u_{mf} – A6*

To summarise, the analysis of the minimum fluidization results showed that the surface to volume mean diameter is not suitable to predict the minimum fluidization velocity using standard correlations when the powders are characterised by a bimodal PSD. The Ergun equation, on the other hand, was capable of predicting trends for u_{mf} with increasing temperature when the appropriate ϕ factor was back calculated from

the experimental data and the experimental values of ε_{mf} were used. Furthermore, this section showed that the voidage of the bed at the minimum fluidization conditions, ε_{mf}, was significantly sensitive to changes in the total fines content and in the fines size distribution of the powders. This finding will be further discussed and linked with the rheological results of this work in chapter 6.

4.2 Bed expansions

The bed expansion profiles were obtained as described in section 3.2.2. Bed expansion profiles for increasing temperatures are reported in Figure 45 - Figure 49 for all the powders. Due to the effect of temperature on the onset of fluidization highlighted in Figure 36 and Figure 37 the homogeneous expansions start at lower velocities when temperature is increased. The magnitude of the homogeneous expansions, on the other hand, was not significantly affected by the increasing temperature, as also shown in Figure 50.

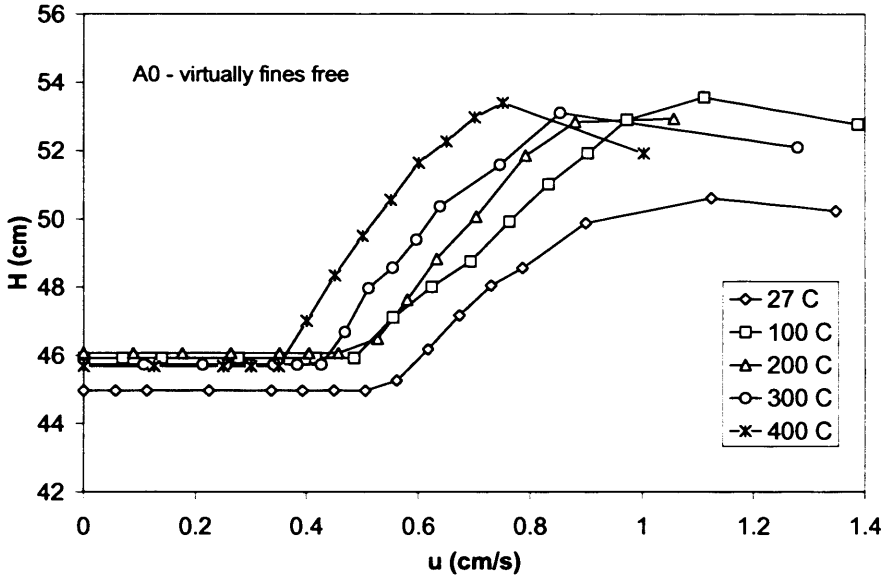

Figure 45 *Effect of temperature on the expansion profiles - A0*

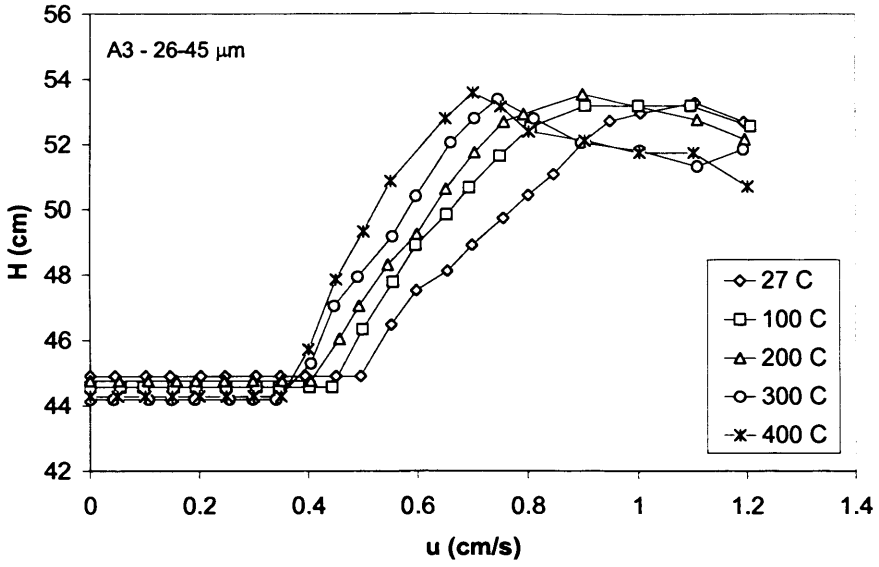

Figure 46 *Effect of temperature on the expansion profiles – A3*

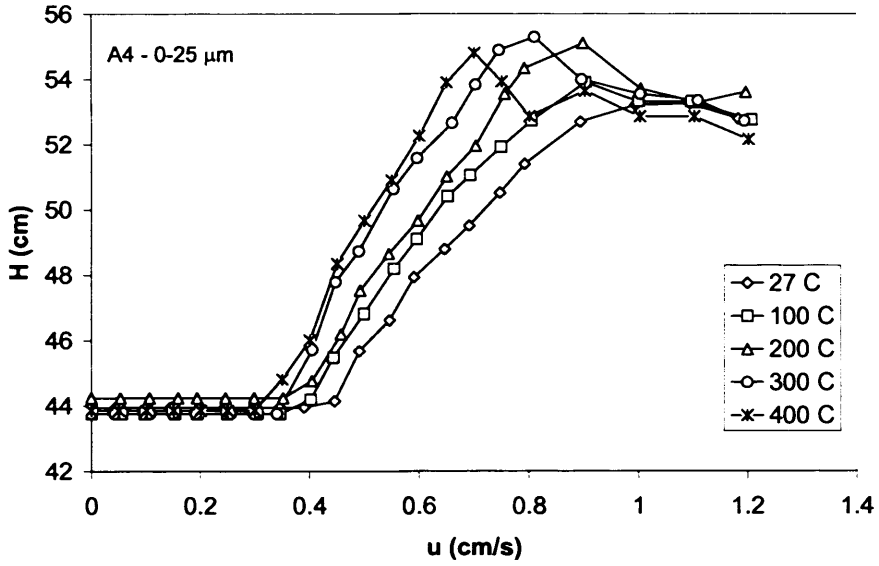

Figure 47 *Effect of temperature on the expansion profiles – A4*

A peculiarity can be noticed in the expansion profiles of powders A5 and A6 (Figure 48 and Figure 49), the samples containing 30%wt of fines. The profiles seem to break into two different lines, having different slopes. This is more evident for powder A6 (Figure 49), but is also noticeable in Figure 48 for powder A5. Interestingly, the X-

rays images showed the appearance of little bursts of gas at the bed surface at gas velocities similar to those corresponding to the change of slope in the bed expansions.

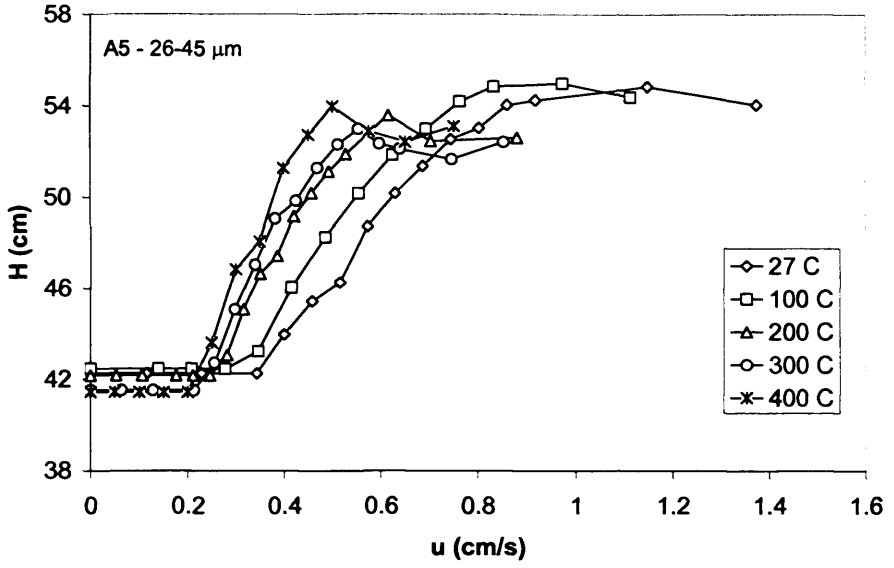

Figure 48 *Effect of temperature on the expansion profiles – A5*

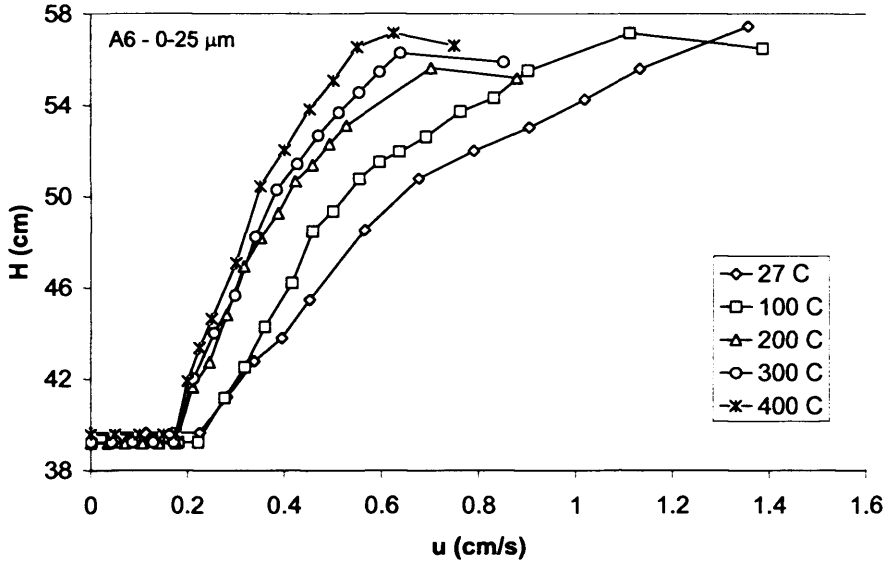

Figure 49 *Effect of temperature on the expansion profiles – A6*

When powders A5 and A6 were fluidized in the msFBR, volcano-like shapes were also visually observed at the bed surface. It is possible therefore that microchannels formed in the bed at gas velocities below the minimum bubbling. Khoe at al. (1991)

and before Donsi' and Massimilla (1973) reported similar observations for the homogeneous expansion of powders. This characteristic of the expansions of samples A5 and A6 is further discussed in section 4.2.2.

A comparison between the expansions of the various powders is shown in Figure 50, which reports the maximum bed expansion attained by each powder as a function of temperature, $(H_{max}-H_s)/H_s$ x 100. H_{max} corresponds to the value of the bed height where the profiles level off. Maximum expansions were normalised over the height of the settled bed, therefore allowing the evaluation of the bed expansion with respect to the same base line. No significant effect of temperature was observed. The lowest expansion was recorded for sample A0 (~15%), the highest for sample A6 (~43%). The values of all the maximum bed expansions with increasing temperature are reported in Appendix 1, Table A1.1. The samples containing 22%wt fines, A3 and A4, expanded more than A0 and the samples containing 30%wt fines, A5 and A6, expanded more than A3 and A4. This trend is in line with the well known beneficial

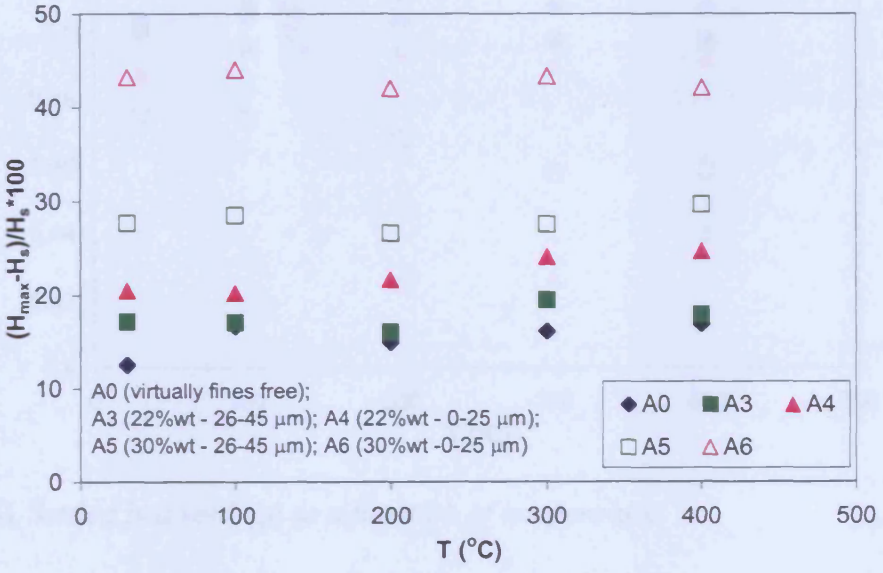

Figure 50 *Maximum bed expansions with increasing temperature for all powders*

effect of increasing fines content on fluidization. Most notably, the alumina samples containing smaller fines, A4 and A6, expanded more than the corresponding samples A3 and A5, containing the same amount of bigger fines. Therefore, we can conclude

that the fines size distribution affects significantly the maximum expansion attained by the bed of particles.

4.2.1 Settled bed voidage ε_s

Figure 51 reports the voidage of the settled bed as a function of temperature for all the powders analysed in this study. Botterill et al. (1982) reported that the voidage of the loosely settled bed, ε_s, of group B particles increases with increasing temperature. Later, Formisani et al. (1998) reported a similar finding for group A powders. However, for our powders the voidage of the settled bed was not affected by temperature in a significant way for sample A0 and for the samples containing 22%wt fines A3 and A4. A slight decrease with temperature was observed for the samples containing 30%wt fines, A5 and A6.

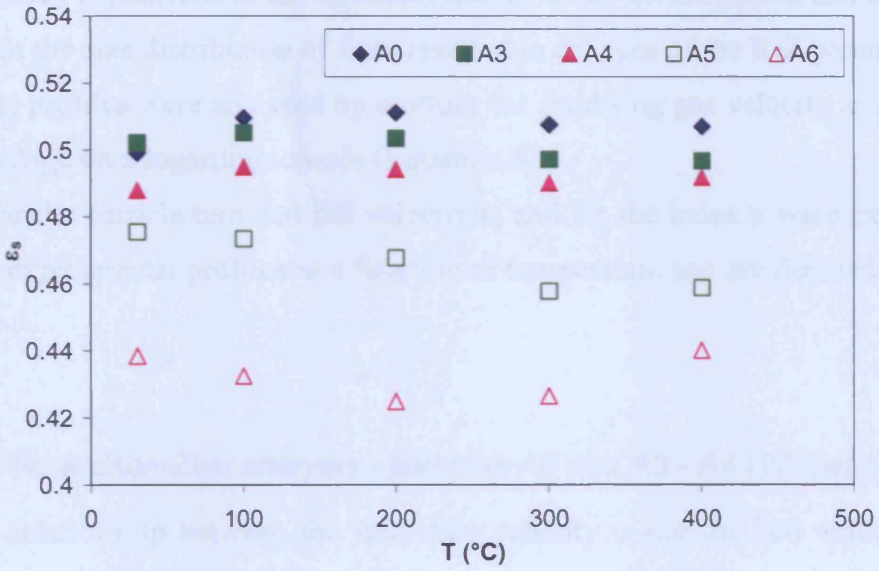

Figure 51 *Settled bed voidage as a function of temperature*

Powders A3 and A4 arranged in the settled bed in very similar packings and only slightly more compacted than the fines free powder A0, (see Figure 51). When the fines content was increased to 30%wt to make powders A5 and A6, however, much more evident differences could be seen in the bed packings. The sample containing smaller fines, A6, at each temperature arranged in a more compacted structure than

the sample containing the same amount of bigger fines, A5. This finding is quite surprising considering that powders A3 and A4 contain 19%wt more fines than powder A0 and yet arranged in very similar packings. However, increasing the total fines content to 30%wt (sample A5 and A6), only 8%wt more than the fines content in samples A3 and A4, caused a much bigger difference in the bed voidage. Moreover, the difference between the two powders containing the same amount of smaller and bigger fines (A3-A4 and A5-A6) was greatly emphasised when the fines content was increased 30%wt. These observations will be further discussed in section 4.2.2.2 and will be linked to the rheological measurements below u_{mf} reported in chapter 6.

4.2.2 Expansion profiles in the Richardson and Zaki form

In order to verify the applicability of the Richardson and Zaki correlation to the homogeneous expansions of the alumina samples under investigation, and to assess if changes in the size distribution of fines resulted in changes of the R-Z parameters, the expansion profiles were analysed by plotting the fluidising gas velocity as a function of the voidage on a logarithmic scale (Equation 5).

Values for the particle terminal fall velocity u_t and for the index n were extrapolated from the experimental profiles as a function of temperature and are denoted as n* and u_t*.

4.2.2.1 Richardson-Zaki analysis - samples A0 and A3 - A4 (22%wt fines)

A linear relationship between the fluidizing velocity u and the bed voidage ε was observed at each temperature for samples A0, A3 and A4 (Figure 52 - Figure 54). This shows that the Richardson-Zaki equation is suitable to describe the expansion of these powders even if they are not perfectly spherical and are characterised by a wide (and bimodal) particle size distribution.

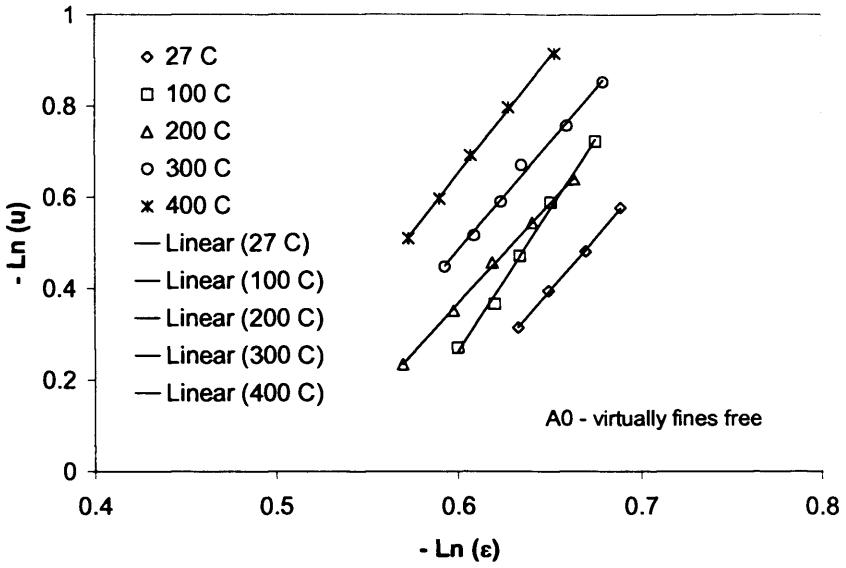

Figure 52 *Bed expansions in the Richardson-Zaki form A0*

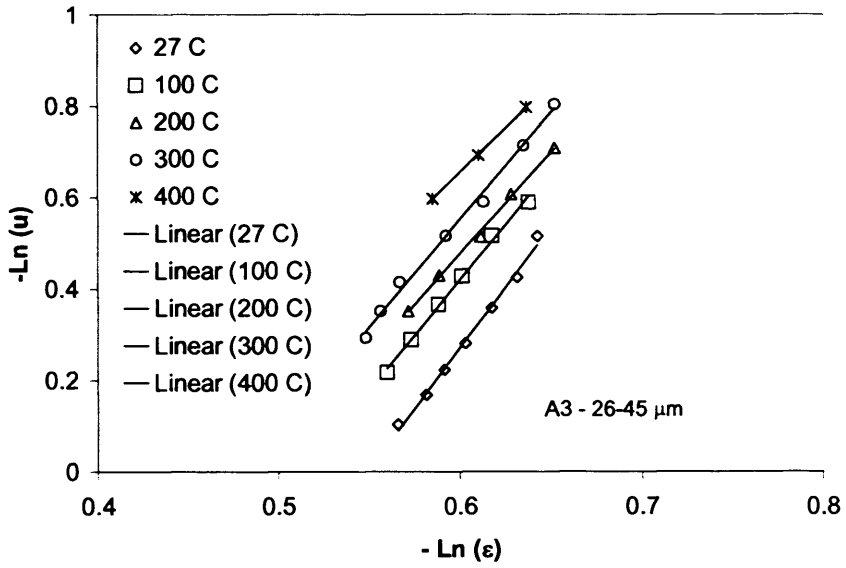

Figure 53 *Bed expansions in the Richardson-Zaki form A3*

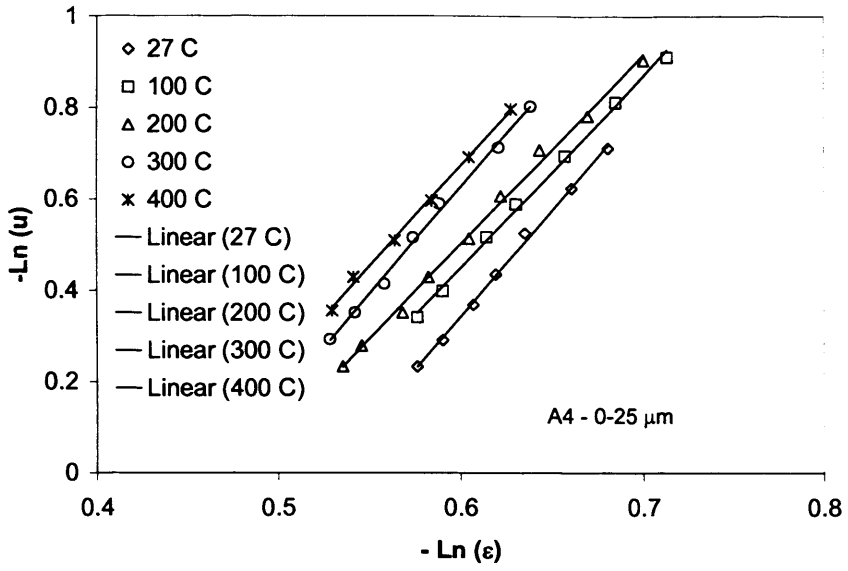

Figure 54 *Bed expansions in the Richardson-Zaki form A4*

Figure 55 and Figure 56 show trends for the slope n* and the intercept u_t* with increasing T for powders A0, A3 and A4, determined from the expansion profiles. Both n* and u_t* were found to decrease with increasing temperature for powders A0, A3 and A4, in agreement with Lettieri et al. (2002). The Richardson-Zaki parameters did not discriminate between powder A3 and A4, i.e. between powders having the same fines content but differing in fines size distribution. However, at each temperature both n* and u_t* were greater for powder A0, virtually fines free, than for powders A3 and A4, containing around 22%wt fines. This showed that values of n and u_t are significantly influenced by the total fines content and less by the fines size distribution. A significant effect of fines content on u_t* was also reported by Avidan and Yerushalmi (1982), who represented the dense phase of the turbulent regime in a Richardson-Zaki form and found that increasing fines content considerably reduced u_t* values. Similar results were also reported by Lettieri et al (2002), who found lower values of u_t* for those catalysts characterised by a higher content of fines.

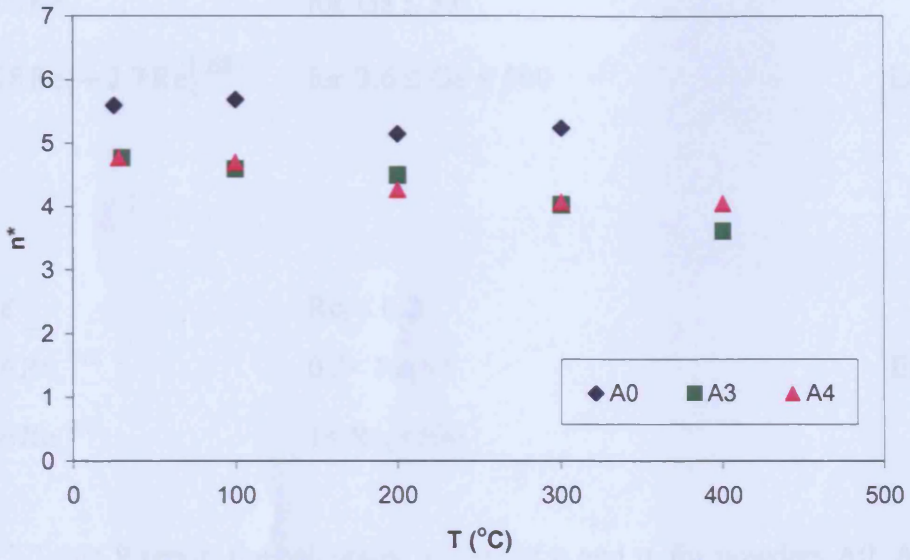

Figure 55 *Effect of temperature on experimental n* for A0, A3 and A4*

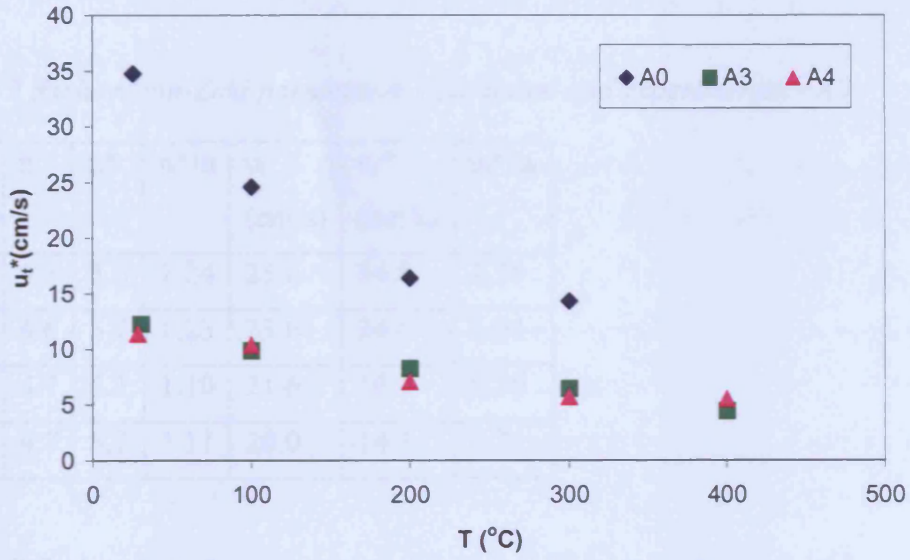

Figure 56 *Effect of temperature on u_t* values for A0, A3 and A4*

In keeping with Lettieri et al. (2002), predictions for the parameters of the Richardson-Zaki equation were obtained using the drag equation for the settling of an individual particle, using Stokes Law to determine u_t and the Richardson-Zaki $n=n(Re_t)$ correlations employed for liquids to determine n:

$$Ga = 18Re_t \qquad \text{for } Ga \leq 3.6$$

$$Ga = 18Re_t + 2.7Re_t^{1.687} \qquad \text{for } 3.6 \leq Ga \leq 500 \qquad \text{Eq. 8}$$

and

$$n = 4.8 \qquad Re_t < 0.2$$

$$n = 4.6Re_t^{-0.03} \qquad 0.2 < Re_t < 1 \qquad \text{Eq. 9}$$

$$n = 4.6Re_t^{-0.1} \qquad 1 < Re_t < 500$$

Table 7-Table 9 report the calculated values of n and u_t for powders A0, A3 and A4 with increasing temperature. Experimental values of n* and u_t* are also reported for comparison and ratios between the experimental values and the calculated ones are also shown.

Table 7 *Richardson-Zaki parameters, calculated and experimental - A0*

T (°C)	n	n*	n*/n	u_t (cm/s)	u_t* (cm/s)	u_t*/u_t
21	4.5	5.6	1.24	25.6	34.8	1.36
100	4.6	5.7	1.23	23.6	24.6	1.04
200	4.7	5.1	1.10	21.6	16.4	0.76
300	4.7	5.2	1.11	20.0	14.3	0.71

Table 8 *Richardson-Zaki parameters, calculated and experimental - A3*

T (°C)	n	n*	n*/n	u_t (cm/s)	u_t* (cm/s)	u_t*/u_t
30	4.7	4.8	1.02	14.5	12.3	0.85
100	4.8	4.6	0.97	13.3	9.8	0.74
200	4.8	4.5	0.93	12.0	8.2	0.68
300	4.8	4.0	0.84	11.5	6.4	0.56
400	4.8	3.6	0.75	10.6	4.4	0.42

Table 9 *Richardson-Zaki parameters, calculated and experimental - A4*

T (°C)	n	n*	n*/n	u_t (cm/s)	u_t* (cm/s)	u_t*/u_t
30	4.8	4.8	0.99	8.7	11.4	1.31
100	4.8	4.7	0.98	8.2	10.4	1.26
200	4.8	4.3	0.89	7.3	7.1	0.97
300	4.8	4.1	0.85	6.6	5.7	0.86
400	4.8	4.1	0.85	6.1	5.5	0.90

For powders A3 and A4 due to the small mean particle size, and thus low Re_t, the calculated values of the index n are the same, 4.8, at each temperature. The values of u_t predicted from the drag equation of the settling of an individual particle show a decreasing trend with temperature, which is in agreement with the trends of u_t* extrapolated using the Richardson and Zaki correlation.

However, the u_t* values were generally smaller than the u_t values. This discrepancy may be partly explained with the large extrapolation in the data that must be employed when calculating u_t*, as observed by Di Felice (1999) and Di Felice and Kehlenbeck (2000) for the fluidization and sedimentation of concentrated systems (see section 2.3). On the other hand, the calculated values of u_t are dependent on the mean particle diameter used for the calculation. Lettieri et al. (2002) underlined the importance of defining appropriate mean particle diameters to describe correctly the particle systems under study, in particular with regard to the prediction of the Richardson and Zaki parameters. Within this framework, the low experimental values of u_t* could be implying that the surface to volume mean particle diameter used to calculate u_t is not the best choice for the powders analysed. This will be discussed further in the next section.

4.2.2.2 Richardson-Zaki analysis - samples A5 and A6 (30%wt fines)

When the bed expansions are plotted in the Richardson-Zaki form for powders A5 and A6 (Figure 57 and Figure 58), a different picture arises. As observed already at the

beginning of this section, the expansions for powders A5 and A6 are represented by two lines of differing slope rather than by a single line like that obtained for powders A0, A3 and A4. The Richardson and Zaki parameters were evaluated for each line. Results are reported in Figure 59-Figure 62 and in Table 10-Table 11.

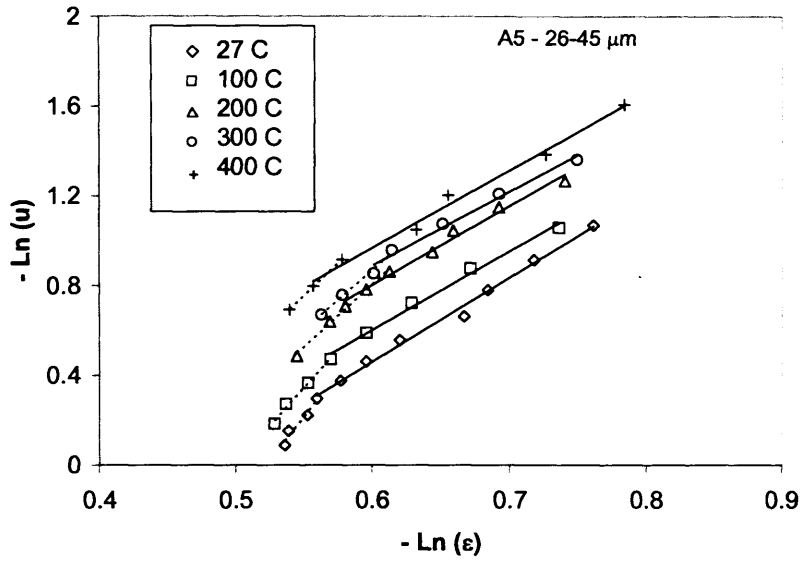

Figure 57 *Bed expansions in the Richardson-Zaki form A5*

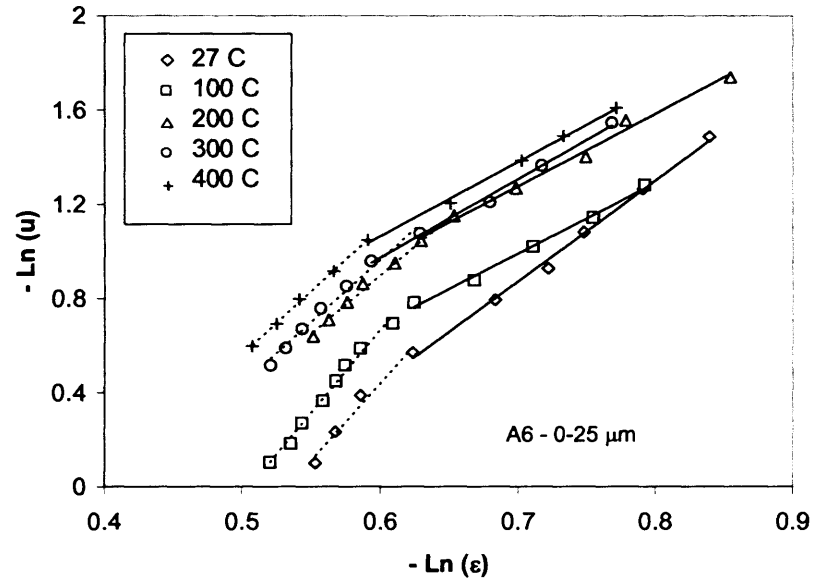

Figure 58 *Bed expansions in the Richardson-Zaki form A6*

When the Richardson and Zaki parameters were evaluated using the part of the expansion profiles corresponding to the lower values of the voidage (solid lines in Figure 57 and Figure 58), the values of u_t* and n* were very small, as reported in Figure 59 - Figure 60 and Table 10 and Table 11. In particular, values for u_t* were as low as 30% of the calculated values for the terminal fall velocity.

When the part of the expansion corresponding to higher values of the voidage were used to extrapolate the Richardson-Zaki parameters (dotted lines in Figure 57 and Figure 58), more reasonable values of u_t* and n* were obtained, as shown in Figure 61 - Figure 62 and reported in Table 10 and Table 11. However, the experimental values so obtained this time were bigger than the calculated ones.

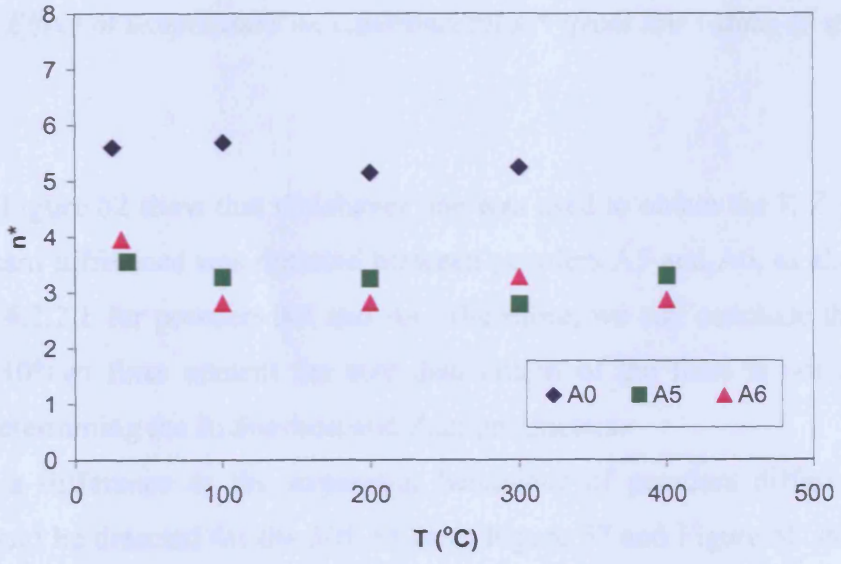

Figure 59 *Effect of temperature on experimental n* (from low values of ε) for A0, A5 and A6*

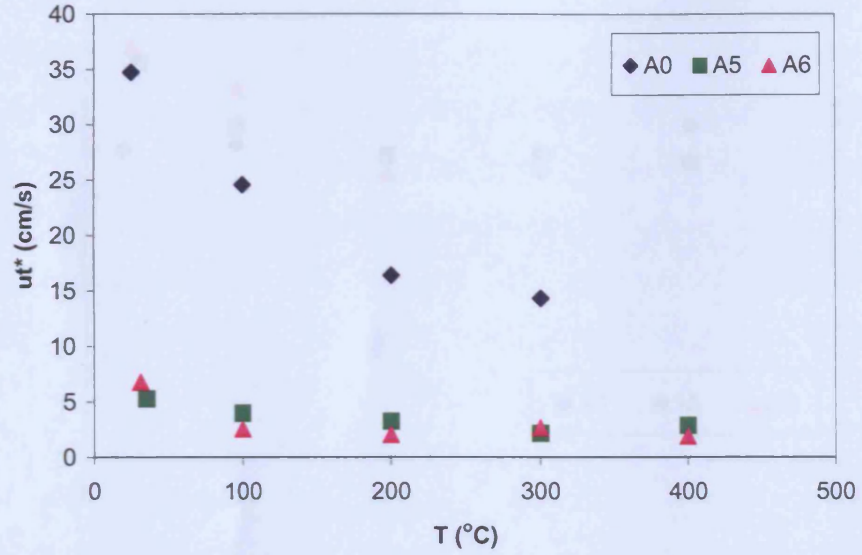

Figure 60 *Effect of temperature on experimental u_t* (from low values of ε) for A0, A5 and A6*

Figure 59-Figure 62 show that whichever line was used to obtain the R-Z parameters, no significant difference was detected between powders A5 and A6, as also observed in section 4.2.2.1 for powders A3 and A4. Therefore, we can conclude that for both 22% and 30%wt fines content the size distribution of the fines is not a dominant factor in determining the Richardson and Zaki parameters.

However, a difference in the expansion behaviour of powders differing in fines content could be detected for the 30%wt case. Figure 57 and Figure 58 show that the change detected in the slope of the homogeneous expansion was more accentuated for powder A6 than for powder A5 and that for powder A5 it was shifted towards the minimum bubbling velocity. This finding will be related to the rheological measurements below u_{mf} in chapter 5.

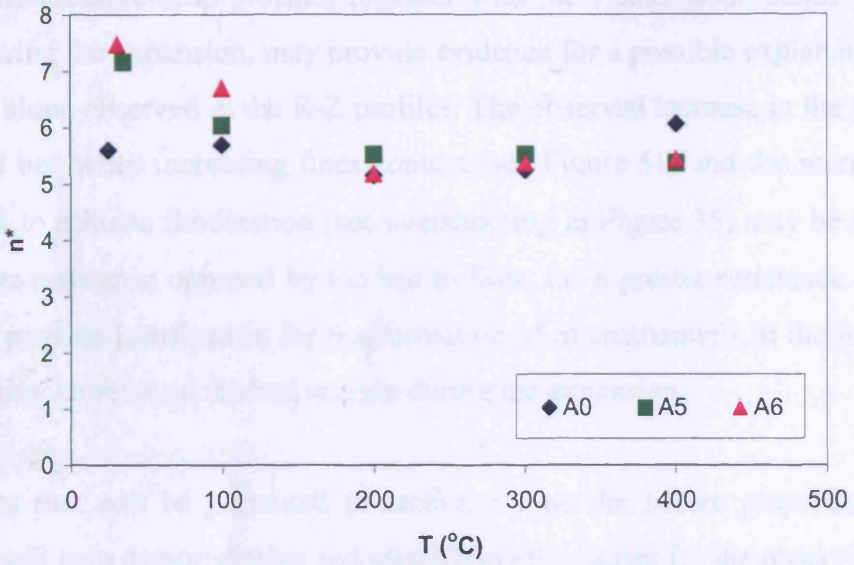

Figure 61 *Effect of temperature on experimental n* (from high values of ε) for A0, A5 and A6*

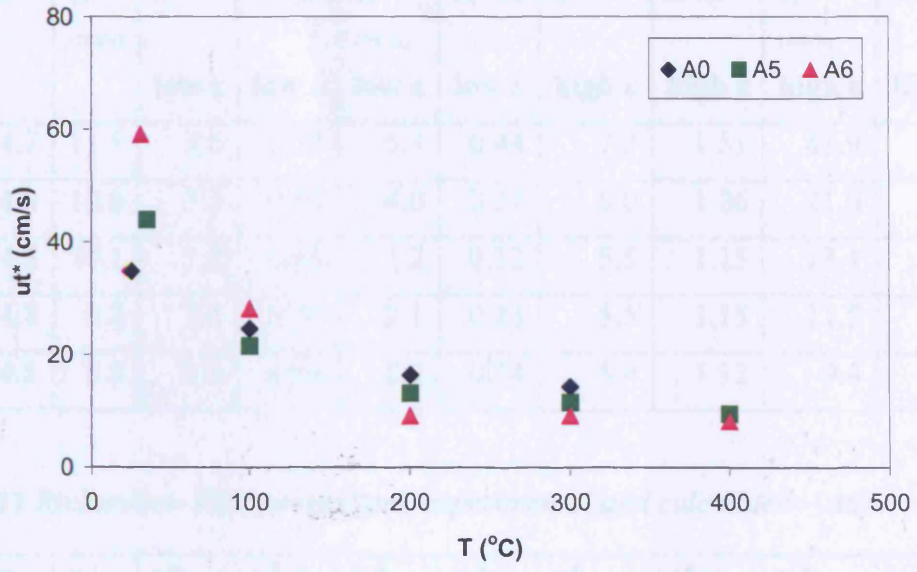

Figure 62 *Effect of temperature on experimental u_t* (from high values of ε) for A0, A5 and A6*

On the other hand, increasing the total fines content from 22%wt to 30%wt changed the expansions dramatically, with the expansion profiles for the 30%wt case happening in two different stages. In regard of this, the results obtained for the settled

bed and the pressure drop profiles, together with the visual observations of the bed surface during the expansion, may provide evidence for a possible explanation for the change in slope observed in the R-Z profiles. The observed increase in the packing of the settled bed when increasing fines content (see Figure 51) and the increase in the ΔP needed to achieve fluidization (see overshooting in Figure 35) may be interpreted as a greater resistance opposed by the bed to flow, i.e. a greater resistance to expand. This may provide justification for the formation of microchannels in the bed and the observed tiny bubbles on the bed surface during the expansion.

The results that will be presented in section 5.1 on the failure properties of these materials will help demonstrating and quantifying the causes for the observed changes in the fluidization behaviour of powders A5 and A6.

Table 10 *Richardson-Zaki parameters, experimental and calculated – A5*

T (°C)	n	u_t (cm/s)	n* **low ε**	n*/n **low ε**	u_t* (cm/s) **low ε**	u_t*/u_t **low ε**	n* **high ε**	n*/n **high ε**	u_t* (cm/s) **high ε**	u_t*/u_t **high ε**
35	4.7	11.9	3.6	0.75	5.3	0.44	7.2	1.51	43.9	3.68
100	4.8	10.8	3.3	0.68	4.0	0.37	6.0	1.26	21.5	2.00
200	4.8	10.1	3.2	0.68	3.2	0.32	5.5	1.15	13.1	1.29
300	4.8	9.2	2.8	0.58	2.1	0.23	5.5	1.15	11.5	1.25
400	4.8	8.5	3.3	0.69	2.9	0.34	5.4	1.12	9.4	1.11

Table 11 *Richardson-Zaki parameters, experimental and calculated – A6*

T (°C)	n	u_t (cm/s)	n* **low ε**	n*/n **low ε**	u_t* (cm/s) **low ε**	u_t*/u_t **low ε**	n* **high ε**	n*/n **high ε**	u_t* (cm/s) **high ε**	u_t*/u_t **high ε**
31	4.8	6.5	4.0	0.82	6.8	1.04	7.5	1.56	59.1	9.05
100	4.8	5.8	2.8	0.58	2.5	0.44	6.7	1.40	28.1	4.85
200	4.8	5.1	2.8	0.59	2.0	0.40	5.2	1.08	9.2	1.78
300	4.8	4.7	3.3	0.68	2.6	0.56	5.4	1.12	9.2	1.97
400	4.8		2.9	0.60	1.9	0.44				

Finally, the expansion behaviour exhibited by samples A5 and A6 demonstrates the importance of defining appropriate mean particle diameters to describe correctly a particle system, as observed by Lettieri et al. (2002). When using the surface to volume mean particle diameter, d_p, to calculate the values of the Richardson and Zaki equation, the values of n and u_t never matched the experimental values n* and u_t*, whatever part of the expansion was used. In particular, for low values of ε the values of n* and u_t* were underestimated and for high values of ε overestimated (see Table 10 and Table 11). Therefore, the expansions in this cases are not described well when using the Sauter mean diameter.

4.4 Bed Collapse Tests

4.4.1 Choice of initial gas velocity

The influence of the initial fluidizing velocity on the bed collapse profiles has been investigated at ambient temperature on the alumina sample A0, the virtually fines free powder.

Figure 63 shows the bed collapse profiles obtained for different initial fluidizing velocities ranging from 1 to 5 cm/s. It is clear that the bed collapse parameters were affected by the initial gas velocity: the slope of the sedimentation stage decreased with increasing gas velocity, so did the intercept with the height axis, H, at t = 0, i.e. H_d. At the same time, the overall time of the collapse, t_s in Figure 9a, decreased with increasing gas velocity and so did the height at which the bed settled. However, the biggest differences appear to be between profiles corresponding to low gas velocities and become less and less significant with increasing gas velocity. For gas velocities 4cm/s and 5cm/s the collapse profiles are almost the same. Figure 64 shows this effect by plotting the dense phase heights H_d extrapolated from the bed collapse tests (BCT) as a function of the gas velocity. The total bed heights obtained from the expansion curves, H_{tot}, are also reported in Figure 64. After a peak at around 1 cm/s both the height of the dense phase H_d and the total bed height H_{tot} decreased with increasing gas velocity until a plateau was reached in both cases. The difference between the two heights represents the volume occupied by the gas in the form of bubbles. A fluidising

velocity of 4 cm/s can be identified from Figure 63 to be the minimum velocity to employ in order to obtain a collapse profile independent on the initial gas velocity. However, a value lower than 4 cm/s was imposed in the present work by the risk of fines elutriation when the alumina samples A3, A4, A5 and A6 were fluidized. The BCT in this work are used to compare the collapse parameters obtained for the various samples with each other. Therefore, the same initial gas velocity had to be employed for all the experiments in order to produce meaningful results. A velocity of 1.5cm/s was chosen as the initial gas velocity for all the BCTs, for all the powders, at all the temperatures investigated. As a consequence of this choice, as already highlighted in Chapter 3, the results produced by the BCT are valid only for the initial gas velocity chosen, 1.5 cm/s. However, the BCT can be used to make comparisons between the aeratability of the different powders under analysis and to assess the influence of process conditions, i.e. temperature and fines size distribution, on the powders' flowability.

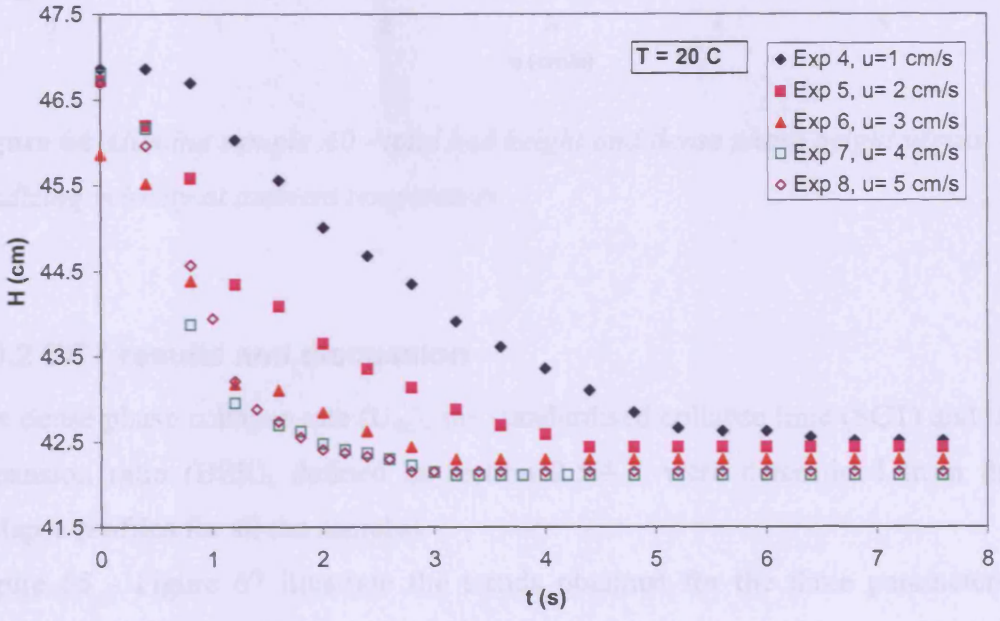

Figure 63 *Alumina A0, BCT at ambient temperature at different initial gas velocities*

The value of the velocity chosen, 1.5 cm/s, was the highest velocity which would keep the visually observed elutriated fines to a minimum when sample A6 was fluidized. This is the sample containing the greatest amount of small fines (30%wt, 0-

25 μm), hence it was believed to be the sample most likely to have significant elutriation. The small amount of fines collected in the top section of the bed at the end of each collapse (less than 1% of the fines initially present in the powder) confirmed the appropriateness of this choice.

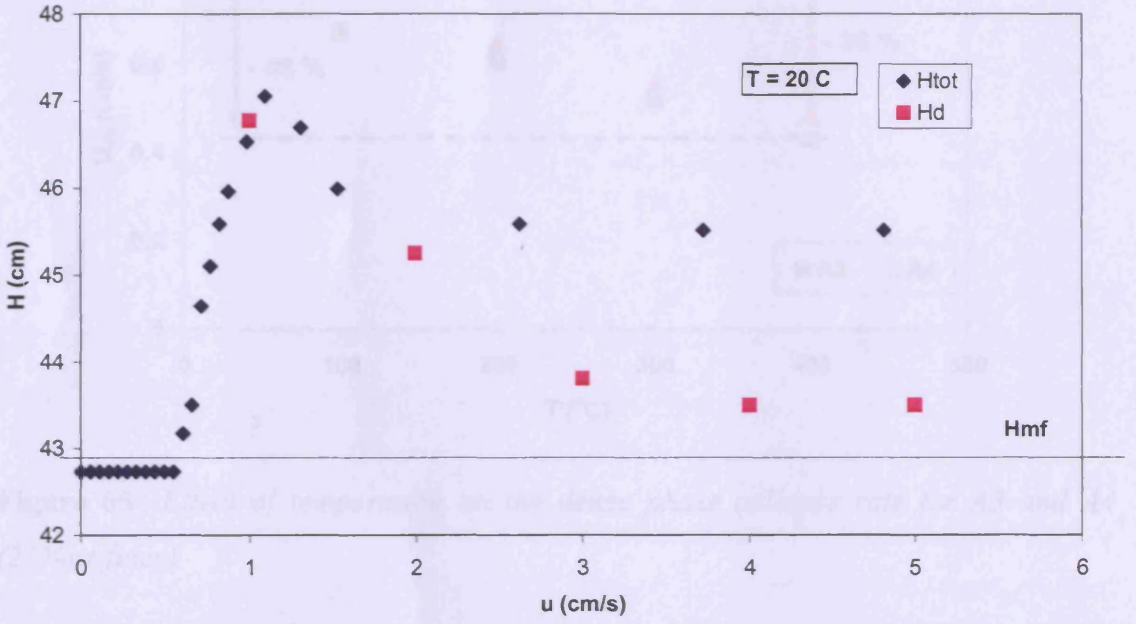

Figure 64 *Alumina sample A0 - total bed height and dense phase height versus fluidizing velocity at ambient temperature*

4.4.2 BCT results and discussion

The dense phase collapse rate (U_{de}), the standardised collapse time (SCT) and the bed expansion ratio (BER), defined in section 2.5.4.1, were determined from the bed collapse profiles for all the samples.

Figure 65 - Figure 67 illustrate the trends obtained for the three parameters with increasing temperature for samples A3 and A4.

U_{de} measures how quickly the bed loses its interstitial aeration gas. Figure 65 shows that for both powders A3 and A4 the dense phase collapse rate decreased significantly with increasing temperature by about 48% for sample A3 and 38% for sample A4. This is in agreement with the Abrahamsen and Geldart (1980) correlation (see Equation 29), which predicts that the dense phase should collapse at a slower rate with

increasing temperature. However, no significant difference was observed between the dense phase collapse rate of the two powders having different fines size distribution, A3 and A4.

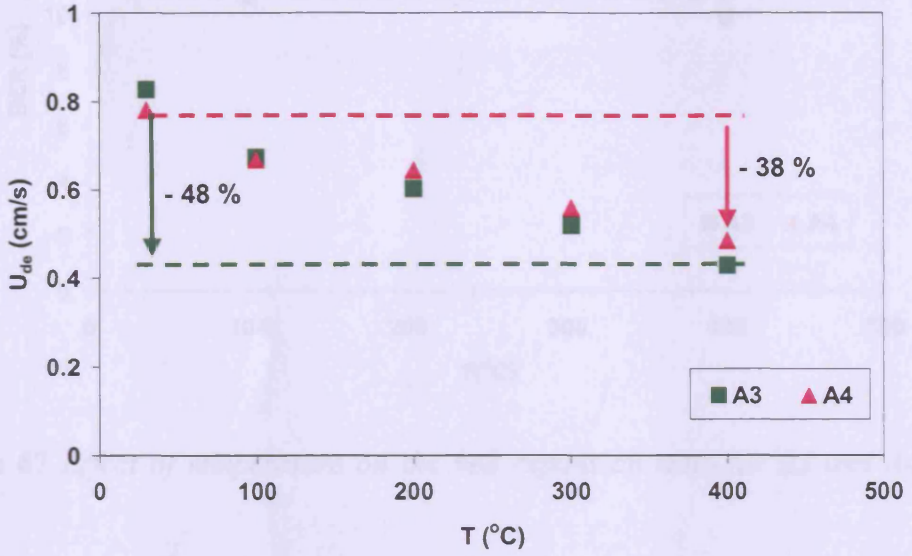

Figure 65 *Effect of temperature on the dense phase collapse rate for A3 and A4 (22%wt fines)*

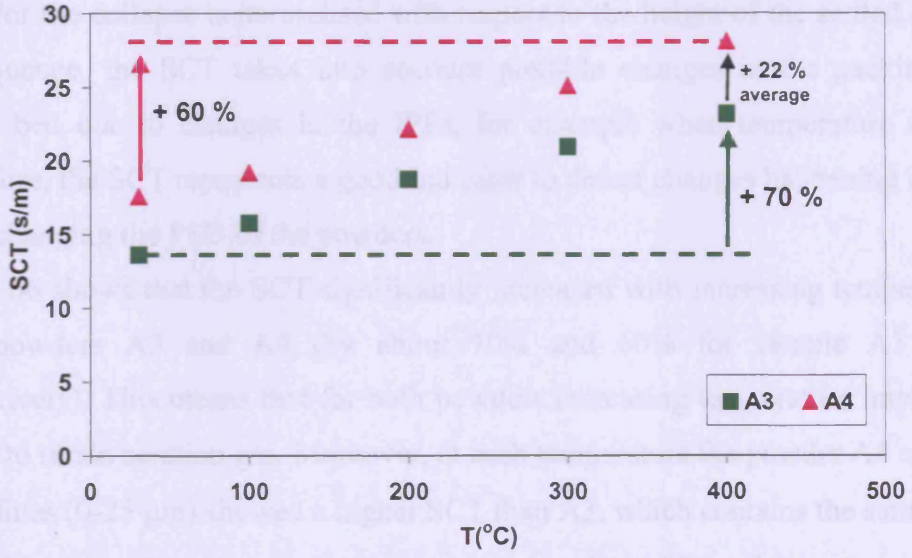

Figure 66 *Effect of temperature on the standardised collapse time for A3 and A4 (22%wt fines)*

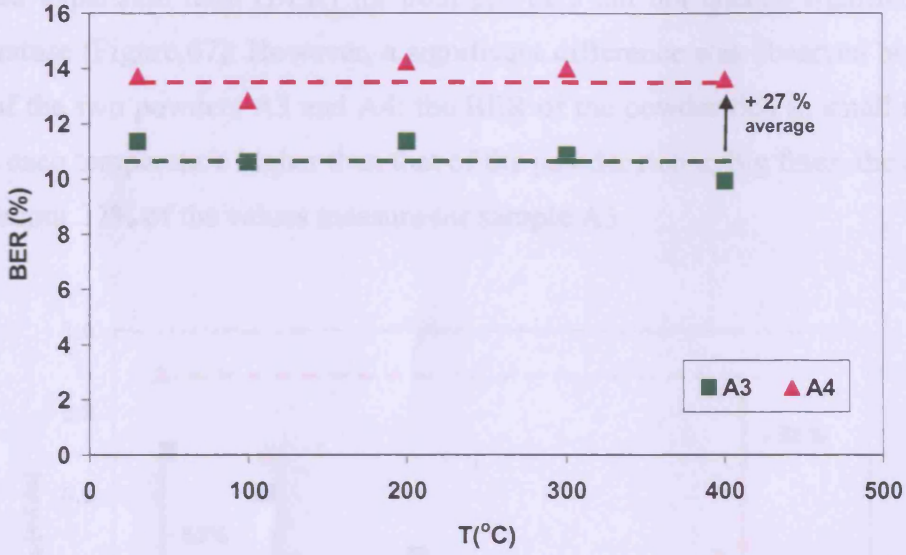

Figure 67 *Effect of temperature on the bed expansion ratio for A3 and A4 (22%wt fines)*

The standardised collapse time, first introduced by Geldart and Wong (1985), is also related to the capability of powders to retain aeration gas. The time required for the powder to deaerate depends not only on the collapse rate, but also on the height through which the bed surface has to fall. The SCT takes into account this, as the time taken for the collapse is normalised with respect to the height of the settled bed. As a consequence, the SCT takes into account possible changes in the packing of the settled bed due to changes in the IPFs, for example when temperature increases. Therefore, the SCT represents a good indicator to detect changes happening in the bed when changing the PSD of the powders.

Figure 66 shows that the SCT significantly increased with increasing temperature for both powders A3 and A4 (by about 70% and 60% for sample A3 and A4 respectively). This means that for both powders increasing temperature improved the ability to retain aeration gas. Moreover, at each temperature the powder A4 containing small fines (0-25 μm) showed a higher SCT than A3, which contains the same amount of the big fines (26-45 μm), the difference being about 22% of the values measured for sample A3. The powder containing small fines is therefore more "aeratable". Therefore, unlike U_{de}, the SCT showed to be sensitive to changes in the fines size distribution of the materials.

The bed expansion ratio (BER) for both powders did not change significantly with temperature (Figure 67). However, a significant difference was observed between the BER of the two powders A3 and A4: the BER of the powder rich in small fines (A4) was at each temperature higher than that of the powder rich in big fines, the difference being about 27% of the values measure for sample A3.

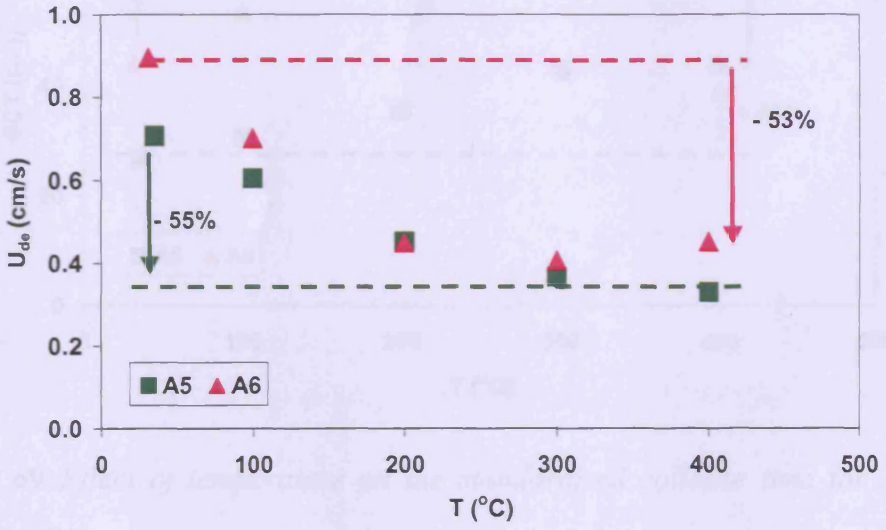

Figure 68 *Effect of temperature on the dense phase collapse rate for A5 and A6 (30%wt fines)*

The trends for the bed collapse parameters with increasing temperature observed when the fines content was increased to 30%wt, i.e. for samples A5 and A6 were different from those obtained for powders A3 and A4 (22%wt fines). The SCT of sample A5 and A6 (see Figure 69) was found to increase with increasing temperature, in line with the trends observed for the samples A3 and A4 containing a lower amount of fines. However, for sample A5 and A6 the increase with temperature of the SCT was not linear but levelled off at temperatures above about 300°C. Similarly, the BER for sample A5 and A6 was found to decrease slightly with temperature (see Figure 70) whereas it had been found to be unaffected by temperature for the samples containing 22%wt fines, A3 and A4 (Figure 67). Moreover, the decrease with temperature was greater for sample A6 than for sample A5, thus highlighting the sensitivity of this parameter to the presence of smaller fines fractions. These results will find a

qualitative correspondence with the rheological measurements reported in chapter 5 and will be further discussed in chapter 6.

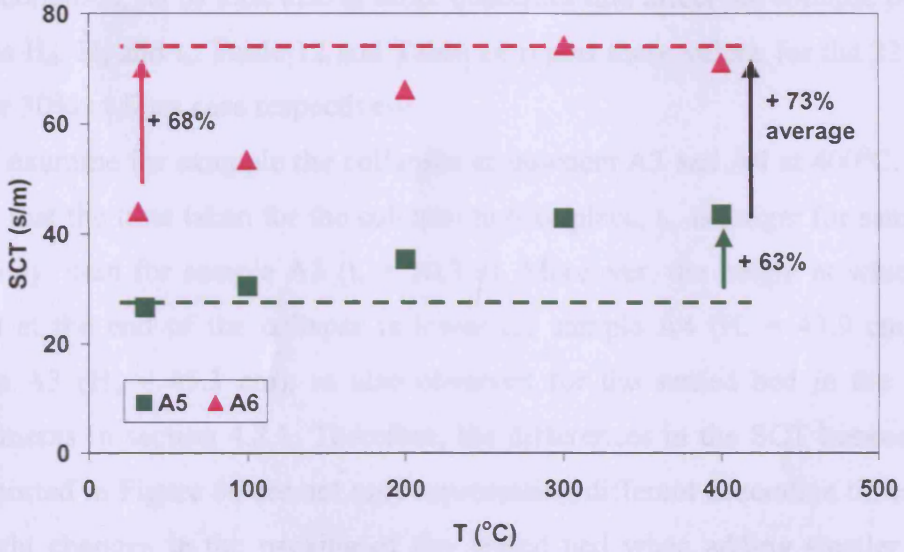

Figure 69 *Effect of temperature on the standardised collapse time for A5 and A6 (30%wt fines)*

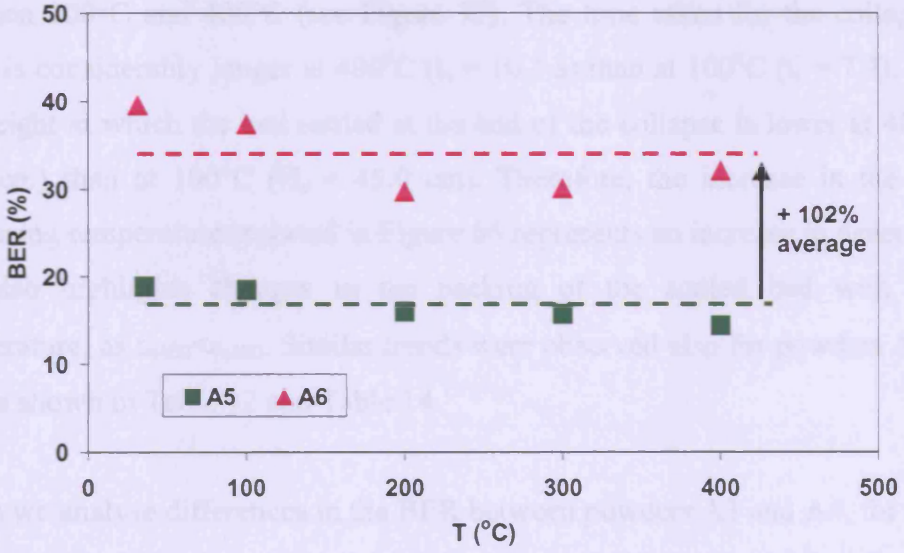

Figure 70 *Effect of temperature on the bed expansion ratio for A5 and A6 (30%wt fines)*

The bed collapse test parameters are very useful tools to assess the powders' capability of retaining aeration gas. However, in order to aid the physical interpretation of the collapse tests, and better understand the role played by the IPFs in the collapses, let us look also at other quantities that affect the collapse parameters, such as H_d, H_s and t_s. Table 12 and Table 14 report these values for the 22%wt fines and the 30%wt fines case respectively.

Let us examine for example the collapses of powders A3 and A4 at 400°C. Figure 71 shows that the time taken for the collapse to take place, t_s, is longer for sample A4 (t_s = 11.5 s) than for sample A3 (t_s = 10.3 s). Moreover, the height at which the bed settled at the end of the collapse is lower for sample A4 (H_s = 43.9 cm) than for sample A3 (H_s = 45.3 cm), as also observed for the settled bed in the expansion experiments in section 4.2.1. Therefore, the differences in the SCT between A3 and A4 reported in Figure 66 are not only representing different deaeration times, but also highlight changes in the packing of the settled bed when adding smaller or bigger fines, as $\varepsilon_{sA4}<\varepsilon_{sA3}$. Similar trends were observed at each temperature and also when comparing the collapses of powders A5 and A6, as shown in Table 12 and Table 14.

Let us now look at the effect of temperature on SCT, for example for powder A3 between 100°C and 400°C (see Figure 72). The time taken for the collapse to take place is considerably longer at 400°C (t_s = 10.3 s) than at 100°C (t_s = 7.2). Moreover, the height at which the bed settled at the end of the collapse is lower at 400°C (H_s = 43.9 cm) than at 100°C (H_s = 45.0 cm). Therefore, the increase in the SCT with increasing temperature reported in Figure 66 represents an increase in deaeration time, but also highlights changes in the packing of the settled bed with increasing temperature, as $\varepsilon_{s400}<\varepsilon_{s100}$. Similar trends were observed also for powders A4, A5 and A6, as shown in Table 12 and Table 14.

When we analyse differences in the BER between powders A3 and A4, for instance at 400°C (Figure 71), we find that the height that the bed has to travel to collapse, H_d-H_s, is higher for sample A4 than A3, as the height of the dense phase for sample A4 (H_d = 50.3 cm) was higher than that for sample A3 (H_d = 48.3 cm), whereas the height of the settled bed was smaller for sample A4 than A3, as already shown. Therefore, the differences in the BER between A3 and A4 reported in Figure 67 highlight changes in

the packing of the settled bed and also changes in the voidage of the dense phase, as $\varepsilon_{dA4}>\varepsilon_{dA3}$. Similar trends were observed at each temperature and also when comparing the collapses of powders A5 and A6, as shown in Table 12 and Table 14.

Interestingly, the sample rich in small fines, A4, arranged in a more compacted structure when settled than the powder rich in big fines ($\varepsilon_{sA4}<\varepsilon_{sA3}$). Whereas the dense phase of the powder rich in small fines arranged in a more porous structure than the dense phase of the powder rich in big fines ($\varepsilon_{dA4}>\varepsilon_{dA3}$).

Table 12 *Dense phase and settled bed voidage and collapse time as a function of temperature for powders A3 and A4 (22%wt fines)*

T (°C)	ε_d - A3	ε_d - A4	ε_s - A3	ε_s - A4	t_s (s) – A3	t_s (s) – A4
27	0.558	0.559	0.508	0.500	6.2	7.4
100	0.555	0.557	0.508	0.499	7.2	7.9
200	0.553	0.556	0.503	0.493	8.5	9.8
300	0.549	0.552	0.497	0.489	9.4	10.6
400	0.548	0.551	0.495	0.491	10.3	11.5

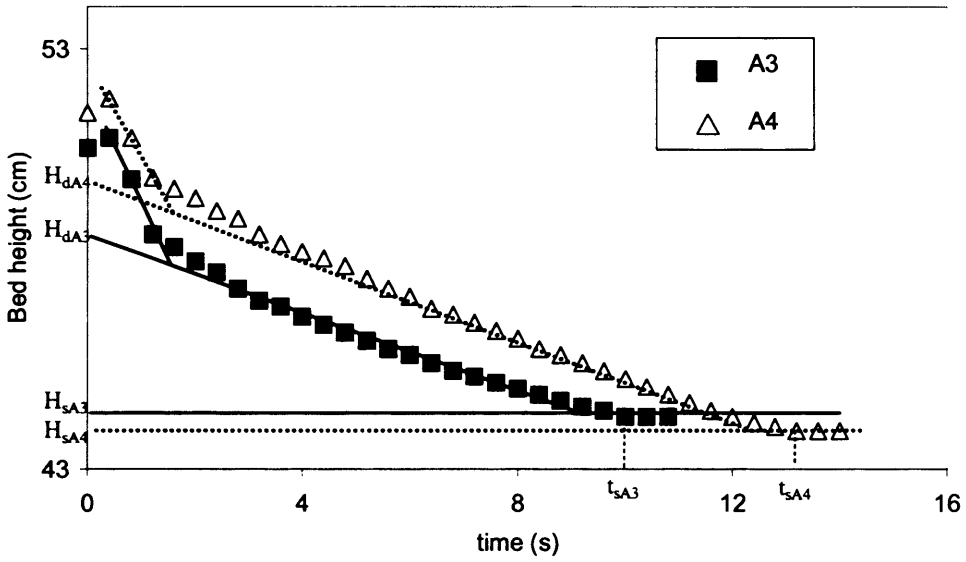

Figure 71 *A typical bed collapse experiment for sample A3 and A4. T = 400°C*

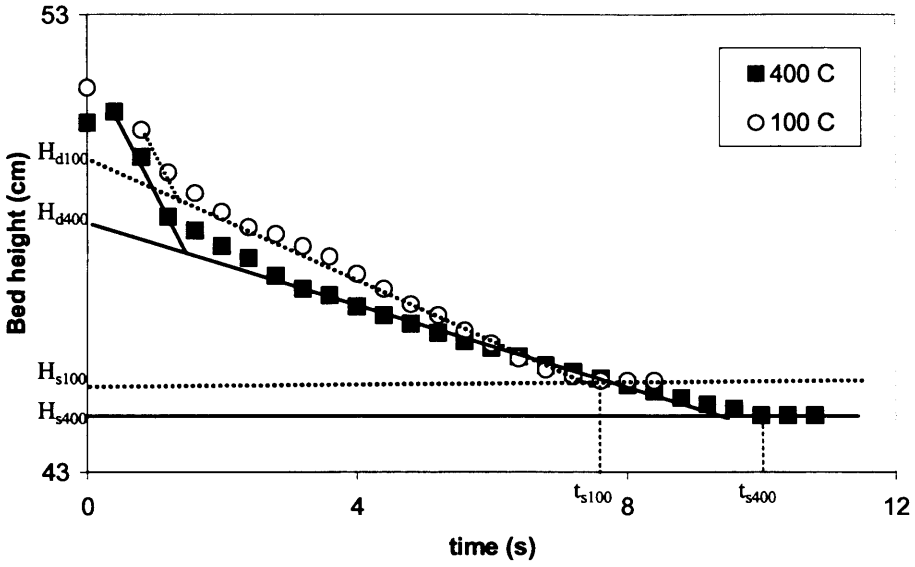

Figure 72 *Temperature effect on BCT profiles – Sample A3*

The effect of temperature on the BER can also be related to changes of the packing of the bed with increasing temperature. The height that the bed has to travel to collapse, H_d-H_s, is just slightly smaller at 400°C than at 100°C, as both the height of the settled bed and the height of the dense phase decreased with increasing temperature. As a consequence of these parallel changes of the packing of the settled bed and of the dense phase, the BER was not much changed by temperature for samples A3, as shown in Figure 67.

Table 13 *Dense phase, settled bed voidage and BER for powders A5 and A6*

	A5				A6			
T (°)	H_d (cm)	H_s (cm)	H_d-H_s (cm)	BER (%)	H_d (cm)	H_s (cm)	H_d-H_s (cm)	BER (%)
27	51.0	42.9	8.1	18.9	55.8	40.0	15.8	39.5
100	50.6	42.7	7.9	18.5	54.4	39.6	14.8	37.4
200	49.0	42.3	6.7	15.8	50.4	38.9	11.5	29.6
300	48.2	41.6	6.6	15.9	50.9	39.1	11.8	30.2
400	47.6	41.7	5.9	14.1	52.8	40.0	12.8	32.0

Table 14 *Dense phase and settled bed voidage and collapse time as a function of temperature for powders A5 and A6 (30%wt fines)*

T (°C)	ε_d – A5	ε_d – A6	ε_s – A5	ε_s – A6	t_s (s) – A5	t_s (s) – A6
27	0.558	0.596	0.475	0.437	11.4	17.6
100	0.555	0.586	0.473	0.431	13.0	21.2
200	0.541	0.553	0.467	0.421	14.9	25.7
300	0.532	0.557	0.459	0.424	17.8	29.0
400	0.527	0.574	0.459	0.437	18.1	28.4

A similar trend was observed also for powder A4, as shown in Table 12. For powders A5 and A6 the height of the settled bed and the height of the dense phase also decreased with increasing temperature, as shown in Table 14. However, for these powders the difference H_d-H_s decreased more with temperature than H_s, as shown in Table 13, thus the ratio H_d-H_s/H_s= BER/100 decreased with increasing temperature.

In summary, for both sets of powders containing 22% and 30%wt of fines, the differences detected in the bed collapse parameters of the two samples containing big and small fines and the changes of the bed collapse parameters with temperature were related to changes in the bed "structure". In particular, at each temperature the structure of the settled bed was found to become more compacted for the samples containing the small fines (A4 and A6) than for the samples containing the big fines (A3 and A5), whereas the structure of the dense phase showed the opposite trend.
For all powders, when increasing temperature both the structure of the settled bed and that of the dense phase became more compacted.
For each fines content (22% and 30%wt) the samples richer in smaller fines, A4 and A6, showed at each temperature to be more aeratable than the corresponding samples containing the same amount of bigger fines, A3 and A5.
Moreover, the effects of changing the fines size distribution on the SCT and the BER were enhanced when increasing the total fines content from 22% to 30%wt. The dense phase collapse rate did not detect any differences between powders differing in the fines size distribution, whatever the fines content.

Temperature caused the SCT to increase and the U_{de} to decrease for all powders and for each total fines content. The BER was not affected by temperature for the 22%wt case and decreased for the 30%wt case.

Lettieri (1999) reported results on the bed collapse tests carried out on a wide range of FCC catalysts and silica catalysts doped with different amounts of potassium acetate KOAc. Lettieri found that increasing temperature caused the SCT to increase for those catalysts which were free from any dominant effect of IPFs (fresh FCC catalysts and silica doped with a low amount of KOAc) and a decrease for those whose behaviour was dominated by the IPFs (E-Cat containing process residuals and silica doped with a higher amount of KOAc).

In keeping with Lettieri (1999), we can conclude that for the powders containing 22%wt fines the collapse behaviour was not dominated by the IPFs. However, the results from the BCTs with increasing temperature highlighted that the effects of the IPFs on the maximum capability of the bed to aerate become more evident for the case of 30%wt fines and in particular for the powder containing the smaller fines, A6.

Furthermore, section 4.2.2 showed that the effects on fluidization of the IPFs created by the addition of fines were visible in the expansion profiles. When the fines content was higher (30%) the IPFs present in the settled bed affected the expansion behaviour, in a different extent when the same amount of small (0-25 μm) or big fines (26-45 μm) was added. In fact, the expansion happened in two stages, the second of which was characterized by the weakening of the bed structure and the formation of microchannels in the bed.

The different role of the IPFs in the collapsing and in the expansion behaviour and the changes detected at high temperature for powders A5 and A6 may be explained considering that when the bed is made to collapse from a vigorous bubbling state any previous "history" of the packing of the bed is erased and the effect of the IPFs is diminished. However, increasing temperature for powders A5 and A6 seemed to enhance the effect of the IPFs, affecting the maximum capability of the bed to aerate.

Moreover, adding IPFs through the addition of fines made the powders containing smaller fines (A4 and A6) more capable of expanding than the powders containing the same amount of bigger fines (A3 and A5).

Therefore, different fluidization tests highlighted a different role of the IPFs on the fluidization behaviour. IPFs were shown to dominate according to whether or not the "memory" of the packing of the settled bed was still affecting the fluidization behaviour. With this regard, the study of the rheological behaviour of the aerated powders reported in chapter 5 is extremely relevant, as it provides a means of measuring the effects of the IPFs on the bulk properties of the materials.

4.5 Prediction of U_{de} using the Richardson-Zaki equation

Section 6.4 showed that the SCT was the bed collapse test parameter most capable of discriminating between powders having different fines size distribution, whereas the dense phase collapse rate U_{de} did not distinguish between powders A3 and A4 or between powders A5 and A6. However, U_{de} is the parameter which is usually employed to predict the collapse behaviour of fluidized beds and for which correlations have been derived. It is therefore of interest to examine the applicability of the existing correlations used to predict U_{de}.

In this section we also look at the Richardson-Zaki equation for predicting the bed collapse rate with increasing temperature and to describe the expansion/collapse mechanism.

Gibilaro et al. (1984), derived a simple equation for the homogeneous bed expansion/contraction rate, U_p, following a velocity change as a function of the gas velocity prior to and after the flow change, u_1 and u_2:

$$U_p = u_2 - u_1 \qquad \text{Eq. 43}$$

Following the approach used by Lettieri (1999), this concept has been applied to the bed collapse test, which represents the limiting case of the contraction mechanism in which $u_2=0$ and where the rate at which the particles fall, $U_p=U_{de}$, is given by

$$U_p = U_{de} = -u_1 = u_t \varepsilon_d^n \qquad \text{Eq. 44}$$

where ε_d is the voidage of the dense phase.

Therefore, using Equation 44 values of the dense phase collapse rate U_{de} were calculated using the experimental values of u_t* and n* obtained from the bed expansion profiles and the experimental values of ε_d obtained from the collapse test. The value of U_{de} so calculated was designated U_{de}*. Values of the dense phase collapse rate U_{de} were also determined from Equation 44 using the values of u_t and n predicted using the Stokes law and the Richardson-Zaki correlations with experimental values of ε_d obtained from the collapse test (See Table A1.6 in Appendix 1). The value of U_{de} so calculated was designated U_{de}^1. Figure 73 (a-c) show the comparison between the experimental values of U_{de} and the calculated U_{de}* and U_{de}^1 for powders A0, A3 and A4.

Both predicted values of U_{de} (U_{de}* and U_{de}^1) decreased with increasing temperature matching the experimental trends for all powders. This shows the capability of the Richardson-Zaki equation to describe the dense phase collapse mechanism for all the powders analysed. The predicted value U_{de}* seemed to better match the experimental values at each temperature. However, it should be emphasized again that experimental values of U_{de} are a function of the starting fluidizing velocity, as discussed in section 4.4.1, which in this study was arbitrarily set at 1.5 cm/s in order to minimize elutriation of fine particles. Therefore, the experimental values are to be taken as trends rather than absolute values and any matching between the experimental values and predictions has to be regarded as circumstantial.

Therefore, the validity of the Richardson-Zaki equation to describe the collapse mechanism was assessed and values for the dense phase collapse rate, U_{de}, calculated using the Richardson-Zaki equation matched the experimental trends with temperature.

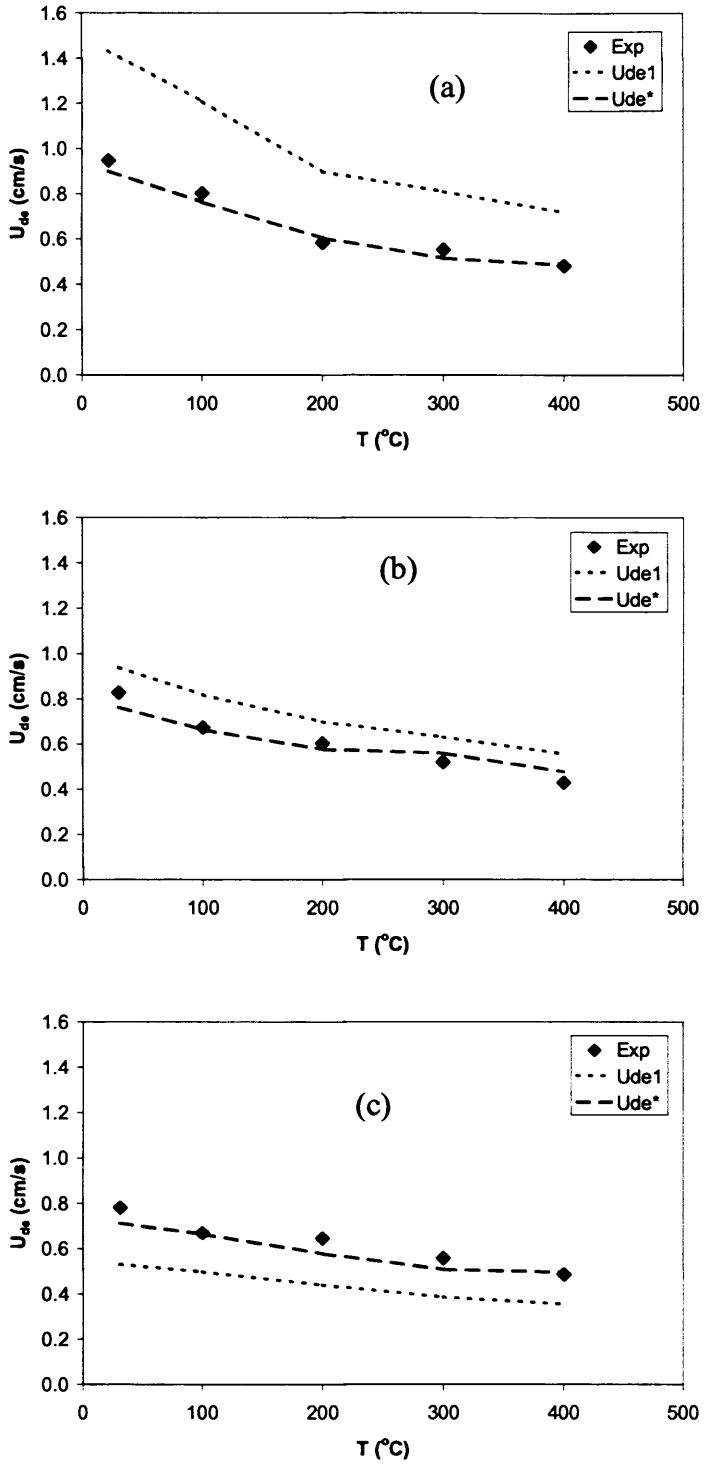

Figure 73 *Comparison between experimental Ude values with predictions obtained from Eq. 44, using experimental values for ε_d, n^*, u_t^* (U_{de}^*) or experimental values for ε_d and predicted values for n, u_t (U_{de}^1). (a) A0; (b) A3; (c) A4.*

Furthermore, Figure 74 showed that values for the dense phase collapse rate predicted using the Richardson-Zaki equation did not discriminate between powders differing in particle size distribution (A3 and A4) when values of the Richardson-Zaki parameters obtained from the experimental expansions (n* and u_t*) are used, as values of n* and u_t* were very similar for the two powders A3 and A4 (as shown in Figure 55 and Figure 56). However, when using the predicted Richardson-Zaki parameters (n, u_t), the dense phase collapse rate obtained using the Richardson-Zaki equation, U_{de}^1, detected differences between A3 and A4, as $U_{de}{}^1{}_{A3} > U_{de}{}^1{}_{A4}$ at each temperature. This is in line with the fact that u_t calculated using the Stokes law is very sensitive to the mean particle diameter, which is slightly bigger for A3 than for A4. Therefore, the dense phase collapse rate should not be used as a means for predicting the fines size distribution effect on fluidization behaviour when experimental values of the Richardson-Zaki equation are not available.

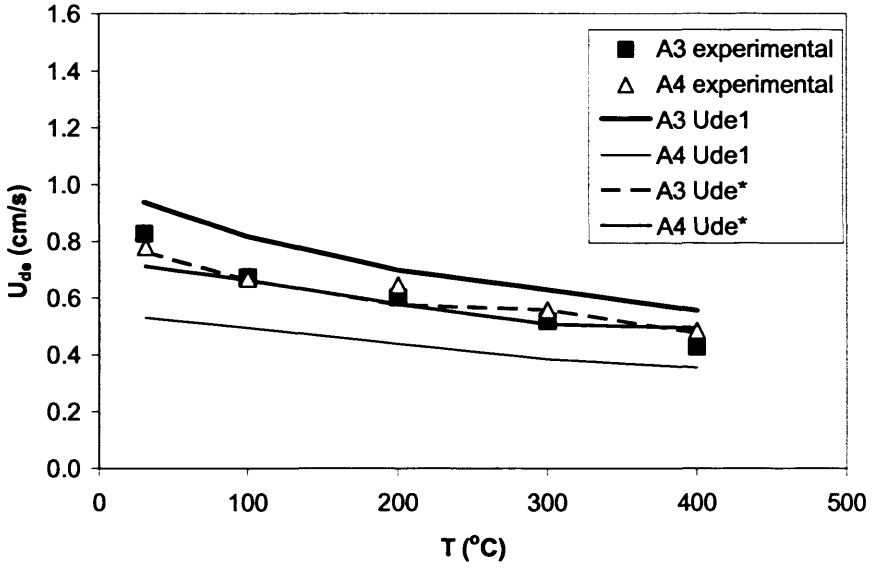

Figure 74 *Comparison between U_{de} values for sample A3 and sample A4*

Similar results were obtained when the Richardson-Zaki relationship was used to predict the dense phase collapse rate of samples A5 and A6, containing 30%wt of fines, as shown in Figure 75 - Figure 77. This time, however, a choice had to be made on which set of values n* and u_t* to use, those determined for the higher or lower

values of ε. Figure 75 and Figure 76 show that the values of U_{de}* are unaffected by either choice.

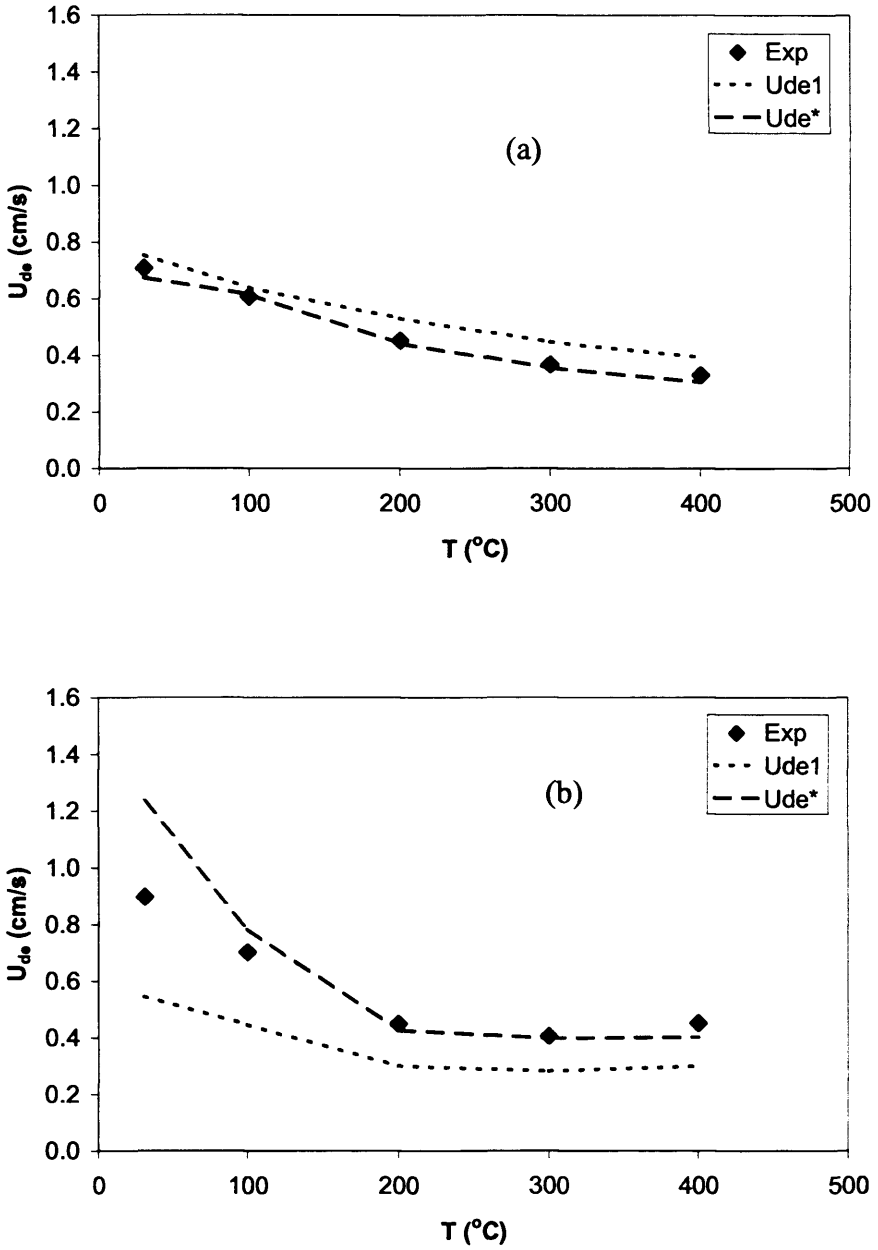

Figure 75 *Comparison between experimental Ude values with predictions obtained from Eq. 44, using experimental values for ε_d, n^*, u_t^* (high values of ε) (U_{de}^*) or experimental values for ε_d and predicted values for n, u_t (U_{de}^1). (a) A5; (b) A6.*

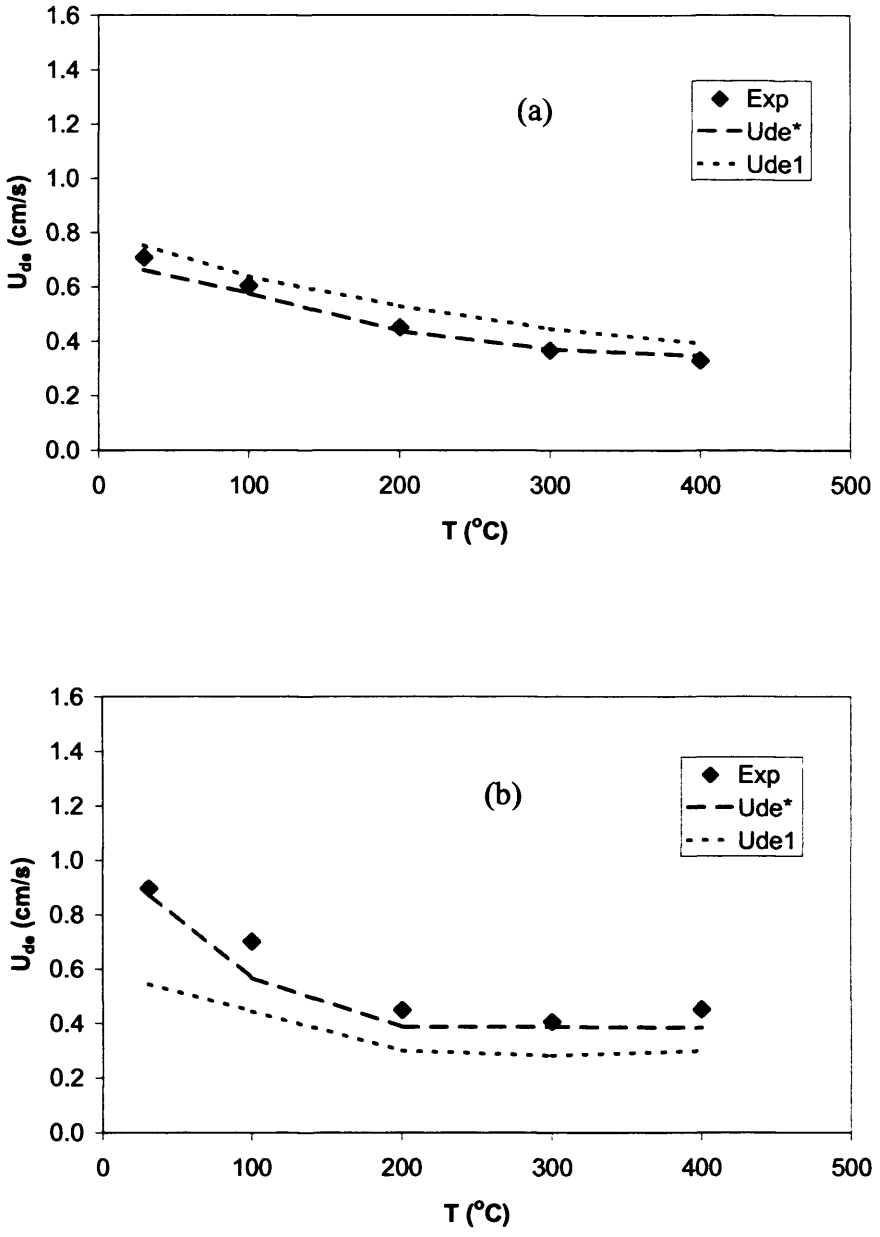

Figure 76 *Comparison between experimental Ude values with predictions obtained from Eq. 44, using experimental values for ε_d, n^*, u_t^* (low values of ε) (U_{de}^*) or experimental values for ε_d and predicted values for n, u_t (U_{de}^1). (a) A5; (b) A6.*

Figure 77 shows the importance, when a higher fines content is present, of using experimental values rather than calculated values of the R-Z parameters in order to predict correctly the collapsing behaviour of powders differing in fines size distribution.

These results show once again that the use of correlations based on a mean particle diameter can be misleading when the effects of fines size distribution on fluidization has to be assessed.

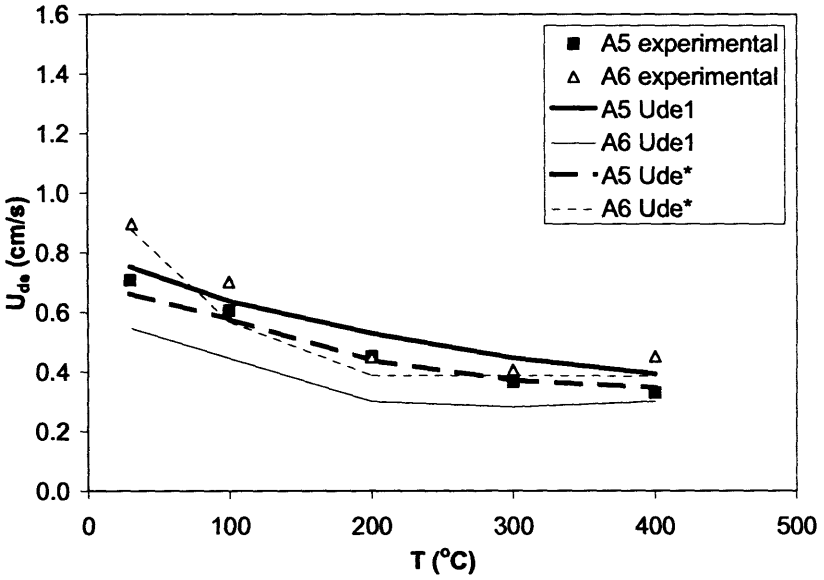

Figure 77 *Comparison between U_{de} values for samples A5 and A6*

4.6 Summary

The fluidization tests reported in this chapter showed that there are significant differences in the fluidization behaviour of the alumina powders having different fines content and fines size distribution. In particular:

Slow aeration tests

- the alumina samples A4 and A6, containing small fines (0-25 μm), arranged in a more compacted packing when settled than the alumina samples containing the same amount of big fines (26-45 μm), A3 and A5. This held true both when the bed was slowly settled in an expansion experiment and when the bed settled at the end of a quick collapse.
- a bigger overshooting in the pressure drop profiles was observed when the fines content was increased from 22% to 30%wt. This is an indication of an increasing resistance opposed by the bed to flow, which may be caused by a

combination of increasing the powder cohesiveness and the friction at the wall.

- the behaviour of all the materials at minimum fluidization showed similarities with that of the compacted bed. With increasing the total fines content and with changing the fines size distribution, the bed voidage at minimum fluidization showed similar trends as the voidage of the settled bed.
- a different mechanism was observed in the R-Z expansion profiles when increasing the fines content. The expansion of powders containing 30%wt fines, A5 and A6, happened in two stages characterised by different slopes. This phenomenon was more emphasised for the powder rich in small fines A6.
- formation of microchannels during the expansion of the dense phase of samples containing small fines was detected, showing a sudden weakening of the homogeneous bed structure before bubbling occurs.
- the maximum bed expansion increased with increasing fines content. The alumina samples containing small fines expanded more than the alumina samples containing the same amount of big fines.
- the use of the Sauter mean particle diameter to predict the minimum fluidization velocity and the u_t parameter of the R-Z equation of bimodal powders was found to produce misleading results when the fines content was increased to 30%wt.

Bed Collapse tests

- the capability of the alumina samples of retaining aeration gas increased with increasing fines content. Moreover, the SCT for the samples containing small fines was higher than for the samples containing the same amount of big fines.
- the dense phase collapse rate decreased when increasing fines content but did not discriminate between different fines size distributions.
- temperature increased the aeratability of the alumina samples containing 22%wt fines, showing that for these powders the IPFs caused by the addition of fine particles do not dominate the fluidization behaviour at high temperature. For the powders containing 30%wt fines high temperature diminished the maximum capability of the powders to expand, thus showing an increasing effect of the IPFs at high temperature.

- the Richardson and Zaki correlation described well the mechanism of the expansion and of the collapse. The parameters of the R-Z equation did not discriminate between different fines size distributions.

The experimental campaign described in this chapter highlighted a link between the fluidization behaviour and the "structure" of the settled bed. This is particularly true when adding IPFs through fines addition. The settled bed is highly affected by IPFs and these need to be overcome in order to achieve fluidization. Moreover, below the minimum fluidization conditions the friction at the wall is significant and affects the stress distribution down the bed. This in turn affects the attainment of fluidization and the ability of the bed to expand. Therefore, in order to shed light on this link, a study of the rheological behaviour of the alumina powders below minimum fluidization conditions was devised. In particular, the investigation of the failure properties of the material, which relate the capability of powders to fail, and hence flow, to the load put on them, was utilised to link the rheological and fluidization behaviour of the powder analysed. Given that the greatest effects of the IPFs and the bigger differences in the fluidization behaviour of powders having different fines content were observed for the powders containing 30%wt fines, A5 and A6, the rheological study presented in chapter 5 was carried out on these two powders only.

5 Rheological results and discussion

Chapter 4 showed how process conditions such as temperature and the addition of different size cuts of fine particles can affect the fluidization behaviour of powders. In particular, the role of the IPFs on changes in the fluidization behaviour of alumina powders differing in fines content and fines size distribution was investigated. The fluidization tests highlighted significant differences between powders containing the same amount of fines but rich in small (0-25 μm) or big fines (26-45 μm). IPFs are believed to be responsible for these changes and it would be therefore desirable to quantify the effect of these forces on the fluidization behaviour. Within this framework powder rheology represents a promising means to determine the effect of IPFs on the bulk behaviour of powders.

This chapter reports on the experimental results of the rheological tests carried out on some of the powders examined in chapter 4. Samples A0, A5 and A6 were chosen to test the capability of rheological measurements made at ambient temperature to detect the changes highlighted by the fluidization tests. Group B ballotini were also tested as a reference material.

Section 5.1 reports the experimental values of the failure properties of the powders obtained using the Peschl Shear Cell described in section 3.7. The torque measurements obtained with the msFBR below minimum fluidization conditions when changing impeller depth and aeration rate are reported in section 5.2. The stress distribution in the msFBR below the minimum fluidization conditions was investigated and is described in section 5.2.4 using a modified version of the Janssen's analysis for silo design (Janssen, 1895). A model to predict the torque measured with the msFBR below minimum fluidization conditions, based on the knowledge of the failure properties of the materials, was derived and is described in section 5.2.4.2. This approach allowed a comparison between the rheological behaviour of the four powders taking into account the real load under which each experiment was carried out. This comparison is presented in sections 5.2.3 and 5.2.6.

The effect of aeration on the rheological behaviour of the powders was also assessed by means of the Jansses's approach and is reported in section 5.2.5.3. Torque measurements on the alumina sample A0 and the ballotini samples were carried out at $u=u_{mf}$. The effect of the impeller depth on those measurements is reported in section 5.2.7.

5.1 Failure properties of the materials

The measurements of the failure properties were made using the Peschl Shear Cell, described in section 3.7.1, and kindly provided by the University of Salerno, Italy.

5.1.1 Static angle of internal friction and cohesion

Figure 78 shows a typical experimental shear stress chart, obtained for powder A5 under compaction with normal stress equal to 1106.2 Pa. Figure 79 shows the corresponding yield locus from which the static angle of internal friction, φ, was worked out from the slope of the yield locus and the cohesion, C, from the intercept with the shear stress axis.

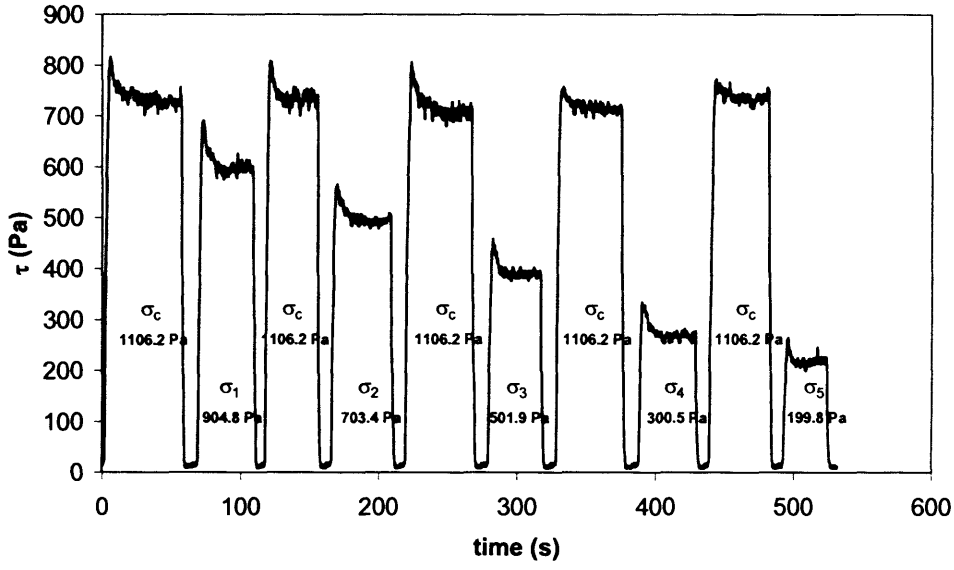

Figure 78 *Experimental shear stress chart – Alumina A5, σ_c=1106.2 Pa*

For each powder four static yield loci were obtained corresponding to the normal consolidation stresses reported in Table 15. Table 16 reports the decreasing normal stresses σ_i (calculated using Equation 39) used for each consolidation stress σ_c.

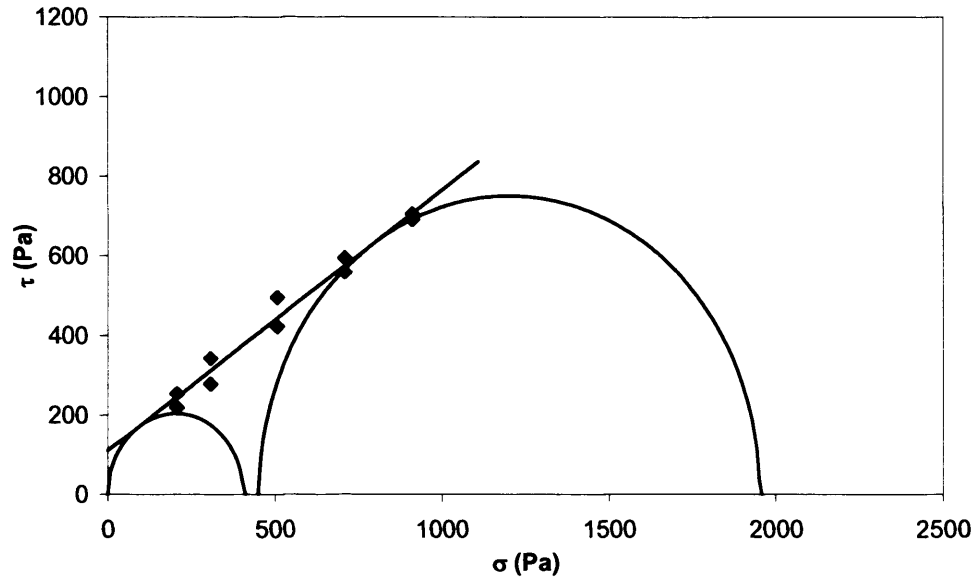

Figure 79 *Experimental static yield locus – Alumina A5, σ_c=1106.2 Pa*

Table 15 *Consolidation stresses in internal yield loci experiments*

Normal load (g)	300	210	150	90
Normal stress σ_c (Pa)	1106.2	804.1	602.6	401.2

Table 16 *Shearing stresses in internal yield loci experiments*

σ_c = 1106.2 Pa	σ_c = 804.1 Pa	σ_c = 602.6 Pa	σ_c = 401.2 Pa
σ_i (Pa)	σ_i (Pa)	σ_i (Pa)	σ_i (Pa)
904.8	602.6	401.2	300.5
703.4	401.2	300.5	250.1
501.9	300.5	199.8	199.8
300.5	199.8	149.4	149.4
199.8	149.4	-	-

As outlined in section 3.7.2, the static angle of internal friction and the cohesion of a granular material are a function of the consolidation stress. Therefore, they can be expressed also as a function of the major principal stress σ_1. Figure 80 and Figure 81

report the static angle of internal friction and the cohesion respectively as a function of the major principal stress σ_1 for all the powders investigated.

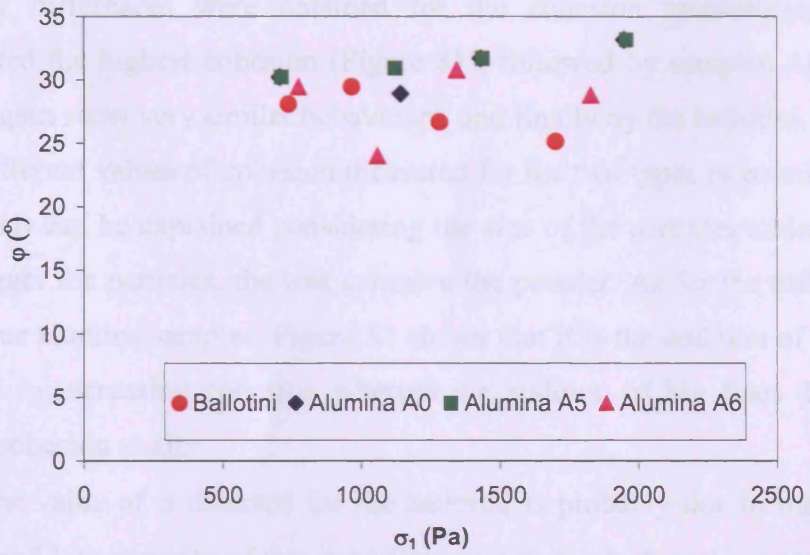

Figure 80 *Static angle of internal friction as a function of the major principal stress*

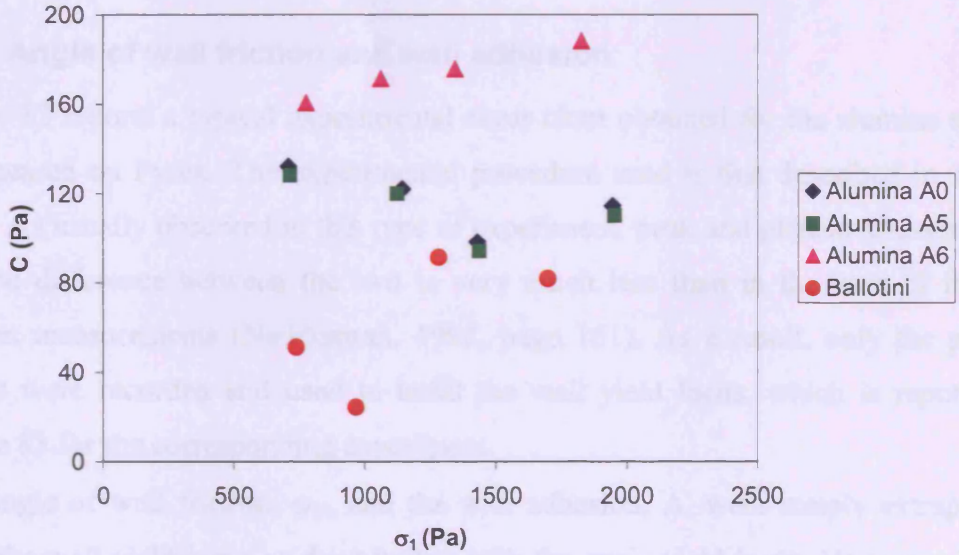

Figure 81 *Cohesion as a function of the major principal stress*

Small differences between the angle of internal friction of the powders analysed can be seen in Figure 80. Powders A0 and A5, the virtually fines free alumina powder and the alumina sample rich in big fines respectively, showed very similar angles of

internal friction, in the range of 30-35 degrees. The ballotini showed lower values of φ, in the range of 25-30 degrees. The alumina sample A6, richer in smaller fines showed a more scattered trend.

Clearer differences were obtained for the cohesion measurements. Sample A6 exhibited the highest cohesion (Figure 81), followed by samples A0 and A5, which once again show very similar behaviours, and finally by the ballotini.

The different values of cohesion measured for the two types of powders (alumina and ballotini) can be explained considering the size of the particles under analysis, where the bigger the particles, the less cohesive the powder. As for the differences between the three alumina samples, Figure 81 shows that it is the addition of small fines to be critical in increasing cohesion whereas the addition of big fines does not seem to affect cohesion at all.

The low value of φ detected for the ballotini is probably due to the perfectly round shape and low rugosity of this modelling material, which make it easier to shear than the alumina samples which are not perfectly spherical, as shown in the SEM picture, in section 3.1.4.

5.1.2 Angle of wall friction and wall adhesion

Figure 82 reports a typical experimental shear chart obtained for the alumina sample A6 sheared on Pyrex. The experimental procedure used is that described in section 3.7.3. As usually observed in this type of experiment, peak and plateau stresses occur but the difference between the two is very much less than in the case of internal friction measurements (Nedderman, 1992, page 161). As a result, only the plateau values were recorded and used to build the wall yield locus, which is reported in Figure 83 for the corresponding experiment.

The angle of wall friction, φ_w, and the wall adhesion, A, were simply extrapolated from the wall yield locus as done before with the static yield locus. However, in this case the angle of friction and the adhesion are not dependent on the stress distribution. Table 17 reports the values of the increasing σ_i used in the experiments and Table 18 the results obtained for the four powders analysed when sheared on Pyrex.

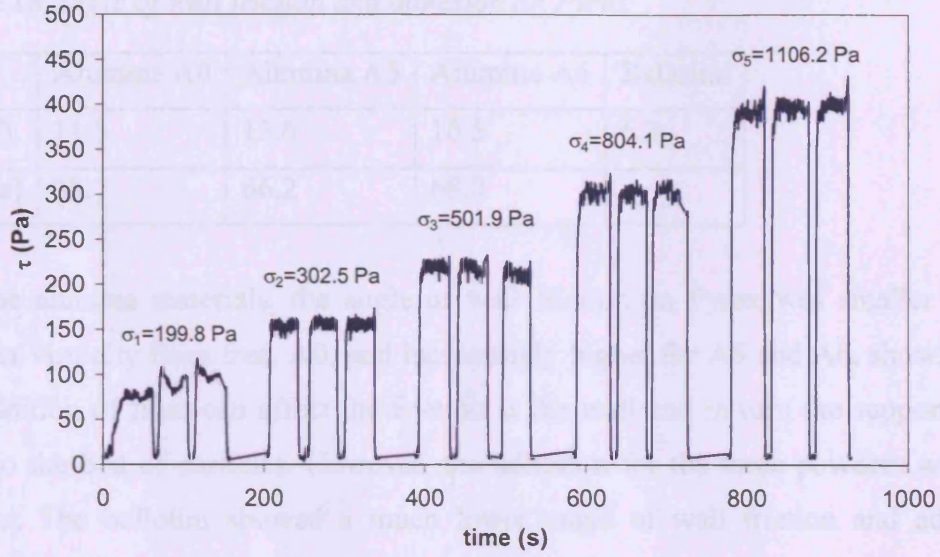

Figure 82 *Experimental wall shear stress chart – Alumina A6 sheared on Pyrex*

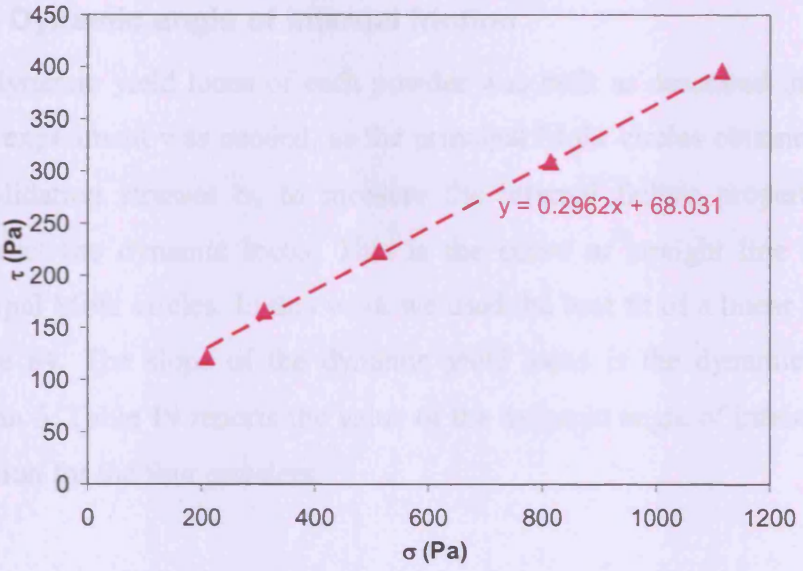

Figure 83 *Experimental wall yield locus – Alumina A6 sheared on Pyrex*

Table 17 *Consolidation stresses in wall yield loci experiments*

Normal load (g)	30	60	120	210	300
Normal stress σ_i (Pa)	199.8	300.5	501.9	804.1	1106.2

Table 18 *Angle of wall friction and adhesion on Pyrex*

	Alumina A0	Alumina A5	Alumina A6	Ballotini
φ_w (°)	11.3	13.6	16.5	6.2
A (Pa)	68.7	66.2	68.0	43.3

For the alumina materials, the angle of wall friction on Pyrex was smaller for the powder virtually fines free, A0, and increasingly higher for A5 and A6, showing that the addition of fines can affect the friction at the wall and in turn the support of the wall to the bed of particles. However, the adhesion for the three powders was very similar. The ballotini showed a much lower angle of wall friction and adhesion, consistent with the fact that the ballotini are made from the same material as the wall (glass). Therefore a low friction at the wall was expected.

5.1.3 Dynamic angle of internal friction

The dynamic yield locus of each powder was built as described in section 5.3.4. No extra experiment was needed, as the principal Mohr circles obtained for the different consolidation stresses σ_c to measure the internal failure properties were used to construct the dynamic locus. This is the curve or straight line tangent to all the principal Mohr circles. In this work we used the best fit of a linear locus, as shown in Figure 84. The slope of the dynamic yield locus is the dynamic angle of internal friction δ. Table 19 reports the value of the dynamic angle of internal friction and the cohesion for the four powders.

Table 19 *Dynamic angle of internal friction and cohesion*

	Alumina A0	Alumina A5	Alumina A6	Ballotini
δ (°)	34	33	31	26
C_δ (Pa)	90	120	158	80

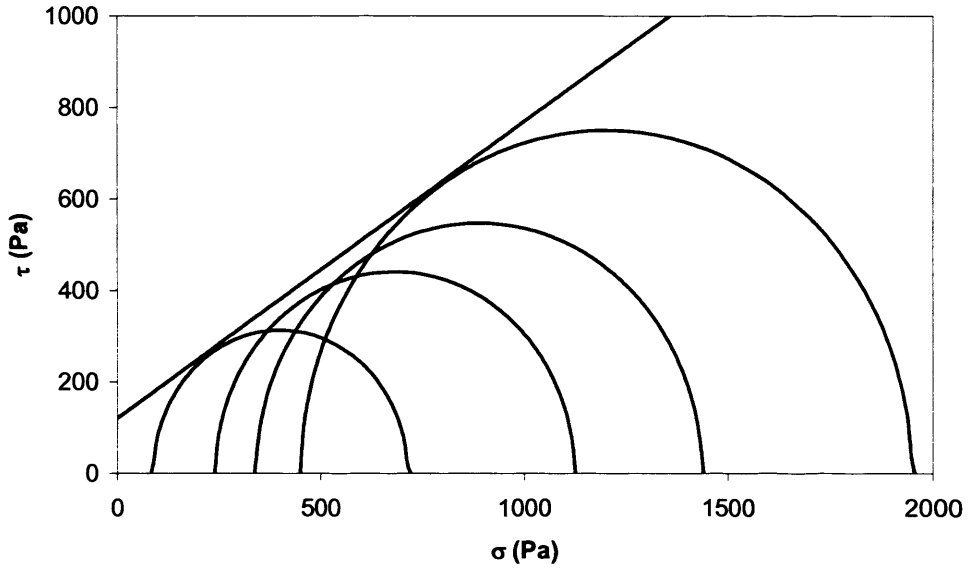

Figure 84 *Dynamic yield locus – Alumina A6*

5.1.4 Effective angle of internal friction

The effective angle of internal friction φ_e represents the angle of internal friction that the material would have if it were cohesionless. Therefore, the difference between the effective and the internal angle of friction is an indication of the degree of cohesiveness of the powders (Molerus, 1975). Values for φ_e are reported in Appendix 1, Table A1.15 for all the powders. Figure 85 shows the difference between the effective and the internal angle of friction as a function of the major principal stress for all the powders. In agreement with previous results, samples A0 and A5 showed the same degree of cohesiveness, whereas sample A6, containing small fines, is the most cohesive and the ballotini are the least cohesive. Therefore, the effective angle of internal friction showed how it is the addition of small fines (0-25 μm) rather than the same amount of big fines (26-45 μm) to determine significant changes in the cohesiveness of the alumina samples.

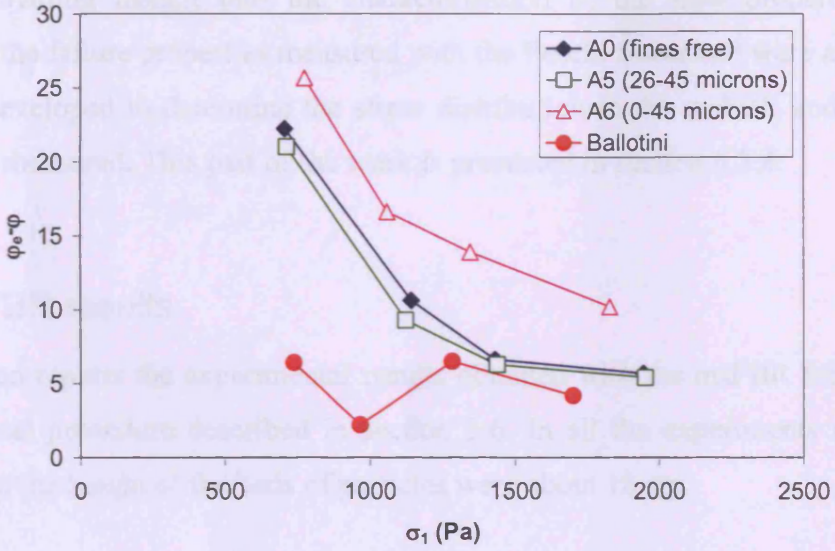

Figure 85 *Difference between the angle of effective and internal friction*

5.1.5 Summary of the rheological measurements using the Peshl shear cell

The measurements of the failure properties of the alumina samples showed that:

- shear cell measurements discriminated between powders having a different size distribution of the fines.
- the results obtained from the cohesion and the effective angle of internal friction showed that the alumina sample containing small fines, A6, was more cohesive, hence less flowable, than the alumina sample containing the same amount of big fines, A5. A5 in turn showed to be rheologically very similar to the fines free material A0.
- The angle of wall friction discriminated between the alumina samples. In particular, the alumina rich in small fines showed the highest angle, i.e. the support offered by the wall is higher for sample A6. Samples A5 and A0 followed with slightly smaller angles.
- Results for the ballotini sample, which was used as a reference "free flowing" material, confirmed that the above trends were correct.

Beside providing insight into the characterization of the flow properties of the materials, the failure properties measured with the Peschl Shear cell were also used in a model developed to determine the stress distribution in the msFBR and to predict the torque measured. This part of the work is presented in section 5.2.4.

5.2 msFBR results

This section reports the experimental results obtained with the msFBR following the experimental procedure described in section 3.6. In all the experiments reported in this section the height of the beds of particles were about 18 cm.

5.2.1 Effect of impeller depth on torque measurements below u_{mf}

Figure 86-Figure 89 show the measured torque versus the impeller depth (ID or z_i, defined as in Figure 95) at various rates of aeration ($\Delta P/\Delta P_c$) for the alumina samples A0, A5 and A6 and the ballotini sample. The rate of aeration was expressed as the ratio of the ΔP across the bed measured during the experiment and the calculated ΔP_c corresponding to full bed support, $\Delta P_c = Mg/A$. Therefore, different rates of aeration correspond to $0<\Delta P/\Delta P_c<1$ with $\Delta P/\Delta P_c=1$ corresponding to minimum fluidization conditions and $\Delta P/\Delta P_c=0$ to settled bed.

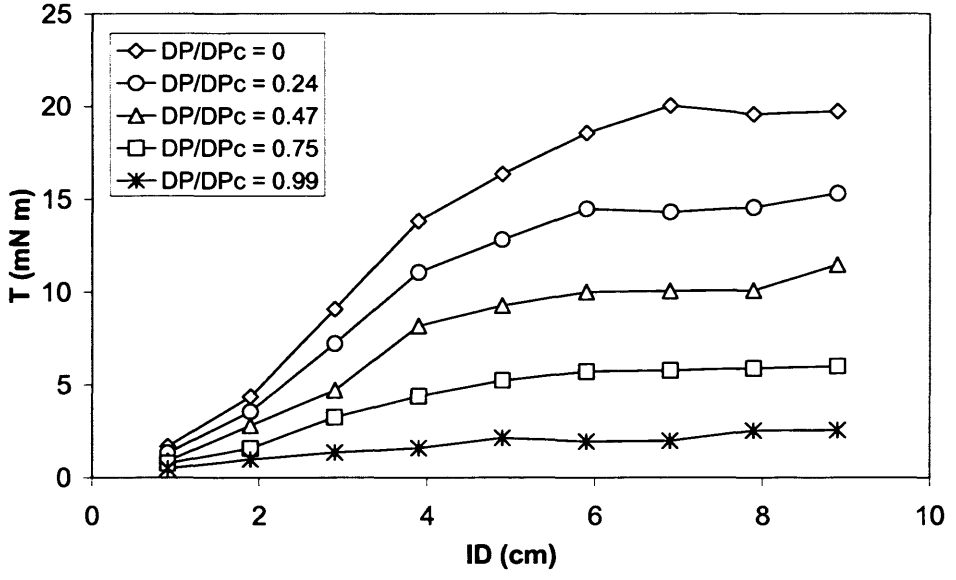

Figure 86 *Effect of impeller depth (ID) on torque – Alumina A0*

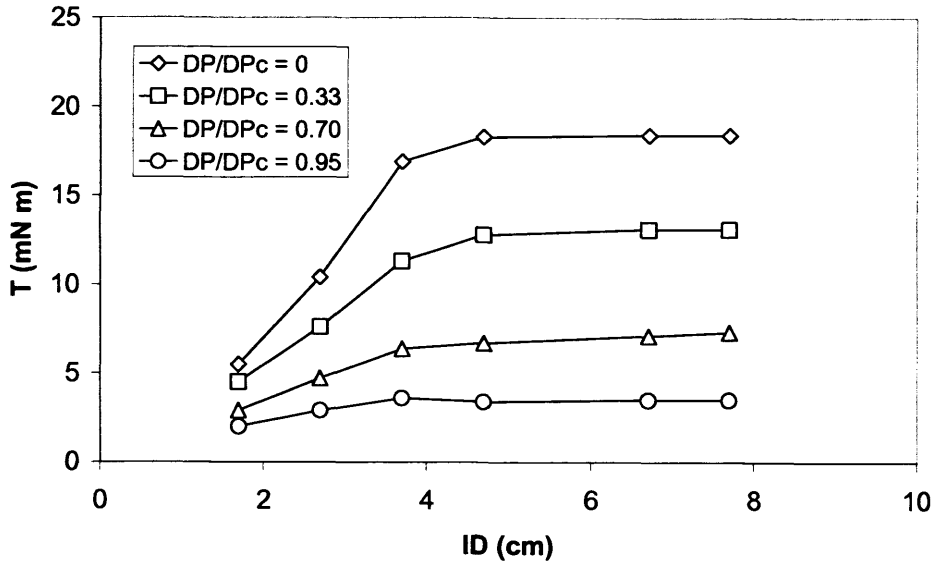

Figure 87 *Effect of impeller depth (ID) on torque – Alumina A5*

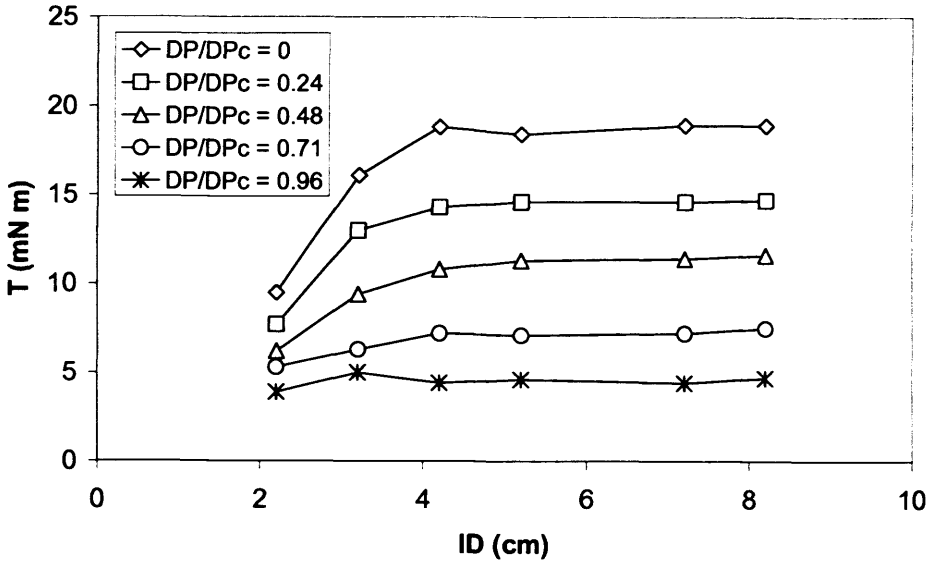

Figure 88 *Effect of impeller depth (ID) on torque – Alumina A6*

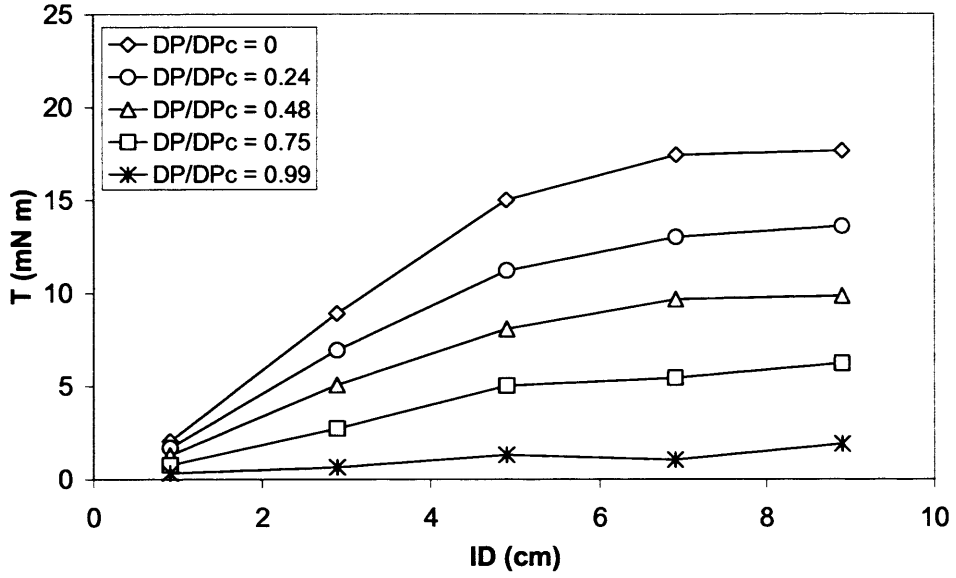

Figure 89 *Effect of impeller depth (ID) on torque – Ballotini*

For all the powders analysed at each aeration rate the effect of increasing the impeller depth was to increase the torque needed to stir the material. However, this increase is not linear but reaches a plateau for impeller depths greater than about 7 cm for the alumina sample A0 and the ballotini and 5 cm for the alumina samples A5 and A6.

The shape of the torque profiles shown in Figure 86-Figure 89 resembles the normal stress profiles typically found in silos (see Janssen, 1895). At a set aeration rate, when the impeller depth is increased the normal load on the impeller also increases, as a greater amount of powder is exerting its net weight from above onto the bed around the impeller. If the bed material were a liquid, the normal stress profile would be linear with increasing depth (hydrostatic conditions). However, in a bulk powder, due to the wall shear stress the increase of the normal stress with increasing depth is less than linear and tends asymptotically to a maximum value, as frequently demonstrated from studies on stresses in silos (Janssen, 1895).

It is plausible to assume a direct proportionality between the torque needed to stir a sample and the normal stress acting on it. Therefore, the plateau values reached by the torque in Figure 86-Figure 89 above a certain impeller depth could correspond to the maximum/asymptotic value of the normal stress in the bed. These observations have been developed further to determine the stress distribution in the msFBR and are reported in section 5.2.4.

5.2.2 Effect of aeration on torque measurements below u_{mf}

Figure 90-Figure 93 show the measured torque values versus the aeration rate at various impeller depths for the alumina samples A0, A5 and A6 and the ballotini sample.

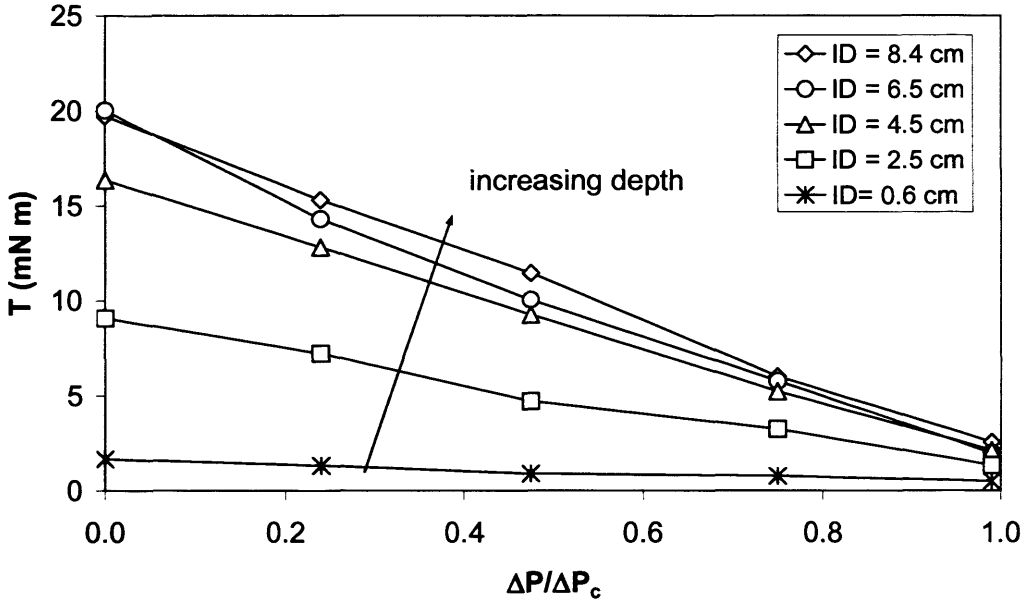

Figure 90 *Effect of aeration rate ($\Delta P/\Delta P_c$) on torque – Alumina A0*

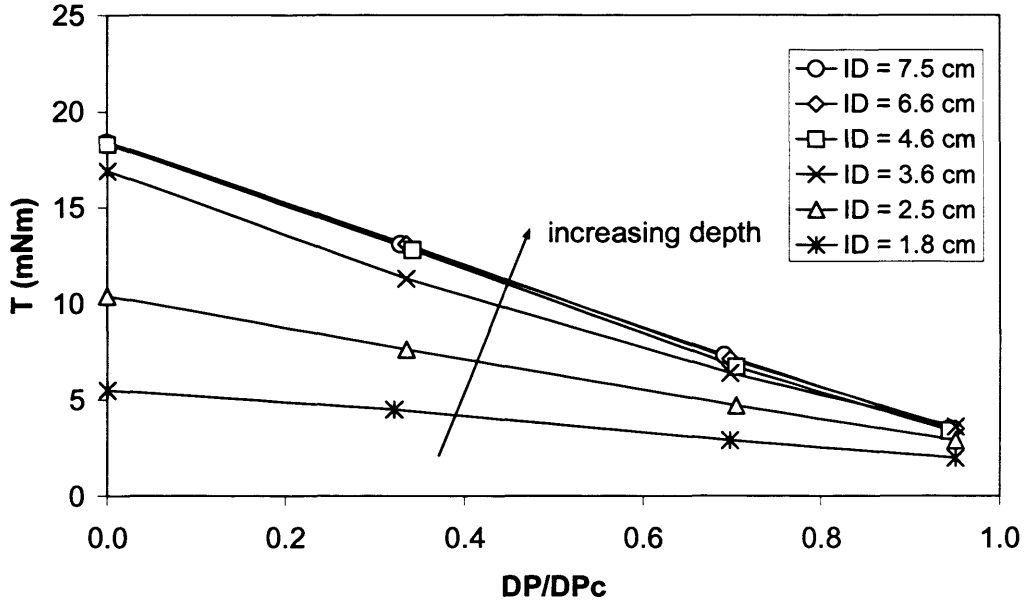

Figure 91 *Effect of aeration rate ($\Delta P/\Delta P_c$) on torque – Alumina A5*

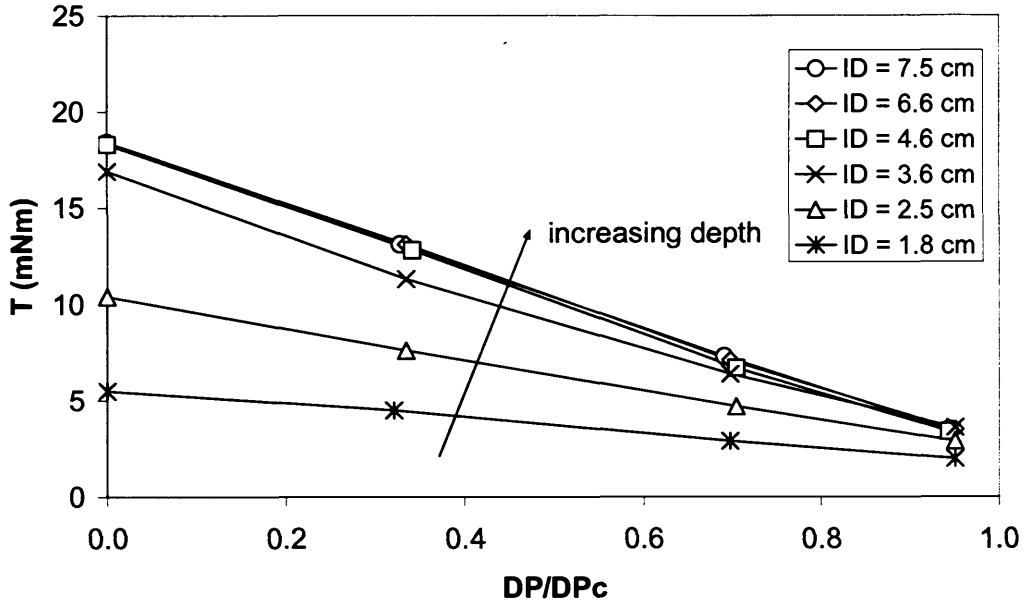

Figure 92 *Effect of aeration rate ($\Delta P/\Delta P_c$) on torque – Alumina A6*

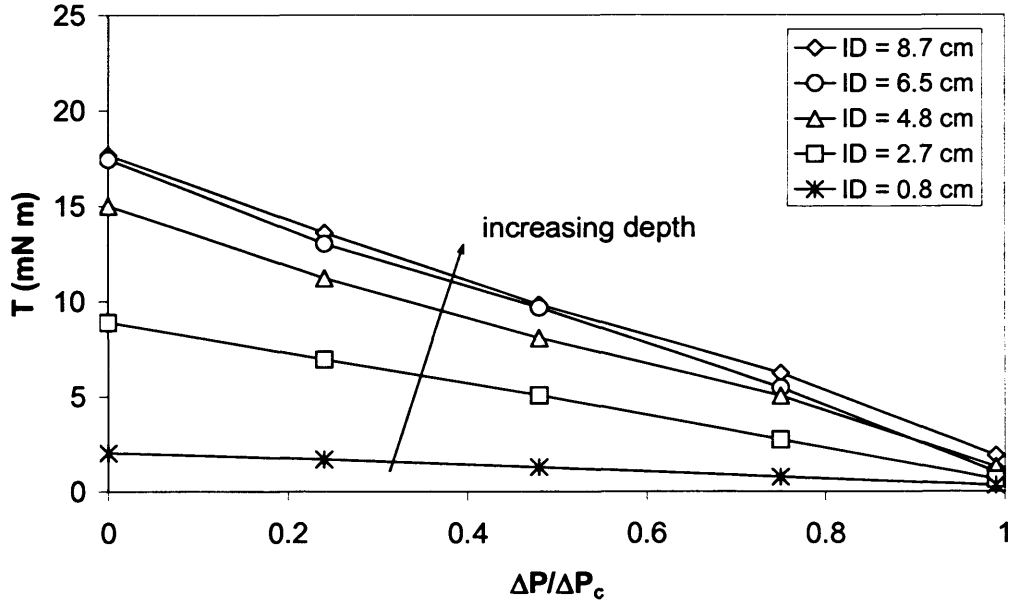

Figure 93 *Effect of aeration rate ($\Delta P/\Delta P_c$) on torque – Ballotini*

The effect of increasing the aeration rate was to linearly decrease the torque needed to stir the materials. These trends can be explained considering that the stress distribution in the bed changes with changing aeration. At a constant impeller depth

when the aeration rate is increased the normal load on the impeller will decrease, due to the additional upward force (drag) exerted by the gas on the powder, which "lightens" the impeller from the full weight of the powder above. In turn, the torque measured under a lower load will be lower. However, aeration could be changing also the rheological properties of the powders as well as the effective normal load under which the tests were conducted. Therefore, the overall effect on the torque measurements of increasing aeration might be a combination of decreasing the normal stress and also changing the flow properties of the powders. Thus, in order to analyse the effect of aeration on the bed rheology the stress distribution in the bed was determined.

5.2.3 Comparison between torque measurements for different materials

When comparing the measured torque values for the alumina samples and the ballotini at the same rate of aeration and impeller speed (see Figure 94), we find values to be surprisingly similar considering the differing powder properties, with the alumina samples generally showing higher torque values than the ballotini. However, we should also consider the normal stress profiles down the bed when making these comparisons. The alumina particles are less dense than the ballotini, therefore at the same impeller depth the normal load (effective bed weight) on the impeller is expected to be higher for the ballotini than for the alumina. Moreover, the different wall failure properties measured for the materials showed that a different degree of support from the wall to the bed of particles can be generated, therefore affecting the effective weight on the impeller. In other words, the comparison between the rheological behaviour of the two materials by means of measurements of the resisting torque is not as straightforward as it may seem, and it ought to be done at equal normal loads. Similarly, due to the different PSD of the alumina samples A5 and A6, they can arrange in different packings, generating different bulk densities and also different wall failure properties. Thus, the "net weight" exerted on the impeller can be different for A5 and A6, even at the same ID and aeration. Therefore, comparisons to detect the influence of fines size distribution on the rheological behaviour ought to be done using measurements carried out at equal normal loads.

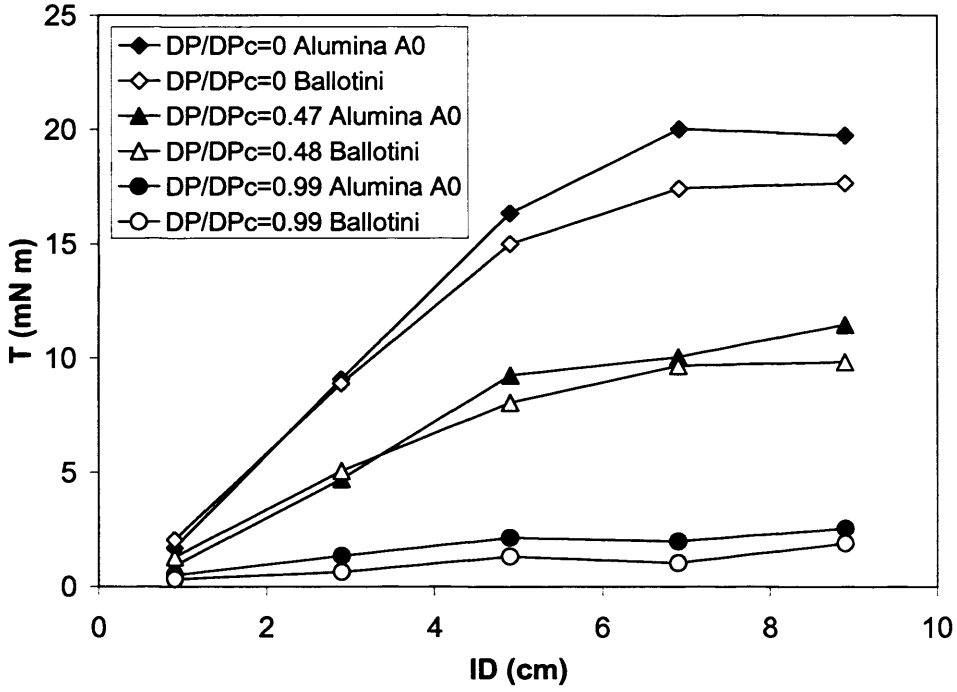

Figure 94 *Comparison between torque measurements for Alumina A0 and Ballotini*

5.2.4 Rheological analysis below u_{mf}

Sections 5.2.2 and 5.2.3 highlighted how knowledge of the stress distribution can help to interpret the experimental results obtained using the msFBR below the minimum fluidization condition. In particular, the effect of aeration on the bed rheology can be assessed only when one can distinguish between changes in the tensional state, i.e. different $\sigma-\tau$ points when changing aeration but belonging to the same yield locus, and changes in the bed rheology, i.e. different $\sigma-\tau$ points when changing aeration belonging to different yield loci. Similarly, the effect of fines size distribution can only be assessed when the stress distribution in each experiment is known.

In the following section (5.2.4.1) the stress distribution of the material is determined. Once the shear and normal stresses acting on the powder around the impeller are known, a simple model can be derived to predict the torque measured by the msFBR (section 5.2.4.2) and comparisons can be drawn between the predicted and experimental values of the torque (section 5.2.4.3). In particular, comparisons between the predicted trends with increasing aeration and the experimental ones will shed light on the effect of aeration on the bed rheology.

5.2.4.1 Determination of the stress distribution in the msFBR

The model reported in this section describes the tensional state of the powder in the msFBR using the original Janssen's analysis for silo design (see Nedderman, 1992, page 85), generalised here to take into account the aeration of the bed and the possible cohesiveness of the material.

Following visual observations, the material is assumed to be stagnant over all the cross section (diameter D) in the top region of the bed from z = 0 to z = z* and in movement only in a cylindrical region around the impeller having height h and diameter d, from z = z* to z = z* + h as indicated in Figure 95.

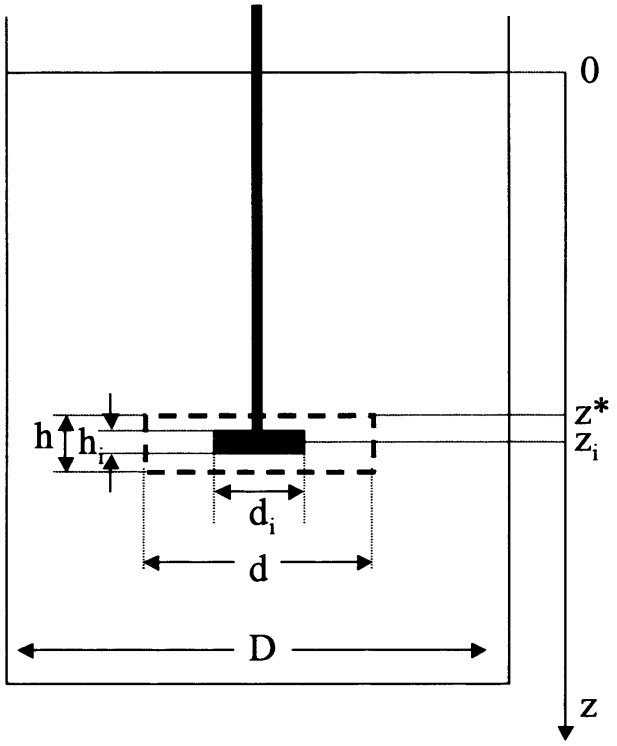

Figure 95 *Regions in the msFBR*

In other words, the model assumes that the cylindrical region circumscribing the impeller rotates in shear against a stationary powder bed. For simplicity, this cylindrical region is assumed to have dimensions proportional to the dimensions of the impeller:

$$\frac{d}{h} = \frac{d_i}{h_i} = \text{known constant} \qquad \text{Eq. 45}$$

Moreover, following Janssen's analysis, we will assume here that:

1. the vertical and the horizontal stresses are principal stresses
2. the stresses are uniform across any horizontal section of the material

1) Stagnant region – Characteristic dimension D, $z \in [0, z^*]$

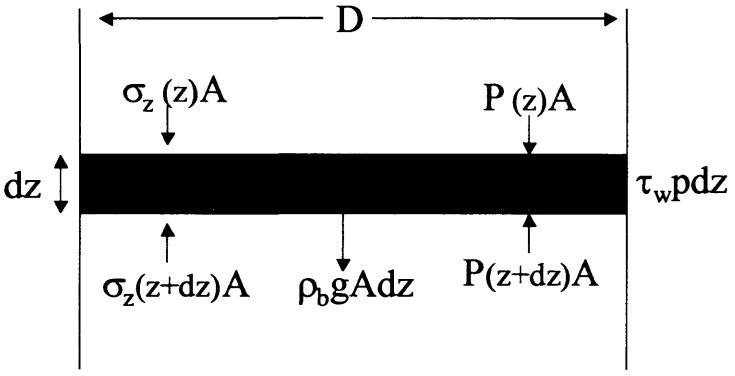

Figure 96 *Elemental slice at depth z*

Let us introduce a system of cylindrical coordinates and perform a force balance on an elemental slice at depth z below the top surface as shown in Figure 96. There is a downward force $A\sigma_z(z)$ on the top surface of the element and an upward force $A\sigma_z(z+dz)$ on the base. Strictly, the force on the top surface should be $\int \sigma_z dA$ but in view of assumption 2 above, integration is unnecessary and the simple product is sufficient.

The weight of the material within the element is given by ρ_b gAdz, where ρ_b is the bulk density $\rho_b=(1-\varepsilon)\rho_p$ and V is the volume of the element, and there is an upward force $\tau_w \pi D dz$ on the side of the element due to the wall shear stress τ_w.

Finally, due to the aeration, there is also an upward force P(z+dz)A exerted by the gas on the base of the element and a downward force on the top surface P(z)A. The force balance is:

$$\sigma_z(z)\frac{\pi D^2}{4}+\rho_b g\frac{\pi D^2}{4}dz+P(z)\frac{\pi D^2}{4}=$$

$$=\sigma_z(z+dz)\frac{\pi D^2}{4}+P(z+dz)\frac{\pi D^2}{4}+\tau_w \pi D dz \qquad \text{Eq. 46}$$

Dividing by $\frac{\pi D^2}{4}dz$ and rearranging gives

$$\frac{d\sigma_z}{dz}+\frac{4\tau_w}{D}+\frac{dP}{dz}=\rho_b g \qquad \text{Eq. 47}$$

The wall shear stress is given by

$$\tau_w=\sigma_r(z)\tan\varphi_w+A \qquad \text{Eq. 48}$$

where σ_r is the horizontal normal stress, φ_w is the static wall friction angle and A is the wall adhesion.

In order to solve Equation 47 a relationship between σ_r and σ_z is needed. In view of assumption 1 above, σ_r and σ_z are principal stresses. However, assumption 1 does not specify which of the two normal stresses σ_r and σ_z is the major principal stress. Therefore, we can have two possibilities:

a) Active case

The vertical stress is the major principal stress:

$$\sigma_1=\sigma_z$$

$\sigma_2 = \sigma_r$

b) Passive case

The horizontal stress is the major principal stress:

$\sigma_1 = \sigma_r$

$\sigma_2 = \sigma_z$

It can be shown (see Appendix 5) that for a cohesive material the principal stresses are related to each other as follows:

$$\sigma_1 = \sigma_2 \frac{1+\sin\varphi}{1-\sin\varphi} + \frac{2C\cos\varphi}{1-\sin\varphi} \qquad \text{Eq. A.54}$$

or

$$\sigma_2 = \sigma_1 \frac{1-\sin\varphi}{1+\sin\varphi} - \frac{2C\cos\varphi}{1+\sin\varphi} \qquad \text{Eq. A.55}$$

where φ and C are the static angle of internal friction and the cohesion of the material respectively.

Therefore, a general equation can be written which encompasses both the active and the passive case for a cohesive material:

$$\sigma_r = \sigma_z \frac{1+k\sin\varphi}{1-k\sin\varphi} + \frac{2kC\cos\varphi}{1-k\sin\varphi} \qquad \text{Eq. 49}$$

where

k = 1 passive case

k = -1 active case

Substituting Equation 49 in Equation 48 and then Equation 48 in Equation 47 yields:

$$\frac{d\sigma_z}{dz} + \alpha\sigma_z = \beta \qquad \text{Eq. 50}$$

where

$$\alpha = \frac{4}{D}\frac{1+k\sin\varphi}{1-k\sin\varphi}\tan\varphi_w \qquad \text{Eq. 51}$$

and

$$\beta = \rho_b g - \frac{dP}{dz} - \frac{4}{D}\frac{2kC\cos\varphi}{1-k\sin\varphi}\tan\varphi_w - \frac{4A}{D} \qquad \text{Eq. 52}$$

The boundary condition for Equation 50 is that the top surface of the material is open to the atmosphere so that the normal stress on it may be taken to be zero:

B.C. $\sigma_z(z=0) = 0$

As φ and C would usually depend on the consolidation stress, they will be a function of z and therefore Equation 50 needs to be solved step wise.
If the dependence of φ and C upon z can be neglected and constant values can be used, then an analytical solution can be written for Equation 50:

$$\sigma_z(z) = \frac{\beta}{\alpha}\left[1 - \exp(-\alpha z)\right] \qquad \text{Eq. 53}$$

Equation 53 shows that the normal stress tends exponentially to an asymptotic value at great depth. Moreover, the rate of approach to the asymptote is governed by the term:

$$\exp(-\alpha z) = \exp\left(-\frac{4}{D}\frac{1+k\sin\varphi}{1-k\sin\varphi}\tan\varphi_w z\right) \qquad \text{Eq. 54}$$

so that we can define a characteristic depth z_c given by

$$z_c = \frac{D}{4\tan\varphi_w}\frac{1-k\sin\varphi}{1+k\sin\varphi} \qquad \text{Eq. 55}$$

Clearly z_c is the depth over which the departure from the asymptote decreases by a factor of e. The normal stress will therefore reach 90% of its final value at a depth $z_{90} = 2.5z_c$. Taking a typical material for which φ=30° and φ_w=20° we see that

$z_c \approx 2D$ active case

$z_c \approx 0.22D$ passive case

Thus, the normal stress will reach 90% of its final value at a depth $z_{90} \approx 5D$ and $z_{90} \approx 0.5D$ for the active and passive case respectively.

It ought to be pointed out that the rate of approach to the asymptote is independent of the rate of aeration. Therefore, in the msFBR the asymptote of the normal stress is expected to be reached at the same impeller depth regardless of the rate of aeration. However, the value of the asymptote β/α depends upon dP/dz and decreases with increasing aeration. Both features of the model were found to be in agreement with the experimental evidence shown in Figure 86-Figure 89 for the torque measured with the msFBR.

As shown in sections 3.7.2 and 3.7.3, φ and C can be obtained experimentally for each powder under various consolidation stresses and φ_w and A can be obtained for each powder. Values of φ, C, φ_w and A for the alumina samples A0, A5, A6 and the ballotini are reported in Appendix A1, Table A1.15 and A1.16.

2) Impeller region – Characteristic dimension d, $z \in [z^*, z^*+h]$

Given the small height of the impeller region, the assumption is made that changes of σ_z with z are negligible and therefore the normal stress σ'_z in the impeller region is given by

$$\sigma'_Z(z) = \sigma_Z(z^*) \qquad \text{Eq. 56}$$

As for the stagnant region, in the impeller region the normal stress can be related to the horizontal stress σ_r using Equation 49 and in turn the shear stress on the lateral surface of the impeller region τ_{zr} (stress in the z direction on a plane normal to r) can be calculated from σ'_r, this time using the dynamic angle of internal friction and cohesion as defined in section 3.7.4. Values of δ and C_δ are reported Appendix A1, Table A.16.

$$\sigma'_r = \sigma'_z \frac{1+k\sin\varphi}{1-k\sin\varphi} + \frac{2kC\cos\varphi}{1-k\sin\varphi} \qquad \text{Eq. 57}$$

$$\tau_{zr} = \sigma'_r(z)\tan\delta + C_\delta \qquad \text{Eq. 58}$$

5.2.4.2 A model for predicting the torque measured with the msFBR

The knowledge of the failure properties of the materials and the definition of the stress distribution corresponding to any given impeller depth and rate of aeration allowed a model to be written to predict the torque measured with the msFBR.

The region surrounding the impeller was assumed to be shaped like a disc having height h and diameter d, which are related to each other by Equation 45. Hence, when a value is assumed for either d of h, the dimensions of the disc are defined.

The resisting torque will be the sum of three contributions, the torque on the upper surface, the torque on the lower surface and the torque on the lateral surface of the rotating "disc".

$$T = T_{up} + T_{down} + T_{lateral} \qquad \text{Eq. 59}$$

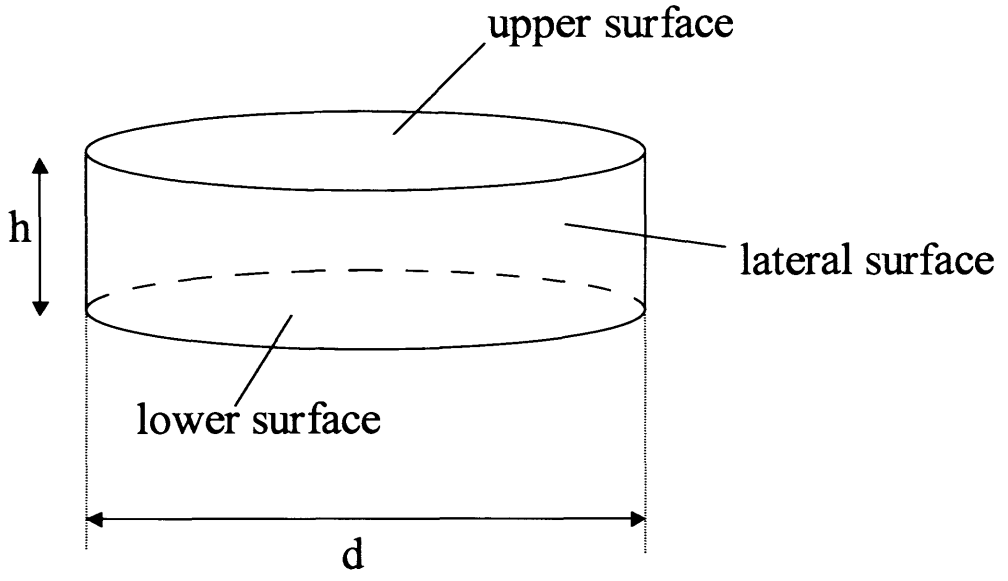

Figure 97 *Shearing surfaces of the rotating disc*

a) Upper surface

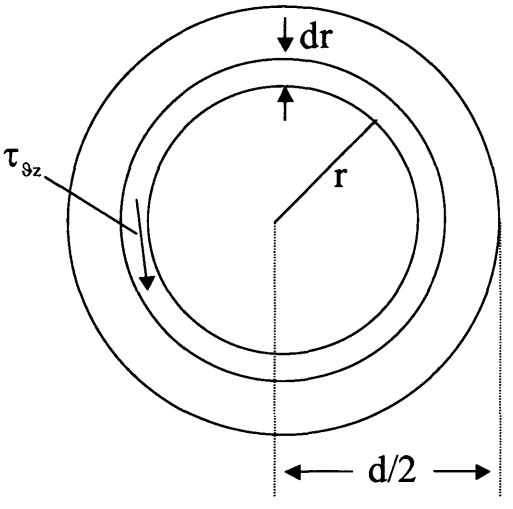

Figure 98 *Elemental slice on a horizontal surface*

The stress acting on a horizontal section is $\tau_{\vartheta z}$, i.e. the shear stress in the ϑ direction on a plane perpendicular to the z direction. $\tau_{\vartheta z}$ is a function of r and z only, as we are assuming that the stresses are uniform across any horizontal section (assumption 2), i.e. there is no dependence on ϑ.
In particular, on the upper surface of the "disc":

$$\tau_{\vartheta z} = f(z^*, r) \qquad \text{Eq. 60}$$

Let us consider the force dF acting on the annular elemental slice between r and r+dr

$$dF = \tau_{\vartheta z}(r, z^*)2\pi r dr \qquad \text{Eq. 61}$$

Therefore, the torque on the elemental slice will be

$$dT = dFr = \tau_{\vartheta z}(r, z^*)2\pi r^2 dr \qquad \text{Eq. 62}$$

Integrating between r = 0 and r = d/2 gives:

$$T_{up} = \int_0^{d/2} \tau_{\vartheta z} 2\pi r^2 dr = \frac{\pi}{12} \bar{\tau}_{\vartheta z}(z^*) d^3 \qquad \text{Eq. 63}$$

where $\bar{\tau}_{\vartheta z}(z^*)$ is the average $\tau_{\vartheta z}$ on the horizontal section at $z=z^*$ and can be calculated using the dynamic yield locus:

$$\bar{\tau}_{\vartheta z}(z^*) = \sigma_z(z^*)\tan\delta + C_\delta \qquad \text{Eq. 64}$$

b) Lower surface

Following an analogous procedure as that used in the upper surface, it can be shown that the contribution to the measured torque due to the lower surface is:

$$T_{down} = \frac{\pi}{12}\bar{\tau}_{\vartheta z}(z^*+h)d^3 \qquad \text{Eq. 65}$$

where

$$\bar{\tau}_{\vartheta z}(z^*+h) = \sigma'_z(z^*+h)\tan\delta + C_\delta = \sigma_z(z^*)\tan\delta + C_\delta \qquad \text{Eq. 66}$$

since we have assumed σ'_z to be constant in the impeller region and equal to the normal stress in the stagnant region evaluated at $z=z^*$.
Therefore

$$T_{up} = T_{down} \qquad \text{Eq. 67}$$

c) Lateral surface

The stress acting on the lateral surface is $\tau_{\vartheta r}$, i.e. the stress in the ϑ direction on a plane perpendicular to the r direction. $\tau_{\vartheta r}$ is a function of z only, as we are assuming that the stresses are uniform across any horizontal section (assumption 2), i.e. there is no dependence on ϑ.

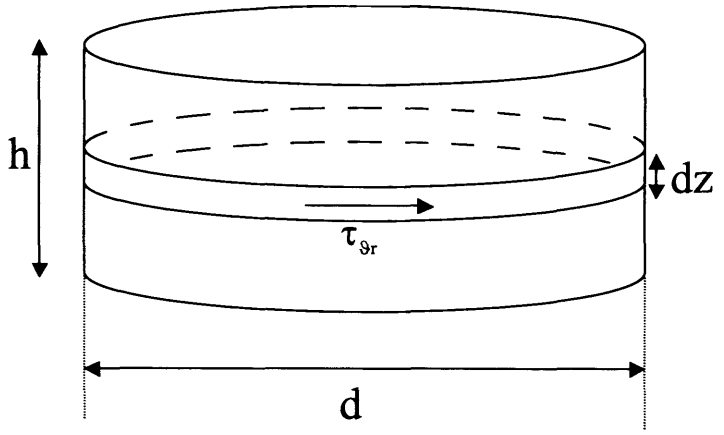

Figure 99 *Elemental slice on the lateral surface*

Let us consider the force dF acting on the ring element between z and z+dz

$$dF = \tau_{\vartheta r}(z)\pi d dz \qquad \text{Eq. 68}$$

Therefore, the torque on the elemental slice will be

$$dT = dF\frac{d}{2} = \tau_{\vartheta r}(z)\frac{\pi}{2}d^2 dz \qquad \text{Eq. 69}$$

Integrating between z = z* and z = z*+h gives:

$$T_{lateral} = \frac{\pi}{2}d^2 \int_{z^*}^{z^*+h} \tau_{\vartheta r}(z)dz \qquad \text{Eq. 70}$$

where

$$\tau_{\vartheta r}(z) = \sigma_r'(z)\tan\delta + C_\delta = \left[\sigma_z'(z)\frac{1+k\sin\varphi}{1-k\sin\varphi} + \frac{2kC\cos\varphi}{1-k\,sen\varphi}\right]\tan\delta + C_\delta =$$
$$= \left[\sigma_z(z^*)\left(\frac{1+k\sin\varphi}{1-k\sin\varphi}\right)\Big|_{z^*} + \left(\frac{2kC\cos\varphi}{1-k\sin\varphi}\right)\Big|_{z^*}\right]\tan\delta + C_\delta \qquad \text{Eq. 71}$$

Therefore,

$$T_{lateral} = \frac{\pi}{2}d^2h\left\{\left[\sigma_z(z^*)\left(\frac{1+k\sin\varphi}{1-k\sin\varphi}\right)\Big|_{z^*} + \left(\frac{2kC\cos\varphi}{1-k\sin\varphi}\right)\Big|_{z^*}\right]\tan\delta + C_\delta\right\} \qquad \text{Eq. 72}$$

Finally, the predicted torque will be:

$$T = \frac{\pi}{6}d^3\left[\sigma_z(z^*)\tan\delta + C_\delta\right] +$$
$$+\frac{\pi}{2}d^2h\left\{\left[\sigma_z(z^*)\left(\frac{1+k\sin\varphi}{1-k\sin\varphi}\right)\Big|_{z^*} + \left(\frac{2kC\cos\varphi}{1-k\sin\varphi}\right)\Big|_{z^*}\right]\tan\delta + C_\delta\right\} \qquad \text{Eq. 73}$$

Therefore, once the functions C(z), φ(z) and the values of δ, C_δ and $\sigma_Z(z^*)$ are known at the desired aeration rate, a value for the torque can be calculated for each given impeller depth z_i ($z^*=z_i-h/2$).

It is worth emphasising that the model takes into account the effect of the aeration only for the determination of the normal stress profile $\sigma_z(z)$, i.e. in the model the aeration is only responsible for changes in the tensional state of the powder. Implications of this characteristic of the model will be discussed later.

5.2.5 Results of the model

In this section the experimental values of the torque measured with the msFBR are compared with values predicted using the model derived in sections 5.2.4 and 5.2.5. The emphasis in this work is to apply a model, whose physical premises are well known, to the real experimental conditions and use the matching or mismatching

between model predictions and experimental data to better understand the physical reasons behind the observed changes of torque.
Moreover, the determination of the value of $\sigma_z(z^*)$ corresponding to each experimental condition allows a true comparison to be made between different powders, as pointed out in section 5.2.3, and this therefore aids the assessment of the effect of fines size distribution on the powder rheology.

The application of the model was limited to aeration rates corresponding to $\Delta P/\Delta P_c$=0.48 for the alumina samples and $\Delta P/\Delta P_c$=0.75 for the ballotini. Above these values the model generated negative values for the normal stress $\sigma_z(z)$, which are clearly not acceptable. The reason for this limitation may lie in the way the wall shear stress is expressed in the model. Equation 48 assumes a limiting state of stress at the wall, i.e. the powder at the wall is fully mobilised. However, when the aeration is above a certain value and the bed of particles is partly supported by the gas flow, the stress state at the wall might be below the yield condition and therefore Equation 48 would not apply any more. If this is the case, the use of Equation 48 for values of the aeration above 0.48 (alumina) and 0.75 (ballotini) would lead to an overestimation of the shear stress at the wall, which in turn generates negative values of $\sigma_z(z)$.

5.2.5.1 Choice of model – active or passive?

The first step when applying the model to the msFBR was to determine whether to use the active or the passive form to relate the two principal stresses σ_z and σ_r. In other words, for each powder we needed to determine whether the major principal stress was vertical or horizontal. In order to shed light on this issue, the experimental torque profiles with increasing impeller depth shown in Figure 86 - Figure 89 were compared to the torque profiles predicted by the model when assuming active or passive tensional state. The model line which best fits the experimental trends will indicate which type of tensional state is acting in the msFBR in each case.
Figure 100 and Figure 101 show these comparisons for the alumina sample A6 and the ballotini respectively, without aeration. Similar results were obtained for the alumina samples A0 and A5 and also when increasing aeration.

Figure 100 shows that above 3 cm impeller depth the passive state seems to best describe the changes of torque with increasing impeller depth. It ought to be pointed out that visual observations made during the experiments showed that any experiment carried out at impeller depths lower than 3 cm exhibited some movement of the surface of the bed corresponding to the impeller. Therefore, the application of the model, which is based on the assumption that a stagnant region exists above the impeller, should be somehow limited to impeller depths greater than a certain value. Hence, the mismatch between model and experiments below 3 cm should not be surprising and does not affect the suitability of applying the model to the powders under analysis.

As a consequence of these observations, a passive tensional state was postulated for all the alumina samples, i.e. the horizontal normal stress was assumed to be the major principal stress.

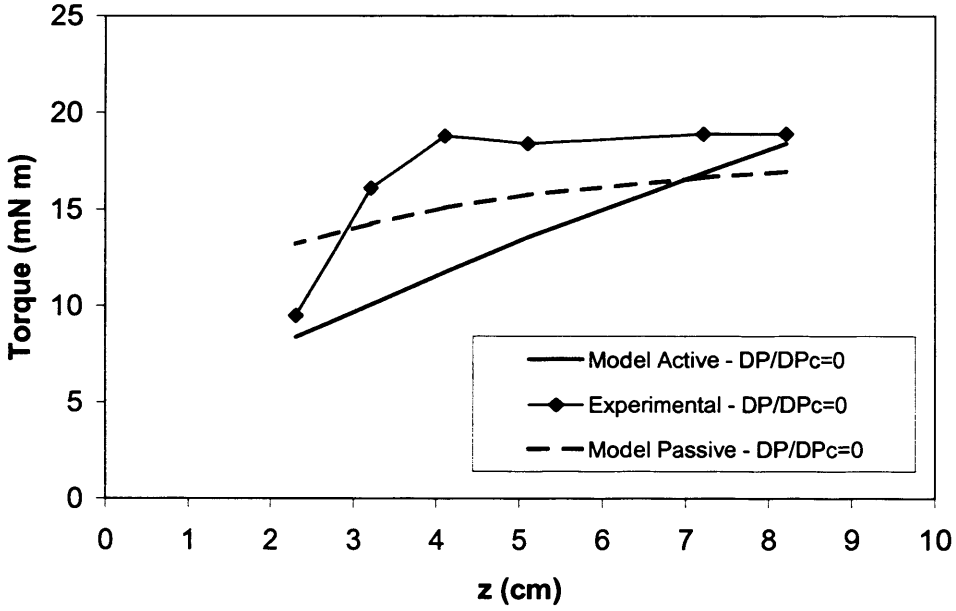

Figure 100 *Comparison between active model and passive model – Alumina A6*

A different situation is shown in Figure 101 for the ballotini, where the active state seem to better fit the experimental values. However, both predicted trends fail in reproducing satisfyingly the experimental trends at higher impeller depths. Therefore, for the ballotini sample results for both the active and passive state were shown in this study and comparisons between the two models were drawn each time.

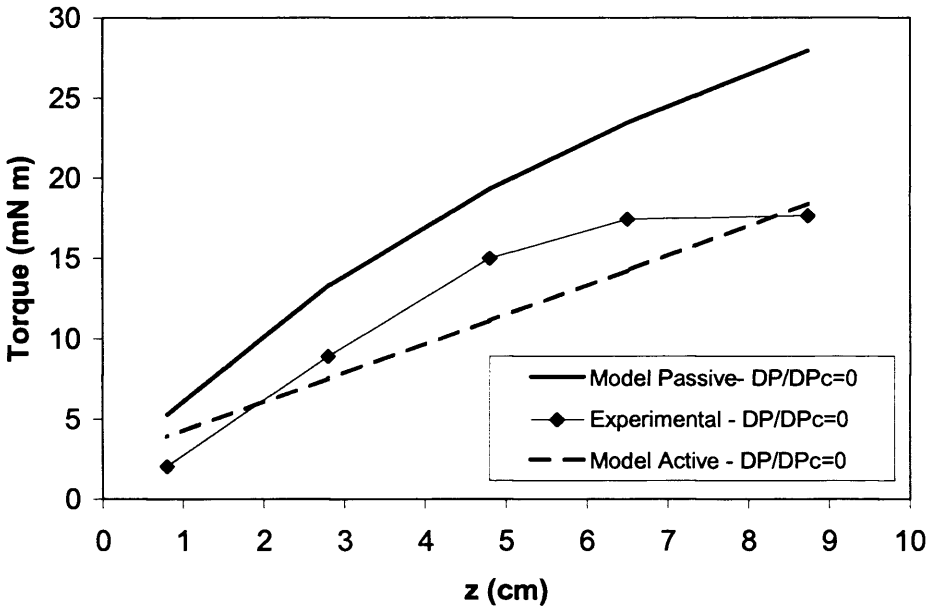

Figure 101 *Comparison between active model and passive model – Ballotini*

5.2.5.2 Effect of impeller depth on torque

The experimental torque profiles with increasing impeller depth were compared with the predicted values, obtained assuming a passive state, at different rates of aeration. Figure 102, Figure 103 and Figure 104 show that a good matching was attained for each alumina sample for impeller depths greater than 3 cm for each aeration rate. As previously pointed out, below 3 cm depth there was no stagnant region above the impeller and therefore comparisons between model and experimental values are not valid.

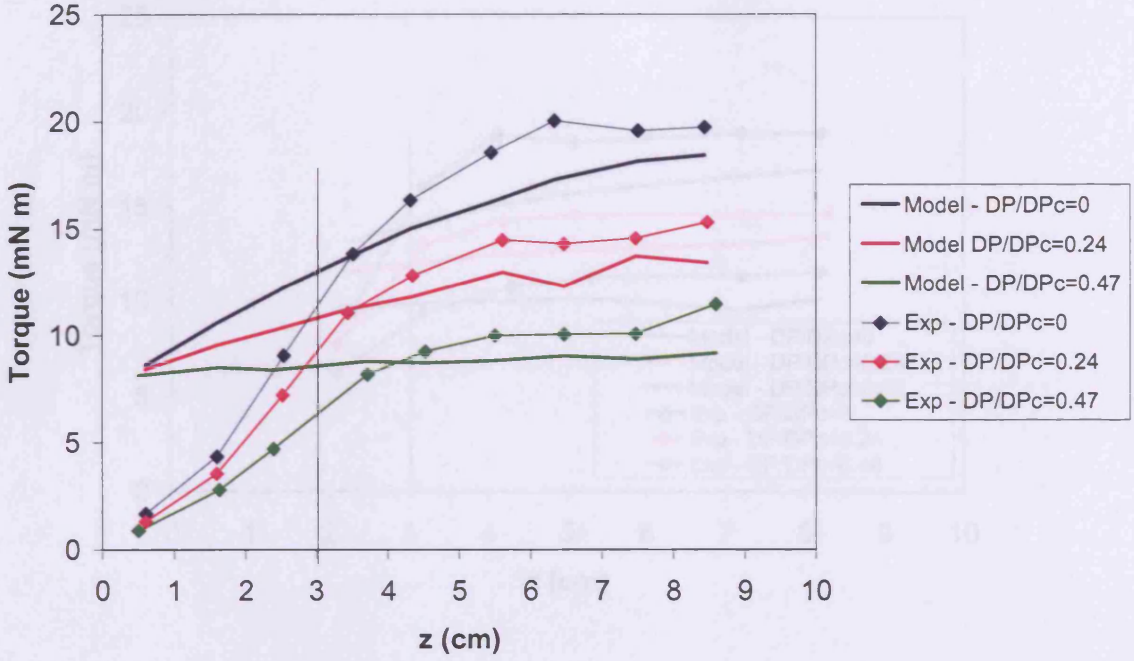

Figure 102 *Depth effect on torque – Alumina A0*

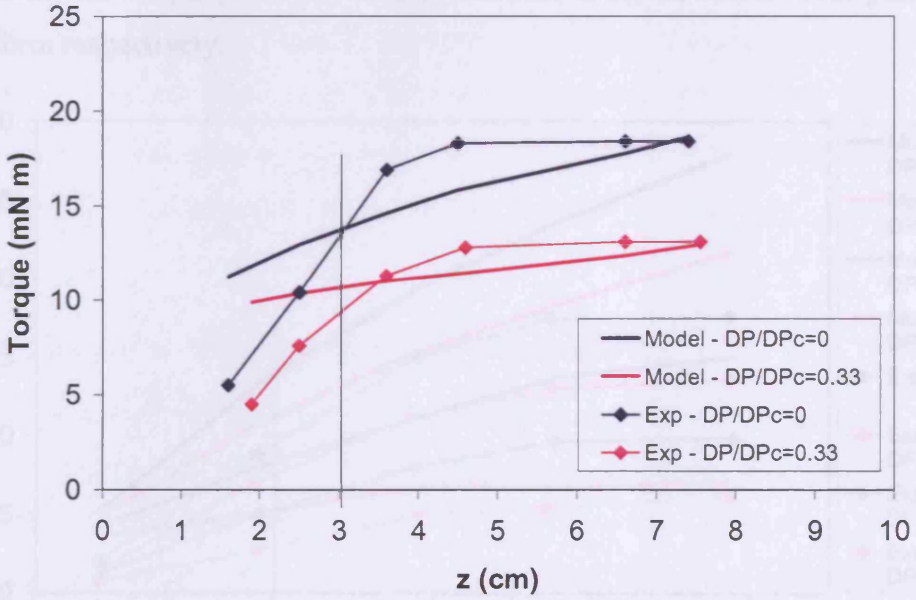

Figure 103 *Depth effect on torque – Alumina A5*

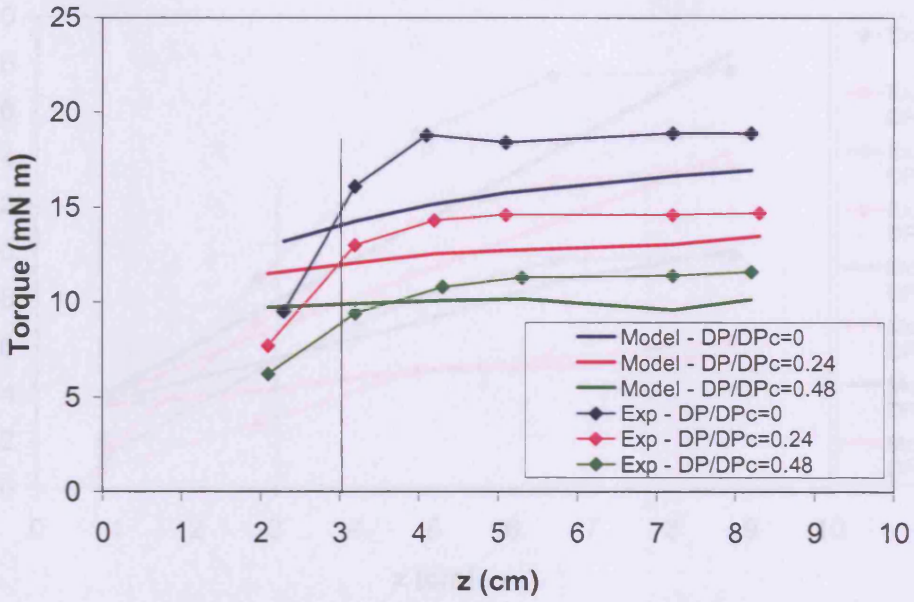

Figure 104 *Depth effect on torque – Alumina A6*

Figure 105 and Figure 106 show trends of the torque with increasing impeller depth for the ballotini sample at various rates of aeration, using the model in the passive and active form respectively.

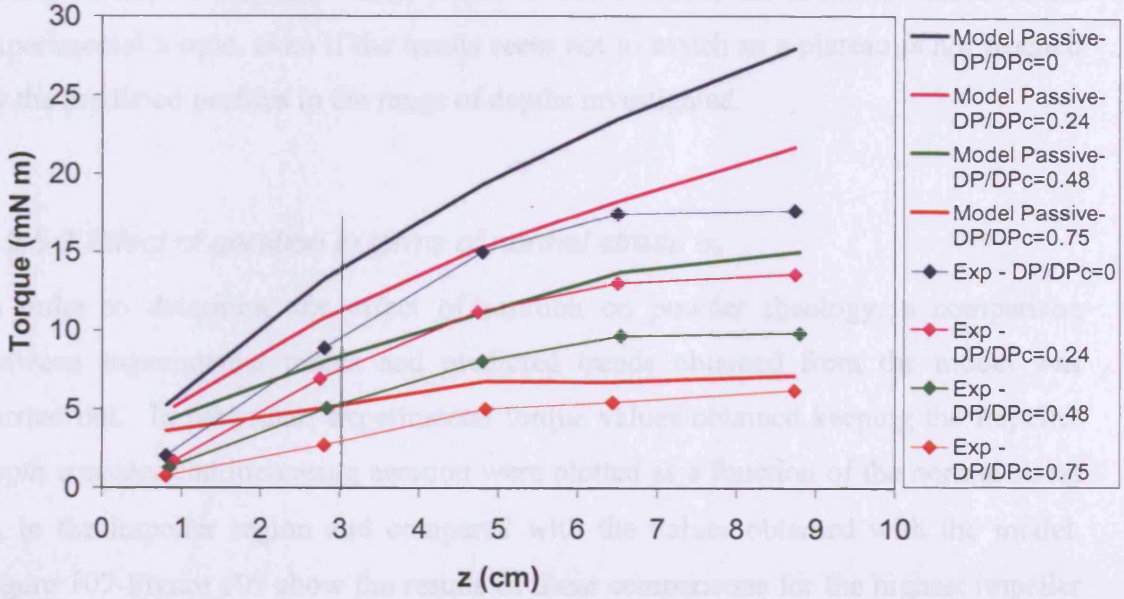

Figure 105 *Depth effect on torque – Ballotini (passive model)*

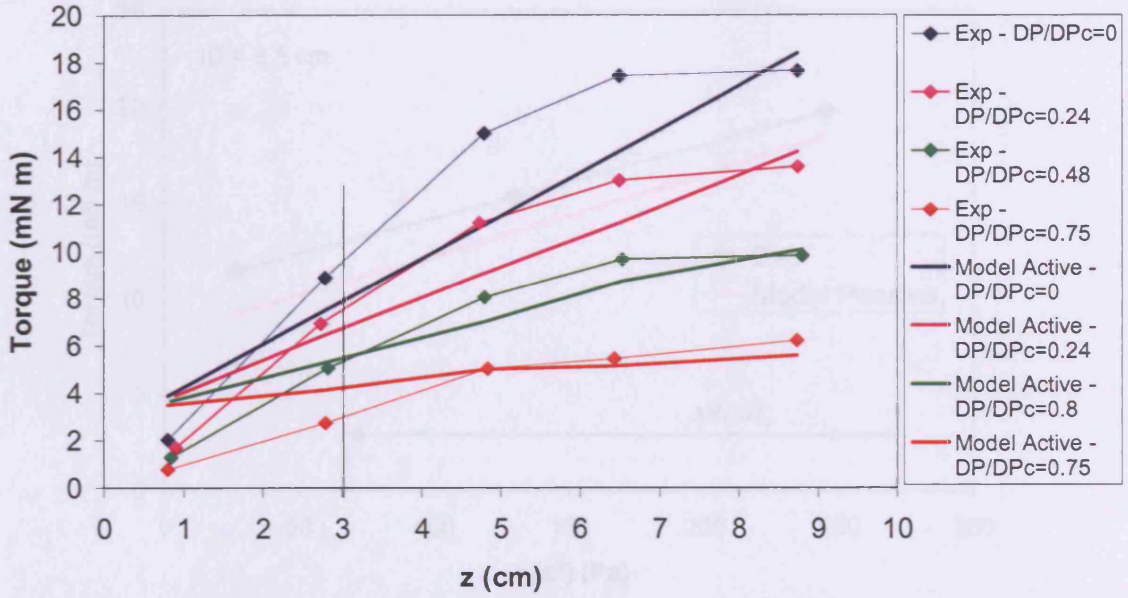

Figure 106 *Depth effect on torque – Ballotini (active model)*

While for the alumina samples the passive model systematically underestimated the experimental values but satisfyingly matched the experimental trends with increasing depth, for the ballotini it overestimates the experimental trends (Figure 105). The active model, on the other hand, seems to better match the absolute values of the experimental torque, even if the trends seem not to match as a plateau is not reached by the predicted profiles in the range of depths investigated.

5.2.5.3 Effect of aeration in terms of normal stress σ_z

In order to determine the effect of aeration on powder rheology, a comparison between experimental trends and predicted trends obtained from the model was carried out. In particular, experimental torque values obtained keeping the impeller depth constant and increasing aeration were plotted as a function of the normal stress σ_z in the impeller region and compared with the values obtained with the model. Figure 107-Figure 109 show the results of these comparisons for the highest impeller depths investigated for each powder, which were 8.5 cm for A0, 7.5 cm for A5 and 8.2 cm for A6. Similar results were obtained for every other depth analysed and are reported in Appendix 1, Tables A1.11-A1.14.

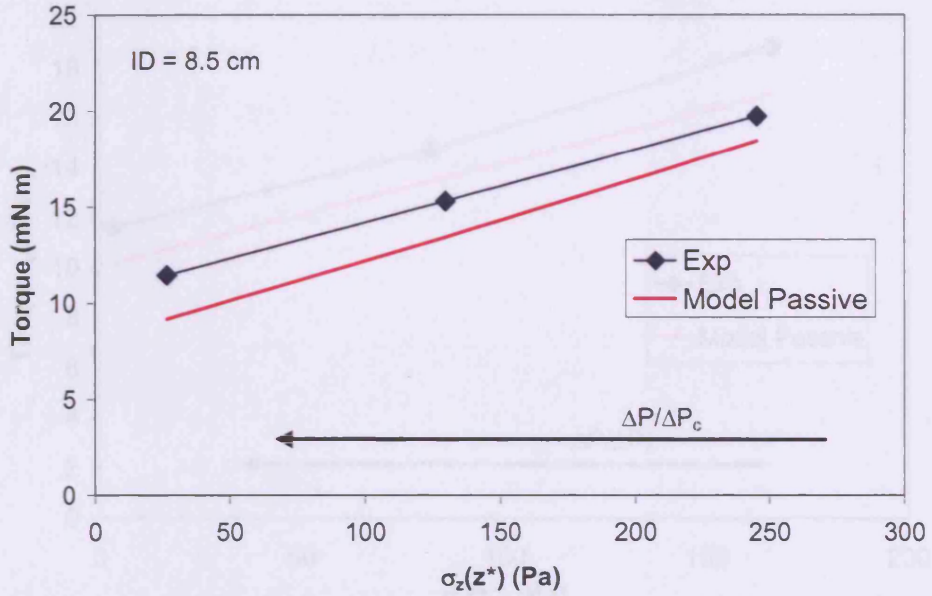

Figure 107 *Effect of aeration in terms of the normal stress* σ_z *(*$0<\Delta P/\Delta P_c<0.47$*) - Alumina A0*

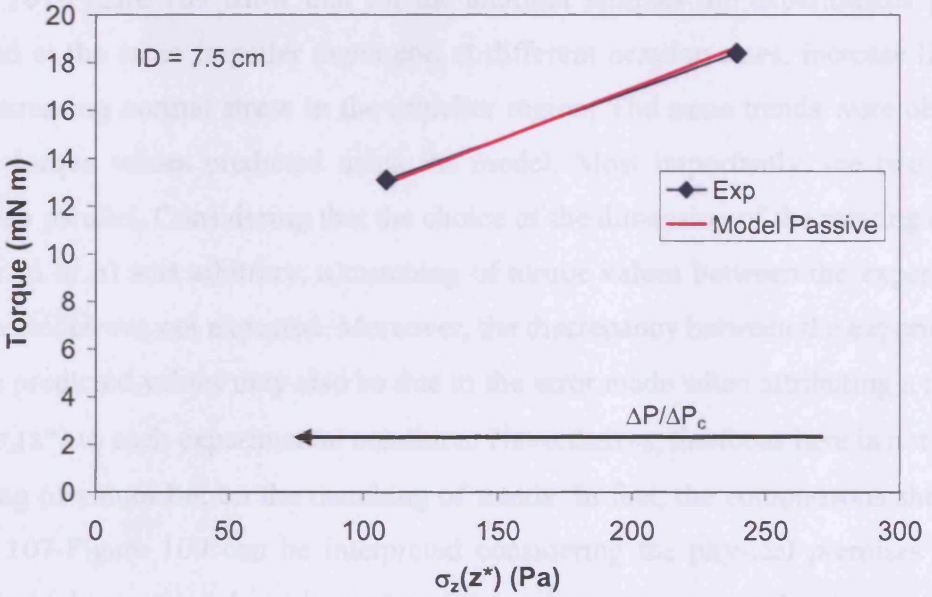

Figure 108 *Effect of aeration in terms of the normal stress* σ_z *(*$0<\Delta P/\Delta P_c<0.33$*) - Alumina A5*

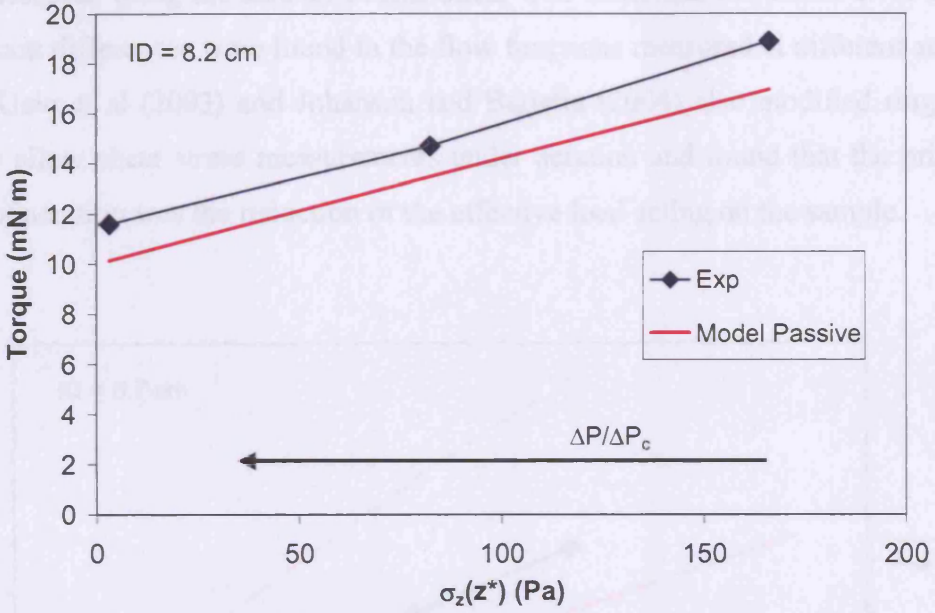

Figure 109 *Effect of aeration in terms of the normal stress σ_z ($0<\Delta P/\Delta P_c<0.48$) - Alumina A6*

Figure 107-Figure 109 show that for the alumina samples the experimental points, obtained at the same impeller depth and at different aeration rates, increase linearly with increasing normal stress in the impeller region. The same trends were obtained for the torque values predicted using the model. Most importantly, the two trends were also parallel. Considering that the choice of the dimension of the rotating disc of powder (d or h) was arbitrary, a matching of torque values between the experiments and the model was not expected. Moreover, the discrepancy between the experimental and the predicted values may also be due to the error made when attributing a normal stress $\sigma_z(z^*)$ to each experimental condition. Nevertheless, the focus here is not on the matching of values but on the matching of trends. In fact, the comparisons shown in Figure 107-Figure 109 can be interpreted considering the physical premises of the model, which, as pointed out in section 5.2.4, takes into account the changes due to aeration only in terms of changes in the stress distribution and not in terms of changes of bed rheology. Therefore, the fact that the experimental values of the torque have the same trends with increasing aeration as the model implies that aeration is not changing the rheological properties of the powder, but instead it is just changing the tensional state under which the measurements were taken. This result is in agreement with the work of Barletta et al. (2004) where the flow properties of an FCC catalyst

were measured using the aerated Peschl Shear Cell described in section 3.7.1 and no significant differences were found in the flow functions measured at different aeration rates. Klein et al (2003) and Johanson and Barletta (2004) also modified ring shear cells to allow shear stress measurements under aeration and found that the principal effect of aeration was the reduction of the effective load acting on the sample.

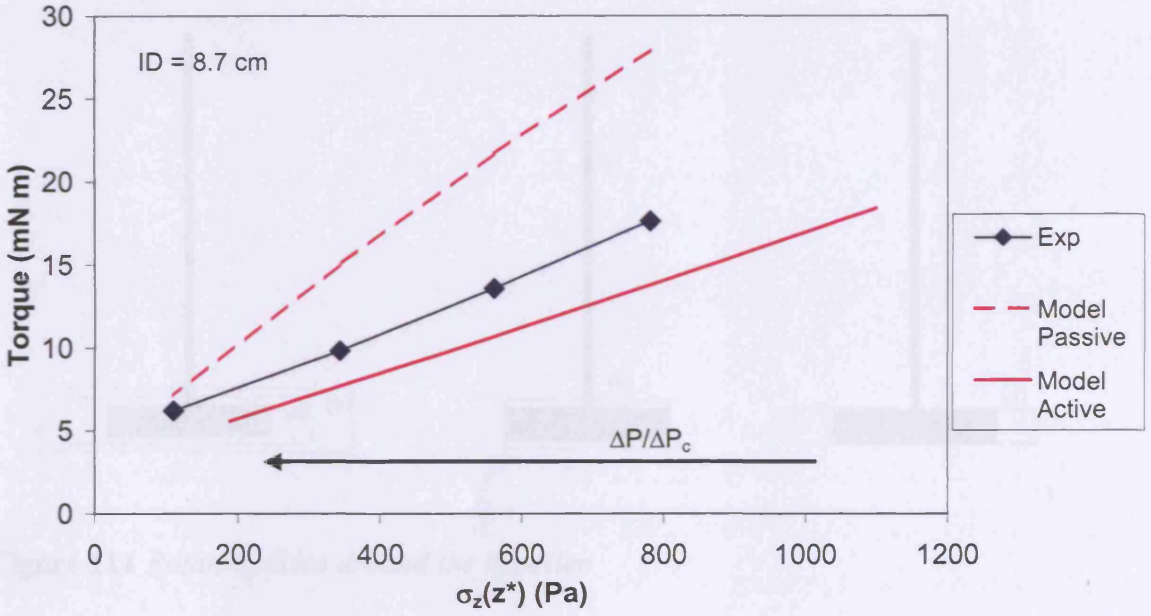

Figure 110 *Effect of aeration in terms of σ_z ($0<\Delta P/\Delta P_c<0.75$) - Ballotini*

Figure 110 shows that for the ballotini the same interpretation on the effect of aeration on the bed rheology as that given for the alumina samples can be reached if the active tensional state is used in the model.

5.2.5.4 Model sensitivity analysis

The values of the torque predicted by the model and reported in Figure 100-Figure 110 depend on a number of parameters. The values of the failure properties (φ, C, δ, C_δ, φ_w, A) determined with the shear cell and the assumptions made for the shape and the dimensions of the rotating powder can all affect the value of the predicted torque. In this study we assumed that the mass of rotating powder has a cylindrical shape (disc) and that the dimensions of the rotating disc are proportional to the dimensions of the impeller (Equation 45). In particular, we assumed that $d=d_i=3.6$ cm and

$d/h=d_i/h_i=5.14$. In this section a sensitivity analysis is reported in which the assumptions made on d and d/h are in turn changed. The effects of changing the values of d and d/h on the values of the torque predicted for the alumina powders (passive model) are reported in Table 20. Figure 111 provides a qualitative visualisation of the rotating discs corresponding to the four cases analysed in Table 20.

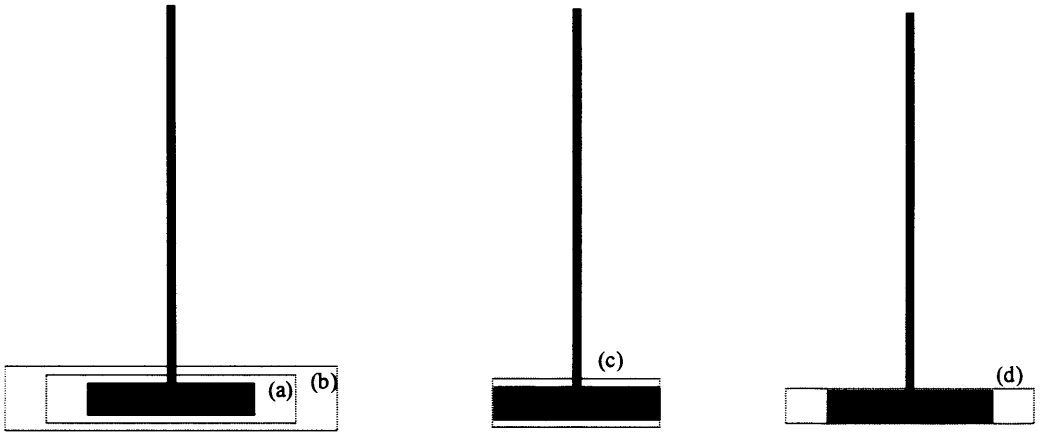

Figure 111 *Rotating discs around the impeller*

The value of the diameter of the disc d was increased by 5% and 10% with respect to the impeller diameter d_i keeping the same ratio $d/h=d_i/h_i=5.14$, case (a) and (b). Then, the value of the ratio d/h was decreased by -5% (taller disc) keeping the same diameter $d=d_i=3.6$ cm, case (c). Finally, the value of the ratio d/h was increased by +5% (larger disc) keeping the same height $h=h_i=0.7$ cm, case (d). Changes in the predicted torque were evaluated with respect to the predicted torque corresponding to $d=d_i$ and $h=h_i$.

The percentage torque changes were the same for all the alumina powders. Table 20 shows that the predicted torque values are very sensitive to the diameter chosen for the disc and less to its height. In particular, cases (a) and (d) show that an increase of 5% in the diameter d caused an increase of 12% or 15% in the value of the torque, when keeping the same ratio d/h or the same h respectively. On the other hand, when the shape of the disc was changed decreasing the ratio d/h by –5% and keeping the same diameter d_i, i.e. assuming a taller disc, the predicted values of the torque were only 3.4% higher.

Table 20 *Torque changes with changing d and d/h – Passive model*

	(a)	(b)	(c)	(d)
	d = 3.78 cm (+5%) h = 0.735 cm (+5%) d/h = d_i/h_i = 5.14 (-)	d = 3.96 cm (+10%) h = 0.770 cm (+10%) d/h = d_i/h_i = 5.14 (-)	d = d_i = 3.6 cm (-) h = 0.738 cm (+5.2%) d/h = 4.88 (-5%)	d = 3.78 cm (+5%) h = h_i = 0.7 cm (-) d/h = 5.40 (+5%)
T %change	+ 15.8	+ 33.1	+3.4	+12.2

Figure 112-Figure 117 show the comparison between the experimental torque data and the predicted values when changing d and d/h for the three alumina samples A0, A5 and A6. Figure 112-Figure 114 show that a diameter in the range of the impeller diameter, 3.6-3.8 cm, can predict reasonably well the experimental values of the torque measured for the alumina samples with the msFBR.

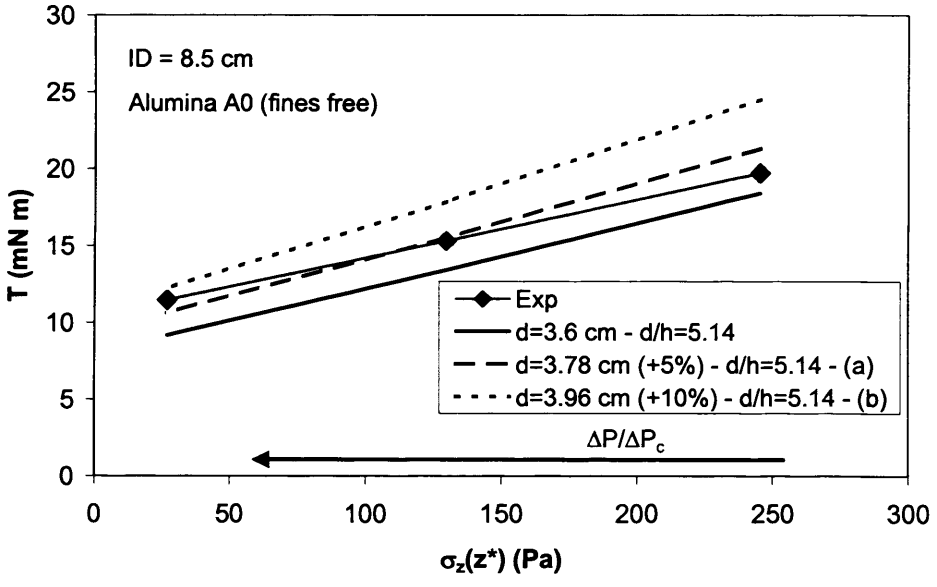

Figure 112 *Effect of disc diameter d on predicted torque – Alumina A0*

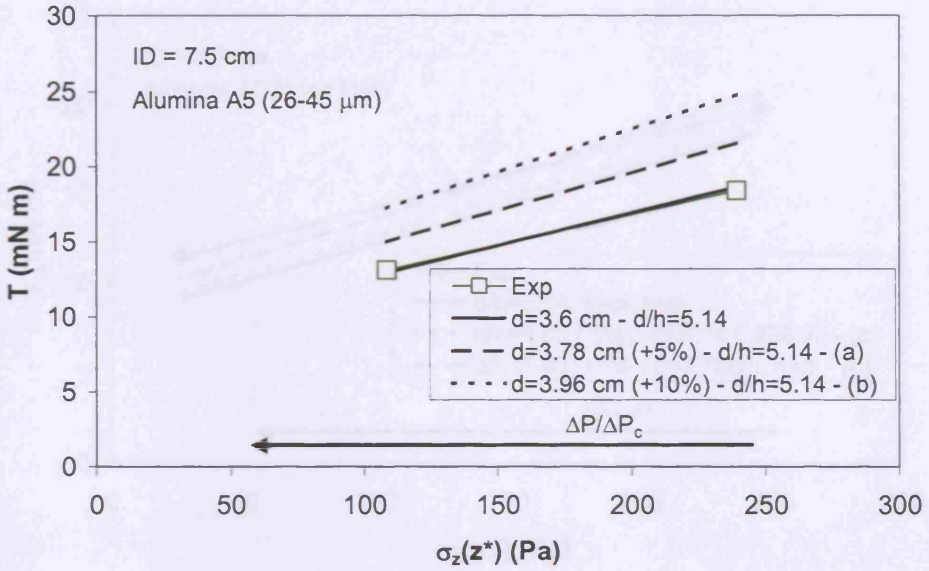

Figure 113 *Effect of disc diameter d on predicted torque – Alumina A5*

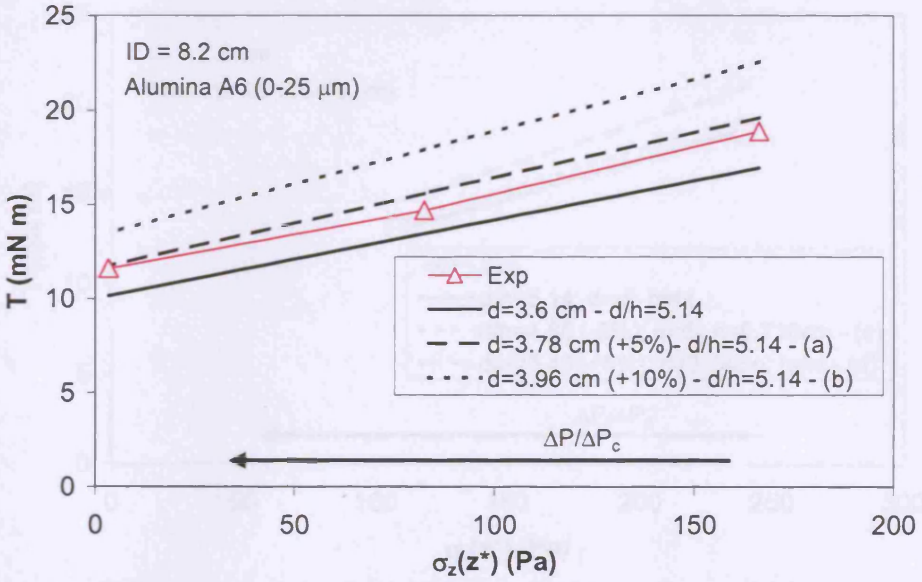

Figure 114 *Effect of disc diameter d on predicted torque – Alumina A6*

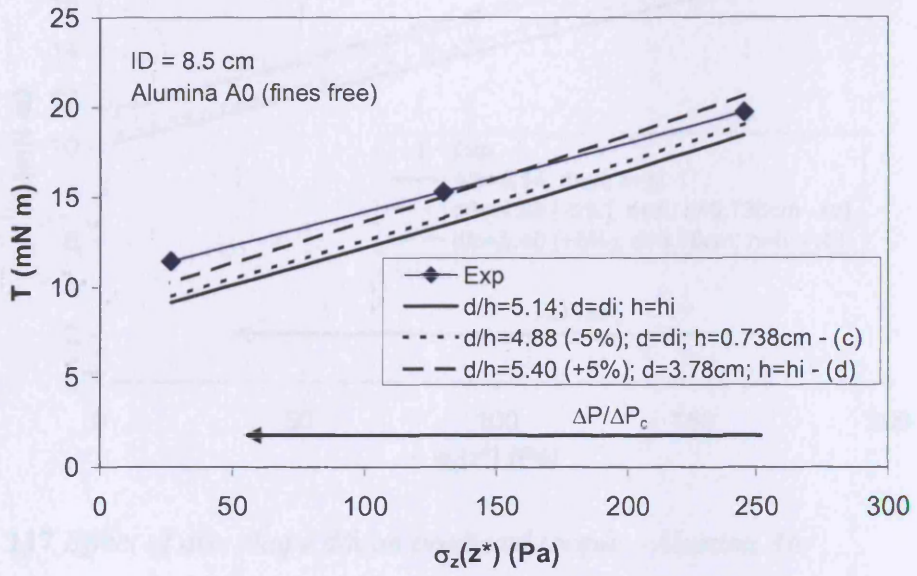

Figure 115 *Effect of disc shape d/h on predicted torque – Alumina A0*

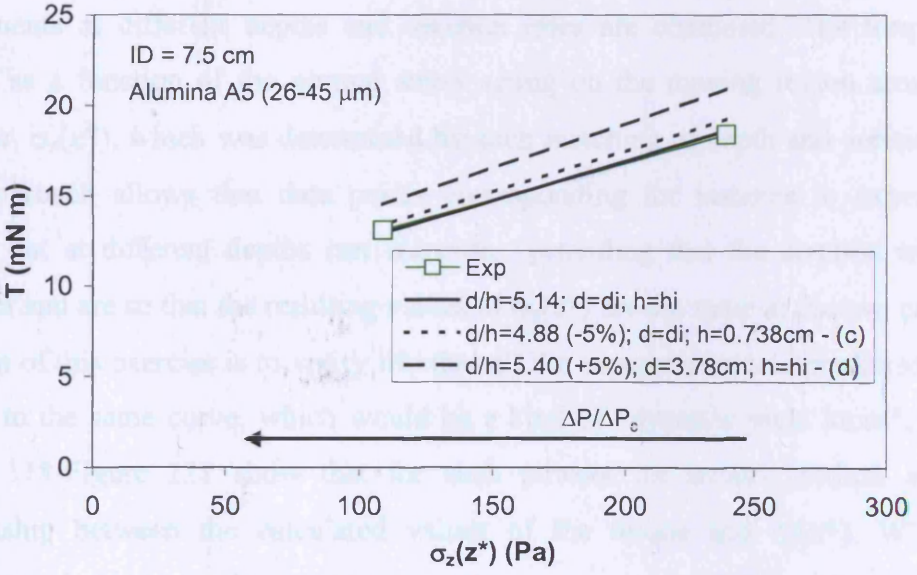

Figure 116 *Effect of disc shape d/h on predicted torque – Alumina A5*

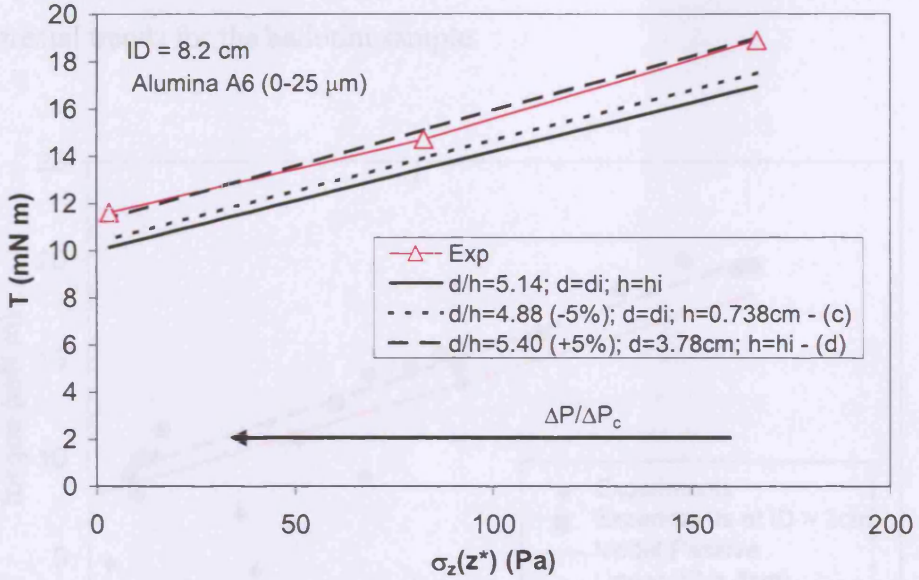

Figure 117 *Effect of disc shape d/h on predicted torque – Alumina A6*

5.2.5.5 Torque versus normal stress σ_z

So far, the effect of changing the impeller depth and the effect of changing the aeration rate on the torque have been investigated separately. In this section, all the experiments at different depths and aeration rates are combined. The torque was plotted as a function of the normal stress acting on the moving region around the impeller, $\sigma_z(z^*)$, which was determined by each matching of depth and aeration rate. This approach allows that data points corresponding for instance to experiments carried out at different depths can coincide, providing that the aeration rates are different and are so that the resulting values of $\sigma_z(z^*)$ are the same in the two cases.

The aim of this exercise is to verify whether all the experimental and predicted points belong to the same curve, which would be a kind of "dynamic yield locus", or not. Figure 118-Figure 121 show that for each powder the model predicts a linear relationship between the calculated values of the torque and $\sigma_z(z^*)$. When the experimental points are plotted, a large scatter between experiments and prediction is noticeable, especially at lower values of the normal stress. However, when the experimental points corresponding to impeller depths lower than 3 cm are not included a linear trend was obtained for each powder. This line runs parallel to the

model predicted one. Once again, the active state seems to best describe the experimental trends for the ballotini sample.

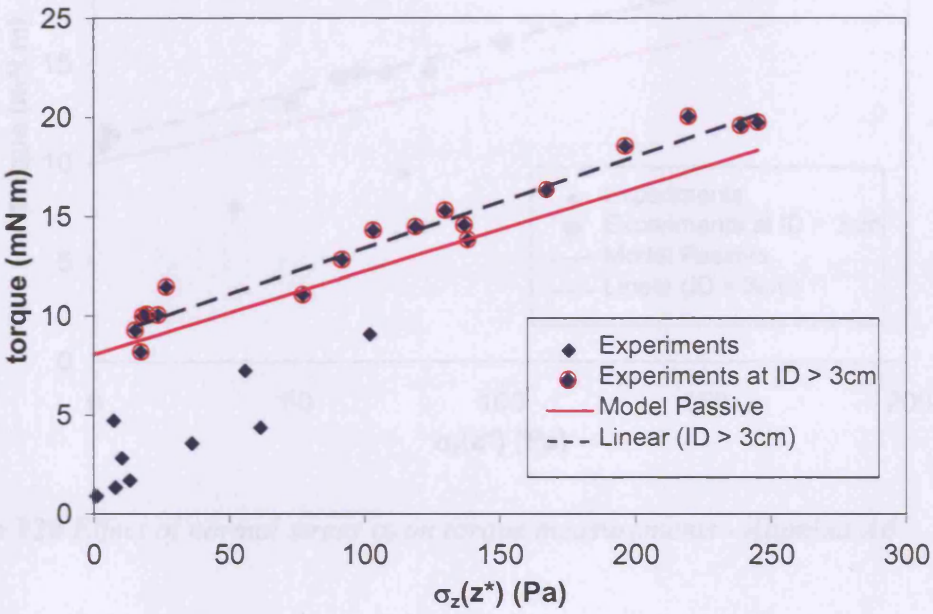

Figure 118 *Effect of normal stress σ_z on torque measurements - Alumina A0*

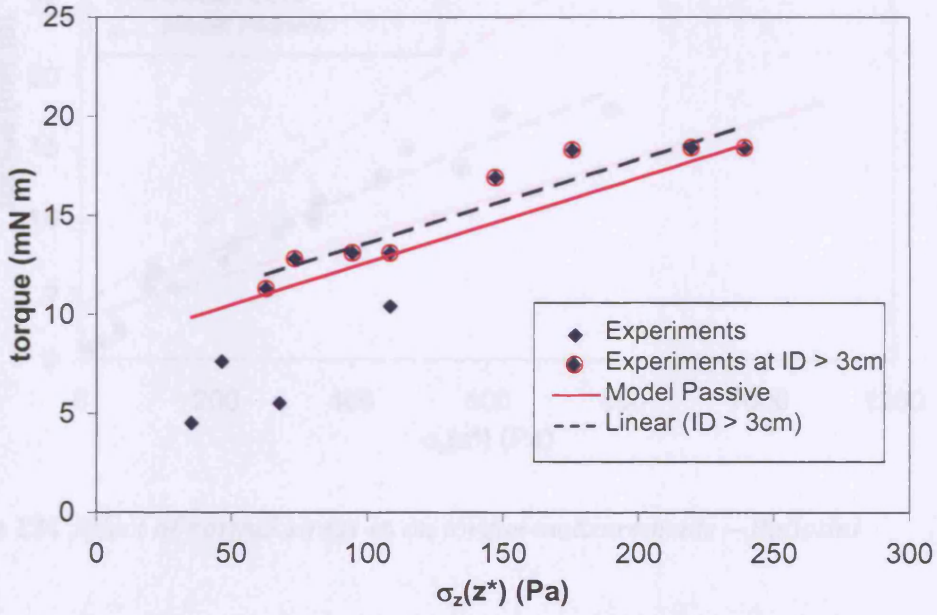

Figure 119 *Effect of normal stress σ_z on torque measurements - Alumina A5*

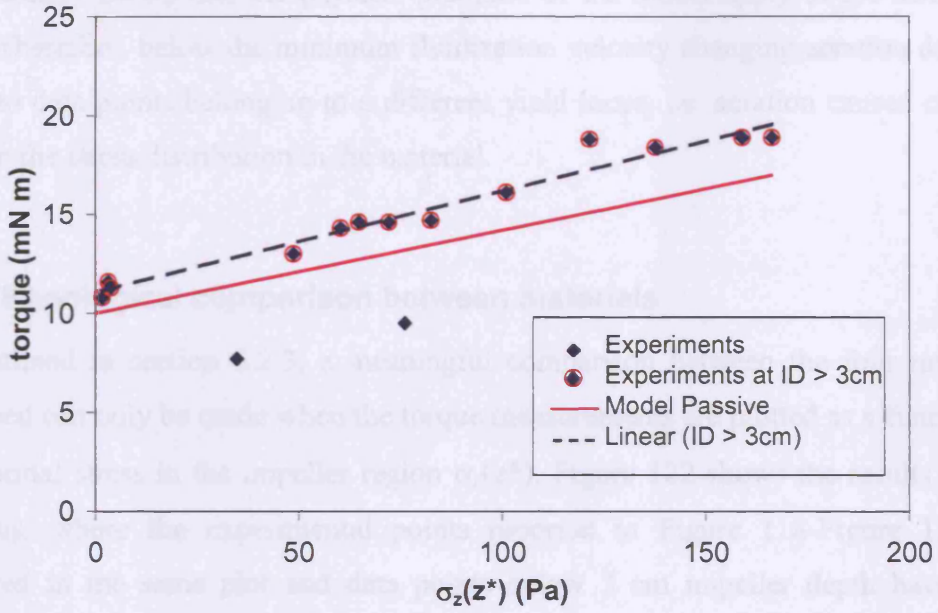

Figure 120 *Effect of normal stress σ_z on torque measurements - Alumina A6*

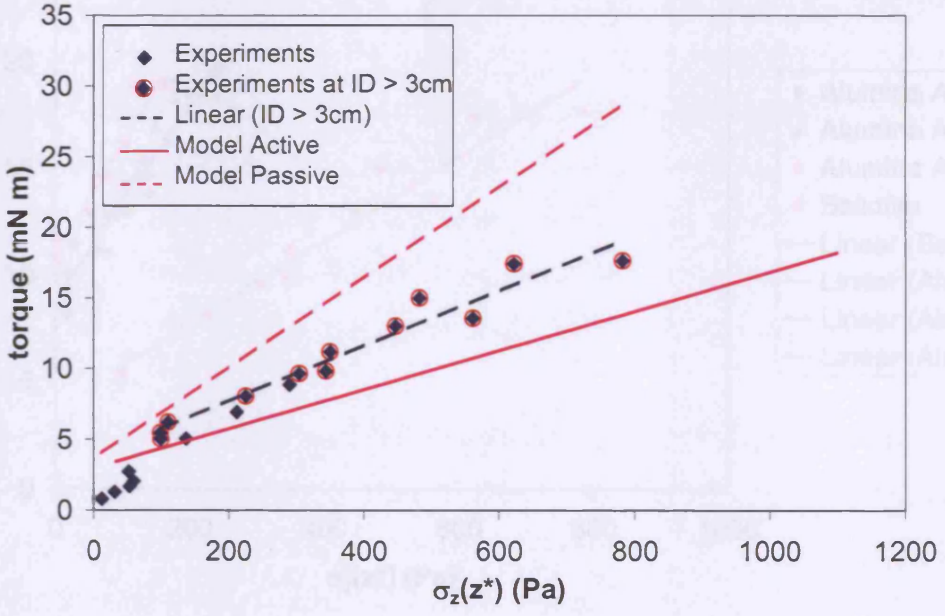

Figure 121 *Effect of normal stress σ_z on torque measurements – Ballotini*

The plots T versus $\sigma_z(z^*)$ are somehow similar to internal yield loci, if one considers the torque as a kind of shear stress integrated over the shearing surface. Therefore, the fact that all the experimental points belong to the same curve/straight line and that this is parallel to the one obtained with a model based on changes in the tensional state

only, clearly shows that the physical premises of the model apply to the msFBR as well. Therefore, below the minimum fluidization velocity changing aeration does not yield to data points belonging to a different yield locus, i.e. aeration caused changes only in the stress distribution in the material.

5.2.6 Rheological comparison between materials

As outlined in section 5.2.3, a meaningful comparison between the four materials analysed can only be made when the torque measurements are plotted as a function of the normal stress in the impeller region $\sigma_z(z^*)$. Figure 122 shows the results of this analysis, where the experimental points reported in Figure 118-Figure 121 are gathered in the same plot and data points below 3 cm impeller depth have been removed.

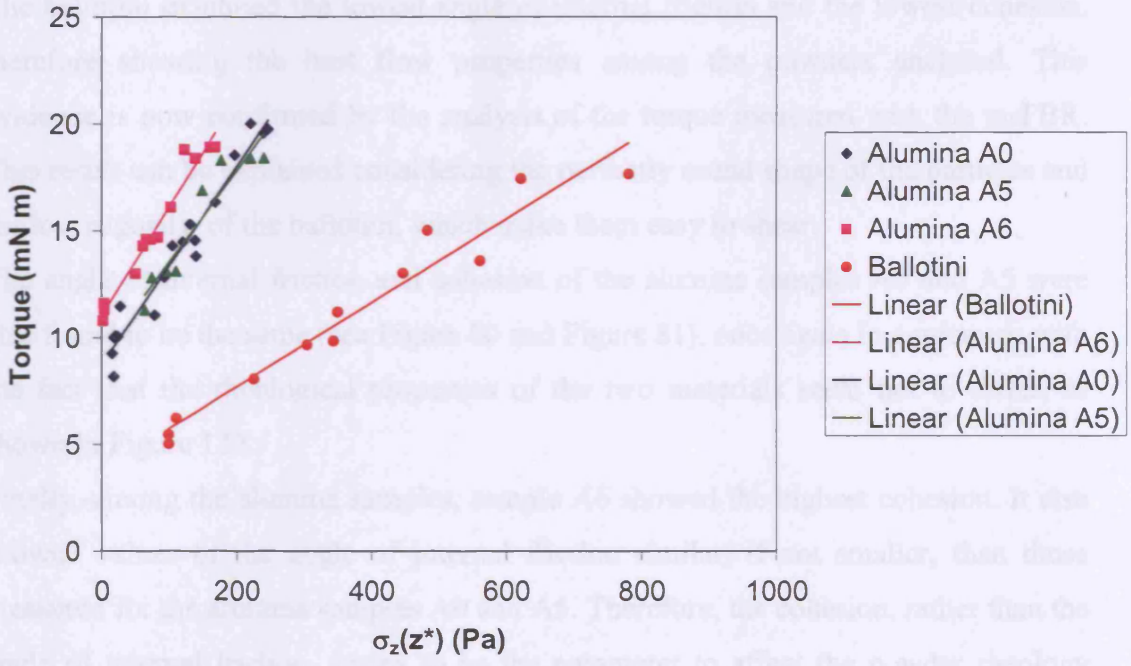

Figure 122 *Effect of σ_z on torque measurements - All materials*

If we look at the plots T vs $\sigma_z(z^*)$ as a kind of yield loci, it is clear from Figure 122 that the ballotini sample has a rheological behaviour very different from the alumina samples. Under the same stress distribution the torque needed to stir the ballotini is much smaller than the torque needed to stir the alumina samples. This result was not

at all obvious when looking at Figure 86 -Figure 89 as pointed out in section 5.2.3, and highlights the importance of determining the stress distribution in any measurement carried out below the minimum fluidization.

When we look at comparing the rheological behaviour of the three alumina samples, no significant difference can be noted between the alumina sample A0, the virtually fines free sample, and the alumina sample A5, the sample containing the bigger fines. However, the smaller fines contained in A6 cause a significant change in the rheological behaviour. In particular, under the same stress distribution the torque needed to stir the alumina sample A6 is higher than the torque needed to stir the virtually fines free powder A0 and sample A5.

These results are in line with the measurements of the failure properties found with the Peschl Shear Cell, discussed in section 5.1.
The ballotini exhibited the lowest angle of internal friction and the lowest cohesion, therefore showing the best flow properties among the powders analysed. This evidence is now confirmed by the analysis of the torque measured with the msFBR. This result can be explained considering the perfectly round shape of the particles and the low rugosity of the ballotini, which make them easy to shear.
The angle of internal friction and cohesion of the alumina samples A0 and A5 were also found to be the same (see Figure 80 and Figure 81), once again in agreement with the fact that the rheological properties of the two materials seem not to differ, as shown in Figure 122.
Finally, among the alumina samples, sample A6 showed the highest cohesion. It also showed values of the angle of internal friction similar, if not smaller, than those measured for the alumina samples A0 and A5. Therefore, the cohesion, rather than the angle of internal friction, seems to be the parameter to affect the powder rheology when smaller fines are present.

5.2.7 Effect of impeller depth on torque measurements at u_{mf}

A set of experiments, some of which reported in section 3.6.3, was carried out at the minimum fluidization conditions on the alumina sample A0 and on the ballotini sample to look into the dependence of the torque measurements on the impeller speed

at and above u_{mf}. Although these experiments are not related to the assessment of the effect of process conditions on fluidization, as they were performed only on one of the alumina samples, they add some useful insight into the model developed in section 5.2.4 to predict the torque measured using the msFBR.

Given the dependence of the measured torque at u_{mf} upon the impeller speed, a direct comparison between experiments carried out at different impeller depths was not straightforward. To this end, in this section an averaged value of the torques measured at different impeller speeds was taken for each impeller depth. It is worth emphasizing that the values of the torque measured at minimum fluidization were two order of magnitude smaller than those measured below umf (see Figure 86), therefore limiting the the following analysis to a qualitative study of the trends of the torque with increasing impeller depth.

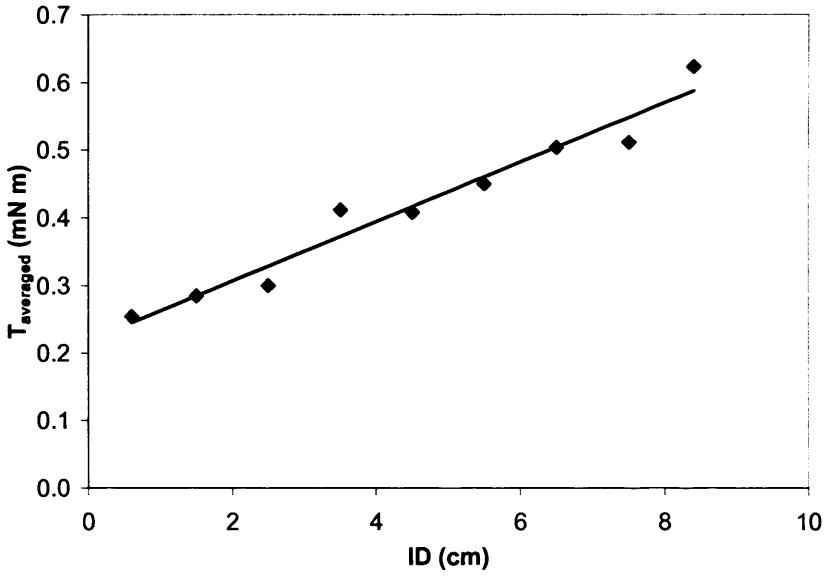

Figure 123 *Effect of impeller depth on averaged torque - Alumina A0; $\Delta P/\Delta P_c = 1$*

Figure 123 and Figure 124 show the results of this analysis for the alumina sample A0 and the ballotini respectively. Interestingly, no plateau was recorded for any of the powders at high values of the impeller depth, unlike the experiments below the minimum fluidization shown in Figure 86-Figure 89. This result can be interpreted once again as a sign that a change to liquid-like behaviour occur when full bed support is attained. In fact the linear trends seem to be reflecting the hydrostatic

conditions established in a liquid, where the normal stress increases linearly with increasing depth, i.e. $\sigma_z(z) = \rho_p(1-\varepsilon_{mf})gz$. However, further work is needed to develop a model to describe the tensional state of the powder when fluidization is attained. Appendix 4 reports an ongoing work in which flow curves for powders A0 and the ballotini were obtained using an analogy with mixing of non-Newtonian fluids.

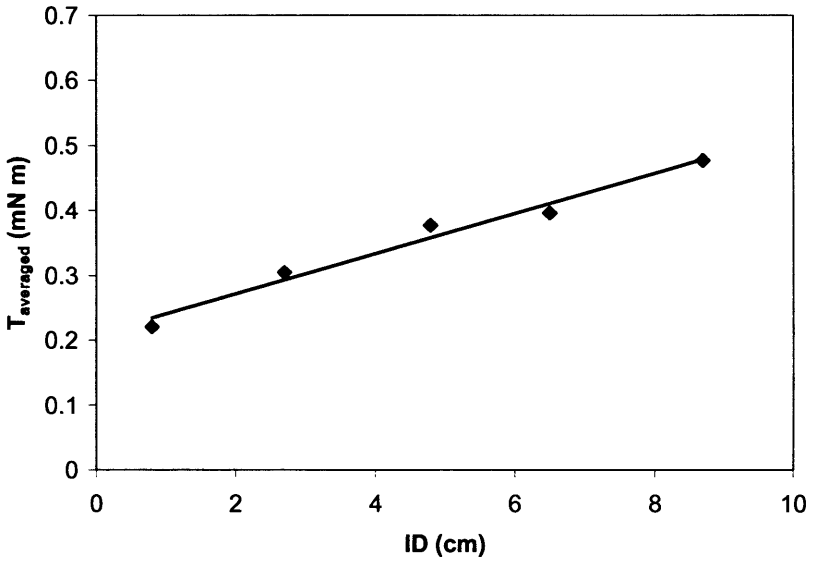

Figure 124 *Effect of impeller depth on averaged torque - Ballotini; $\Delta P/\Delta P_c$ = 1*

5.2.8 Summary of the rheological measurements using the msFBR

In section 5.2 the importance of determining the stress distribution corresponding to any torque measurement carried out with the msFBR below minimum fluidization was highlighted and the issue was addressed. The knowledge of the stress distribution led to the following findings:

Effect of changing the fines size distribution on the rheological behaviour

- significant differences in the rheological behaviour of the alumina sample A6, containing small fines, and that of sample A5, containing the same amount of big fines, were observed. However, sample A5 showed the same rheological behaviour as A0, virtually fines free.

- under the same normal load the torque needed to stir the alumina sample A6 is higher than the torque needed to stir sample A5 and A0. In other words, the presence of small fines increases the powder's resistance to flow. This results is in agreement with the results on the failure properties reported in section 5.1.
- under the same stress distribution the torque needed to stir the ballotini sample, a reference "free flowing" material, is much smaller than the torque needed to stir the alumina samples, thus confirming the results reported above.

Effect of changing aeration on the rheological behaviour

- for all the powders increasing aeration caused no changes to the bed rheology, interpreted as the relationship between the measured torque and σ_z at the impeller depth, but only changes to the stress distribution in the material.

The stress distribution corresponding to each aeration rate was determined by means of a model based on the failure properties of the material. A model to predict the values of the torque measured with the msFBR was also developed and produced a good matching with the experimental results.

Sections 5.1 and 5.2 showed some interesting features of the rheological behaviour of the alumina samples differing in fines content and in fines size distribution and highlighted possible links between the rheological and the fluidization behaviour of these powders. These links are discussed in chapter 6.

6 Link between fluidization and rheological results

Chapter 4 showed that the size distribution of the fines fractions affects significantly the fluidization behaviour of the powders investigated. In particular, significant differences were observed in the fluidization behaviour of powders containing the same amount of small fines (0-25μm), A3 and A5, or big fines (26-45μm), A4 and A6. These differences were enhanced when the total fines content was increased from 22%wt (A3 and A4) to 30%wt (A5 and A6).

A significant overshooting in the pressure drop profiles was observed for all powders and was higher for the powders containing 30%wt fines, indicating an increasing resistance to flow opposed by the bed plausibly due to a combined effect of an increase in the wall friction and in the IPFs introduced with fines addition.

In this framework, bed rheology was identified to be a useful tool to quantify the effects on fluidization of the IPFs introduced when adding small or big fines. In particular, the investigation of the failure properties of the material, which relate the capability of powders to fail, and hence flow, to the load put on them, was utilised to link changes observed in the rheological and the fluidization behaviour when changing the fines size distribution.

Chapter 5 highlighted significant differences in the rheological behaviour of the alumina sample A6, containing small fines (0-25 μm), and that of sample A5, containing the same amount of big fines (26-45 μm). Moreover, sample A5 showed the same rheological behaviour as A0, virtually fines free. Under the same normal load the torque needed to stir the alumina sample A6 is higher than the torque needed to stir sample A5 and A0. In other words, the presence of small fines increases the

powder's resistance to flow. This result was found to be in agreement with the results obtained from the failure properties of the materials measured with a shear cell.

In this chapter links between the fluidization behaviour observed for samples A5 and A6 and their rheological behaviour are outlined and discussed. Table 21 reports the main parameters analysed in this section.

Table 21 *Fluidization and rheological parameters at ambient temperature*

	A5 (26-45μm)	**A6 (0-25μm)**
FLUIDIZATION PARAMETERS		
ε_s	0.476	0.438
ε_{mf}	0.474	0.441
microchanneling	lower	higher
Maximum bed expansion	27%	43%
BER (%)	18.8	39.5
SCT (s/m)	26.6	44.1
RHEOLOGICAL PARAMETERS		
T under same $\sigma_z(z^*)$	lower	higher
C (Pa)	94-128	160-188
φ_e-φ (deg)	5-21	10-25
φ_w (deg)	13.6	16.5

1. A correspondence was found between the differences in the rheological behaviour of powders A5 and A6 and the results obtained for the voidage of the settled bed and the voidage of the bed at the minimum fluidization velocity.

   The alumina sample A6, containing small fines (0-25 μm), arranged in a more compacted packing when settled and at the minimum fluidization than the alumina sample containing the same amount of big fines (26-45 μm), A5. These results are in line with the rheological finding that a higher torque is needed to stir powder A6 than powder A5 under the same load: powder A6 arranges in a more compacted structure and therefore opposes a higher resistance to fail/flow. The values of the powders cohesion C, extrapolated from the static yield locus, and of the difference

between the effective and the static angle of internal friction φ_e-φ were also significantly higher for sample A6 than for sample A5, showing that the sample containing the small fines is more cohesive and thus more difficult to make flow.

2. The bed expansions of the two powders were also affected by the rheological differences between the two powders. The sample containing small fines, A6, required more energy to fail/flow due to higher IPFs (see T under same $\sigma_z(z^*)$ in Table 21). It also exhibited a more pronounced change in slope during bed expansion, which was interpreted as a weakening of the bed structure before the onset of bubbling. This interpretation was supported by visual observation of microchannels in the bed. Microchanneling was less severe for the powder containing big fines, A5, implying a less significant role of the IPFs in the expansion mechanism for sample A5 than for sample A6

The parallel analysis of the rheological findings and the fluidization behaviour showed that the different interparticle forces introduced in the settled bed when adding small or big fines affect the capability of the powder to oppose resistance to flow. However, the addition of fines improved also the capability of the powders to expand and to retain aeration gas. This effect was enhanced when the added fines were small (0-25μm), i.e. for powder A6, as the SCT and the BER were much higher for sample A6 than for sample A5.

These results can be interpreted considering that in the bubbling regime the cohesion, exhibited by the powders in the rheological and in the low aeration tests, is overcome by the vigorous mixing caused by the bubbles and therefore the bed loses memory of the IPFs that had determined the packed structure. Thus, at ambient temperature the collapses happened without any dominant effect of the IPFs.

This behaviour was observed also when fluidizing the volcanic ashes (see Appendix 6). This powder was difficult to fluidize due to significant IPFs. However, when mechanical agitation was used to mechanically break the channels, fluidization was attained and the powder would collapse in a group A fashion.

Finally, the significant role of the IPFs highlighted by the rheological measurements at ambient temperature for powders A5 and A6 and the differences observed between

the two powders, can also help explain changes observed in the fluidization behaviour at high temperature by means of the bed collapse test.

The SCT of sample A5 and A6 was found to increase with increasing temperature, in line with the trends observed for the samples A3 and A4 containing a lower amount of fines. However, for sample A5 and A6 the increase with temperature of the SCT was not linear but levelled off at temperatures above about 300°C, as shown in Figure 69. Similarly, the BER for sample A5 and A6 was found to decrease slightly with temperature (see Figure 70) whereas it had been found to be unaffected by temperature for the samples containing 22%wt fines, A3 and A4 (Figure 67). Moreover, the decrease with temperature was greater for sample A6 than for sample A5, thus highlighting the sensitivity of this parameter to the presence of smaller fines fractions.

The results from the BCTs with increasing temperature highlighted that the effects of the IPFs on the maximum capability of the bed to aerate become more evident for the case of 30%wt fines and in particular for the powder containing the smaller fines, A6. These results find a qualitative correspondence with the rheological measurements done at ambient temperature, which exhibited a greater effect of the IPFs for the sample containing smaller fines.

In summary, several links were found between the rheological and the fluidization behaviour of the powders analysed. The rheological results obtained with the msFBR were capable of aiding the understanding of the phenomena responsible for changes in the fluidization behaviour of powders at process conditions, i.e. at high temperature and with changing the fines size distribution.

7 Conclusions

The main objective of this work was to find a link between the fluidization and the rheological behaviour of powders at process conditions (temperature and addition of different fines sub cuts). To this end, during this PhD work:

→ a new equipment, the msFBR, has been designed, developed and built to assess the rheological behaviour of the materials at ambient and with increasing temperature.

→ an experimental campaign was carried out, using the msFBR at ambient temperature, to assess the effect on the torque measurements below u_{mf} of changing the aeration and the fines size distribution of the powders.

→ a model based on the failure properties of the material was developed to determine the stress distribution in the bed. The model was also used to predict the values of the torque measured with the msFBR and produced a good matching with the experimental results.

→ changes in the fluidization behaviour when changing the fines content, the fines size distribution and the operating temperature were assessed by means of standard fluidization tests at ambient and high temperature.

→ a link between the rheological and the fluidization behaviour of the powders analysed was found.

In particular, the multidisciplinary rheology/fluidization approach adopted in this work led to the following conclusions:

- Fines content and fines size distribution affect significantly the fluidization behaviour of powders. In particular, the effects of the IPFs become more evident

for powders containing smaller fines than for powders containing the same amount of bigger fines.

- For both the 22%wt and the 30%wt fines content cases, temperature increased the aeratability of the powders.
  For the 20% case the SCT increased linearly with temperature whereas the BER remained constant. For the 30%wt case, the SCT reached a maximum value at about 300°C with the BER decreasing with temperature, thus showing an increased effect of the IPFs at high temperature when increasing the fines content.

- The theoretical model developed to determine the stress distribution in the bed allowed to discriminate between the rheological behaviour of powders having different fines size distribution.

- The rheological results obtained with the msFBR were capable of providing an insight into the phenomena responsible for changes in the fluidization behaviour of powders at process conditions.

7.1 Recommendations for further work

The experimental campaign and the theoretical effort carried out in this work highlighted the existence of a relationship between the fluidization behaviour of powders and their rheological behaviour, interpreted as the capability of the powder to fail, hence flow. However, the analysis was limited to measurements carried out below the minimum fluidization conditions. Further work is envisaged to extend the rheological analysis to gas velocities above the minimum fluidization conditions also to further investigate the concept of fluid bed viscosity. A possible avenue to look into this concept is described in Appendix A4.

The fluidization tests showed that temperature can have a significant effect on the IPFs and that this influence is different for powders having a different fines content and fines size distribution. It would be therefore interesting to carry out rheological experiments at high temperature to quantify these effects. To this end, the alternative

agitating system developed for the msFBR and designed to run at temperatures up to 300°C, described in Appendix A3, could be employed.

Given the success of the msFBR technique to detect rheological differences due to the IPFs caused by fines particles, the technique could be used to look at the effects on fluidization of IPFs of different nature. Several works reported in literature showed that the IPFs caused by the presence of liquid can greatly influence fluidization and highlighted the need for a multidisciplinary fluidization/rheological work. In this regard, rheological measurements at high temperature would be ideal to couple the effect of temperature and presence of liquid. Ultimately, a systematic study of the simultaneous effects of fines addition, presence of liquid and temperature will provide a complete picture of fluidization at realistic process conditions.

The study of the effects on fluidization of changing the fines content showed that the IPFs introduced when adding fines play a double beneficial/detrimental role on fluidization. Therefore, further work is needed to quantify the effects of the IPFs when systematically increasing the fines content. To this end, the rheological approach used in this work to investigate the effects of changing the fines size distribution could be used to look into the effects of changing the total fines content.

The rheological study carried out in this work showed that aeration does not change the rheological behaviour of powders below the minimum fluidization conditions. This finding is particularly relevant for studies concerning hopper discharge. Further work could exploit the msFBR for these purposes.

Finally, the fluidization tests carried out on the volcanic ashes, reported in Appendix 6, showed how the IPFs present in such fine materials can dramatically affect their capability to flow at high temperature. In this work rheological measurements on these materials were not carried out. A quantification of the effects of the IPFs on the rheological behaviour of volcanic materials is therefore devised. With this regard, the study of pyroclastic flows would greatly benefit from the possibility of carrying out rheological tests at high temperature, given the significant role of temperature in changing the HDFs/IPFs for these materials.

Nomenclature

a	surface separation in Hamaker theory (Å)
A_H	Hamaker constant (J)
A_{cell}	shear cell cross sectional area (m^2)
A	wall adhesion (Pa)
BER	bed expansion ratio (%)
C	cohesion (Pa)
C_δ	cohesion from dynamic yield locus (Pa)
d_p	mean particle diameter (m)
d_{sv}	surface to volume diameter (m)
d	impeller (moving) region diameter (m)
d_i	impeller diameter (m)
d_b	bubble diameter (m)
D	msFBR diameter (m)
F	adhesive force per particle contact (N)
F_a	attractive force between rigid particles (N)
F_{45}	size fraction < 45 μm (%wt)
Ga	Galileo number
H_r	material hardness ($N\ m^{-2}$)
H_{mf}	bed height at minimum fluidization (m)
H_{mb}	bed height at minimum bubbling (m)
H_{bed}	bed height from X-ray images (m)
$H_{midline}$	height of midline in X-ray images (m)
H	bed height (m)
H_f	bed height at beginning of collapse (m)
H_d	dense phase height (m)
H_b	height of bed at t_b in collapse (m)
H_c	height of bed before solids consolidation in collapse (m)

H_s	settled bed height (m)
h	height of moving region in msFBR (m)
h_i	impeller height (m)
ID	impeller depth (m)
k	active/passive constant (-)
M	weight of bed material (kg)
N	impeller speed (rpm)
N_i	normal load in shearing phase i (kg)
N_c	nomal consolidation load (kg)
n	Richardson and Zaki index (-)
n*	experimental Richardson and Zaki index (-)
Re_{mf}	Reynolds number at minimum fluidization (-)
Re_t	particle terminal Reynolds number (-)
Re_b	bubble Reynolds number (-)
SCT	standardised collapse time (s/m)
t_o	time t=0 in bed collapse test (s)
t_b	bubble escape time in collapse (t)
t_s	collapse time (s)
T	torque (Nm)
u	gas velocity (m/s)
u_b	bubble rise velocity (m/s)
u_{mf}	minimum fluidization velocity (m/s)
u_{mb}	minimum bubbling velocity (m/s)
u_t	particle terminal velocity (m/s)
u_t*	particle terminal velocity extrapolated from R-Z profiles (m/s)
U_p, U_{de}	dense phase collapse rate (m/s)
U_{de}*	calculated dense phase collapse rate using n*, u_t*(m/s)
U_{de}^1	calculated dense phase collapse rate using n, u_t(m/s)
W_p	JKR "pull-off" force (N)
XSA	fluidized bed cross sectional area (m^2)
Y	plastic deformation (Pa)
z*	depth of top surface of moving region in msFBR (m)
z_i	impeller depth (m)
P	msFBR perimeter (m)

Greek symbols

γ	surface free energy (J m^{-2})
Γ	adhesion energy (J m^{-2})
δ	dynamic angle of internal friction (deg)
ΔP	pressure drop across the bed (Pa)
ΔP_c	calculated pressure drop when full support is achieved (Pa)
ΔP_m	measured pressure drop (Pa)
ε	bed voidage (-)
ε_{mf}	bed voidage at minimum fluidization (-)
ε_s	bed voidage of the settled bed (-)
ε_{mb}	bed voidage at minimum bubbling (-)
ε_d	dense phase bed voidage (-)
ϑ	bubble wake angle (deg)
μ	gas viscosity (Pa s)
μ_e	dense phase viscosity (Pa s)
μ_A	apparent viscosity (Pa s)
ν_A	apparent kinematic viscosity (m^2 s^{-1})
ρ_f	gas density (kg m^{-3})
ρ_b	bulk density (kg m^{-3})
ρ_p	particle density (kg m^{-3})
ρ_{BDP}	packed bulk density (kg m^{-3})
ρ_{BDL}	loose bulk density (kg m^{-3})
$\sigma_{f,mb}$	fracture strength at minimum bubbling (Pa)
σ_i	normal stress in shearing phase i (Pa)
σ_c	normal consolidation stress (Pa)
σ_w	normal stress at the wall (Pa)
σ_z	normal stress in the z direction in stagnant region (Pa)
σ_r	normal stress in the radial direction in stagnant region (Pa)
σ'_z	normal stress in the z direction in moving region (Pa)
σ'_r	normal stress in the radial direction in moving region (Pa)
σ_1	major principal stress (Pa)

σ_2	minor principal stress (Pa)
τ	shear stress (Pa)
τ_w	wall shear stress (Pa)
ϕ	particle sphericity (-)
φ	static angle of internal friction (deg)
φ_w	angle of wall friction (deg)

References

Abrahamsen, A. R.and D. Geldart (1980) "Behaviour of gas-fluidized beds of fine powders Part II. Voidage of the dense phase in bubbling beds." *Powder Technol.*, 26: 47-55.

Anjaneyulu, P. and D. V. Khakhar (1995), "Rheology of a gas-fluidized bed", *Powder Technol.*, 83: 29-34.

Avidan, A., J. Yerushalmi (1982) "Bed expansion in high velocity fluidization" *Powder Technol.* 32: 223.

Baerns, M. (1966), "Effect of interparticle adhesive forces on fluidization of fine particles", *Ind. Eng. Chem. Fundam.*, 5(4): 508-516.

Barletta, D., G. Donsi', G. Ferrari and M. Poletto (2004) "A modified Peschl Shear Cell for shear stress measurement of powders under aeration" In *Proceedings of Partec 2004, Nuremberg, Germany* 20.

Barnes, H. A., M. F. Edwards and L. V. Woodcock (1987) "Applications of computer simulations to dense suspension rheology" *Chem. Engng. Sci.*, 42(4): 591-608.

Barreto, G. F., J.G. Yates and P. N. Rowe (1983), "The measurement of emulsion phase voidage in gas fluidized beds of fine powders", *Chem Engng Sci.* 38: 345.

Botterill, J.S.M., Y. Teoman and Y.K.R. (1982), "Effect of operating temperature on the velocity of minimum fluidization, bed voidage and general behaviour." *Powder Technol.*, 31: 101.

References

Bruni, G., A. Colafigli, P.Lettieri and T. Elson (2005) 'An investigation into the rheological behaviour of powders using a mechanically stirred Fluidized Bed Rheometer (msFBR)', *Chemical Engineering Research and Design*, 83(A11): 1311.

Calderbank, P. H. and M. B. Moo-Young (1959) "The prediction of power consumption in the agitation of Non-Newtonian fluids." *Trans. Instn. Chem. Engrs*, 37: 26-33.

Carr, R.L. (1965), "Evaluating flow properties of solids." *Chemical Engineering*, 18:163-168.

Carr, R.L. (1970), "Particle behaviour storage and flow." *British Chemical Engineering*, 15(12): 1541-1549.

Daniels, T. C. (1965), *J. Mech Eng Sci*, 4:103.

Diekman, R. and W. L. Forsythe (1953), "Laboratory predictions of flow properties of fluidized systems" *Ind Eng Chem*, 45: 1174.

Di Felice, R. (1999) "The sedimentation velocity of dilute suspensions of nearly monosized spheres" *Int. J. Multiphase Flow* 25: 559.

Di Felice, R. and R. Kehlenbeck (2000) "Sedimentation velocity of solids in finite size vessels" *Chem. Eng. Technol.* 23: 12.

Donsi', G. and L. Massimilla (1973) "Bubble-free expansion of gas fluidized beds of fine particles" *AIChE Journal*, 19(61): 1104-1110.

Druitt, T.H.(1988), "Pyroclastic density currents" In: J. Gilbert and R.S.J. Sparks, The Physics of Explosive Volcanic Eruptions, *Geological Society of London Special Publication*, 145: 145-182.

Ergun, S. (1952), "Fluid Flow Through Packed Columns." *Chem. Eng. Prog.*, 48(2): 89-94.

Fairbrother, R. (1999), "A microscopic investigation of particle-particle interactions in the presence of liquid binders in relation to the mechanisms of "wet" agglomeration processes". *Ph.D. Dissertation*, Department of Chemical Engineering, University College London.

Formisani, B., R. Girimonte and L. Mancuso (1998), "Analysis of the Fluidization Process of Particle Beds at High Temperature." *Chem. Eng. Sci.,* 39(12): 1667-1675.

Foscolo, P.U. and L.G. Gibilaro (1984), "A fully predictive criterion for the transition between particulate and aggregate fluidization" *Chem. Eng. Sci.,* 39(12):1667-1675.

Foscolo, P.U. and L. Gibilaro (1987), "Fluid dynamic stability of fluidised suspensions: the particle bed model" *Chem. Eng. Sci.*, 42(6): 1489-1500.

Freeman, R. (2000) "The flowability of powders, an empirical approach." *Proc. International Conference on Powder and Bulk Solids Handling*, London, ImechE.

Furukawa, J. and T. Ohmae (1958), "Liquidlike properties of fluidized systems", *Ind and Eng Chem,* 50(5): 821-828.

Geldart, D. (1973), "Types of fluidization." *Powder Technol.*, 7:285.

Geldart, D., N. Harnby and A. C. Y. Wong (1984), "Fluidization of cohesive powders", *Powder Technol.*, 37: 25-37.

Geldart, D. and A.C.Y. Wong (1984), "Fluidization of powders showing degrees of cohesiveness-I. Bed Expansion" *Chem. Eng. Sci.*, 39(3):607-610.

Geldart, D. and A. C. Y. Wong (1985), "Fluidization of powders showing degrees of cohesiveness-II. Experiments on rate fo de-aeration" *Chem. Eng. Sci.*, 40 (4): 653-661.

Geldart, D. (1986), "Gas Fluidization Technology" Wiley and Sons Ltd., London

Gibilaro, L., S. P. Waldram and P. U. Foscolo (1984) "A simple mechanistic description of the unsteady state expansion of liquid fluidized beds." *Chem. Eng. Sci.* 39(3): 607-610.

Godard K. M. S. and J. F. Richardson (1968) "The behaviour of bubble-free fluidised beds" *I.Chem.E Symposium Series*, 30: 126.

Grace, J. R. (1970), "The viscosity of fuidized beds" *Can J. Chem Eng*, 48: 30.

Grace, J. R. and R. Clift (1974), *Chem Engng Sci.*, 29: 327.

Grace, J. R. and G. Sun (1991), "Influence of particle size distribution on the performance of fluidized bed reactors" *Can. J. Chem. Eng.*

Griffith, A. A. (1920), "The phenomena of rupture and flow in solids" *Phil Trans Roy Soc*, 221: 163-198.

Hagyard T. and A. M. Sacerdote (1966), "Viscosity of suspensions of gas-fluidized spheres" *I & EC Fundamentals*, 5: 500.

Hamaker, H. C. (1937) "The London-van der Waals attraction between spherical particles" *Physica IV*, 10: 1059-1068.

Hartley, P. A. and G. D. Parfitt (1984), "An improved split-cell apparatus for the measurement of tensile strength of powders", *J. Phys. E: Sci. Instrum.*, 17: 347.

Hertz, H. (1882), in *Miscellaneous Papers by H. Hertz (1896) (Jones and Schott eds.)*, Macmillan, London.

Hobbel, E. F. and B. Scarlett (1985) "Measurements of the flow behaviour of aerated and fluidised powders using a rotating viscometer." *Part. Charact.*, 2: 154-159.

Irwin, J. (1957), "Analysis of stress and strains near the end of a crack traversing a plate", *Applied Mechanics*, 24: 361-364.

Israelachvili, J. (1991), "Intermolecular and surface forces", Academic Press, London.

Jackson, R.M.A. (1963), "The mechanics o fluidized beds: Part I: the stability of the state of uniform fluidization" *Trans. Instn. Chem. Engrs.*, 41: 13-21.

Janssen, H. A. (1895) "Getreidedruck in silozellen." *Z. Ver. Dt. Ing.* 39: 1045-1049.

Jean, R.H. and L.S. Fan (1992), " On the model equations of Gibilaro and Foscolo with corrected buoyancy force" *Powder Technol.*, 72: 201-205.

Jenike, A.E. (1961) "Gravity flow of bulk solids" *Buletin 108, Utah Engineering Experimental Station.*

Johanson, K. and D. Barletta (2004) "The influence of air counter-flow through powder materials as a means of reducing cohesive flow problems." To appear in *Particle & Particle Systems Characterization.*

Johnson, K.L., K. Kendall and A.D. Roberts (1971), *Proc. Roy. Soc. (London)*, A324: 301

Kai, T., A. Iwakiri and T. Takahashi (1987), *J. Chem. Eng. Japan*, 20: 282.

Kai, T., M. Murakami, K. Yamasaki and T. Takahashi (1991) "Relationship between apparent bed viscosity and fluidization quality in a fluidized bed with fine particles", *J. Chem. Eng. Japan*, 24(4): 494.

Klein, J., D. Hohne and K. Husemann (2003) "The influence of air permeation on the flow properties of bulk solids." *Chem. Eng. Technol.*, 26: 139-146.

T. M. Knowlton, T. M (1992) "Pressure and temperature effects on fluid-particle systems" in *Proceedings of the seventh engineering foundation conference on*

fluidization (Fluidization VII) Brisbane, Australia, Eds. O.E. Potter and D.J. Nicklin, p. 27-46.

Kohe G. K.,T. L. Ip, J. R. Grace (1991) "Rheological and fluidization behaviour of powders of different particle size distribution". *Powder Technol.* 66: 127-141.

Kono, H. O., S. Chiba, T. Ells and M. Suzuki (1986), "Characterization of the emulsion phase in fine particle fluidized beds", *Powder Technol.*, 48: 51-58.

Kono, H. O., E. Aksoy, Y. Itani (1994), "Measurement and application of the rheological parameters of aerated fine powders-a novel characterization approach to powder flow properties", *Powder Technol.*, 81: 177-187.

Kono, H. O., S. Narasimhan, L. M. Richman, T. Ohtake (2002), "Flow properties of homogeneously aerated, expanded emulsion phase of fine powders (quasi-solid emulsion phase viscosity)", *Powder Technol.*, 122: 168-176.

Kramers, H. (1951), "On the "viscosity" of a bed of fluidized solids", *Chem Eng Sci*, 1: 35.

Kunii, D. and O. Levenspiel (1991), "Fluidization Engineering". Butterwort-Heinmann, London.

Lettieri, P. (1999), "A study on the influence of temperature on the flow behaviour of solid materials in a gas fluidized bed." PhD Dissertation, Department of Chemical Engineering, University College London.

Lettieri, P., Newton, D. and Yates, J.G., (2001), "High temperature effects on the dense phase properties of gas fluidised beds". *Powder Technol.*, 120: 34 – 40.

Lettieri, P., S. Brandani, J. G. Yates and D. Newton (2001), "A generalization of the Foscolo and Gibilaro particle-bed model to predict the fluid bed stability of some fresh FCC catalysts at elevated temperatures", *Chem. Engng. Sci.*, 56 (18): 5401-5412.

References

Lettieri, P., D. Newton, J.G. Yates (2001) "Characterization of the fluidization behaviour of solid materials at high temperature", In *Proceedings of the 6 World Congress of Chemical Engineering, Melbourne,* Australia.

Lettieri, P., D. Newton, J. G. Yates (2002) "Homogeneous bed expansion of FCC catalysts, influence of temperature on the parameters of the Richardson–Zaki equation" *Powder Technol.* 123: 221.

Lucas, A., J. Arnaldos, J. Casal and L. Puigjaner (1986), "High temperature incipient fluidization in mono and polydisperse systems." *Chem. Eng. Comm.,* 41:121-132.

Massimilla, L., G. Donsi' and C. Zucchini (1972), "The structure of bubble-free gas fluidized beds of fine fluid cracking catalyst particles", *Chem Eng Sci*, 27: 2005-2015.

Massimilla, L., and G. Donsi' (1976), "Cohesive forces between particles of fluid-bed catalysts." *Powder Technol.*, 15(2): 253-260.

Matheson, G.L., Herbst W.A. and P.H. Holt, (1949), "Characteristics of fluid-solid systems", *Ind Eng Chem*, 41: 1099.

Mathur, A. and S.C. Saxena (1986), "Particle classification scheme of Saxena and Ghanza and high temperature bed voidage data at minimum fluidization." *Powder Technol.,* 45: 287-289.

Metzner, A. B. and R. E. Otto (1957) "Agitation of Non-Newtonian fluids." *AIChE Journal*, 3: 3-10.

Molerus, O. and M. Nywlt (1984), *Powder Technol.*, 37: 145.

Molerus, O. (1978), *Powder Technol.*, 20: 161.

Molerus, O. (1975), *Powder Technol.*, 12: 259.

References

Musters, S.M.P. and K. Rietema (1977), "The effect of interparticle forces on the expansion of a homogeneous gas-fluidized bed" *Powder Technol.*, 18: 239-248.

Naito, M., S. Usuda, N. Kato, J. Tsbaki and G. Jimbo, (1987*), Powder Technol Jpn*, 24: 455.

Nedderman, R. M. (1992) "Statics and kinematics of granular materials" Cambridge University Press, Cambridge.

Newton, D. (1984), "The influence of fine particles on the performance of a fluidised bed reactor", PhD Dissertation, Department of Chemical Engineering, University College London.

Newton, D., G. Smith and N. Hird (1999), "Comments on experimental data on the suitability of assigning a viscosity to the fluidized bed dense phase" *Unpublished paper presented at the Fifth International Conference on Fluid Particle Interactions.*

Pagliai, P. (2005), "...", *PhD Dissertation*, Department of Chemical Engineering, University College London.

Park, J. J., J. H. Park, I. S. Chang, S. D. Kim and C. S. Choi (1991), "A new bed-collapsing technique for measuring the dense phase properties of gas-fluidize beds", *Powder Technology*, 66: 249-257.

Pattipati, R. and C.Y. Wen (1981), "Minimum fluidization velocity at high temperature" *Ind. Eng. Chem. Process Des. Dev.*, 20: 705-708.

Peschl, I.A.S.Z. and H. Cloijn (1976) "New rotational shear testing technique" In *Proceedings of the Bulk Solids Handling and Processing Conference, Chicago, USA.*
Schwedes, J. (2003) "Review on testers for measuring flow properties of bulk solids" *Granular Matter* 5: 1-43.

Rapagna', S., P.U. Foscolo and L.G. Gibilaro (1994), "The influence of temperature on the quality of gas fluidization" *Int. J. Multiphase Flow*, 20(2): 305-313.

Raso, G., M. D'Amore, B. Formisani and P.G. Lignola (1992), "The influence of temperature on the properties of the particulate phase at incipient fluidization." *Powder Technol.,* 72: 71-76.

Reiling, V. G. (1992), "The effects of ultrafine particles on powder cohesion and fluidization", PhD Thesis, Case Western Reserve University.

Rietema, K., E.J.E. Cottaar and H.W. Piepers (1993), "Effect of interparticle forces on the stability of gas fluidized beds – II. Theoretical derivation of bed elasticity on the basis of van der Walls forces between powder particles." *Chem. Eng. Sci.*, 48(9): 1687-1697.

Rietema, K. (1991), "The dynamics of fine powders" *Elsevier Science Publication Ltd.*

Rietema, K. (1984), *Powder Technol.,* 37: 5.

Rietema, K. and H.W. Piepers (1990), "Effect of interparticle forces on the stability of gas-fluidized beds – I. Experimental evidence" *Chem. Eng. Sci.*, 45(6):1627-1639.

Rice W. J. and R. H. Wilhelm (1958) "Surface dynamics of fluidized beds and quality of fluidization", *AIChE Journal*, 4: 423.

Richardson, J. F., W. N. Zaki (1954) "Sedimentation and Fluidization: Part I." *Trans. Inst. Chem. Eng.* 32: 35.

Romero, J. B., L. N. Johanson (1962) "Factors affecting fluidized bed quality", *Chem. Eng. Prog. Symp. Ser.*, 58(38): 28.

Rowe, P. N., L. Santoro and J. G. Yates (1978), "The division of gas between bubble and interstitial phases in fluidised beds of fine powders", *Chem Engng Sci.*, 33: 133.

Rumpf, H. (1958), *Chem Eng Ing Tech*, 30: 144.

Santomaso, A., P. Lazzaro and P. Canu (2003), "Powder flowability and density ratios: the impact of granules packing", *Chem. Eng. Sci.*, 58(13):2857-2874.

Saxena, S.C. and V.L. Ganzha (1984), *Powder Technol.,* 39: 199.

Schugerl, K. (1971), "Rheological behaviour of fluidized systems" In Fluidization, ed. Davidson and Harrison, Academic Press, London. 261.

Seville, J.P.K., and R. Clift (1984), "The effect of thin liquid layers on fluidization characteristics." *Powder Technol.*, 37: 117-129.

Shuster, W. W. and F. C. Haas (1960), "Point viscosity measurements in a fluidized bed" *J. Chem Eng Data*, 5: 525.

Simons, S.J.R. and Fairbrother, R.J. (2000), "Direct observations of liquid binder-particle interactions: the role of wetting behaviour in agglomerate growth." *Powder Technol.*, 110: 44-58.

Sparks, R. S. J. (1976), "Grain size variations in ignimbrites and implications for the transport of pyroclastic flows" *Sedimentology*, 23: 147-188.

Sutton, H. M. and R. A. Richmond (1973), "Improving the storage conditions of fine powders by aeration" *Trans Instn Chem Engrs*, 51: 97-104.

Sutton, H. M., in Parfitt, G. D. and K. S. W. Sing, (eds) (1976) "Characterization of powder surfaces" Academic Press, London.

Tardos, G.I., S. McNamara and I. Talu (2003), "Slow and intermediate flow of a frictional bulk powder in the Couette geometry", *Powder Tech.*, 131: 23

Toomey, R. D. and H. F Johnstone (1952), *Chem Engng Prog.*, 48: 220.

References

Verloop, J. and P.M. Heertjes (1970), "Shock waves as a criterion for the transition from homogeneous to heterogeneous fluidization" *Chem Eng Sci*, 25: 825-832.

Viora, L. (1994) "Mixing of Newtonian and non-Newtonian fluids." Undergraduate Research Project, Department of Chemical and Biochemical Engineering, University College London.

Weimer, A.W and G.J. Quarderer (1985), *AIChE J.*, 31: 1019.

Wen, C.Y. and Y.H. Yu (1966), "Mechanics of fluidization" *Chem. Engng. Prog. Symp. Ser.*,62: 100-111.

Wilson, C. J. N. (1984), "The role of fluidization in the emplacement of pyroclastic flows, 2: Experimental results and their interpretation" *J. Volcanol. Geotherm. Res.*, 20: 55-84.

Xie, H.Y. and D. Geldart (1995), "Fluidization of FCC powders in the bubble-free regime: effect of types of gases and temperature" *Powder Technol.*, 82: 269-277.

Yaomin, Z. and L. Wei (2000), "Rheology of gas-solid fluidized bed" *Fuel Processing Technology*, 68: 153-160.

Yates, J. G. and D. Newton (1986), "Fine particle effects in a fluidized-bed reactor", *Chem Engng Sci.* 41: 801.

Yates, J. G (1996) "Effects of temperature and pressure on gas-solid fluidization" *Chem. Eng. Sci.*, 51(2): 167-205.

Zhao, Y. and L. Wei (2000), "Rheology of gas-solid fluidized bed", *Fuel Processing Technology*, 68: 153-160

A1 Tables of results

A1.1 Fluidization results

A1.1.1 Results from ΔP tests and expansions

Table A1.1

A0					
T (°C)	**u_{mf} (cm/s)**	**ε_{mf}**	**ε_s**	**H_s (cm)**	**$(H_{max}-H_s)/H_s$**
27	0.54	0.501	0.499	45.0	12.6
100	0.52	0.515	0.510	45.9	16.6
200	0.44	0.511	0.511	46.1	14.9
300	0.39	0.508	0.508	45.7	16.1
400	0.33	0.507	0.507	45.7	16.9
A3					
T (°C)	**u_{mf} (cm/s)**	**ε_{mf}**	**ε_s**	**H_s (cm)**	**$(H_{max}-H_s)/H_s$**
27	0.47	0.506	0.502	44.9	17.2
100	0.41	0.506	0.505	44.6	17.1
200	0.36	0.503	0.503	44.8	16.1
300	0.38	0.505	0.497	44.2	19.5
400	0.37	0.502	0.497	44.3	17.9

Table A1.1 (contd)

A4					
T (°C)	**u_{mf} (cm/s)**	**ε_{mf}**	**ε_s**	**H_s (cm)**	**$(H_{max}-H_s)/H_s$**
27	0.40	0.492	0.488	44.0	20.5
100	0.37	0.499	0.495	43.8	20.3
200	0.35	0.499	0.494	44.2	21.7
300	0.31	0.494	0.490	43.8	24.1
400	0.34	0.502	0.492	43.9	24.7
A5					
T (°C)	**u_{mf} (cm/s)**	**ε_{mf}**	**ε_s**	**H_s (cm)**	**$(H_{max}-H_s)/H_s$**
27	0.36	0.474	0.476	42.9	27.7
100	0.33	0.468	0.473	42.8	28.6
200	0.26	0.469	0.468	42.3	26.6
300	0.26	0.465	0.458	41.5	27.6
400	0.24	0.471	0.459	41.6	29.7
A6					
T (°C)	**u_{mf} (cm/s)**	**ε_{mf}**	**ε_s**	**H_s (cm)**	**$(H_{max}-H_s)/H_s$**
27	0.25	0.441	0.438	40.1	43.2
100	0.24	0.433	0.433	39.7	44.0
200	0.20	0.438	0.425	39.2	42.1
300	0.19	0.445	0.427	39.3	43.3
400	0.19	0.443	0.440	40.2	42.1

A1.1.2 Experimental and predicted u_{mf}

Table A1.2

A0				
T (°C)	**Exp. (cm/s)**	**Ergun (cm/s)**	**Baeyens (cm/s)**	**Wen & Yu (cm/s)**
27	0.54	0.54	0.40	0.32
100	0.52	0.54	0.37	0.29
200	0.44	0.47	0.34	0.26
300	0.39	0.41	0.32	0.23
400	0.33	0.38	0.30	0.22
A3				
T (°C)	**Exp. (cm/s)**	**Ergun (cm/s)**	**Baeyens (cm/s)**	**Wen & Yu (cm/s)**
27	0.47	0.47	0.23	0.17
100	0.41	0.42	0.21	0.16
200	0.36	0.37	0.19	0.14
300	0.38	0.34	0.18	0.13
400	0.37	0.31	0.17	0.12
A4				
T (°C)	**Exp. (cm/s)**	**Ergun (cm/s)**	**Baeyens (cm/s)**	**Wen & Yu (cm/s)**
27	0.40	0.40	0.139	0.100
100	0.37	0.38	0.129	0.090
200	0.35	0.34	0.118	0.080
300	0.31	0.30	0.110	0.072
400	0.34	0.29	0.104	0.067

Table A1.2 (contd)

A5				
T (°C)	**Exp. (cm/s)**	**Ergun (cm/s)**	**Baeyens (cm/s)**	**Wen & Yu (cm/s)**
27	0.36	0.36	0.19	0.14
100	0.33	0.31	0.17	0.12
200	0.26	0.28	0.16	0.11
300	0.26	0.24	0.15	0.10
400	0.24	0.24	0.14	0.09
A6				
T (°C)	**Exp. (cm/s)**	**Ergun (cm/s)**	**Baeyens (cm/s)**	**Wen & Yu (cm/s)**
27	0.25	0.25	0.102	0.070
100	0.24	0.21	0.095	0.063
200	0.20	0.20	0.087	0.056
300	0.19	0.19	0.081	0.051
400	0.19	0.17	0.076	0.047

A1.1.3 Calculated and experimental n and u_t

Table A1.3

A0						
T (°C)	**n**	**n***	**n*/n**	**u_t (cm/s)**	**u_t* (cm/s)**	**u_t*/u_t**
27	4.5	5.6	1.24	25.6	34.8	1.36
100	4.6	5.7	1.23	23.6	24.6	1.04
200	4.7	5.1	1.10	21.6	16.4	0.76
300	4.7	5.2	1.11	20.0	14.3	0.71
A3						
T (°C)	**n**	**n***	**n*/n**	**u_t (cm/s)**	**u_t* (cm/s)**	**u_t*/u_t**
27	4.7	4.8	1.02	14.5	12.3	0.85
100	4.8	4.6	0.97	13.3	9.8	0.74
200	4.8	4.5	0.93	12.0	8.2	0.68
300	4.8	4.0	0.84	11.5	6.4	0.56
400	4.8	3.6	0.75	10.6	4.4	0.42
A4						
T (°C)	**n**	**n***	**n*/n**	**u_t (cm/s)**	**u_t* (cm/s)**	**u_t*/u_t**
27	4.8	4.8	0.99	8.7	11.4	1.31
100	4.8	4.7	0.98	8.2	10.4	1.26
200	4.8	4.3	0.89	7.3	7.1	0.97
300	4.8	4.1	0.85	6.6	5.7	0.86
400	4.8	4.1	0.85	6.1	5.5	0.90

Table A1.4

A5										
T (°C)	**n**	**u_t (cm/s)**	**n* low ε**	**n*/n low ε**	**u_t* (cm/s) low ε**	**u_t*/u_t low ε**	**n* high ε**	**n*/n high ε**	**u_t* (cm/s) high ε**	**u_t*/u_t high ε**
35	4.7	11.9	3.6	0.75	5.3	0.44	7.2	1.51	43.9	3.68
100	4.8	10.8	3.3	0.68	4.0	0.37	6.0	1.26	21.5	2.00
200	4.8	10.1	3.2	0.68	3.2	0.32	5.5	1.15	13.1	1.29
300	4.8	9.2	2.8	0.58	2.1	0.23	5.5	1.15	11.5	1.25
400	4.8	8.5	3.3	0.69	2.9	0.34	5.4	1.12	9.4	1.11
A6										
T (°C)	**n**	**u_t (cm/s)**	**n* low ε**	**n*/n low ε**	**u_t* (cm/s) low ε**	**u_t*/u_t low ε**	**n* high ε**	**n*/n high ε**	**u_t* (cm/s) high ε**	**u_t*/u_t high ε**
35	4.8	6.5	4.0	0.82	6.8	1.04	7.5	1.56	59.1	9.05
100	4.8	5.8	2.8	0.58	2.5	0.44	6.7	1.40	28.1	4.85
200	4.8	5.1	2.8	0.59	2.0	0.40	5.2	1.08	9.2	1.78
300	4.8	4.7	3.3	0.68	2.6	0.56	5.4	1.12	9.2	1.97
400	4.8		2.9	0.60	1.9	0.44				

A1.1.4 Experimental results from BCT

Table A1.5

A3								
T (°C)	**H_d (cm)**	**ε_d**	**H_s (cm)**	**ε_s**	**t_s (s)**	**U_{de} (cm/s)**	**SCT (s/m)**	**BER (%)**
35	51.4	0.558	45.3	0.508	6.2	0.83	13.6	11.4
100	50.2	0.555	45.0	0.508	7.2	0.67	15.8	10.6
200	50.6	0.553	44.6	0.503	8.5	0.60	18.7	11.4
300	49.3	0.549	44.1	0.497	9.4	0.52	20.9	10.9
400	48.3	0.548	43.9	0.495	10.3	0.43	23.2	9.9
A4								
T (°C)	**H_d (cm)**	**ε_d**	**H_s (cm)**	**ε_s**	**t_s (s)**	**U_{de} (cm/s)**	**SCT (s/m)**	**BER (%)**
35	50.7	0.559	44.5	0.500	7.4	0.78	17.6	13.7
100	50.7	0.557	44.5	0.499	7.9	0.67	19.2	12.8
200	50.9	0.556	44.2	0.493	9.8	0.64	22.1	14.2
300	50.3	0.552	43.8	0.489	10.6	0.56	25.1	14.0
400	50.3	0.551	43.9	0.491	11.5	0.48	28.1	13.6

Table A1.5 (contd)

A5								
T (°C)	**H_d (cm)**	**ε_d**	**H_s (cm)**	**ε_s**	**t_s (s)**	**U_{de} (cm/s)**	**SCT (s/m)**	**BER (%)**
35	51.0	0.558	42.9	0.475	11.4	0.71	26.6	18.8
100	50.6	0.555	42.7	0.473	13.0	0.61	30.4	18.4
200	49.0	0.541	42.3	0.467	14.9	0.45	35.3	16.0
300	48.2	0.532	41.6	0.459	17.8	0.37	42.8	15.7
400	47.6	0.527	41.7	0.459	18.1	0.33	43.5	14.4
A6								
T (°C)	**H_d (cm)**	**ε_d**	**H_s (cm)**	**ε_s**	**t_s (s)**	**U_{de} (cm/s)**	**SCT (s/m)**	**BER (%)**
35	55.8	0.596	40.0	0.437	17.6	0.90	44.1	39.5
100	54.4	0.586	39.6	0.431	21.2	0.70	53.4	37.4
200	50.4	0.553	38.9	0.421	25.7	0.45	66.2	29.7
300	50.9	0.557	39.1	0.424	29.0	0.41	74.3	30.0
400	52.8	0.574	40.0	0.437	28.4	0.45	71.1	32.0

A1.1.5 Experimental and predicted U_{de}

Table A1.6

A0				**A3**			
T (°C)	**U_{de} (cm/s)**	**U_{de}* (cm/s)**	**U_{de}^1 (cm/s)**	**T (°C)**	**U_{de} (cm/s)**	**U_{de}* (cm/s)**	**U_{de}^1 (cm/s)**
35	0.95	0.90	1.43	35	0.83	1.43	0.94
100	0.80	0.76	1.21	100	0.67	1.21	0.82
200	0.58	0.60	0.90	200	0.60	0.90	0.70
300	0.55	0.52	0.81	300	0.52	0.81	0.63
400	0.48	0.49	0.72	400	0.43	0.72	0.56
A4				**A5 (low ε)**			
T (°C)	**U_{de} (cm/s)**	**U_{de}* (cm/s)**	**U_{de}^1 (cm/s)**	**T (°C)**	**U_{de} (cm/s)**	**U_{de}* (cm/s)**	**U_{de}^1 (cm/s)**
35	0.78	0.71	0.53	35	0.71	0.67	0.75
100	0.67	0.66	0.50	100	0.61	0.61	0.64
200	0.64	0.58	0.44	200	0.45	0.44	0.53
300	0.56	0.51	0.38	300	0.37	0.36	0.45
400	0.48	0.49	0.35	400	0.33	0.31	0.39
A6 (low ε)							
T (°C)	**U_{de} (cm/s)**	**U_{de}* (cm/s)**	**U_{de}^1 (cm/s)**				
35	0.90	1.24	0.55				
100	0.70	0.78	0.45				
200	0.45	0.43	0.30				
300	0.41	0.40	0.28				
400	0.45	0.40	0.30				

A1.2 Rheological results from msFBR

A1.2.1 Torque measurements

Table A1.7

Torque (mn m)

A0					
ID (cm)	**$\Delta P/\Delta P_c$=0**	**$\Delta P/\Delta P_c$=0.24**	**$\Delta P/\Delta P_c$=0.47**	**$\Delta P/\Delta P_c$=0.75**	**$\Delta P/\Delta P_c$=0.99**
8.9	19.74	15.31	11.46	6.00	2.55
7.9	19.57	14.55	10.08	5.89	2.53
6.9	20.03	14.30	10.05	5.76	1.98
5.9	18.55	14.48	9.99	5.72	1.95
4.9	16.34	12.82	9.26	5.23	2.13
3.9	13.82	11.06	8.17	4.38	1.59
2.9	9.07	7.22	4.71	3.24	1.34
1.9	4.35	3.55	2.80	1.57	0.97
0.9	1.68	1.33	0.90	0.76	0.50

Table A1.8

A5				
ID (cm)	**$\Delta P/\Delta P_c$=0**	**$\Delta P/\Delta P_c$=0.33**	**$\Delta P/\Delta P_c$=0.70**	**$\Delta P/\Delta P_c$=0.95**
7.7	18.4	13.1	7.3	3.5
6.7	18.4	13.1	7.1	3.5
4.7	18.3	12.8	6.7	3.4
3.7	16.9	11.3	6.38	3.6
2.7	10.4	7.6	4.7	2.9
1.7	5.5	4.5	2.9	2

Table A1.9

A6					
ID (cm)	**$\Delta P/\Delta P_c=0$**	**$\Delta P/\Delta P_c=0.24$**	**$\Delta P/\Delta P_c=0.48$**	**$\Delta P/\Delta P_c=0.71$**	**$\Delta P/\Delta P_c=0.96$**
8.2	18.9	14.7	11.6	7.5	4.7
7.2	18.9	14.6	11.4	7.2	4.4
5.2	18.4	14.6	11.3	7.1	4.6
4.2	18.8	14.3	10.8	7.2	4.4
3.2	16.1	13	9.4	6.3	5
2.2	9.5	7.7	6.2	5.3	3.9

Table A1.10

Ballotini					
ID (cm)	**$\Delta P/\Delta P_c=0$**	**$\Delta P/\Delta P_c=0.24$**	**$\Delta P/\Delta P_c=0.48$**	**$\Delta P/\Delta P_c=0.75$**	**$\Delta P/\Delta P_c=0.99$**
8.9	17.65	13.58	9.83	6.22	1.89
6.9	17.43	13.02	9.66	5.45	1.04
4.9	15.00	11.20	8.06	5.03	1.31
2.9	8.88	6.93	5.06	2.73	0.64
0.9	2.04	1.69	1.29	0.77	0.32

A1.2.2 Predicted torque from model (d = 3.6 cm)

Table A1.11

A0									
	$\Delta P/\Delta P_c=0$			$\Delta P/\Delta P_c=0.24$			$\Delta P/\Delta P_c=0.47$		
ID (cm)	$\sigma_z(z^*)$ (Pa)	T_{exp} (mN m)	T_{model} (mN m)	$\sigma_z(z^*)$ (Pa)	T_{exp} (mN m)	T_{model} (mN m)	$\sigma_z(z^*)$ (Pa)	T_{exp} (mN m)	T_{model} (mN m)
8.9	245.3	19.74	18.43	129.8	15.31	13.42	26.8	11.46	9.17
7.9	239.0	19.57	18.15	136.8	14.55	13.71	19.6	10.08	8.88
6.9	219.4	20.03	17.28	103.2	14.30	12.30	23.7	10.05	9.04
5.9	196.1	18.55	16.26	118.9	14.48	12.96	18.0	9.99	8.82
4.9	167.1	16.34	15.00	91.7	12.82	11.82	15.2	9.26	8.71
3.9	138.1	13.82	13.77	77.4	11.06	11.23	17.3	8.17	8.79
2.9	101.9	9.07	12.25	56.0	7.22	10.36	7.2	4.71	8.39
1.9	61.6	4.35	10.58	36.1	3.55	9.55	10.3	2.80	8.51
0.9	13.2	1.68	8.63	7.9	1.33	8.41	0.9	0.90	8.14

Table A1.12

A5						
	$\Delta P/\Delta P_c=0$			$\Delta P/\Delta P_c=0.33$		
ID (cm)	$\sigma_z(z^*)$ (Pa)	T_{exp} (mN m)	T_{model} (mN m)	$\sigma_z(z^*)$ (Pa)	T_{exp} (mN m)	T_{model} (mN m)
7.7	239.1	18.4	18.63	108.5	13.1	12.95
6.7	219.3	18.4	17.75	94.5	13.1	12.36
4.7	175.5	18.3	15.82	73.4	12.8	11.44
3.7	147.2	16.9	14.60	62.8	11.3	11.03
2.7	108.6	10.4	12.95	46.4	7.6	10.35

Table A1.13

A6									
	$\Delta P/\Delta P_c=0$			$\Delta P/\Delta P_c=0.24$			$\Delta P/\Delta P_c=0.48$		
ID (cm)	$\sigma_z(z^*)$ (Pa)	T_{exp} (mN m)	T_{model} (mN m)	$\sigma_z(z^*)$ (Pa)	T_{exp} (mN m)	T_{model} (mN m)	$\sigma_z(z^*)$ (Pa)	T_{exp} (mN m)	T_{model} (mN m)
8.2	166.3	18.9	16.95	82.5	14.7	13.47	3.2	11.6	10.14
7.2	159.0	18.9	16.65	72.1	14.6	13.04		11.4	
5.2	137.3	18.4	15.75	64.7	14.6	12.73	3.8	11.3	10.16
4.2	121.3	18.8	15.09	60.3	14.3	12.54	1.7	10.8	10.08
3.2	101.0	16.1	14.24	48.7	13	12.06		9.4	
2.2	76.1	9.5	13.20	34.8	7.7	11.47		6.2	

Table A1.14

Ballotini					
	$\Delta P/\Delta P_c=0$				
ID (cm)	T_{exp} (mN m)	$\sigma_z(z^*)_{passive}$ (Pa)	$T_{model\ -\ passive}$ (mN m)	$\sigma_z(z^*)_{active}$ (Pa)	$T_{model\ -\ active}$ (mN m)
8.9	17.65	781.1	27.94	1099.3	18.39
6.9	17.43	621.7	23.46	813.5	14.24
4.9	15.00	482.1	19.33	593.4	11.12
2.9	8.88	290.4	13.28	330.1	7.49
0.9	2.04	59.0	5.25	62.7	3.89
	$\Delta P/\Delta P_c=0.24$				
ID (cm)	T_{exp} (mN m)	$\sigma_z(z^*)_{passive}$ (Pa)	$T_{model\ -\ passive}$ (mN m)	$\sigma_z(z^*)_{active}$ (Pa)	$T_{model\ -\ active}$ (mN m)
8.9	13.58	560.9	21.69	812.0	14.22
6.9	13.02	446.4	18.24	598.4	11.19
4.9	11.20	349.8	15.20	439.4	8.99
2.9	6.93	211.8	10.67	248.3	6.38
0.9	1.69	53.4	5.14	63.0	3.90

Table A1.14 (contd)

Ballotini					
	$\Delta P/\Delta P_c$=0.48				
ID (cm)	**T_{exp} (mN m)**	**$\sigma_z(z^*)_{passive}$ (Pa)**	**$T_{model\ -\ passive}$ (mN m)**	**$\sigma_z(z^*)_{active}$ (Pa)**	**$T_{model\ -\ active}$ (mN m)**
8.9	9.83	343.8	15.01	518.3	10.08
6.9	9.66	304.4	13.71	421.2	8.73
4.9	8.06	225.3	11.12	295.1	7.01
2.9	5.06	136.5	8.08	169.9	5.33
0.9	1.29	31.3	4.34	46.1	3.67
	$\Delta P/\Delta P_c$=0.75				
ID (cm)	**T_{exp} (mN m)**	**$\sigma_z(z^*)_{passive}$ (Pa)**	**$T_{model\ -\ passive}$ (mN m)**	**$\sigma_z(z^*)_{active}$ (Pa)**	**$T_{model\ -\ active}$ (mN m)**
8.9	6.22	109.7	7.14	188.4	5.57
6.9	5.45	98.4	6.75	156.2	5.14
4.9	5.03	98.9	6.77	145.7	5.00
2.9	2.73	51.8	5.09	80.7	4.13
0.9	0.77	12.1	3.62	32.8	3.50

A1.3 Failure properties from Shear Cell

Table A1.15

A0				
σ_1 (Pa)	**C (Pa)**	**φ (deg)**	**φ_e (deg)**	**φ_e-φ (deg)**
707	132.1	30.2	52.5	22.3
1141	122.1	28.9	39.6	10.6
1429	98.3	31.7	38.3	6.6
1944	114.5	33.2	38.9	5.7
A5				
σ_1 (Pa)	**C (Pa)**	**φ (deg)**	**φ_e (deg)**	**φ_e-φ (deg)**
713	128.2	30.2	51.3	21.0
1122	119.9	30.9	40.2	9.3
1436	94.2	31.7	38.0	6.3
1951	110.1	33.2	38.6	5.4
A6				
σ_1 (Pa)	**C (Pa)**	**φ (deg)**	**φ_e (deg)**	**φ_e-φ (deg)**
775	160.7	29.5	55.2	25.7
1059	171.5	24.0	40.6	16.6
1344	175.8	30.8	44.7	13.9
1825	188.4	28.8	39.0	10.2

Table A1.15 (contd)

Ballotini				
σ_1 **(Pa)**	**C (Pa)**	φ **(deg)**	φ_e **(deg)**	φ_e-φ **(deg)**
739	51.1	28.1	34.5	6.4
966	24.2	29.5	31.7	2.2
1282	91.3	26.7	33.2	6.5
1698	81.8	25.2	29.4	4.2

Table A1.16

	φ_w **(deg)**	**A (Pa)**	δ **(deg)**	C_δ **(Pa)**
A0	11.3	68.7	34	90
A5	13.6	66.2	33	120
A6	16.5	68.0	31	158
Ballotini	6.2	43.3	26	80

A2 A commercial evaluation of the msFBR

NTV Group Report
December 2004

Giovanna Bruni
Simon Pilgrim
Musa Sönmez

London Business School

CSEL
Centre for Scientific Enterprise Limited

UCL

Table of Content

Introduction

The technology object of this study is the mechanically stirred Fluidized Bed Rheometer, developed by the Fluidization Group in the Department of Chemical Engineering at University College London, UK. This is a device to measure the flow properties of aerated/fluidized powders, where powder is intended to be any granular material used in industrial processes. The msFBR has been conceived as a tool to improve the performance of fluidized beds, which are industrial units employed in a range of processes (see Fig. 1). In order to frame the potential use of the msFBR in the fluidization industry, a brief description of fluidization is given in the next chapter, followed by a description of the msFBR.

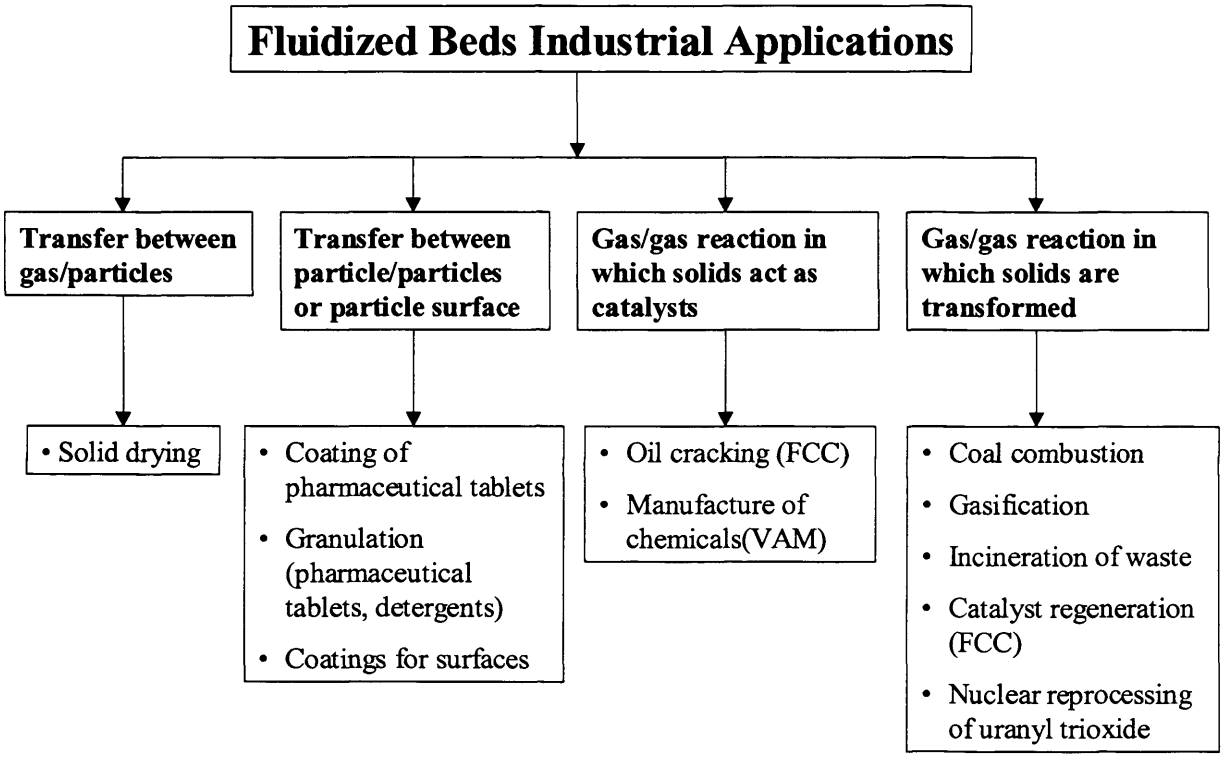

Figure 1 – Fluidized Beds Industrial Applications

1.1. Fluidization

1.1.1. Origins

In 1942 a desperate need for aviation gasoline during World War II brought together a group of oil companies, which included Standard Oil Indiana (later Amoco, now BP Amoco), M.W. Kellogg, Shell and Standard Oil Development Company (now Exxon), to design the first Fluidized Solids Process for Catalytic Cracking. Fluidization arrived as an innovative and successful oil refining technology, revealing the potential of the technique for gas-solid reaction engineering. Since then it has been applied to many other areas, becoming a firmly established technique in the processing industries[1].

1.1.2. What is a Fluidized Bed?

Fluidized beds are beds of particles suspended in an upward flowing gas (see Fig. 2). The loss of friction between particles due to the presence of gas makes such systems (particles + gas) acquire liquid-like properties - hence the term "fluidized solids". For example, objects less dense than the bed material will float on top of the bed; the surface stays horizontal when the vessel is tilted; two beds having different heights, level off when connected; the rapid mixing of the particles allows for a uniform temperature in the system; the solids can flow through an opening in the vessel just like a liquid. These fluid-like properties make fluidized beds attractive for industrial processes where a solid (often the catalyst for the reaction) and a gas are to be put in contact and need to circulate around the unit.

[1] Lettieri, P.: "A study on the influence of temperature on the flow behaviour of solid materials in a gas fluidized bed" PhD Dissertation, Department of Chemical Engineering, University College London (1999)

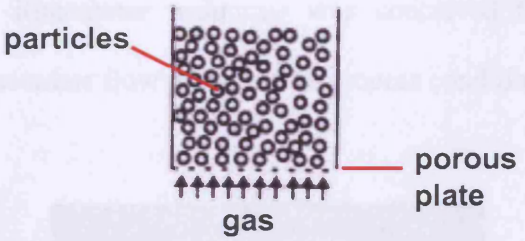

Figure 2 – Fluidized bed schematic

1.1.3. Flow Properties of Fluidized Powders

The flow properties of the fluidized powders are a crucial issue for fluidized bed processes, both in the design stage and during the process. These properties are highly dependent on the process conditions (temperature, presence of liquids, moisture, size distribution of the powder) and in most of the commercial fluidized beds units their changeability under process conditions can cause the plant to operate at productivity rates much lower than the nominal ones, with a consistent loss of profit for the company.

The problems caused by the lack of knowledge on realistic flow properties, and therefore the profit lost by operating below the optimal production rate, change according to the process. In section 2 we describe the main processes where problems related to the fluidization occur and in section 5 we discuss their financial impact.

1.2. The msFBR

The existing tests to measure the flow properties of powders (described in detail in section 5) often fail to predict the real flow behaviour of fluidized powders. The main reason for this failure is that these tests are not done at realistic process conditions and are not tested against the real behaviour of powders in the fluidized bed. The mechanically

stirred Fluidized Bed Rheometer technique was conceived to fill this gap in the measurement tests for powders flow properties at process conditions.

Figure 3 – An industrial fluidized bed (Fluid Catalytic Cracking unit, FCC)

1.2.1. The Device & Its Novelty

The msFBR consists of a laboratory scale fluidized bed equipped with an agitating system. An impeller rotates in the fluidized powder at a set speed and the torque (force) needed for the rotation is measured (Fig. 4). The experimental procedure is that standard for measuring the rheological properties of liquids, where the "resistance" of the material to flow (move) is quantified and related to the force applied to impose the motion. For each set impeller speed N a measurements of the torque T is recorded and a constitutive equation for the material (rheogram) is built by means of the theory of mixing of non-Newtonian fluids. The methodology to obtain the rheograms constitutes the uniqueness of

the technique, as it is the first time that this theory, developed for fluids, is applied to fluidized powders. Moreover, the device was designed so to run measurement at realistic process temperatures and this also represents an advancement in flow properties measurement devices.

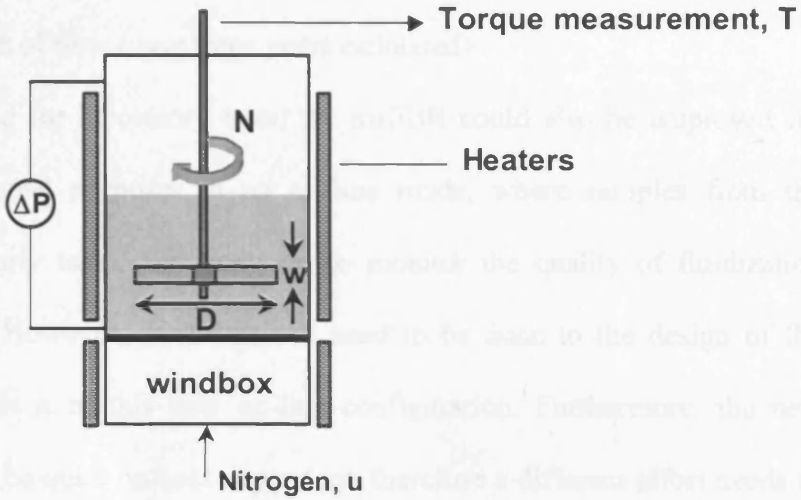

Figure 4 – msFBR Schematic

1.2.2. Current status of the technology

So far, experimental results have shown that the msFBR technique can produce rheological data that are directly related to the flow properties of powders, i.e. it is capable of characterizing the powders according to their flowability[2]. Most importantly, a link was established between the rheological measurements and the flow properties in the fluidized state for some process conditions (temperature, fines size distribution effect).

[2] Bruni et al., "An investigation into a mechanically stirred Fluidized Bed Rheometer", in Proceedings of the 9th International Conference on Multiphase Flow in Industrial Plants (2004)

Further research needs to be done to span a wider range of process conditions (presence of liquids and temperature). This additional research is expected to take a full time researcher approximately six months.

Furthermore, a database could be built based on a large number of experiments using a range of different materials utilised in industrial processes. However, this effort would take a considerable length of time (over three years estimated).

In addition to being used for laboratory tests, the msFBR could also be employed for monitoring/feedback control purposes in an on-line mode, where samples from the industrial bed are regularly taken and analysed to monitor the quality of fluidization throughout the process. However, modifications need to be done to the design of the equipment in order to fit it in this new on-line configuration. Furthermore, the new designs are envisaged to be quite process dependent, therefore a different effort needs to be put into this advancement according to the industrial process. For some processes, such as in the nuclear industry, this option might also prove to not be feasible due to the hazards associated with handling radioactive materials.

2. *Possible Applications*

Given that over 50% of all material used in industry are, at some stage, in powder form, the applications of a powder flow tester are "endless". The msFBR could cover almost all the applications of powder technology. However, since its most advanced feature to date is the measurement in the fluidized state, we decided to focus only on this part of the market, the fluidization industry. Fluidized beds are utilized in a variety of industries

including the oil, chemical, pharmaceutical, nuclear and food industries. Below, we have set out an analysis of the potential application areas divided by industry.

2.1. Oil Industry

In the oil industry, fluidized beds are used for Fluid Catalytic Cracking (FCC). FCC is the primary conversion unit in most refineries. Through this process, low-value heavy components of crude oil are split into a variety of high-value lighter products (fuel) through a reaction with catalysts.[3] The FCC unit consists of a reactor and a regenerator, where a catalyst (in the form of particles) is fluidized throughout the entire unit. In the reactor, liquid hydrocarbon feedstock (oil) and the catalyst get in contact. The feedstock vaporizes and reacts – whilst the lighter products are separated, the heavier products form a coke layer around the catalyst particles, temporarily deactivating it. The spent catalyst is then sent to the regenerator where it is restored by burning off the coke layer.

Due to the need for recirculation of the catalyst between reactor and regenerator, its flow properties are crucial for the FCC process. Problems can occur because the coke layer can cause the catalyst to lose its flow-ability. This can cause suboptimal reaction performance, leading to lower productivity (i.e. less output per input). In the worse case scenario, the stickiness of the catalyst particles can cause de-fluidization – i.e. collapse of the fluidized bed, forcing a shutdown of the entire process.

[3] Handbook of Fluidisation and Fluid Particle Systems (2003); Wen-Ching Yang. pp 379-396.

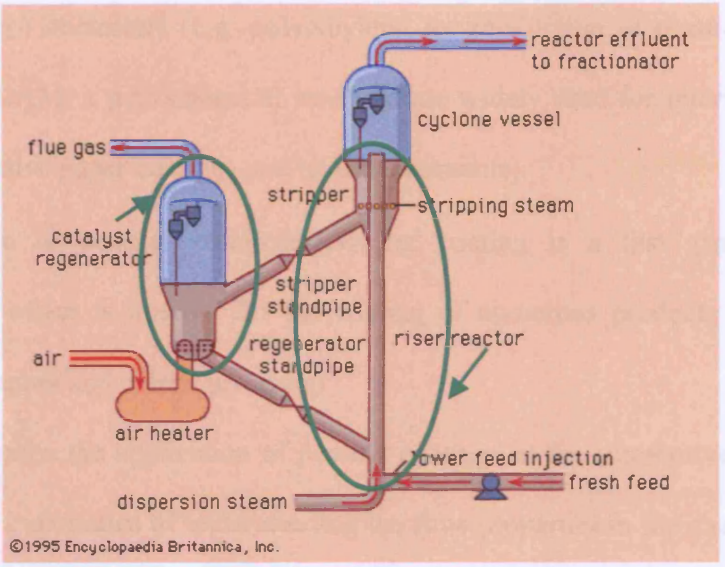

Figure 5 – FCC process schematic

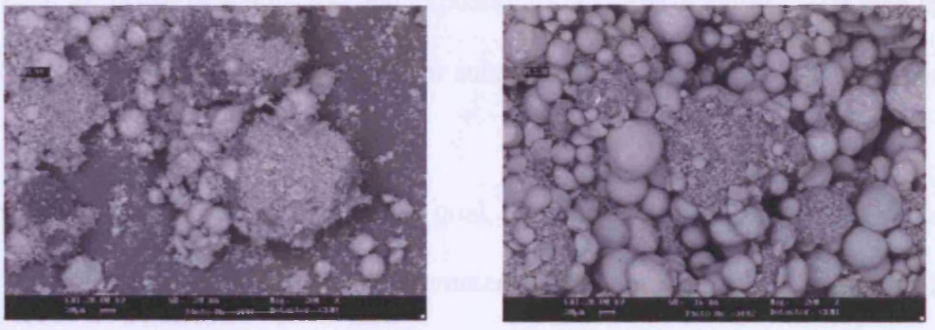

Figure 6 – FCC particles before and after fluidization at high temperature (formation of agglomerates). Courtesy of Dr Paola Lettieri.

2.2. *Chemical Industry*

Fluidized beds are employed in a variety of applications in the chemical industry including the following:

- The manufacture of detergent powder by fluidized bed granulation

- Production of chemicals (e.g. polyethylene for production of plastic, vinyl acetate monomer, VAM, a petrochemical intermediate widely used for interior and exterior paints, adhesive paper coatings and textile treatments).
- Manufacture of powder coatings (powder coating is a fast growing finishing technology which is utilized for the coating of numerous products including cars, home appliances and plastic products)[4]

Below, we describe the application of powder coatings in the automotive industry as an example of the importance of understanding the flow properties in the chemical industry: Automotive powder coatings are a mixture of several components, such as resin, cross-linker, pigments, flow aids and degassing solvent. Their flow-ability is affected by many factors such as moisture absorption and exposure to heat, for example. The way they are stored can also have a large impact on their subsequent performance in the spray-painting booth.

Smooth fluidization in such units is a key goal, and the ability to achieve this depends on finding the optimal balance of critical parameters such as particle shape, size distribution, flow characteristics, moisture content, air velocity and humidity to the bed floor area. A powder coating must be free-flowing and it must fluidize well in the fluidization bed. This ensures that individual particles are separated, improving the electrostatic charge that can be applied to the powder so that it flows more easily through the spray gun to give an even finish.

[4] Powder Coating Institute (www.powdercoating.org)

Today's automotive industry requires the use of fine powders to create thin films of coating on cars. However, due to their cohesiveness, fine powders cause more problems in the fluidization. Therefore, it is crucial, and of increasing importance, to assess the flow properties of the materials used in such processes.

2.3. Pharmaceutical Industry

In the pharmaceutical industry, fluidized beds are mainly employed for the production of pills and tablets. The main industrial processes involved are granulation and the drying and coating of granulates. To make tablets, a granulation liquid is added to a dry powder mix of active ingredients and excipients. This wet mass is then dried, milled and lubricated before being 'tableted' at a range of compression forces. The end-point of the granulation process is the point at which the correct amount of liquid has been added and the mass blended for an appropriate time in order to achieve the optimum rheological properties. Being able to accurately predict the granulation end-point is crucial to final product quality. This is highly dependant on the flow properties of the forming granules and therefore their understanding is crucial in such processes.

2.4. Food Industry

The main uses for fluidization are granulation, drying and mixing of the ingredients. An example of granulation in the food industry is rice production, the process being similar to the one described for the pharmaceutical industry. The rice grains need to be grown to a consistent size and shape, via the use of a binding ingredient, which can be realized through constant inspection of the grain mash.

2.5. Nuclear Industry

Fluidized bed processing has been successfully applied to the production of uranium trioxide by calcination of uranyl nitrate solutions through a thermal decomposition reaction (TDN process). During the operation (see Fig. 7), the fluidized bed consists of three phases – the solid oxide, the liquid uranyl feed and the fluidizing gas (air). Uranium trioxide particles are coated by the feed and continuously withdrawn as product through an overflow tube. The bed can be described as a mixture of solid particles and liquid drops that are becoming solid particles. Hence, there will also be liquid layers present on the solid particles each time they pass through the spray cone. When these particles come together, depending on process conditions, agglomerates can form. These agglomerates, being heavier than the individual constituent particles, are less easy to keep fluidised and eventually the entire bed could de-fluidize unless the agglomerates are kept below a certain size limit via breakage processes[5]. Knowledge of the effects of process conditions on the flow behaviour of the particles coated with liquid layers would greatly improve the process in its design and operation.

[5] Simons et al.: "Micro-Scale Observations And Measurements Of High Temperature Particle-Particle Interactions", in Proceedings of the World Congress in Chemical Engineering (2005)

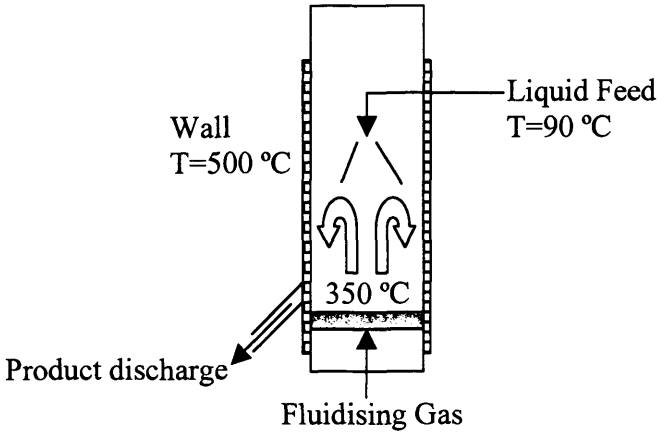

Figure 7 - Schematic and process temperatures for the TDN process

2.6. *Gasification & Combustion for Energy Production*

In recent years, fluidized beds applications for gasification and combustion of coals and biomasses for energy production have been gaining increasing commercial interest. In these processes, a carbonaceous fuel is converted into a primarily gaseous form having significant heating value, i.e. it can be used to produce energy in the form of steam or heat (reused in the process) or of electric power. The design of this processes can change radically according to the fuel used and the specific application. Therefore, a detailed description of the process is not attempted here but general characteristics common to all gasification and combustion processes are analyzed. The feature that all gasifiers and combustor have in common is that commercial equipment design and selection need to be guided by a clear understanding of the fluidization behaviour of the fluidized material. For instance, when biomass fuels are employed (e.g. urban waste), the gasification process is relatively simple due to the generally highly reactive nature of biomass fuels. However, there is a great risk in biomass fuel gasification associated with ash, or ash-inert particle agglomeration within the bed that may lead to de-fluidization and plugging

of nozzles and drains. The commercial success of such emerging technologies is therefore highly dependent on the advancement of laboratory scale testing and simulations. However, the recent practical advancement of fluidized bed gasifiers and combustors have occurred with little dependence on the fundamental understanding of fluidization phenomena and the associated problems involved[6]. These fluidized bed technologies compete directly with commercially established non-fluidized gasifiers and combustors and therefore they could highly benefit from flow properties studies at realistic process conditions.

3. *How can the msFBR help?*

The industrial processes described in section 2 are all characterized by process conditions that in different ways change the particles' properties during the process, hence affecting the flow properties of the powders. Section 2 showed how it is of paramount importance for the fluidization industry to be able to analyze the fluidization behaviour of powders in real or simulated process conditions, in order to avoid mal-performance or shut downs of the entire plant.

The fluidization industry lacks a device to monitor the flow properties of the powders in the same way as a thermocouple[7] does with the temperature. The msFBR could serve this purpose by producing a clear indication of the quality of fluidization, either in an online mode for feedback control or by means of laboratory tests to predict the flow properties of the powders to be used.

[6] Handbook of Fluidisation and Fluid-Particle Systems (2003), Wen-Ching Yang (Ed.) pp 397-420
[7] A thermocouple is an electrical temperature measurement device.

4. Competition

4.1. Alternative Techniques for Flow Properties Measurements

A great deal of research has been carried out over the decades in order to define and measure, by means of simple tests, parameters apt to characterize and predict the flow properties of solid materials. To this end, various approaches have been undertaken, but only a few have been commercialized and none of them satisfactorily addressed the problem of powders' flow-ability characterization at the process conditions typical of fluidized beds applications.

- Angle of repose - the constant angle to the horizontal assumed by a cone-like pile of the material. It is used as a direct indication of the potential flow-ability of a material: materials with good flow-ability are characterized by low angles of repose.
- Shear cell – it is based on measurements of the force needed to shear loaded samples of compressed powders. The flow function obtained in this way can be used also as an indication of the capability of the powders to fluidize.
- Falling sphere – A sphere is let fall in the fluidized bed and its trajectory recorded with time. A viscosity of the medium is calculated with standard equations for the fall of an object in a fluid.
- Bubble shape – The deformation of a bubble rising in the fluidized bed is related to the bed viscosity as if it was a liquid.

The angle of repose technique is a very empirical technique widely used in powder technology, which has the disadvantage of having no standard procedure, with poor

reproducibility. This problem was overcome by Prof Derek Geldart (an internationally recognized expert in fluidization), who recently commercialized an Angle of Repose measuring device, Mark4[8] through his company Powder Research Ltd. However, this technique finds its application mainly for problems related to the storage, discharge or transportation of powders rather than to predict the fluidization behaviour. This is because the measurement is taken in a static condition, very far from the flow conditions typical of fluidization, and important process conditions (high temperature) are not taken into account. Moreover, it has been demonstrated that the angle of repose can sometime even be misleading in predicting the fluidization behaviour of powders[9] The shear cell technique is an established and patented technique widely used in powder technology for the design of bins and hoppers, so that the contained material can be reliably discharged by gravity flow. However, like the angle of repose, the measurement is taken in flow conditions totally different from fluidization and therefore it is unlikely to reproduce real effects. Moreover, the measurement is taken at ambient conditions, neglecting one of the process conditions that affect mostly the flow properties of powders (temperature).

The falling sphere and bubble shape techniques have the advantage of being carried out in the fluidized state. However, they have been treated so far just as academic studies and no commercialization effort was attempted. The falling sphere is the only technique where measurements of the flow properties have been taken at high temperature[10].

[8] Powder Research Ltd. (www.powderresearch.co.uk)

[9] Bruni et al., "An investigation into a mechanically stirred Fluidized Bed Rheometer", in Proceedings of the 9th International Conference on Multiphase Flow in Industrial Plants (2004)

[10] Newton et al., "Comments and experimental data on the suitability of assigning a viscosity to the fluidized bed dense phase", in Proceedings to the 5th international conference on Fluid Particle Interactions (1999)

The described techniques show how the focus of most powder characterization instruments has been to assist in the design of powder handling machinery rather than to characterize and classify material flow properties in the fluidization state.

4.2. Freeman Technology Ltd.

In the late 1980s a new technique to measure the flow properties of powders was launched: the FT4 Powder Rheometer developed by Freeman Technology[11]. This device measures the energy required to displace a powder sample contained in a vessel with a specifically designed blade. These energies are derived from the measurements of the axial force and torque acting on the blade in an up and down cycle. From the energy measured, a series of indexes are derived which are related to the flow properties of powders. The FT4 rheometer seems also to be available in a fluidized mode, where an alternative kit is provided to replace the bottom of the vessel with a porous plate through which gas is passed. However, it was shown that measurements obtained with the FT4 Powder Rheometer have poor capability to reproduce the real fluidization behaviour at process conditions (temperature)[12] Like other existing techniques for flow properties measurements, the FT4 is mainly useful to assess the changes in the flow properties of powders in storage and transportation rather than in fluidization applications, as a direct link with fluidization has not been established. Moreover, the measurements are carried out at ambient temperature only. Freeman Technology's FT4 Powder Rheometer is

[11] Freeman Technology Ltd. (www.freemantech.co.uk)
[12] P. Lettieri, D. Newton, J.G. Yates (2001) "Characterization of the fluidization behaviour of solid materials at high temperature", In *Proceedings of the 6 World Congress of Chemical Engineering, Melbourne,* Australia.

marketed at a price ranging between £20,000 and £30,000, according to the features required.

4.2.1. Potential Patent Infringement

The patent filed by Freeman Technology is set out in the appendix. The patent covers mainly the principle of the simultaneous rotation and axial movements of the blade with respect to the vessel and the shape of the twisted blade used. Based on our analysis, we believe that the msFBR technique would not infringe Freeman Technology's patent, the main reasons being the different torque measurement method and analysis used by the msFBR. Conversations with Prof. Geldart (who commonly acts as an expert witness in patent cases) confirmed our view regarding the potential for patent infringement. Given the similarity of the two techniques, Freeman Technology is likely to thoroughly scrutinize any possibility of patent infringement. This was evident in their response to Stable Micro Systems' Manumit Powder Rheometer, which more blatantly infringed the IP on the stirring blade and, therefore, was eventually withdrawn from the market in 2002.

4.3. Technology Comparison – msFBR's Advantage

Compared to all existing techniques, the msFBR is unique because it replicates realistic process conditions by:

- Taking flow property measurements in the fluidisation state
- Including temperature as a test parameter.

As shown in the Appendix, most industrial applications of fluidized beds involve high temperatures and/or extremes ranges of temperature. The msFBR is the only technique

that provides flow property measurements under realistic process temperature and therefore represents a potentially unique tool for the fluidization industry.

5. *Commercialization*

Potential clients for the msFBR include:

- Companies that use fluidized beds as part of their production processes (Chapter 2)
- Companies that produce materials for use in fluidized bed processes (e.g. producers of catalysts for catalytic cracking)
- Research laboratories that are active in the powder characterization field

There are various options for providing these potential clients with the technology:

- Lab test kit
- Industrial process monitoring kit
- Consultancy
- Powder Process Database Modeling

Selling the technology in kit form is the most straightforward business model. A lab test kit would be most probably sold as a standard design, whilst kits suitable to be incorporated into a particular industrial process plant as an online monitoring device would involve a much higher degree of value added bespoke design and consultancy. A monitoring kit would help companies constantly monitor the properties of the material in the fluidized bed. Based on this, process parameters could be changed in order to improve the process' performance and avoid production stops. Much of the value of any

kits sold to companies and research labs would be in an accompanying analytical software suite, with a suitable sliding scale of licensing charges for annual usage, online database access, upgrades, etc. The software suit would, among others, serve as a means to protect the IP – the underlying analysis methodology would be embedded in the software and would, therefore, not be revealed.

The production of the kit would either have to be done internally or outsourced. Freeman Technology does the production in-house.

Consultancy work would include the following:

- Operation of a laboratory which would serve industrial clients' occasional testing needs on an annual flat fee basis or a fee per test made basis
- Consulting services for the design of fluidized bed processes – the knowledge gained through testing will help the company develop know-how for the optimization of fluidized bed processes
- Consulting services regarding materials to be used in fluidized bed processes – based on a database developed through testing, the company would be able to advise its clients on the materials to be used – i.e. which materials would be best suitable for which process, etc.

A database could be built based on a large number of experiments using a range of different materials utilized in industrial processes. The information included in the database could be used as a basis for consulting services and / or sold directly sold as software to companies. Companies would use the software for classifying materials based on their properties – something that would help in selecting the right materials for the right process.

An important issue regarding the commercialization of the msFBR is the difficulty of gaining access and establishing credibility with a customer base that mainly consists of medium- to large-sized corporations. Most large companies do not have the time, energy, manpower, or motivation to meet with every small company that wants to do business with them. Moreover, in most companies the acceptance of a new technology involves a long path – just finding the right people to begin the discussion will take quite a while. Having found this person, we would have to find the strategic buyer (not the purchasing agent, but the one person in the organisation that has the full authority to say yes to implement a new technology). Along the way, there will be numerous people with little real authority to say yes (though they may believe they do), but do have the authority to say no.

We believe, that the above issue can be dealt with in three ways (not mutually exclusive):

(i) leveraging the already existing relationships with BP[13] - given the existing relationship with BP, we believe that convincing BP to try the technology will not be too difficult. Being able to use BP as a precedent, a first implementer will help getting access to other big corporations, especially in the oil industry.

(ii) partnering with an established company that already has contacts and knows how our targeted customers make decisions regarding new technologies. Many companies with new technologies typically partner with a distributor or a manufacturers rep - this is an appropriate strategy for products that are a drop-in replacement for products currently being used by the customer, but not a suitable strategy for new technologies

[13] BP is involved in the msFBR project.

as there will be a long period of "educating" the customer - distributors and manufacturer reps rarely have that capabilities to do this. Therefore, partnering with companies that have to sell new technologies frequently would be more promising. Examples for potential partners are (i) analytical instrument companies, (ii) fluidized bed makers (process engineering companies) and (iii) value-added raw material suppliers (e.g. makers of catalysts for catalytic cracking).

(iii)Leveraging the relationships in academia (e.g. partnering with Prof. Geldart's consulting firm that is specialized on fluidization).

5.1. Potential Value for Customers[14]

Companies operating fluidized beds face two relevant issues:

- Mal-performance of the process due to suboptimal flow of the material
- Production shut-downs due to the collapse of the fluidized bed or due to the flow properties falling below a certain critical value

In an FCC plant, the former can cause productivity losses in the range of $50,000 to $250,000 per day.[15] For chemical processes, these numbers are estimated at $5,000 to $20,000.

A shutdown could cost some $1 million per day for an FCC plant and some $50,000 for a chemical plant. In the pharmaceuticals industry, production is done in the form of

[14] Source for estimates of potential losses: conversations with BP.

[15] In the oil industry, the potential losses also depend on the oil price – i.e. the higher the oil price, the higher the loss. The numbers given here are based on an oil price at "normal" levels ($30 per barrel).

batches. A shutdown is estimated to cost some $50,000 to $500,000 per batch. In the nuclear industry, a shutdown would cause a loss of £1 million per day.[16]

The msFBR would help to reduce the losses caused by suboptimal productivity and, also, reduce the number of production shutdowns.

5.2. Financial Viability

In order to get a feeling for the potential market size, we looked at the worldwide number of plants using fluidized bed processes:

Industry	Plants	Sources
FCC	320	BP
Chemical industry	1,000	BP, Prof. Yates of UCL and own estimates
Pharma industry	500	Prof. Yates of UCL and own estimates
Nuclear industry	50	Prof. Yates of UCL and own estimates
Food industry	1,000	Prof. Yates of UCL and own estimates
Energy	3,000	Prof. Yates of UCL and own estimates
Total	**5,870**	

We then determined the potential revenues by making assumptions regarding prices and volumes. Assuming that 5% of the fluidized bed plants would buy the kit and another 5% would buy the monitoring system, the total revenue potential from sales of the lab kit and the monitoring could be in the order of £20 million. We based our analysis on a low penetration rate because we believe that global roll-out will only happen very slowly.

	Average Price (£)	Market Volume	Penet-ration	# of Customers	Potential Total Rev. (£)
Sale of lab test kit	25,000	5,870	5%	293.5	7,337,500
Sale of bespoke monitoring system	50,000	5,870	5%	293.5	14,675,000
Total					**22,012,500**

[16] Source: conversations with BNFL (British Nuclear Fuel).

Assuming that we would be able to capture 10% of this volume annually, the turnover per year would be around £2 million. Assuming a licensing fee of £5,000 and assuming that we would be able to convince some 200 clients to license the technology, we would add another £1 million to the annual revenue. Consulting services could add another £1 million:

	Average Price (£)	Market Volume	# of Customers	# of Consult. Projects / Customer	Potential Annual Rev. (£)
Consultancy / database	500	5,870	200	10	1,000,000

Based on the above, total annual revenue would be in the order of £4 million.

Obviously, pricing is a key determinant of the revenue potential. The prices we used for the above analysis are based on Freeman Technology's pricing. Given the value that the msFBR could potentially generate for customers, significantly higher prices could be justified. At £25,000, most of the value added is captured by the clients and not by us. However, given that the technology is new and given that it has not proven its benefits in a real life environment, it will be difficult to demand very high prices (at the outset). On the other hand, if the company starts with a low price, it will have difficulties to raise it at a later stage – given that the major client industries are dominated by a few players makes this an even bigger issue (e.g. in the oil industry the 320 FCC units are owned by a handful oil companies – once we sell a device to one of BP's FCCs for £25,000, we will not be able to charge more on BP's purchases for its remaining FCCs. A possible way of disguising high prices is packaging the product in a way that it includes a lot of seemingly high-value-added services (consulting).

6. Conclusions

The key findings of our analysis could be summarized as follows:

- The technology addresses real problems and there are customers who would be interested in a technology that solves these problems.
- The technology has unique features, which are currently not provided by any other technology on the market.
- There is one major competitor on the market, Freeman Technology. Whilst Freeman Technology targets a very wide range of applications, msFBR only targets the fluidized bed environment. Hence, the potential market for our technology is significantly smaller than the potential market for Freeman's technology.
- In terms of IP, there is considerable risk that Freeman Technology will claim that the msFBR infringes its patent.
- This is a technology for a fairly small niche application – the revenue potential is not huge. This is also proven by the fact that Freeman Technology has not become a major corporation during the 16 years of its existence, despite the fact that it targets a larger market.
- In order to financially viable, the technology needs to be commercialized using a combination different business models – i.e. sale of kit, licensing, consulting and database.
- Against the background of the potential customers mainly consisting of medium- to large-sized corporations, gaining access to the right decision makers within the customers' organisations will be a key challenge. Leveraging the existing BP

relationship and partnering with established companies could help overcoming this difficulty.

- Given the limited size of the market, production of the kit should be outsourced. It will, however, not be easy to find a partner that is prepared to set up the production facilities for such low volumes – especially, at the outset, the volumes will be very low.
- To make the technology viable, there is still a certain amount of research to do, the required time being 6 months to more than 3 years.

To conclude, the venture does not represent a large opportunity. It is a rather small business opportunity to be operated as a company with a few employees. The business could be started by the inventor opening a small laboratory serving companies' testing needs and offering consultancy services. The relationship with BP could be leveraged to start doing business with BP and making BP test the msFBR on a small scale. During the first months and years of its existence, the company could start building relationships with potential customers and, importantly, get a better feeling of what the customers really need (i.e. do we need to do any changes to make the technology more attractive to customers?). This period could also be used to find partners both for the commercialisation and for the production of the kit.

Appendix[17]

Process Conditions of Current Fluidized Bed Applications

Process	**Example / Products**	**Process Conditions**
Drying of solids	Inorganic materials	60-110°C; 1atm
	Pharmaceuticals	60°C; 1atm
Calcination	Limestone	770°C; 1atm
	Alumina	550-600°C, 1atm
Granulation	Soap powders	5°C; 1atm
	Food; Pharmaceuticals	20-40°C; 2-3atm
Coating	Food; Pharmaceuticals	20-80°C; 2-3atm
Roasting	Food industry products	200°C; 1atm
	Sulphide ores (FeS_2)	650-1100°C; 1atm
Synthesis Reactions	Phthalic anhydride	340-380°C; 2.7atm
	Acrylonitrile	400-500°C; 1.5-3atm
	Ethylene dichloride	260-310°C; 1-10atm
	Maleic anhydride	400-500°C; 4atm
	Polyethylene (low/high density)	75-120°C; 15-30atm
Thermal Cracking	Ethylene; Propylene	750°C; 1atm

[17] Lettieri, P.: "A study on the influence of temperature on the flow behaviour of solid materials in a gas fluidized bed" PhD Dissertation, Department of Chemical Engineering, University College London (1999)

Some Other Applications	Process Conditions
Combustion and Incineration of waste solid	800-900°C; 1-10atm
Gasification of coal and coke / solid waste	800°C; 1-10atm
Biofluidization, cultivation of micro-organism	30°C; 1atm
Semiconductor Industries	300-1100°C; 1atm

References

1. Bruni et al., "An investigation into a mechanically stirred Fluidized Bed Rheometer", in Proceedings of the 9th International Conference on Multiphase Flow in Industrial Plants (2004).
2. Freeman Technology Ltd. (www.freemantech.co.uk).
3. Handbook of Fluidisation and Fluid Particle Systems (2003); "Applications for Fluid Catalytic Cracking", Wen-Ching Yang. pp 379-396.
4. Handbook of Fluidisation and Fluid-Particle Systems (2003), "Applications for Gasifiers and Combustors", Wen-Ching Yang (Ed.) pp 397-420.
5. Lettieri, P.: "A study on the influence of temperature on the flow behaviour of solid materials in a gas fluidized bed" PhD Dissertation, Department of Chemical Engineering, University College London (1999).
6. P. Lettieri, D. Newton, J.G. Yates (2001) "Characterization of the fluidization behaviour of solid materials at high temperature", In Proceedings of the 6 World Congress of Chemical Engineering, Melbourne, Australia.
7. Newton et al., "Comments and experimental data on the suitability of assigning a viscosity to the fluidized bed dense phase", in Proceedings to the 5th international conference on Fluid Particle Interactions.
8. Powder Coating Institute (www.powdercoating.org).
9. Powder Research Ltd. (www.powderresearch.co.uk).
10. Simons et al.: "Micro-Scale Observations And Measurements Of High Temperature Particle-Particle Interactions", in Proceedings of the World Congress in Chemical Engineering (2005).

A3 Alternative agitating system for the msFBR

The agitating system used in this study and described in section 5 was the "ancestor" of a more sophisticated system developed within the research project presented here. The new version of the agitating system will allow measurements to be taken at high temperatures, as the torque is measured by means of a high temperature strain gauge (see section A4.3) and all the materials have been chosen to sustain temperatures up to 300°C. Moreover, the measurements of the torque are taken at the base of the shaft near the impeller, rather than at the top near the motor, therefore diminishing the measured torque of any possible torsion of the shaft. This expedient makes the measurement of the low torques typical of fluidized beds more accurate.

A highly precision linear actuator can drive the shaft up and down, so to run tests at different bed depths with the highest accuracy. The linear actuator can also be used to experiment with new procedures or introduce conditioning of the material.

The following sections describe in detail the agitating system and the working principles of its component.

A3.1 Description

This agitating system has been designed so to produce a rotating movement of the impeller as well as an axial movement of the shaft up and down in the bed.

The agitator consists of a 13mm OD stainless steel hollow shaft 2mm thick, fitted with interchangeable impellers, see (6) in Figure 125.

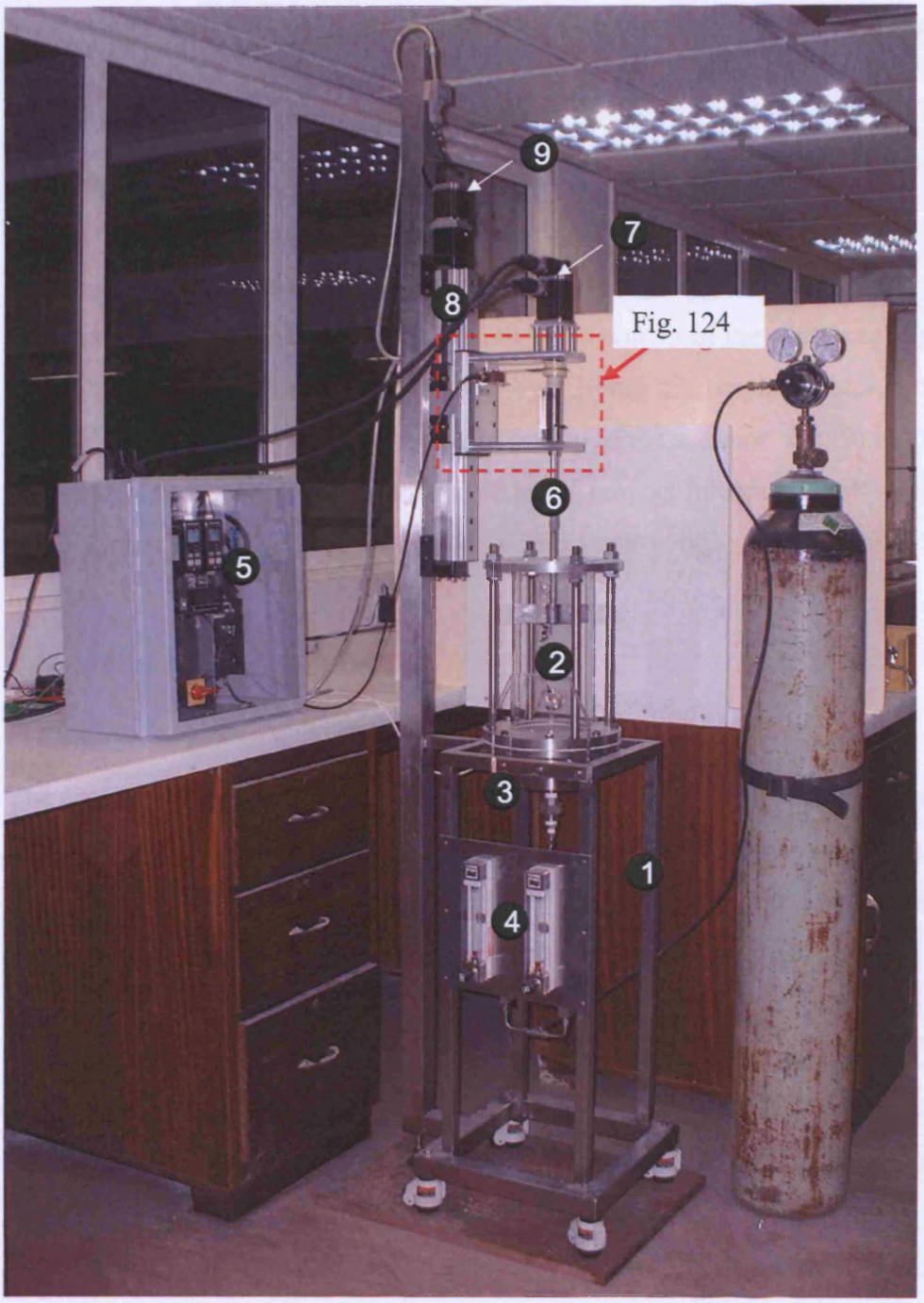

Figure 125 *The msFBR – Alternative agitating system*

Rotational movement

The shaft is driven by a 6000rpm NEMA brushless servo motor (Allen-Bradley, N-2302-1-F00AA) mounted on top of a C-frame that keeps the shaft in place, see (7) in Figure 125. The motor is controlled via the Ultra3000 Digital Servo Drive (Allen-

Bradley, 2098-DSD-005), which is located inside the control box and is plugged into a serial port of the computer.

Axial movement

The C-frame that holds the shaft is mounted on an Electric Linear Actuator, trapezoidal screw driven (Hoerbiger-Origa, OSP-E32-20400-00350) and vertically positioned in order to allow the up and down movement of the shaft, see (8) in Figure 125. The linear actuator is in turn driven by a Nema 23 stepping motor (SmartDrive, SMR232-030-H6-PN), which is mounted on top of the actuator, see (9) in Figure 125. The stepper motor is controlled by the Taranis Compact Integrated DSP controller and drive (SmartDrive,TAR-75P), located in the control box and controlled by serial interface.

A3.2 Torque Measurement Unit

The torque exerted on the shaft by the stirred material is measured by means of a torque cell that converts the applied torque to an electrical output signal. Signal transmission between the rotating shaft and a stationary instrument is then accomplished with telemetry (Single Channel 'D' Range rotary/short range telemetry equipment provided by Astech Electronics Ltd.).

Torque cell

Four electrical resistance strain gauges (see section A4.3), connected into a constant voltage Wheatstone bridge (see section A4.4), are mounted on the shaft in proximity of the impeller on two perpendicular 45-deg helices that are diametrically opposite one other, as shown in Figure 127.

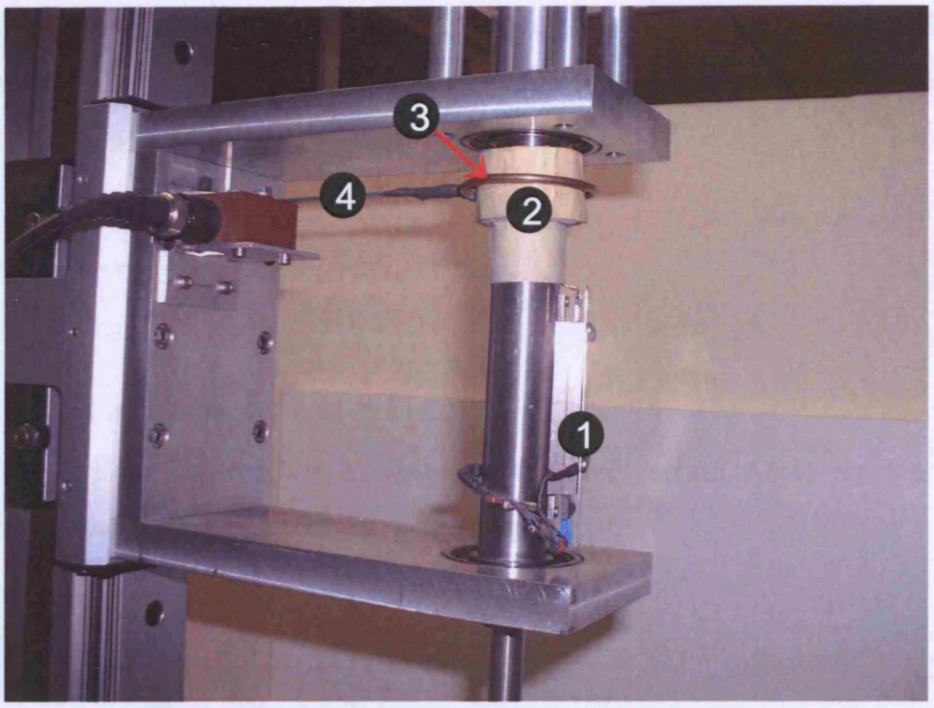

Figure 126 *Telemetric Device*

Every strain gauge exhibits a resistance change $\Delta R_i / R_i$ that is related to the applied strain ε_i in the direction of the grid by the expression (see section A4.3):

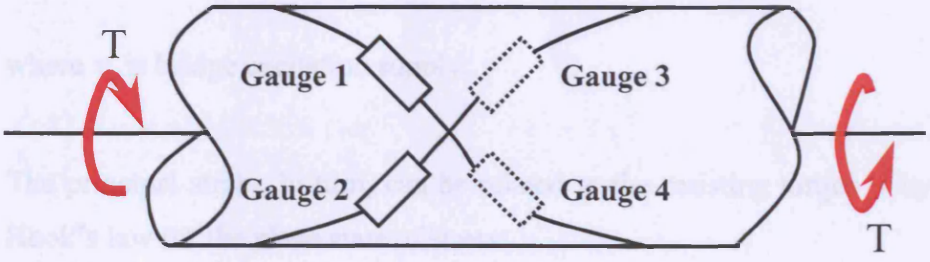

Figure 127 *Torque cell. Gauges 3 and 4 are on opposite side*

$$\frac{\Delta R_i}{R_i} = S_g \varepsilon_i \qquad \text{(A.11)}$$

where S_g is the gauge factor or calibration constant for the gauge.

When the shaft is subjected to torsion like shown in Figure 127, Gauge 1 and 3, mounted on the right-hand helix, sense a positive strain, and Gauges 2 and 4, mounted

on the left-hand helix, sense a negative strain. The two 45-deg helices define the principal stress and strain direction for the circular shaft subjected to pure torsion. Hence

$$\frac{\Delta R_1}{R_1} = -\frac{\Delta R_2}{R_2} = \frac{\Delta R_3}{R_3} = -\frac{\Delta R_4}{R_4} = \varepsilon_1 S_g = -\varepsilon_2 S_g \qquad \text{(A.12)}$$

where ε_1 and ε_2 are the principal strains.

Substituting Equation A.12 in Equation A.33 (see section A4.4) for the output voltage of a constant voltage Wheatstone bridge

$$v_0 = \frac{1}{4}\left(\frac{\Delta R_1}{R_1} - \frac{\Delta R_2}{R_2} + \frac{\Delta R_3}{R_3} - \frac{\Delta R_4}{R_4}\right) v_s \qquad \text{(A.33)}$$

a relationship is obtained between the output voltage of the bridge and the principal strain:

$$v_0 = \varepsilon_1 S_g v_s \qquad \text{(A.13)}$$

where v_s is bridge excitation supply.

The principal strain, in turn, can be related to the resisting torque T by applying the Hook's law for the plane state of stress:

$$\varepsilon = \frac{\tau(1+\nu)2}{E} \qquad \text{(A.14)}$$

and the elastic torsion formula for torsional shearing stresses:

$$\tau = \frac{TD_o}{2J} \qquad \text{(A.15)}$$

where J is the polar moment of inertia that, for a hollow circular cross section of internal diameter D_i and external diameter D_o, is

$$J = \frac{\pi}{32}\left(D_o^4 - D_i^4\right) \tag{A.16}$$

Hence, substituting Equation A.16 and A.15 in Equation A.14 yields

$$\varepsilon = \frac{16T}{\pi}\left(\frac{1+\nu}{E}\right)\frac{D_o}{\left(D_o^4 - D_i^4\right)} \tag{A.17}$$

where ν and E are the Poisson's ratio and the Young's modulus of the material, respectively.

Finally, substituting Equation A.17 in Equation A.13, the voltage output of the Torque Cell is related to the resisting torque at the shaft:

$$v_0 = \frac{16T}{\pi}\left(\frac{1+\nu}{E}\right)\frac{D_o}{\left(D_o^4 - D_i^4\right)} S_g v_s \tag{A.18}$$

Signal transmission

The voltage output from the Torque Cell in then sent out to the data acquisition unit by means of the inductive loop technique.

The basic principle is to use the Wheatstone bridge output to modulate a radio signal, which is then transmitted to a stationary demodulator. This eventually produces an analogue voltage signal to be sent out to the data acquisition unit.

The signal transmission unit consists of:

- a single channel radio transmitter (Astech Electronics, TX30D/1/IFM S/No. 2365) , see (1) in Figure 126, which is attached to the shaft and where the bridge signal modulates the pulse width of a constant-amplitude square wave. The square wave is used to vary the VCO frequency, which is centred at 10.7 MHz;

- a pickup aerial loop mounted on the shaft but spaced away from it with 7-10mm layer of insulating material, where the VCO signal is transmitted at low power, see (2) in Figure 126;
- a stationary loop aerial that encircles the pickup aerial and receives the signal, see (3) in Figure 126. It also acts as an inductive loop power supply for the transmitting unit (Astech Electronics, Inductive Power Supply/Signal Pickup Loop Interface Module IL2 s/No. 2391);
- a mounting bracket for the Inductive Loop Interface Module, see (4) in Figure 126. Due to the very low strain levels, the transmitter sensitivity was set very high – approximately 10 times higher than normal. This makes the transmitters inputs very susceptible to extraneous interference and it is for this reason that the bracket was introduced, so to move the interface transformer further away from the transmitter;
- a Single Channel Demodulator/Decoder (Astech Electronics, RE2D/IFM/1 S/No. 2392) that is enclosed in a stationary box. It amplifies the low-level 10.7 fm signal received from the inductive loop, demodulates it and re-shapes it to re-create the transmitted serial pcm. This is then decoded in two analogue voltage signals – one strain channel and one transmitter power supply voltage. The former ultimately carries the Wheatstone bridge voltage output to the data acquisition unit.

A3.3 Electrical Resistance Strain Gauges

Electrical resistance strain gauges are thin metal-foil grids that can be adhesively bonded to the surface of a component or structure. When the component or structure is loaded, strains develop and are transmitted to the foil grid. The resistance of the foil grid changes in proportion to the load-induced strain.

The strain sensitivity of metals is explained by the following simple analysis.
The resistance R of a uniform metallic conductor can be expressed as

$$R = \frac{\rho L}{A} \qquad (A.19)$$

where ρ is the specific resistance of the metal, L is the length of the conductor and A is the cross-sectional area of the conductor.
Differentiating Equation A.19 and dividing by the resistance R gives:

$$\frac{dR}{R}=\frac{d\rho}{\rho}+\frac{dL}{L}-\frac{dA}{A} \tag{A.20}$$

The term dA represents the change in cross-sectional area of the conductor resulting from the applied load. For the case of uniaxial tensile stress, recall that

$$\varepsilon_a=\frac{dL}{L} \quad \text{and} \quad \varepsilon_t=-\nu\varepsilon_a=-\nu\frac{dL}{L} \tag{A.21}$$

where ε_a is the axial strain in the conductor, ε_t is the transverse strain in the conductor and ν is the Poisson's ratio of the metal used for the conductor.
If the diameter of the conductor is d_0 before application of the axial strain, the diameter of the conductor d_f after it is strained is

$$d_f=d_0\left(1-\nu\frac{dL}{L}\right) \tag{A.22}$$

From Equation A.22 is clear that

$$\frac{dA}{A}=-2\nu\frac{dL}{L}+\nu^2\left(\frac{dL}{L}\right)^2\approx-2\nu\frac{dL}{L} \tag{A.23}$$

Substituting Equation A.23 in Equation A.20 and simplifying yields

$$\frac{dR}{R}=\frac{d\rho}{\rho}+\frac{dL}{L}(1+2\nu) \tag{A.24}$$

which can be written as

$$S_A = \frac{dR/R}{\varepsilon_a} = \frac{d\rho/\rho}{\varepsilon_a} + (1+2\nu) \qquad (A.25)$$

The quantity S_A is defined as the sensitivity of the metal or alloy used for the conductor.

Equation A.25 shows that the strain sensitivity of a metal or alloy is a result of the changes in dimensions of the conductor, as expressed by the term $(1+2\nu)$, and the change in specific resistance, as represented by the term $\frac{d\rho/\rho}{\varepsilon}$.

In a foil grid the resistance change $\frac{\Delta R}{R}$ is related to the strain ε in the direction of the grid by the expression

$$\frac{\Delta R}{R} = S_g \varepsilon \qquad (A.26)$$

where S_g is the gauge factor or constant of the gauge. The gauge factor S_g is always less than the sensitivity of the metallic alloy S_A because the grid configuration of the gauge with transverse conductors is less responsive to axial strain than a straight uniform conductor.

A3.4 Wheatstone Bridge (Constant Voltage)

The Wheatstone bridge, shown in Figure 128, is a circuit commonly used to convert a change in resistance to an output voltage. The output voltage v_0 of the bridge can be determined by treating the top and bottom parts of the bridge as individual voltage dividers. Thus,

$$v_{AB} = \frac{R_1}{R_1 + R_2} v_s \qquad (A.27)$$

$$v_{AD} = \frac{R_4}{R_3 + R_4} v_s \tag{A.28}$$

The output voltage of the bridge is

$$v_0 = v_{BD} = v_{AB} - v_{AD} \tag{A.29}$$

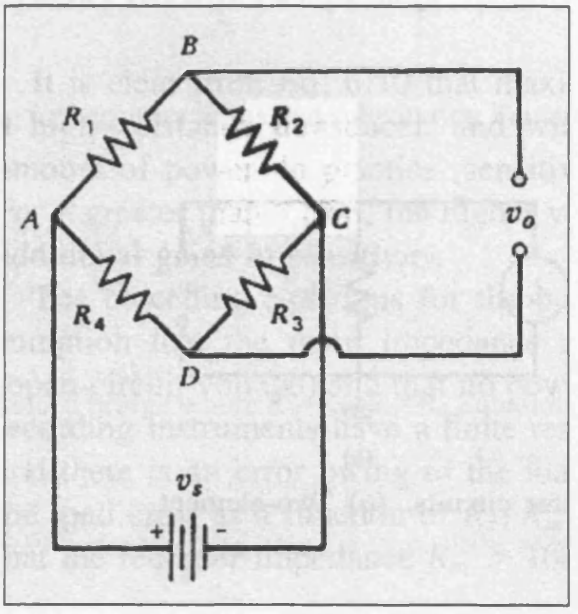

Figure 128 *Wheatstone Bridge – Constant Voltage*

Substituting Equation A.27 and A.28 into A.29 yields

$$v_0 = \frac{R_1 R_3 - R_2 R_4}{(R_1 + R_2)(R_3 + R_4)} v_s \tag{A.30}$$

Equation A.30 indicates that the initial output voltage will vanish ($v_0 = 0$) if

$$R_1 R_3 = R_2 R_4 \tag{A.31}$$

When Equation A.31 is satisfied the bridge is said to be balanced. The ability to balance the bridge (and zero v_0) represents a significant advantage, since it is much

easier to measure small changes in voltage Δv_0 from a null voltage than from an elevated voltage v_0, which can be as much as 1000 times greater than Δv_0.

With an initially balanced bridge, an output voltage Δv_0 develops when resistances R_1, R_2, R_3 and R_4 are varied by amounts $\Delta R_1, \Delta R_2, \Delta R_3, \Delta R_4$ respectively.

From Equation A.30, with these new values of resistances,

$$\Delta v_0 = \frac{(R_1+\Delta R_1)(R_3+\Delta R_3)-(R_2+\Delta R_2)(R_4+\Delta R_4)}{(R_1+\Delta R_1+R_2+\Delta R_2)(R_3+\Delta R_3+R_4+\Delta R_4)} v_s \qquad \text{(A.32)}$$

Expanding, neglecting higher order terms and substituting Equation A.31 yields

$$\Delta v_0 = \frac{R_1 R_2}{(R_1+R_2)^2}\left(\frac{\Delta R_1}{R_1}-\frac{\Delta R_2}{R_2}+\frac{\Delta R_3}{R_3}-\frac{\Delta R_4}{R_4}\right) v_s \qquad \text{(A.32)}$$

In particular for a balanced bridge where $R_1=R_2=R_3=R_4$ Equation 32 becomes

$$\Delta v_0 = \frac{1}{4}\left(\frac{\Delta R_1}{R_1}-\frac{\Delta R_2}{R_2}+\frac{\Delta R_3}{R_3}-\frac{\Delta R_4}{R_4}\right) v_s \qquad \text{(A.33)}$$

Equations A.32 and A.33 indicate that the output voltage from the bridge is a linear function of the resistance changes.

A4 Rheological analysis at u_{mf}

A4.1 Flow curves from torque measurements

In order to analyse fluidized powders in terms of their rheological characteristics a methodology to obtain a shear stress/shear rate relationship from the experimental torque profiles was developed. This stems from an early work by Metzner and Otto (1957) that was looking at predicting the power requirements to agitate non-Newtonian fluids.

In the work presented here, the theory of Metzner and Otto (1957) is applied to fluidized beds of powders, i.e. measuring the power required to stir the materials at a various impeller speeds to infer their rheological properties.

Metzner and Otto measured the power required to mix non-Newtonian, pseudoplastic fluids in stirred vessels. Comparing the measured Power Numbers (Po) with Power Number versus Reynolds (Re) curves obtained by stirring Newtonian fluids in the same vessel with the same impeller, they obtained the apparent Reynolds numbers and hence apparent viscosities (μ_{app}) for the pseudoplastic fluids.

The apparent viscosity of the non-Newtonian fluid defined in this way represents the viscosity of an "equivalent" Newtonian fluid that requires the same power for stirring at the same impeller speed, and hence same rate of shear, as the non-Newtonian fluid under analysis.

From the flow curves (apparent viscosities μ_{app} versus shear rate $\dot{\gamma}$) of the pseudoplastic fluids, obtained from standard viscometers, Metzner and Otto (1957) were able to show that the apparent shear rate ($\dot{\gamma}$) was directly proportional to the impeller rate of rotation, i.e.,

$$\dot{\gamma} = K_s N \qquad \text{(A.34)}$$

In particular, Calderbank and Moo-Young (1959) found a value of :

$$K_s = 10 \tag{A.35}$$

for Bingham and pseudoplastic fluids stirred with two-bladed paddles.

In this study the procedure was to calculate, for each experimental point (T, N), a point of the rheogram ($\tau, \dot{\gamma}$) as follows:

1) The Po vs Re curve for the impellers had been obtained previously with Newtonian glycerol and glycerol-water mixtures (Viora, 1994). In particular, the Power number, Po, is defined as:

$$Po = \frac{P}{N^3 D^5 \rho} \tag{A.36}$$

where P is the power required to stir at speed N a fluid of density ρ, with an impeller having diameter D. On the other hand,

$$P = T\omega = T2\pi N \tag{A.37}$$

where T is the resisting torque. Hence combining Equations A.36 and A.37 gives:

$$Po = \frac{T2\pi}{N^2 D^5 \rho} \tag{A.38}$$

The impeller Reynolds number is defined as:

$$Re = \frac{D^2 N \rho}{\mu} \tag{A.39}$$

where μ is the viscosity of the fluid.

2) The apparent viscosity of the fluidized powder was calculated for each data point (T, N) considering that the laminar region of the plot in Figure 129 (Re<10) is a straight line having slope of -1 described by the relationship:

$$Po = \frac{40}{Re} \tag{A.40}$$

Therefore, combining Equation A.38, A.39 and A.40 gives:

$$\mu_{app} = \frac{2T\pi}{40ND^3} \tag{A.41}$$

3) The shear rate was calculated using Equations A.34 and A.35

$$\dot{\gamma} = 10N \tag{A.42}$$

4) The shear stress was calculated as:

$$\tau = \mu_{app}\dot{\gamma} = \mu_{app}10N \tag{A.43}$$

and, by substituting Equation A.42 in Equation A.43,

$$\tau = \frac{\pi T}{2D^3} \qquad \text{(A.44)}$$

Equation A.42 and Equation A.44 show that the $\tau - \dot{\gamma}$ relationship (flow curve) obtained following the approach described above will have the same "shape" as the experimental T-N plots.

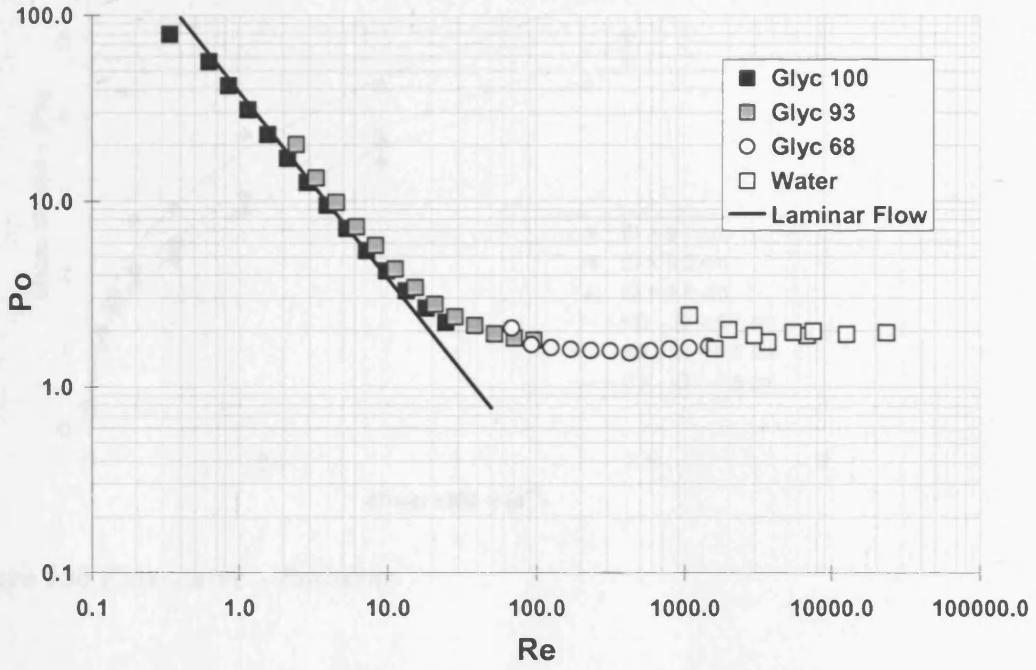

Figure 129 *Power number versus Reynolds experimental plot for two-bladed paddle in the msFBR (Viora, 1994)*

A4.2 Rheological results

Figure 130 reports the flow curves obtained for the ballotini sample at three different impeller depths (ID). Averaged values of the torque obtained with increasing and decreasing impeller speed were used to work out the shear stresses. All curves exhibit a non-Newtonian pseudoplastic behaviour. In line with the averaged results shown in Figure 124, the curve corresponding to the impeller depth 8.7 cm is above the one corresponding to 6.5 cm and so on.

Similar results were obtained for the alumina sample A0. Moreover, Figure 131 reports two experiments at the same impeller depth but carried out at different aeration rates (at and slightly above u_{mf}). The triangles in Figure 131 refer to an experiment carried out at $\Delta P/\Delta P_c=1$ and $u/u_{mf}=1.13$, corresponding to 6.7% bed expansion with respect to the settled bed.

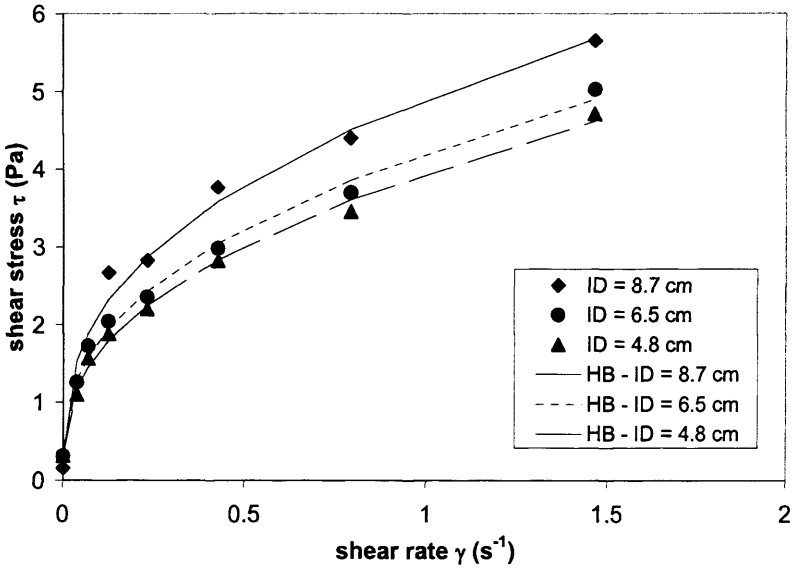

Figure 130 *Flow curve – Ballotini*

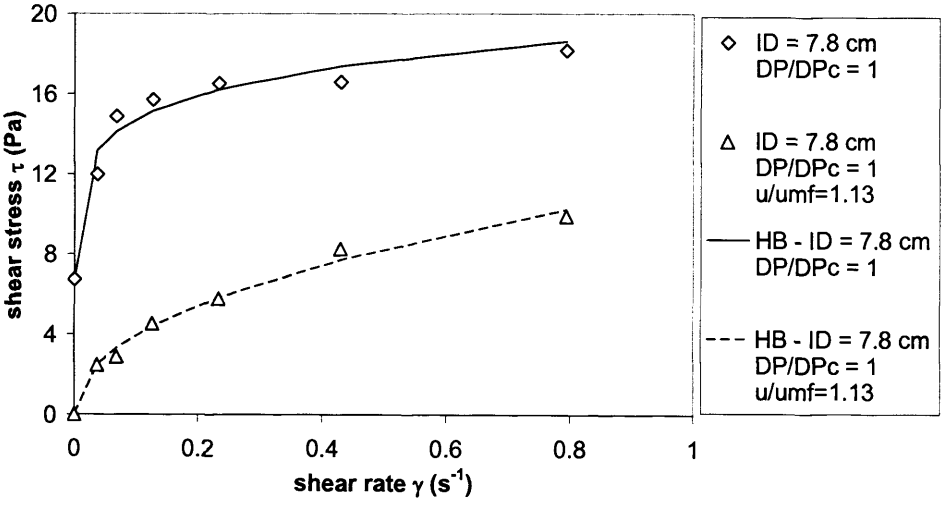

Figure 131 *Flow curve – Alumina A0*

A4 Rheological analysis at u_{mf}

The rheological Herschel-Bulkley model was fitted to the shear stress/shear rate curves:

$$\tau = \tau_y + k\dot{\gamma}^n \qquad (A.45)$$

This model encompasses Bingham plastic behaviour when $n = 1$, power law behaviour when $\tau_y = 0$, yield stress behaviour (solid like) when $n = 0$ and Newtonian behaviour when $\tau_y = 0$ and $n = 1$.

Values for the Herschel-Bulkley parameters were extrapolated for the ballotini sample at each impeller depth and for the alumina sample A0 at the two gas velocities and are reported in Table 22.

Table 22 *Herschel-Bulkley parameters*

	$\Delta P/\Delta P_c$	ID (cm)	τ_y (Pa)	K (Pa s^n)	n
Ballotini	1	8.7	0.31	4.6	0.40
Ballotini	1	6.5	0.31	3.9	0.42
Ballotini	1	4.8	0.31	3.6	0.43
Alumina A0	1	7.8	6.7	19.1	0.11
Alumina A0	1.13	7.8	0	11.3	0.45

Table 4 shows that a small yield stress (0.31 Pa for the ballotini and 6.7 Pa for the alumina) is still present at the minimum fluidization conditions. This can be explained considering that the minimum fluidization condition is not a sharp transition and therefore we might be observing a transition from the solid-like to the fluid-like rheological behaviour. In fact, when the minimum fluidization was slightly exceeded ($\Delta P/\Delta P_c$=1; u/u_{mf}=1.13) the yield stress dropped to zero and a pure power law behaviour was established.

Table 22 also shows that the effect of increasing the impeller depth was to decrease the value of K and slightly increase the value of n. The effect of increasing u/u_{mf} was

to shift the whole torque profiles significantly towards smaller values of the torque, showing once again that a substantial rheological change happens at $u=u_{mf}$.

A5 Relationship between the two principal stresses

a) NON COHESIVE MATERIAL

Let us consider the static yield locus for a non cohesive material, as shown in Figure 132

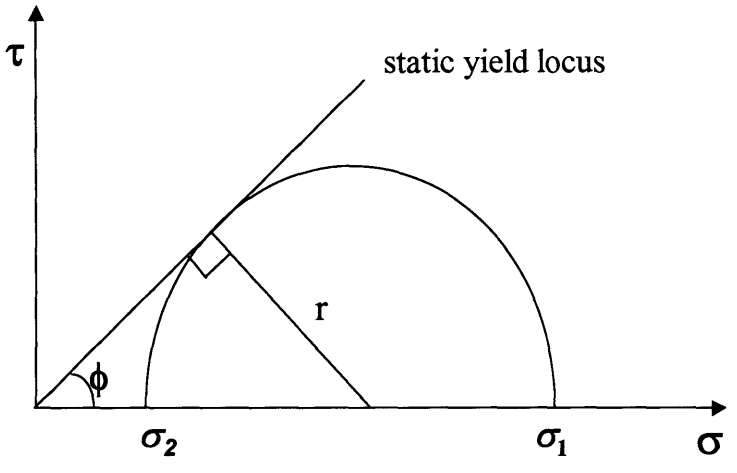

Figure 132 *Yield locus of a non cohesive powder*

In this case the yield locus passes through the origin and C = 0. From Figure 132

$$\sigma_1 = \sigma_2 + 2r \qquad \text{(A.46)}$$

From trigonometry

$$r = \sigma_2 \frac{\sin\varphi}{1-\sin\varphi} \qquad \text{(A.47)}$$

substituting Equation (A.46) in (A.47) gives:

A5 Relationship between the two principal stresses

$$\sigma_1 = \sigma_2 \frac{1+\sin\varphi}{1-\sin\varphi} \qquad \text{(A.48)}$$

Equation (A.48) shows how for a non cohesive material the two principal stresses are directly proportional.

c) COHESIVE MATERIAL

When a powder is cohesive a static yield locus has the aspect shown in Figure 133

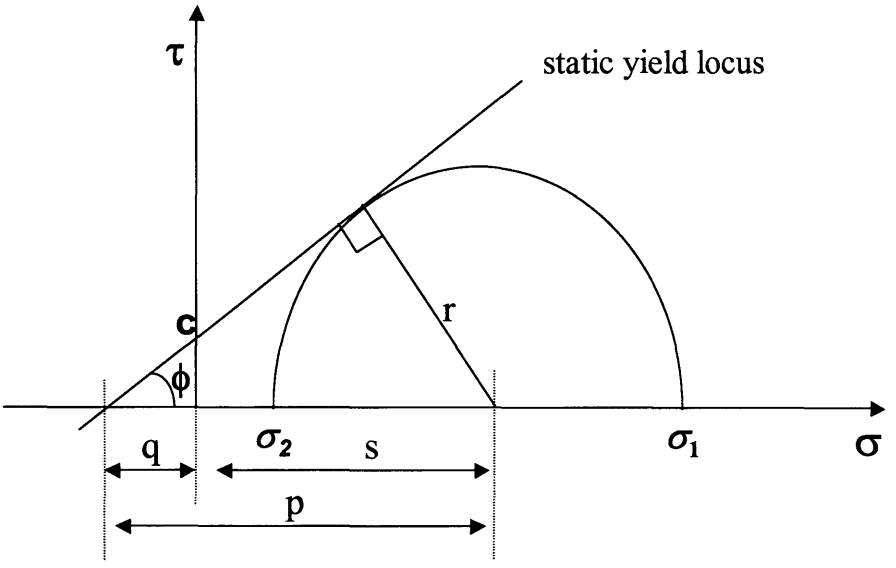

Figure 133 *Yield locus of a cohesive powder*

From Figure 133

$$\frac{\sigma_1 - \sigma_2}{2} = r \qquad \text{(A.49)}$$

From trigonometry:

A5 Relationship between the two principal stresses

$$r = p\sin\varphi = q\sin\varphi + s\sin\varphi \qquad \text{(A.50)}$$

Hence, substituting Equation (A.50) in Equation (A.49) gives

$$\frac{\sigma_1 - \sigma_2}{2} = q\sin\varphi + s\sin\varphi \qquad \text{(A.51)}$$

Also, from Figure 133

$$\sigma_1 + \sigma_2 = 2s \text{ or } s = \frac{\sigma_1 + \sigma_2}{2} \qquad \text{(A.52)}$$

From trigonometry

$$q = \frac{C}{\tan\varphi} \qquad \text{(A.53)}$$

Substituting Equations (A.53) and (A.52) in Equation (A.51) and rearranging gives:

$$\sigma_1 = \sigma_2 \frac{1+\sin\varphi}{1-\sin\varphi} + \frac{2C\cos\varphi}{1-\sin\varphi} \qquad \text{(A.54)}$$

or

$$\sigma_2 = \sigma_1 \frac{1-\sin\varphi}{1+\sin\varphi} - \frac{2C\cos\varphi}{1+\sin\varphi} \qquad \text{(A.55)}$$

A6 Pyroclastic Flows

Pyroclastic flows are high concentration granular avalanches of hot volcanic debris and gas generated during volcanic eruptions. The ability of pyroclastic flows to travel many km on slopes as low as a few degrees, combined with their high temperatures, large volumes and high frontal velocities (commonly reaching 30m/s or more), make them one of the most destructive volcanic phenomena. The magnitude of these phenomena is clearly shown in Figure 134.

Figure 134 *Pyroclastic Flow*

Pyroclastic flows travel further and spread over larger areas than cold-rock avalanches of similar volume. The ability of pyroclastic flows flowing on slopes as low as a few degrees, implies very low internal friction. This has been attributed in part to fluidization of pyroclastic flows by escaping gases (Sparks, 1976), possible gas sources including exsolution from juvenile glass, rupture of gas-filled vesicles, air ingestion, boiling of overridden water or combustion of vegetation.

Fluidization could therefore explain the observed behaviour of pyroclastic flows (Druitt, 1998), hence fluidization tests performed on volcanic ashes represent a possible avenue to advance the understanding of such a destructive natural phenomenon.

In the next pages the paper "The fluidization behaviour of ignibrite at high temperature and with mechanical agitation", published during the present PhD, is reported.

GEOPHYSICAL RESEARCH LETTERS, VOL. 31, L02604, doi:10.1029/2003GL018593, 2004

The fluidization behaviour of ignimbrite at high temperature and with mechanical agitation

T. H. Druitt,[1] G. Bruni,[2] P. Lettieri,[2] and J. G. Yates[2]

0094-8276/04/2003GL018593$05.00

A7 Publications

Bruni, G., P. Lettieri, D. Newton and D. Barletta (2006), 'An investigation of the effect of the interparticle forces on the fluidization behaviour of fine powders linked with rheological studies', To appear in *Chemical Engineering Science.*

Bruni, G., D. Barletta, M. Poletto and P. Lettieri (2006), 'A rheological model for the flowability of aerated fine powders', To appear in *Chemical Engineering Science.*

Bruni, G., P. Lettieri, D. Newton and J. G. Yates (2005), 'The influence of fines size distribution on the behaviour of gas fluidized beds', To appear in *Powder Technology.*

Bruni, G., A. Colafigli, P.Lettieri and T. Elson (2005) 'An investigation into the rheological behaviour of powders using a mechanically stirred Fluidized Bed Rheometer (msFBR)', *Chemical Engineering Research and Design*, 83(A11): 1311.

Bruni, G., P.Lettieri, J. G. Yates, D. Newton (2005) 'The effect of process conditions on the fluidization behaviour of gas fluidized beds' In *Proceedings of the World Congress in Chemical Engineering*, Glasgow, UK

Bruni, G. P. Lettieri, T. Elson, J. G. Yates (2005) 'Rheological studies of aerated solid materials', In *Proceedings of the Particle Systems Analysis*, Stratford upon Avon, UK

Bruni, G., P. Lettieri, T. Elson and J. G. Yates (2004), 'The effect of process conditions on the fluidization behaviour of gas fluidized beds', In *Proceedings of the AIChE annual meeting*, Austin, Texas, USA

Bruni, G., P. Lettieri, T. Elson and J. G. Yates (2004), 'A preliminary study into a mechanically stirred fluidized bed rheometer', in *Proceedings of the 9th International Conference on Multiphase Flow in Industrial Plants*, Rome, Italy

Bruni, G., P. Lettieri, J. G. Yates and D. Newton (2004), 'Some preliminary results on the influence of fine particles on the behaviour of gas fluidized beds at high temperature', In *Proceedings of Partec2004*, Nuremberg, Germany

Druitt, T. H., G. Bruni, P. Lettieri, and J. G. Yates (2004), 'The fluidization behaviour of ignibrite at high temperature and with mechanical agitation', *Geophys. Res. Lett.*, 31, L02604, doi:10.1029/2003GL018593

Bruni, G., R. Solimene, A. Marzocchella, P. Salatino, J. G. Yates, P. Lettieri and M. Fiorentino (2002), 'Self-segregation of high-volatile fuel particles during devolatilization in a fluidized bed reactor', *Powder Technology*, Volume 128, Issue 1 Pages 11-21

Marzocchella, A., G. Bruni, R. Solimene, P. Salatino, J. Yates, P. Lettieri, M. Fiorentino (2000), 'Self-segregation of high-volatile fuel particles during devolatilization in a fluidized bed reactor', In *Proceedings of the AIChE annual meeting*, Los Angeles, California, USA.